**Università degli Studi di Torino**
Doctoral School of the University of Torino
PhD Programme in Chemical and Materials Sciences XXXIII Cycle

**Southern Federal University**
PhD in Mathematics and Physics

# Understanding the nature and the evolution of chemical species by advanced data analysis techniques of operando and in situ X-ray spectroscopy experiments

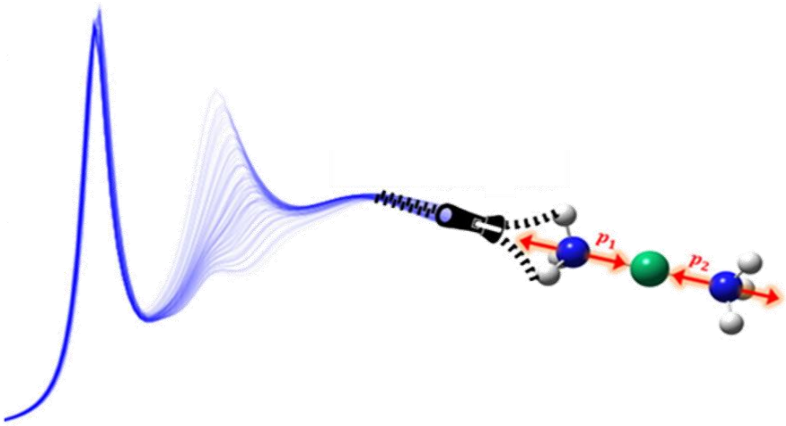

## Andrea Martini

Supervisors:
Prof. Silvia Bordiga (Prof. Carlo Lamberti)
Prof. Alexander V. Soldatov

**Università degli Studi di Torino**

Doctoral School of the University of Torino

PhD Programme in Chemical and Materials Sciences XXXIII cycle

# Understanding the nature and the evolution of chemical species by advanced data analysis techniques of operando and in situ X-ray spectroscopy experiments

Candidate: **Andrea Martini**

Supervisors: Prof. **Silvia Bordiga (Prof. Carlo Lamberti)**
Prof. **Alexander V. Soldatov**

Jury Members: Prof. **Paola D’Angelo**
Università di Roma “La Sapienza”
Dipartimento di Chimica-Fisica

Prof. **Federico Boscherini**
Università di Bologna
Dipartimento di Fisica e Astronomia

Prof. **Lorenzo Mino**
Università degli Studi di Torino
Dipartimento di Chimica

Prof. **Alexander A. Guda**
Southern Federal University
The “Smart Materials” Research Institute

Head of the Doctoral School: Prof. Alberto Rizzuti
PhD Programme Coordinator: Prof. Bartolomeo Civalleri

Torino, 15/11/2020

**Southern Federal University**

Faculty of Science

The "Smart Materials" Research Institute

Department of Physics

# Understanding the nature and the evolution of chemical species by advanced data analysis techniques of operando and in situ X-ray spectroscopy experiments

Thesis submitted in partial fulfilment of the requirements for the degree of *Doctor in Philosophy* at the Southern Federal University, to be defended by

## Andrea Martini

Supervisors:
Prof. Alexander V. Soldatov
Prof. Silvia Bordiga (Prof. Carlo Lamberti)

Rostov on Don, 15/11/2020

*To Professor Carlo Lamberti,*
*A Mentor and a good Friend who left us too early*

*I always thought*
*it was easier to measure*
*X-ray absorption than to calculate it*

Hans Bethe (~1980)

# PREFACE

The main aim of my PhD work is connected to the possibility to give an answer to the following question: given a set of spectroscopic data, referring to a certain sample and acquired under determined experimental conditions (*i.e.* temperature, pressure, gas feed composition, etc.), is it possible to recover i) the spectral signatures and ii) the molecular geometries of the species/sites generating them? These issues are not straightforward, principally for two reasons: first at all, they require to solve an inverse problem: given a spectrum, it is asked to recover the *structure* of the signal-source; second, different molecular species or sites can be collectively responsible of the measured spectral features, making their discrimination and relative speciation sometimes difficult to realize. The main spectroscopic technique that I employed to analyze all the systems reported in this thesis work is the X-ray absorption spectroscopy (XAS). The reason behind the choice of this characterization technique stands in its chemical selectivity and high sensitivity in the interatomic distance and local coordination environment determination. Moreover, XAS can simultaneously provide information on the electronic and local structural properties of the material, contributing significantly to clarify the relation between the atomic structure and the peculiar physico-chemical properties of the system under study.

I tried to solve the first aspect of the main issue assuming that, due to the element selectivity of the XAS technique, an arbitrary XAS spectrum can be decomposed in the sum of a series of spectra referring to all the absorbing element-containing chemical species/sites present in the system, multiplied by their respective fraction. This property, which usually goes under the name of Beer's Law, can be realised using just simple linear algebra concepts, thanks to the relation of linearity among the spectral profiles and their concentrations. Moreover, it can be extended also to the analysis of a XAS dataset, allowing to obtain a clear picture regarding the speciation of the chemical mixture during the variation of a physical or chemical parameter (e.g. time, temperature, gas feed, etc.) [1]. The spectral decomposition procedure, described in this work, combines an unsupervised Machine Learning (ML) approach, named Principal Component Analysis (PCA), with a series of spectral refinements and transformations, which lead to the resolution of a spectral dataset without the employment of any kind of references. The outcomes of this approach are fundamental. Given a XAS dataset, it is possible, in fact, to retrieve a set of physico-chemically meaningful *pure* spectra, without knowing *a priori* their features and realising, in this way, a sort of *blind source* separation.

The possibility to obtain from a XAS spectrum the molecular structure of the species/site generating it constitutes the second aspect of the issues described above. It appears more complicated than the spectral decomposition problem. It requires, in fact, a structural refinement assisted by a series of *ab initio* calculations. During my PhD, I had the honour to take part to the development of the PyFitIt code [2]. This software, written in Python, is the improvement of the old-code named FitIt developed by Smolentsev et al. [3]. PyFitIt allows to retrieve quantitative structural information from the XANES part (X-ray Absorption Near Edge Structure) of a XAS spectrum though a series of ML algorithm, ranging from the linear regression approach till to Extra-Trees and Neural Networks. In particular, this thesis work describes in detail the technique of fitting called *indirect approach*, which allows to predict a XANES spectrum as close as possible to the experimental one starting from a guessed set of structural parameters (e.g. bond lengths, angles, etc.).

Similarly to the XANES case, I extended the *indirect approach* of fit to the Extended X-ray Absorption Near Edge Structure (EXAFS) part of the XAS spectrum. Herein, the ML algorithms were employed to explain the non-linear relation between the *ab initio* derived EXAFS parameters (i.e., the effective scattering amplitude, the total phase shift and the electron mean free path) and the set of user-defined parameters characterising the investigated sample. This approach resulted to be innovative because it allowed retrieving a more general expression of the EXAFS equation detached from the dependency of an input fixed geometry. In this context, I employed the Wavelet Transform (WT) representation of the EXAFS signal [4] to increase the amount of structural information which can be extracted from the experiment and by means of this tool I extended the classical EXAFS fit to the two-dimensional $(k,R)$ space.

The programming knowledges acquired during the PyFitIt design demonstrated to be fruitful also in relation to different topics. In particular, I exploited them in the creation of a second software having as the main purpose the analysis of the soft-XAS (Near Edge X-ray Absorption Fine Structure - NEXAFS) data collected under *in situ* conditions. The code is named THORONDOR [5], it features a graphical user interface (GUI) and it allows the treatment (e.g. background subtraction, de-glitching and normalization) and the pre-edge peak fitting of several NEXAFS spectra preferentially acquired in Total Electron Yield (TEY) mode.

Most of the techniques described above have been applied to the study of a particular class of systems, of relevance in the field of selective redox catalysis: the Cu-exchanged zeolites. These materials are currently the object of intensive research efforts due to their activity in the partial oxidation of methane to methanol (MTM) and to their outstanding performance for deNO$_x$ catalysis *via* NH$_3$-assisted Selective Catalytic Reduction (NH$_3$-SCR) [6, 7]. Understanding which are the active sites characterising these reactions and how, at the atomic scale, the catalyst composition influences the Cu-species formed during the activation is fundamental to unleash the potential of this promising class of catalysts. Concerning this topic, I performed the *in situ* and *operando* spectroscopic characterization of these samples in different experimental and reaction conditions in order to shed light on the electronic and structural properties of the Cu-species relevant for the cited reactions. Herein, the application of the spectral decomposition methods and of the WT analysis of the collected EXAFS profiles allowed accessing an unprecedented level of understanding in a complex multi-component system, yielding novel insights into the identification of the Cu-active sites in the cages of the CHA and MOR zeolites.

The body of this thesis work can be formerly divided in two parts. After a general introduction regarding the XAS spectroscopy provided in **chapter 1**, all the novel analysis methodologies cited before are described in detail in **chapters 2**, **3** and **4**. **Chapters 5** and **6** focus on the *in situ* and *operando* XAS studies conducted over the Cu-CHA and MOR zeolites in connection with the methane to methanol process and the selective catalytic reduction of NO, exemplifying the potential of the developed analysis approaches. Finally, **chapter 7** is dedicated to the conclusions of the dissertation work, while **chapter 8** provides the summary of my publications and conferences/schools attended during the three years of PhD.

## 1.1 REFERENCES

[1] C. Ruckebusch, Resolving Spectral Mixtures: With Applications from Ultrafast Time-Resolved Spectroscopy to Super-Resolution Imaging, Elsevier, 2016.
[2] A. Martini, S.A. Guda, A.A. Guda, G. Smolentsev, A. Algasov, O. Usoltsev, M.A. Soldatov, A. Bugaev, Y. Rusalev, C. Lamberti, A.V. Soldatov, PyFitit: The software for quantitative analysis of XANES spectra using machine-learning algorithms, Comput. Phys. Commun., (2019) 107064.
[3] G. Smolentsev, A.V. Soldatov, FitIt: New software to extract structural information on the basis of XANES fitting, Comput. Mater. Sci., 39 (2007) 569-574.
[4] M. Munoz, P. Argoul, F. Farges, Continuous Cauchy wavelet transform analyses of EXAFS spectra: A qualitative approach, Am. Miner., 88 (2003) 694-700.
[5] D.H. Simonne, A. Martini, M. Signorile, A. Piovano, L. Braglia, P. Torelli, E. Borfecchia, G. Ricchiardi, THORONDOR: a software for fast treatment and analysis of low-energy XAS data, Journal of Synchrotron Radiation, 27 (2020).
[6] E. Borfecchia, P. Beato, S. Svelle, U. Olsbye, C. Lamberti, S. Bordiga, Cu-CHA - a model system for applied selective redox catalysis, Chem. Soc. Rev., 47 (2018) 8097-8133.
[7] M.A. Newton, A.J. Knorpp, V.L. Sushkevich, D. Palagin, J.A. van Bokhoven, Active sites and mechanisms in the direct conversion of methane to methanol using Cu in zeolitic hosts: a critical examination, Chem. Soc. Rev., 49 (2020) 1449-1486.

# CONTENTS

Preface ........ i

1.1 References ........ iii

List of Abbreviations ........ viii

1 Fundamentals of XAS ........ 1

1.1 The origin of the XAFS signal ........ 4

1.1.1 *The XANES signal* ........ 5

1.1.2 *The EXAFS signal* ........ 6

1.1.3 *Understanding the spectroscopic features of the XANES post-edge and EXAFS regions* ........ 9

1.2 Theoretical Construction of an EXAFS spectrum using FEFF ........ 12

1.3 EXAFS quantitative analysis: The fitting metric ........ 14

1.4 Basic detection methods and experimental setups ........ 17

1.4.2 *Fluorescence mode* ........ 18

1.4.3 *High-energy resolution fluorescence detected (HERFD) XANES mode* 19

1.4.4 *Electrons Detection Mode* ........ 19

1.5 References ........ 20

2 XANES Data Analysis: Methods and Improvements ........ 24

2.1 Spectral Decomposition of a XANES dataset ........ 24

2.1.1 *Principal Component Analysis (PCA) of a XANES dataset* ........ 25

2.1.2 *Quantitative methods to extract the correct number of PCs* ........ 30

2.1.3 *Models used to decompose a XANES dataset* ........ 33

2.1.4 *Extending the Spectral Decomposition procedures to an EXAFS dataset* 51

2.2 The Fit of the XANES energy region through a Machine Learning Approach 52

2.2.1 *An application of the indirect approach: The structural refinement of the Fe(terpy)$_2$ excited state* ........ 55

2.3 Machine Learning Powered by Principal Component Descriptors ........ 59

2.3.1 *Two dimensional space of parameters* ........ 61

2.3.2 *N>2 dimensional space of parameters* ........ 63

2.4 References ..... 67

3 EXAFS Data Analysis: Methods and Improvements ..... 74

3.1 Wavelet Transform Analysis of an EXAFS spectrum: A qualitative and quantitative approach ..... 74

3.1.1 *Increasing the EXAFS WT resolution through a FEFF-based wavelet representation* ..... 77

3.1.2 *Retrieving quantitative information from the WT representation: from the power density function plot till to the WT fit* ..... 81

3.2 Fit of the EXAFS energy region through a FEFF-based Machine Learning Approach ..... 84

3.2.1 *Method description* ..... 86

3.3 References ..... 100

4 A new code for the NEXAFS Data Analysis ..... 103

4.1 THORONDOR a software designed for a fast treatment and analysis of NEXAFS spectra ..... 103

4.2 Structure of the Software ..... 104

4.3 Importing and handling raw data ..... 106

4.4 Data treatment ..... 109

4.4.1 *Data energy alignment* ..... 109

4.4.2 *Treating the effect of the window and gas X-ray absorption* ..... 110

4.4.3 *Deglitching* ..... 111

4.5 Background subtraction and second normalization ..... 112

4.5.1 *Splines method* ..... 114

4.5.2 *Single Spline method* ..... 115

4.5.3 *Polynomial curves method* ..... 116

4.5.4 *Asymmetric Least Squares method* ..... 117

4.6 Peak fitting ..... 118

4.6.1 *Estimating the experimental uncertainties* ..... 121

4.6.2 *Evaluation of the goodness of a fit* ..... 121

4.6.3 *Finding uncertainties in fitted parameters* ..... 121

4.7 References ..... 122

5 Investigating by XAS the Active sites for the direct conversion of methane to methanol over Cu-exchanged zeolites ..... 126

5.1 Understanding the Cu speciation and reducibility of Cu-CHA catalysts employing an *in situ* XAS study ........ 130

5.1.1 *Multivariate analysis of temperature-dependent in situ XANES* ..... 134

5.1.2 *Interpretation of the MCR-ALS results: novel elements of complexity affecting reducibility in Cu-CHA* ........ 138

5.1.3 *Structural analysis of the Cu-sites by multi-component EXAFS fits* 141

5.1.4 *Results of single-component fit on the purest He-activated states* 142

5.1.5 *Result of the multi-component fits on the purest He-activated states* 146

5.2 Correlating Cu-speciation from XAS analysis with DMTM productivity for Cu-CHA ........ 149

5.2.1 *EXAFS analysis on CHA (0.5; 12) after $O_2$ Activation at 500 °C* ..... 153

5.2.2 *XAS analysis of composition-dependent reducibility in Cu-CHA and correlation with DMTM productivity* ........ 156

5.3 Comparing He- and $O_2$-activation in Cu-CHA through a MCR analysis of HERFD-XANES data ........ 162

5.3.1 *HERFD-XANES during $O_2$- and He-activation: qualitative analysis.* 162

5.3.2 *MCR-ALS results: evidences for $O_2$-derived Cu(II) species* ........ 164

5.4 Assessing the Nuclearity of the Active sites for the DMTM conversion in Cu-MOR ........ 167

5.4.1 *Cu active site spectroscopic fingerprints from operando XAS* ........ 168

5.4.2 *Enhancing the spectroscopic contrast by MCR analysis of HERFD-XANES* 170

5.4.3 *Quantitative evidences for a di-copper active site* ........ 172

5.5 Identifying Cu-oxo species in Cu-zeolites by XAS: a theoretical survey by DFT-assisted XANES simulation and EXAFS wavelet transform ........ 174

5.5.1 *XANES simulations results* ........ 176

5.5.2 *Wavelet Transform Analysis on simulated EXAFS spectra* ........ 177

5.5.3 *Critical comparison between theoretical and experimental XAS results* 181

5.6 EXAFS WTA of Cu-MOR under model RED-OX conditions: the impact of treatment and composition ........ 184

5.7 Following by EXAFS-WTA the DMTM conversion over MOR (0.18; 7) .. 189

5.7.1 *Key DMTM reaction steps monitored by EXAFS WT* ........ 189

5.7.2 *EXAFS fitting using the WT representation* ........ 191

5.8 Appendix: Experimental Methods 195
5.8.1 *In situ Cu K-edge XAS* 195
5.8.2 *Operando XAS* 195
5.8.3 *HERFD XANES* 196
5.9 References 196
6 Structure and Reactivity of $[Cu_2(NH_3)_4O_2]^{2+}$ Complexes in Cu-CHA catalyst for $NH_3$-Mediated Selective Catalytic Reduction: A XAS study 202
6.1 Oxidation and coordination state of Cu ions 204
6.1.1 *Structure of the* $[Cu_2(NH_3)_4O_2]^{2+}$ *complexes* 205
6.1.2 *EXAFS fitting methods and results* 206
6.1.3 *Validating the structural dynamics of Cu-species by EXAFS Wavelet Transform analysis* 211
6.2 Reactivity of $[Cu_2(NH_3)_4(O_2)]^{2+}$ species towards $NH_3$ and NO 214
6.2.1 *Reactivity towards* $NH_3$ 214
6.2.2 *Reactivity towards NO* 217
6.3 References 219
7 Conclusions 221
7.1 References 226
8 Report on PhD activities 227
8.1 Publications 227
8.1.1 *Papers published in international peer-reviewed journals (ISI Web of Science and/or Scopus).* 227
*8.1.2 Papers submitted in international peer-reviewed journals (ISI Web of Science and/or Scopus).* 229
*8.1.3 Papers in preparation, which will be submitted in international peer-reviewed journals (ISI Web of Science and/or Scopus).* 229
8.2 Contribution to congresses and other scientific events 230
*8.2.1 Oral contributions* 230
*8.2.2 Poster contributions* 230
*8.2.3 School attended during the PhD.* 231
8.3 Teaching Activities 231
8.4 Experiments at Large Scale Synchrotron Facilities 231
Acknowledgements 232

# LIST OF ABBREVIATIONS

- AEY: Auger Electron Yield
- ALS: Alternating Least Squares (approach)
- DFT: Density Functional Theory
- DMTM: Direct Methane to Methanol (conversion)
- DW: Debye-Waller
- EXAFS: Extended X-ray Absorption Spectroscopy Near Edge Structure
- FT: Fourier Transform
- FTIR: Fourier Transform Infrared Spectroscopy
- HERFD-XANES: High Resolution Fluorescence Detected XANES
- HF: Hartree-Fock
- LCA/LCF: Linear Combination Analysis/ Linear Combination FIt
- LCAO: Linear combination of atomic orbitals
- LT: Low Temperature
- LUMO: Lowest Unoccupied Molecular Orbital
- MCR: Multivariate Curve Resolution
- ML: Machine Learning
- MS: Multiple Scattering
- MT: Muffin Tin
- MTM: Direct Methane to Methanol
- NEXAFS: Near Edge X-ray Absorption Spectroscopy Fine Structure
- PCA: Principal Component Analysis
- PFY: Partial Fluorescence Yield
- RMC: Reverse Monte Carlo
- RMS: Root Mean Square
- RSMS: Real Space Multiple Scattering (approach)
- SCR: Selective Catalytic Reduction
- SS: Single Scattering
- SVD: Singular Value Decomposition
- TEY: Total Electron Yield
- TM: Transformation Matrix (approach)
- W.L.: White Line
- WT/WTA: Wavelet Transform/ Wavelet Transform Analysis
- XANES: X-ray Absorption Spectroscopy Near Edge Structure
- XAS: X-ray Absorption Spectroscopy

# 1 FUNDAMENTALS OF XAS

Let’s consider a collimated X-ray beam, possessing a flux $\Phi_0$ evaluated as the number of photons per unit time and unit cross-section. If the beam impacts and traverses a sample of thickness $\mathrm{x}$, as depicted in **Figure 1.1**, its flux is reduced according to the Beer’s Law:

$$\Phi = \Phi_0 \exp[-\mu(\mathrm{E})\mathrm{x}] \tag{1.1}$$

Where $\Phi$ is the photon flux passing through the sample, while $\mu(\mathrm{E})$ is the linear attenuation coefficient depending on the X-ray energy $\mathrm{E} = \hbar\omega$ and on the sample composition and density.

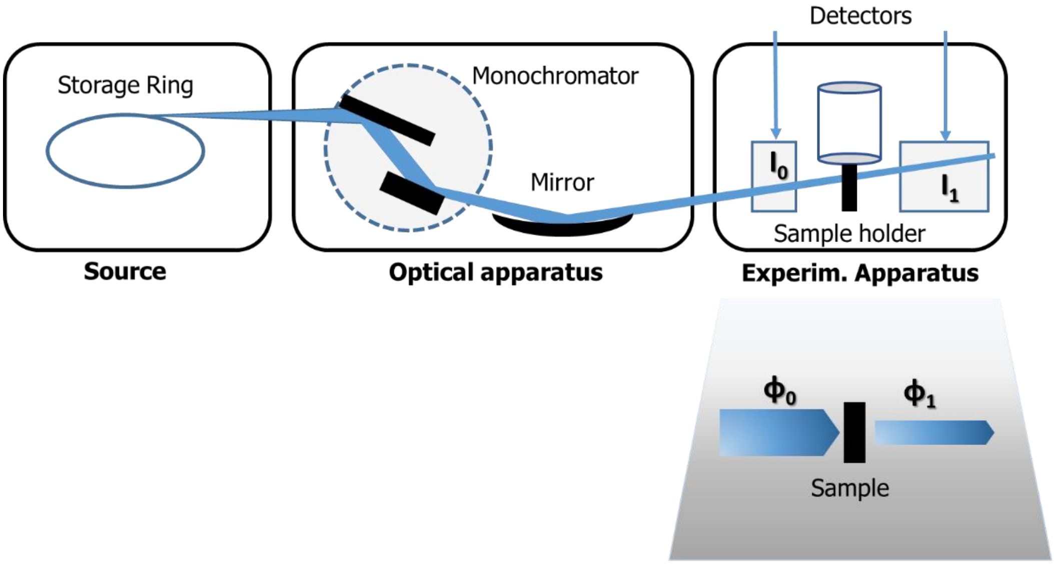

**Figure 1.1:** Schematic picture of a Synchrotron Radiation laboratory for a XAFS experiment (transmission mode). Once that that a high brilliance photon flux has been produced from a storage ring (using a bending magnet or a wiggler for example) only determinate photons, having a defined wave-length, are selected through a double crystal (usually Si 111 or Si 311) monochromator. Afterwards, the beam is focused on the sample using an ellipsoidal mirror. The photon flux before $\phi_0$ and after $\phi_1$ the sample is measured using two detectors consisting, generally of two ion chambers working in Geiger mode regime providing for $\phi_0$ and $\phi_1$ two values of currents $I_0$ and $I_1$. The natural log of their ratio is proportional to the sample absorption coefficient $\mu(E)$. Adapted from [1]

It is possible to assert that, varying the X-ray photon energy, two main mechanism can contribute to the X-ray attenuation: the photo-electric absorption effect and the photon scattering process [1]. In the first-one, when one photon is absorbed from the beam, an atom is ionized or excited, while in the second-one, the photon is deflected from the original trajectory by the collision with an electron. Herein the scattering type can be elastic (Thomson) or inelastic (Compton). In general, the energy range regarding most of the X-ray absorption applications is within (400 eV and 40 keV). In this energy region, the photo-electric-absorption is dominant, see

**Figure 1.2**, and it is possible to approximate the total attenuation coefficient appearing in (1.1) with the photo-electric absorption coefficient. This is the quantity currently derived, as a function of the incident X-ray energy, from an X-ray Absorption Spectroscopy (XAS) experiment. Focusing on it, it is interesting to note that when the beam energy increase, the X-rays become more penetrating and, as a consequence, their intensity generally smoothly decreases approximately as $1/E^3$. This smooth trend is interrupted by sharp discontinuities: the absorption edges, which emerge from the fact that each X-ray photon liberates an electron from an inner atomic level.

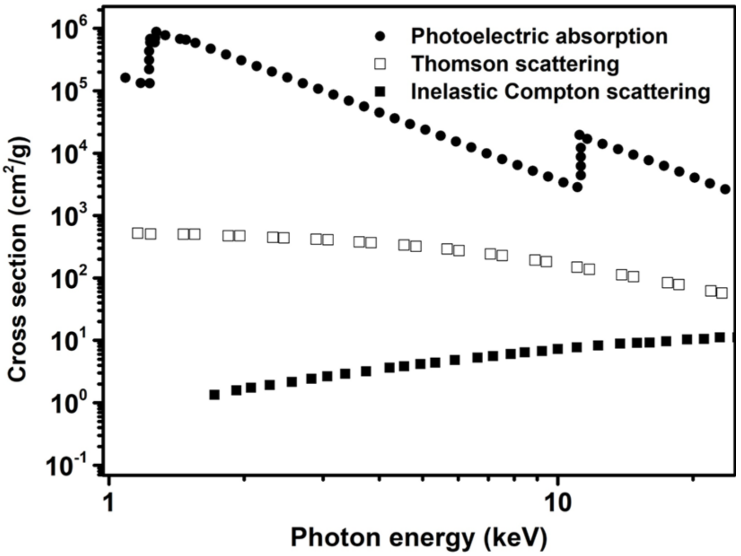

**Figure 1.2:** X-ray cross sections for Germanium. Adapted from [1].

The nomenclature of the edges uses progressive letters and numbers depending on the orbitals from where the electron is extracted, see **Table 1.1**. The following table establishes the connection between the energy edges and the core electronic levels up to the M transitions:

| **Edge** | K | $L_1$ | $L_2$ | $L_3$ | $M_1$ | $M_2$ | $M_3$ | $M_4$ | $M_5$ |
|---|---|---|---|---|---|---|---|---|---|
| **Core Level** | 1s | 2s | $2p_{1/2}$ | $2p_{3/2}$ | 3s | $3p_{1/2}$ | $3p_{3/2}$ | $3p_{3/2}$ | $3p_{5/2}$ |

**Table 1.1:** Edge nomenclature as a function of the core electronic levels. Adapted from [1]

The edge-energies represents, for each elements a sort of *atomic fingerprint*. In fact, the since the binding energies of the electrons increase monotonically with the atomic number, an edge energy corresponds to a well defined atomic species. Here it comes one of the most important property of the XAS spectroscopy, which is the element-selectivity.

After the absorption of an X-ray photon, an isolated atom can be either excited, if the photon energy corresponds to the energy difference between an electronic core level and an occupied bound level, or ionized, if the photon energy is larger than the binding energy, in this case, the electron is ejected from the atom.

In correspondence of an edge, the absorption coefficient exhibits a series of spectral features constituting the so-called: X-ray Absorption Fine Structure (XAFS) [1]. For isolated atoms (e.g. noble gases, metallic vapours), the XAFS region is limited to a few of eV around the edge and reflects the transitions of the core electrons to unoccupied bound levels. On the other hand, considering molecular gases or condensed systems, the XAFS appears to be strongly influenced by the presence of atoms surrounding the absorber and it can extend up to and beyond 1 keV above the edge [1].

Traditionally, the XAFS signal is generally distinguished in in two parts, see **Figure 1.3**(a,b,c):

- The X-ray Absorption Near Edge Structure (XANES) or, Near edge XAFS (NEXAFS), for the soft X-rays. It constitutes the region including a few tens of eV before and after the edge and can be divided, in turn, into three parts: the pre-edge, the edge and finally the post-edge.
- The Extended X-ray Absorption Fine Structure (EXAFS). It regards the fine structure extending from the XANES post-edge region up to typically 1 keV.

In the following a more detailed description of each region of the XAS spectrum is provided.

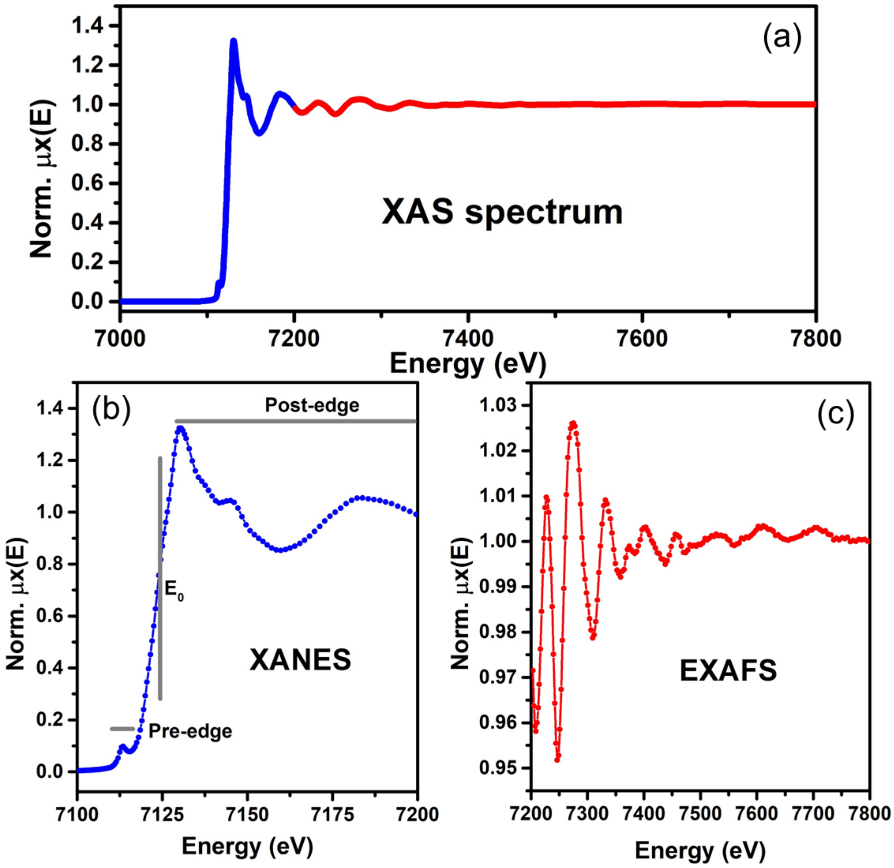

**Figure 1.3:** (a) Pictorial representation of the K-edge Fe XAS spectrum. As it is possible to see, it is formerly divided in two regions: XANES -blue curve- (b) and EXAFS -red curve- (reported as a function of the photon energy) (c). The XANES part is further organised in three parts: the pre-edge, the edge ($E_0$) and the post-edge regions.

## 1.1 THE ORIGIN OF THE XAFS SIGNAL

The physical origin of the XAFS signal can be explained by means of the scattering theory [2]. For simplicity, the one-electron and the non-relativistic approximations are here adopted. In this framework, the photoelectric absorption process is described as a transition between an initial state $|\psi_i\rangle$ (incident photon of energy $\hbar\omega$ and electron in a core orbital with binding energy $E_0$) and a final state $|\psi_f\rangle$ (core hole and excited electron) with final energy equal to: $E_f = \hbar\omega + E_0$ . Here two possible case can appear. i) If the photon energy is lower than $E_0$, in the pre-edge region, the electron is promoted to empty bound atomic states. On the contrary, ii) when the energy of the photon is sufficiently high to promote the electron to the continuum (ionization), then the free electron can be depicted as an outgoing spherical wave with wavenumber $k$:

$$k = \sqrt{\frac{2m}{\hbar^2}(\hbar\omega - E_0)} \tag{1.2}$$

Where $\mathrm{m}$ is the electron mass, $\hbar$ is the reduced Planck constant and the difference $\mathrm{E_k} = \hbar\omega - \mathrm{E_0}$ is the electron kinetic energy. If the photoelectron is scattered by the electrons in the surrounding atoms, its wave function is modified by the atoms potential and the final state is composed not only by the outgoing spherical wave but also by the backscattered waves that perturb the system and consequently the absorption cross section, which is the measured observable. These two processes stand formerly at the basis of the XAFS signal.

### 1.1.1 *The XANES signal*

As previously stated, the extraction of an electron from an atomic core shell can result either in an excited electronic state (if the electron is promoted to an unoccupied discrete level) or in an ionized atom if the electron has sufficient energy to reach the continuum valence band.

In the pre-edge, the so called pre-edge peaks, mainly originate from the dipole allowed transitions from a core level to a discrete bound final state. Their peak position indicates the energy needed for the transition, while the intensity is proportional to the probability that the electron could be promote to a certain state according to the selection rules. In case of solids, in this energy region, the hybridization of the electronic levels is strongly affected by details of the crystalline field caused by the ligand geometry, while in case of molecules the abundance of empty states can be properly described through the Hartree-Fock (HF) LCAO theory. As a consequence, this phenomenon gives rise to large spectral differences also for elements in the same valence state but having different local structure. In general, it is possible to notice that the K pre-edge features are dominated by dipole allowed excitations of s electrons to p-symmetry orbitals, while transitions to d orbitals are definitively scarce (quadrupolar transitions) [3]. However, the hybridization may give origin to a p-d mixing determining intense dipole allowed transitions of 1s electrons to the p-component of the hybrid orbitals [3].

The XANES edge energy $\mathrm{E_0}$ defines the onset of the continuum state and it is related to the oxidation state of the photoabsorber [3]. It is worth noting, in fact, that more the atom is oxidized, higher will be the energy needed to ionize it. The $\mathrm{E_0}$ position has been early recognized as a valuable method to identify the valence state of the absorbing atom [2]. The shape of the edge is often characteristic of the chemical environment and of the ligand geometry. This fact lead to its employment as a fingerprint of particular chemical species [2, 3]. The white line (W.L.) (maximum of the edge), can represent either the more probable transition to a discrete state or to the first unoccupied valence level. An interesting example is represented, for example, by the $L_2$ and $L_3$ edges of the nd metals signalling the $p_{1/2} \rightarrow nd$ and $p_{3/2} \rightarrow nd$ transitions, as it will be showed in **chapter 4**. Dealing with low Z elements or with molecules the analysis can be even more complicated because of transitions of core electron to Rydberg, states localised just below the ionization threshold, or to states present in the continuum due to centrifugal barrier, effect usually named as *shape resonances* [4].

The proper theoretical description of the pre-edge and of the edge region of XANES spectra usually requires the many body corrections which can be treated by: (i) using the multiplet approach [5, 6] and the more robust MLFT method based on Wannier orbitals [7]; (ii) solving the Bethe-Salpeter equation [8, 9]; (iii) applying post HF methods [10, 11]; (iv) by using the dynamic mean field theory [12]; or by expanding the many-electron system self-energy in a series of products of Green functions and the screened Coulomb interaction [13].

Finally, the post-edge region, extending within 30-50 eV above the edge, take places from the to photoelectrons excited in continuum states. Due to the long mean free path (λ) of low energy electrons (see **Figure 1.4**) the absorption signal is dominated by several scattering process involving the ejected photo-electron with the atoms surrounding the absorber, which usually go with the name of Multiple Scattering (MS). The recent progresses in ab-initio XANES modelling, especially with the codes: CONTINUUM [14], FEFF [15] and FDMNES [16], provided a valuable details about the local structure and coordination geometry of the system under study. In **section 1.1.3** a more detailed description of the process at the basis of this region is provided.

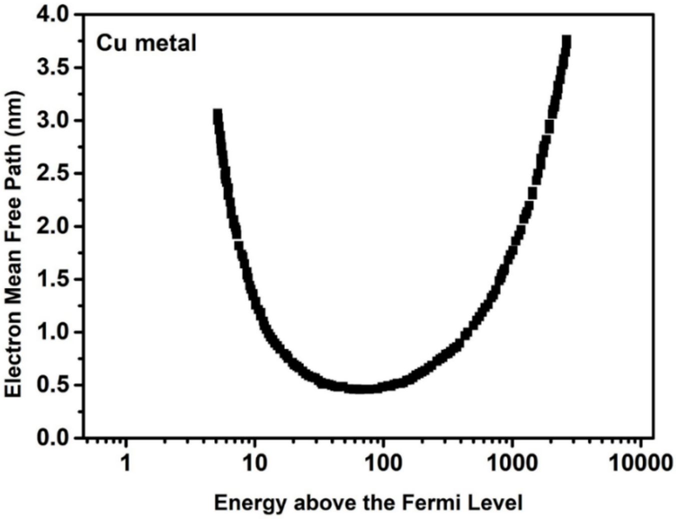

**Figure 1.4:** Electron mean free path $\lambda(E)$ trend for metal Cu. Adapted from [3].

Concerning the possibility to retrieve quantitative structural information from a XANES spectrum, two approaches can be followed. The first-one, consists to guess a particular structure which is supposed to be close to the molecular site responsible of the XANES signal, afterwards the total XANES profile can be simulated and the main XANES features can be compared qualitatively with the experiment [2]. The second method foresees to perform a fit of the XANES region. To this aim, it is possible to follow a Reverse Monte Carlo approach (RMC), as realised by the MXAN code [17], or employ a multidimensional interpolation-based approach, which is at the basis of FitIt [18]and of its new version PyFitIt [19], whose description and applications are reported in **section 2.2** of **chapter 2**.

### 1.1.2 *The EXAFS signal*

The spectroscopic region extending after the XANES post-edge region (from 30-50 eV up to 1 keV) is named EXAFS. It is usually extracted from the XAS spectrum subtracting a spline function fitting the monotonic progress of the absorption curve $\mu_0$ (this profiles tries to mimic the absorption coefficient of a bare atom without any neighbour atoms), see the red profile in **Figure 1.5**(a). Afterwards, the incident photon energy is, for convention, converted in the wavenumber $\mathrm{k}$ of the emitted photoelectron (instead of the photon energy as it has been reported in **Figure 1.3**(c)), showed in **Figure 1.5**(b) and denoted with the symbol: $\chi(\mathrm{k})$.

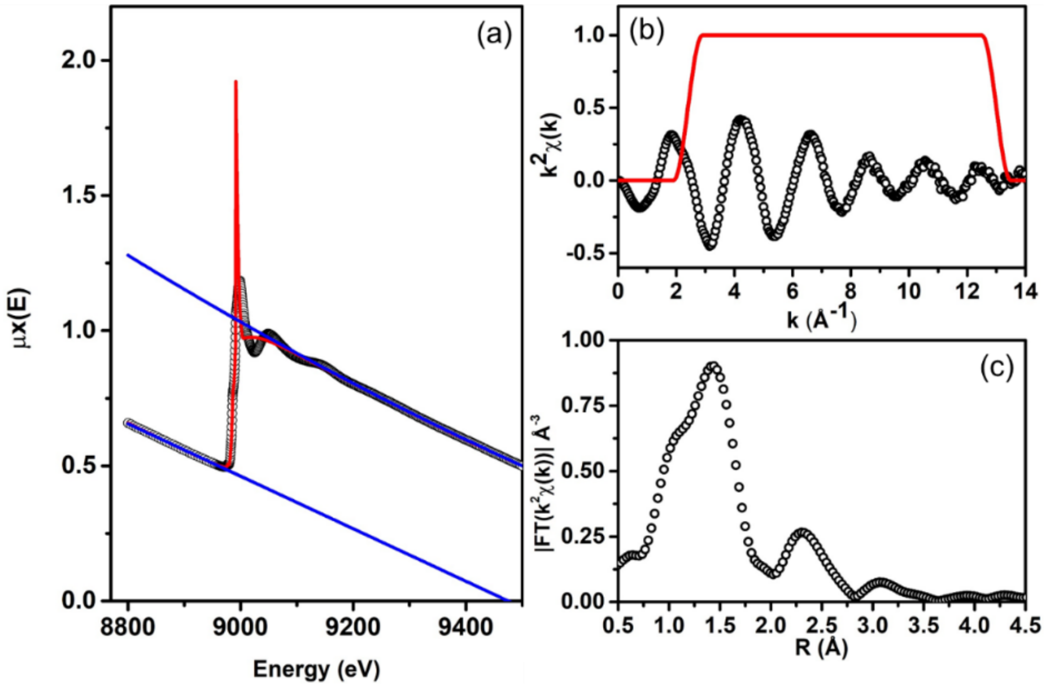

**Figure 1.5:** (a) Experimental XAS (Cu K-edge) signal (black circles) plotted together the bare atom absorption profile $\mu_0$. The blue splines curve are employed to remove the XAS background and to normalize the spectrum to the edge jump. More information about this procedure can be found in **1.4.1.1** and in chapter 4. (b) $\chi(k)$ EXAFS signal weighted for a factor $k^2$ in order to enhance its major spectral features. The red window is an apodization function (here a Hanning window) employed to select the range in $k$ which is then Fourier Transformed. (c) Magnitude of the Fourier transform for the $k^2\chi(k)$ signal showed in (b).

The reason which stands at the basis the distinction between the EXAFS and the XANES post-edge part arises from the profound differences on the major phenomena involved and on the data analysis procedure used to treat the data [3]. Differently from the XANES region, the EXAFS part, due to the lower photoelectron mean free path (see **Figure 1.4**) is characterised mainly by single scattering (SS) phenomena, which are the principal responsible of the train of oscillations characterising the signal. The following phenomenological picture, showed in **Figure 1.6**(a,b,c), can be used to clarify the origin on of the EXAFS signal. As already discussed in the introduction of **section 1.1**, once that a photoelectron is promoted from an atomic core state (e.g. 1s) of an atom A to the continuum region, the electron final state wavefunction would be an outgoing spherical wave (maintaining the symmetry of the 1s orbital) and no fine structure would appear in the absorption coefficient [1]. On the contrary, if the absorber atom is non-isolated, the photo-electron can be scattered by a neighbour atom B, giving rise to incoming spherical waves. Consequently, the total photo-electron wavefunction becomes the superposition of the outgoing and the scattered wave. This is an example of a SS process. In case the photo-electron would be scattered, after the atom B, by a second atom C, see **Figure 1.6**(d) it is possible to use the term MS to describe this kind of process, which, as described in **section 1.1.1,** becomes relevant getting closer to the absorption edge. Returning on the SS process involving the centres A and B, it is possible to assert that the phase relationship between the outgoing and the scattered wave, evaluated at the core site of atom A, depends on the photo-electron wavelength and on the distance $\mathrm{R}$ between the atoms A and B. Moreover, the variation of the phase as a function of the absorbed photon energy influences the amplitude of the total wave-function at the core site, giving rise of the observable modulations of the absorption coefficient. It follows that considering a process characterized uniquely or principally by SS, the Fourier Transform (FT) magnitude can show with its peaks the radial distances of the scatteres evaluated from the absorbing atom position, see **Figure 1.5**(c). As pointed out, for the first time, in 1971, by Sayer, Sterne and Lytle in their pioneering works [20-23], the frequencies position of the EXAFS oscillations, evaluated through the magnitude of the Fourier Transform (in the direct space $\mathrm{R}$), depends on the distances between the absorber and the back-scatterer atoms, while their amplitudes (in absence of MS processes) are proportional to the number of atoms surrounding it. The same authors proposed also an equation, known nowadays as the EXAFS equation, describing the behaviour of the fine structure in the EXAFS region:

$$\begin{gathered}\chi(\mathrm{k}) = \mathrm{S}_0^2 \sum\nolimits_{\mathrm{s}} \frac{\mathrm{N_s}}{\mathrm{kR_s^2}} |\mathrm{F_s(k)}| \sin\big(2\mathrm{kR_s} + \phi_{\mathrm{s}}(\mathrm{k})\big) \\ \times \exp(-2\mathrm{R_s}/\lambda_{\mathrm{s}}(\mathrm{k}))\exp(-2\mathrm{k}^2{\sigma_{\mathrm{s}}}^2)\end{gathered} \tag{1.3}$$

This equation is written in the SS approximation. For a more general equation of the EXAFS equation including also the MS contributions and its further implementations, the reader can refer to **chapter 3** of this thesis. Considering equation (1.3) it is possible to note that the sum is carried out on the variable $\mathrm{s}$ denoting the so called shell number. The concept of shell is widely used in the EXAFS analysis and it generally represents a group of $\mathrm{N_s}$ atoms (which can have also different Z) sited at a common average distance $\mathrm{R_s}$ from the absorber. Each of these scatterers is employed in a SS process with the ejected photoelectron coming from the absorbing atom and it is responsible of an oscillatory contribution $\sin(2\mathrm{kR_s} + \phi(\mathrm{k}))$ abated by the exponentials: $\exp(-2\mathrm{R_s}/\lambda(\mathrm{k}))$ and $\exp(-2\mathrm{k}^2{\sigma_{\mathrm{s}}}^2)$. The parameters appearing in (1.3) can be divided formally in two main groups.

The local structural parameters:

- $\mathrm{N_s}$: is the number of atoms internal to the $\mathrm{s}^{\mathrm{th}}$ coordination sphere and influence the amplitude of the EXAFS signal.
- $\mathrm{R_s}$: is the interatomic distance of the $\mathrm{s}^{\mathrm{th}}$ coordination sphere and influences the frequency of the EXAFS signal.
- ${\sigma_{\mathrm{s}}}^2$: is so called Debye-Waller (DW) factor, it represents the mean square relative displacement of the scattering atoms from their average position [1, 24, 25].

The physical quantities :

- ○ $F_s(k)$ and $\phi_s(k)$: are the effective backscattering amplitude factor and the total phase shift, they can be experimentally obtained from the EXAFS spectrum of a reference sample or from *ab-initio* calculation (as it will be described later), reproducing the potential experienced by photoelectron [1, 24, 25].
- ○ $S_0^2$ and $\lambda_s(k)$: are the passive electron reduction factor (close to 1) and the photoelectron mean free path. They are inelastic terms and modify the amplitude of the EXAFS signal. More information about these terms can be found in [1].

Having a theoretical curve and being in possess of an experimental EXAFS spectrum it is possible to extract through a fit the coordination number of the neighbours atoms and their relative distances from the absorbing center. A detailed description about the EXAFS fitting procedure is reported in **section 1.3** and in **chapter 3**.

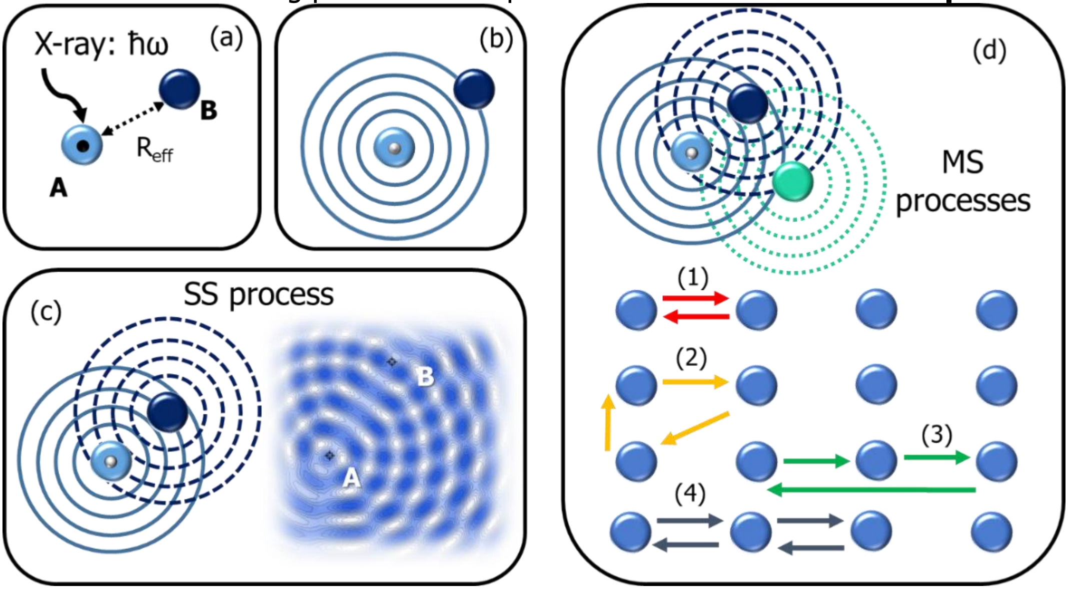

**Figure 1.6:** (a,b,c) Pictorial representation of a SS process. In figure (c), on the left, the stereo plot associated to the SS process, involving atoms A and B, is reported. (d) Scheme depicting arbitrary MS processes. On the bottom are reported, using the arrows notation, different typologies of MS paths (excluding the SS path (1) in red) characterized by different legs and angles: (2) and (3) are three legs MS paths while (4) is a collinear MS characterized by four legs.

### 1.1.3 *Understanding the spectroscopic features of the XANES post-edge and EXAFS regions*

To give a mathematical description of the XANES post-edge and of the EXAFS parts, it is worth underlying that, according to Fermi's golden rule, reported in equation (1.4), the transition rate between two states $|\psi_i\rangle$ and $|\psi_f\rangle$, in presence of a time-dependent perturbation, is a function of the density of the final states and of the matrix element of the Hamiltonian $\mathcal{H}$ describing the interaction of the electron with the electromagnetic field [2]:

$$w_{i\to f} = \frac{2\pi}{\hbar} |\langle\psi_f|\mathcal{H}|\psi_i\rangle|^2 \rho_i(\mathrm{occ.})\, \rho_f(\mathrm{unocc.}) \tag{1.4}$$

For medium-high Z elements and for K and L edges, $\rho_i(\mathrm{occ.}) = 1$ and may be neglected in equation (1.3) [2]. For a sinusoidal time-dependent electromagnetic field, the Hamiltonian $\mathcal{H}$ can be expressed as: $\mathcal{H} \approx \hat{\boldsymbol{\epsilon}} \cdot \mathbf{r}\exp(\mathrm{ik} \cdot \mathbf{r})$ and the coefficient of absorption becomes:

$$\mu(\mathrm{E}) \propto \sum\nolimits_{\mathrm{f}} |\langle\psi_{\mathrm{f}}|\hat{\boldsymbol{\epsilon}} \cdot \mathbf{r}\exp(\mathrm{ik} \cdot \mathbf{r})|\psi_{\mathrm{i}}\rangle|^2 \,\delta(\mathrm{E} - \mathrm{E}_0 - \hbar\omega) \tag{1.5}$$

Where $\hat{\boldsymbol{\epsilon}}$ , $\hbar k$, and $\hbar\omega$ are the X-ray electric polarization vector, momentum, and energy, while the subscript $\mathrm{f}$ denotes that the sum is carried out over all the unoccupied final quasi-particle states $|\psi_{\mathrm{f}}\rangle$.

A quantitative interpretation of the XAS fine structure can be obtained calculating the matrix element present in equation (1.5). In order to simplify the expression, it is possible to introduce a further approximation. The exponential of (1.5) can be expanded as a series as: $\exp(\mathrm{ik} \cdot \mathbf{r}) = 1 + \mathrm{k} \cdot \mathbf{r} + \mathrm{O}(2)$, where the first and dominant term is representing the dipole interaction while the subsequent terms are associated with quadrupole and higher order multipoles. For the complete calculation, different methods can be adopted. The most commonly used is the Real Space Multiple Scattering (RSMS) approach [15], in which the atomic potentials are approximated as spherically symmetric out to a finite radius while the interstitial potential between them is considered constant. This approximation, called Muffin Tin (MT), see **Figure 1.7**, shows however some problems: First, it makes the results dependent on the size of the interstitial region between the so called MT spheres. Second, this approximation becomes serious especially when the photoelectron kinetic energy is close to the value of the approximation made on the potential [2]. Generally, in the EXAFS region, the kinetic energy of the electron is large enough that small variations in the interstitial potential do not make much difference, and the muffin-tin approximation works well [24]. On the contrary, in the XANES region, the muffin-tin approximation is less satisfactory and in order to obtain finer and more quantitative results, it is necessary to employ different techniques involving full-potential methods such as the finite difference approach embodied in FDMNES [16]. Herein the Schrödinger three-dimensional differential equation is solved numerically recurring to the finite difference approach. This solution avoids to impose any constriction on the shape of the potential, but it is very costly in terms of calculation time [2]. To partially reduce the computational time, in concrete terms, the calculation of final states is done differently in three regions, with spherical harmonics development in a short sphere around the center of the atoms, with finite difference methods for a grid of points selected in the inter-atomic zone, and with constant potential in an outer sphere [16].

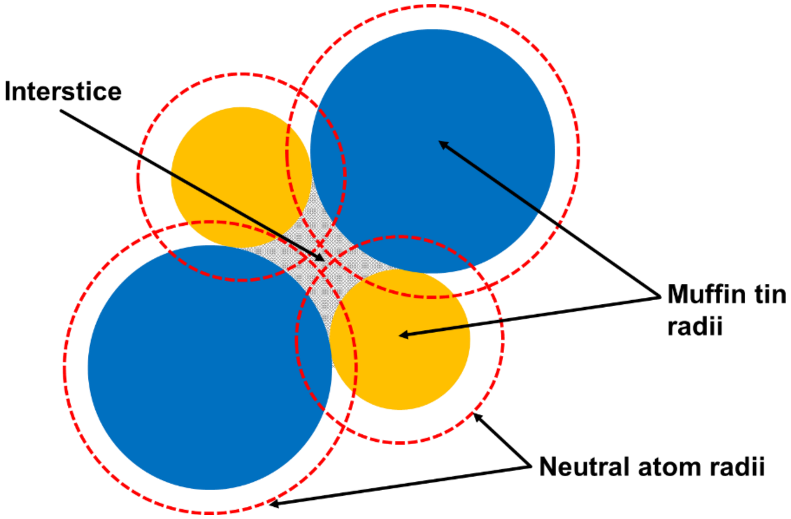

**Figure 1.7:** Schematic representation of the construction of the muffin-tin potential adapted from [26]. The overlap of atoms is handled using some variation of the Mattheiss prescription [27] in which Wigner–Seitz cells are created about each position in the cluster, then spheres are inscribed in the cells. These MT spheres are, in most cases, smaller than the neutral atom spheres, as shown schematically by the red dashed circles in the figure. The MT spheres necessarily contain less electron charge than the larger neutral atom spheres. This excess of charge is distributed uniformly throughout the volume occupied by the cluster.

Focusing on the RSMS theory, the employment of the Green function representation of the scattering processes [28] lead to the possibility to decouple the absorption expression into two contributions, $\mu_0$ and $\chi$:

$$\mu(E) = \mu_0(1 + \chi) \tag{1.6}$$

The first factor $\mu_0$ is the contribution deriving from the bare absorbing atom. On the other hand, the second term appearing in equation (1.6) is the fine structure signal. The fact that the letter has been indicated with the same notation proper of the EXAFS signal written in (1.3) is not surprising. Rehr and Albers, in [29], demonstrated that the total EXAFS signal $\chi(k)$ can be written as an infinite sum of scattering processes: from the simple SS till to the higher order MS. Using this approach the subscript $s$,appearing in equation (1.3), must be changed with the letter $i$ denoting the path followed by the electron during the interaction with one ore more neighbouring atoms, see **Figure 1.6**(c). In case of a SS path, equation (1.3) remain valid: $R_i$, is the half-path length (independently from the scattering type; the total path length of the photon-electron is, in fact, $2R_i$) and it represents always the distance among the absorber and the $i^{\text{th}}$ scatterer having a backscattering amplitude, a phase and an electron free mean path equal to $F_i(k)$, $\phi_i(k)$ and $\lambda_i(k)$, respectively. The parameter $N_i$ continues to maintain the same meaning of the one present in (1.3), indicating those SS processes involving the same type of atoms and providing a comparable contribution to the total EXAFS signal. On the other hand, for any kind of MS path, $R_i$ consists in a function (non-linear) of the relative distances of the scatterers involved in the process. In case of a MS process, the half paths length becomes a useful metric because the contribution, from that path to the FT of the signal, will be peaked at approximately the same place in $R$ as a single scattering path of the same half path length [30].

Similarly for a SS process, it is possible to estimate also for any MS path the related $F_i(k)$, $\phi_i(k)$ and $\lambda_i(k)$ functions, while $N_i$, for these cases, corresponds to the number of MS paths of the same type and it is named as path *degeneracy*.

The approach described above and represented by equation (1.6) can be adopted successfully only when the energy is sufficiently higher than the one characterising the XANES post-edge region. In fact, at relatively lower energies (few eV over the absorption edge), the scattering probability is much higher and the path expansion usually don't converge. In this case more complex and time-consuming alternatives need to be used, such as full matrix inversion based on the Green function approach and implemented in CONTINUUM or in FEFF [31], the finite difference method, introduced by Joly, described before [16] or the Haydock's recursion technique [32].

## 1.2 THEORETICAL CONSTRUCTION OF AN EXAFS SPECTRUM USING FEFF

In the following, a brief description regarding the generation of a FEFF-derived theoretical EXAFS signal is provided. Afterwards, the procedure concerning the EXAFS fit methodology is discussed in detail.

Starting from the input structure provided by the user, the FEFF program calculates through the Dirac-Fock equation, the electronic structure of the atoms of the materials as free, isolated entities. The atomic charge densities are then superimposed in the desired geometry and averaged to create the MT potentials with a prescribed degree of overlap, see **Figure 1.7**, (which can be modified by the user through the keywords FOLP or AFOLP). The mean free path $\lambda_i(k)$ is calculated from the imaginary part of the interstitial potential between the atoms and the core-hole lifetime. Once the spherically symmetric MT potentials are generated, the scattering phase shifts $\phi_i(k)$ can be calculated by integration within the atomic potential outward to the radius, and matching the boundary conditions to free spherical waves between the atoms [24].

Finally, the effective scattering amplitudes $F_i(k)$, calculated through the Rehr and Albers method [29], are associated to the SS and MS scattering process extracted through the Zabinsky algorithm [33]. The latter is discussed now more in detail because it stands at the basis of the result that are showed in **chapter 3** (**section 3.2**).

The first step in the path generation process consists to identify and enumerate all the possible paths which can provide a not negligible contribution to the total, theoretical spectrum. To this aim, the FEFF routine employs the algorithm developed by Zabinsky et al. [33]. .Basically, it begins by first enumerating all single scattering (SS) paths within the input cluster, see **Figure 1.8**(a). Afterwards, every possible scattering process involving two external scatterers (already catalogued as a MS process) are constructed by extending each single scattering path to all possible third atoms, as depicted in **Figure 1.8**(b). Because, the photoelectron cannot scatter twice from the same atom, the successive atom must be clearly different. Each subsequent higher order of scattering, see **Figure 1.8**(c), is then constructed from the previous order by extending from the last atom of every path to every other atoms in cluster [30]. The paths are sorted by increasing half-path length using a heap, which is a tree-like data structure [33], constructed to guarantee that the path with the shortest half-path length is always at the top of the tree. As already stated in **section 1.1.3**, for a SS path, then, the half-path length is the atomic separation. As certain paths are removed from the heap, they are compared for degeneracy with all paths previously removed from it. An obvious example of degeneracy is two SS paths from atoms in the first coordination shell. Since these two paths would produce identical contributions to the EXAFS, they are considered degenerate. Various, non-obvious sorts of degeneracy are considered in FEFF, including the time-reversal (scattering from the atoms in a multiple scattering path in the opposite order) or mirror symmetry about a plane in a high order path [33].

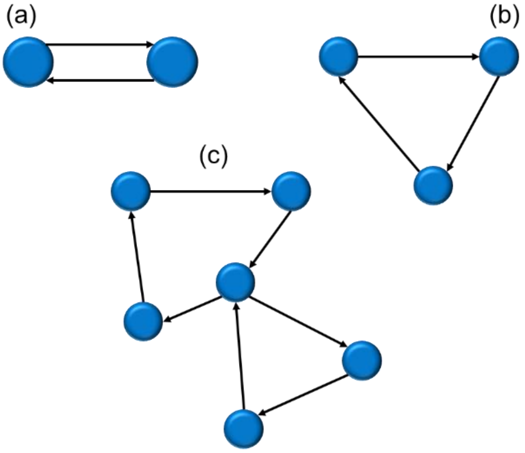

**Figure 1.8:** Schematic illustrating the sequential construction of the MS paths: (a) SS; (b) three leg MS process, (c) higher order MS process generated starting from (b).

As discussed in **section 1.2**, the EXAFS signal can be written as an infinite sum of different scattering paths. Some paths can be degenerate and, for this reason, they can be grouped together. However, there will be always a certain number of paths whose contribution to the total EXAFS signal can be neglected. In FEFF there are in total four filters, which can be applied in order to reduce the number of paths characterised by a low contribution in the total EXAFS representation. These are: the $\mathrm{C_{heap}}$ , $\mathrm{C_{keep}}$ , $\mathrm{C_{pw}}$ and $\mathrm{C_{cw}}$ filters. Using this constraints the paths are eliminated at four stages during the FEFF calculation: (a) during the path construction ($\mathrm{C_{heap}}$), (b) after construction but before the degeneracy checks ($\mathrm{C_{keep}}$), (c) after the path list is complete and the check on the degeneracies has been performed ($\mathrm{C_{pw}}$) and finally after a full curved-wave XAFS calculation on the surviving paths with further full degeneracy checks ($\mathrm{C_{cw}}$). The last two filters, $\mathrm{C_{pw}}$ and $\mathrm{C_{cw}}$, are more accurate but require more computations. They are, in fact, able to filter alone all paths through the third SS distance. $\mathrm{C_{pw}}$ and $\mathrm{C_{cw}}$ are the only two terms whose value can be modified by the FEFF user through the keyword CRITERIA. In particular, the $\mathrm{C_{pw}}$ filter is based on the plane wave approximation (more detail about its implementation can be found in [33]), while the $\mathrm{C_{cw}}$ quantity is calculated for each path employing the mean curve-wave amplitude:

$$\chi_i^{cw} = \frac{1}{\Delta k} \int_0^{k_{max}} dk |\chi_i(k)| \tag{1.7}$$

Where the integral is approximated over nine evenly spaced $\mathrm{k}$ points, and $\chi_{\mathrm{i}}(\mathrm{k})$is the full curved-wave calculation for path $\mathrm{i}$, including degeneracy, electron mean free path …

The curved-wave filter is then implemented as the ratio: $\mathrm{C_{cw}} = \frac{\chi_{\mathrm{i}}^{\mathrm{cw}}}{\chi_1^{\mathrm{cw}}}$ where $\chi_{\mathrm{i}}^{\mathrm{cw}}$ is normalized by the value at the first-neighbour $\chi_1^{\mathrm{cw}}$ distance and expressed as a %. This filter does not save any computation time in paths enumeration, but by eliminating the remaining unimportant paths, it greatly simplifies the analysis, and it provides a quick estimate of actual path importance [33].

The $\mathrm{F_i(k)}$, $\phi_{\mathrm{i}}(\mathrm{k})$ and $\lambda_{\mathrm{i}}(\mathrm{k})$ quantities retrieved by FEFF for each scattering topology are evaluated on a coarse interval of $\mathrm{k}$ values within 0 and 20 Å and then saved in a feffNNN.dat file. Afterwards, external programs (such as IFEFFIT, Larch, Arthemis, …) can extract and interpolated these FEFF derived quantities over a finer $\mathrm{k}$ grid (e.g. 0.05 Å) and use them to reconstruct each oscillatory signal associated to each selected path.

As it is possible to see, the EXAFS expression, retrieved through FEFF, is based on the input cluster structure. This implies that $\mathrm{F_i(k)}$, $\phi_{\mathrm{i}}(\mathrm{k})$ and $\lambda_{\mathrm{i}}(\mathrm{k})$ are geometry dependent terms. In case of SS paths these physical quantities don't vary a lot deforming the molecular structure around the absorber. On the contrary, the MS paths intensities and phases strongly depend on the considered input structure and, similarly on the XANES region, can provide information about the angles of the structure under investigation. The classic codes based on FEFF can refine, through a fitting procedure, just the bond distances and the coordination number of the atoms surrounding the absorber. This fact implies that if the analysis is performed on a fixed geometry, the information about the bond angles cannot be identified (differently for GNXAS [34] where it is possible to estimate the variation of the angles contribution expanding $\mathrm{F_i(k)}$, $\phi_{\mathrm{i}}(\mathrm{k})$ and using a Taylor expansion). In **chapetr 3** it is showed how a multidimensional interpolation approach, based on FEFF and similar to the one implemented in PyFitIt, can allow to provide a direct estimation the bond angles.

## 1.3 EXAFS QUANTITATIVE ANALYSIS: THE FITTING METRIC

All various codes implemented to perform the fit of the EXAFS region of a XAS signal involve always the minimization the square of the residuals between the experimental EXAFS spectrum and the theoretical one. It is worth noting that the number of parameter which can be estimated from the EXAFS fitting procedure is limited by the Nyquist criterion to $\mathrm{N_{ind}} \approx \frac{2\Delta\mathrm{k}\Delta\mathrm{R}}{\pi} + 1$ [25], where $\Delta\mathrm{k}$ and $\Delta\mathrm{R}$ are the $\mathrm{k}$ and $\mathrm{R}$ range of the usable data under consideration. About this topic, in this thesis, the maximum number of fitting parameters has been always estimated using the conservative number of *+1*, although some authors claimed with reasonable theses that the number *+1* should be changed with *+2* [35]. Focusing on the fitting routing realised by IFEFFIT [36] (and now by the its more advanced version embedded in the Larch package [35]), the EXAFS parameters $\mathrm{S_0^2}$, $\Delta\mathrm{R_i}$, $\mathrm{N_i}$, $\sigma_{\mathrm{i}}^2$ and $\Delta\mathrm{E_0}$ (shift in energy from the edge value) can be refined through a fit, minimising the following target function:

$$\Xi = \frac{N_{\mathrm{ind}}}{N}\sum_{i=1}^{N}\frac{[k^{n}(\chi_i(k)^{\mathrm{DATA}}-\chi_i(k)^{\mathrm{THEORY}})]^{2}}{\varepsilon_i^{2}} \tag{1.8}$$

Where $\chi^{\mathrm{DATA}}$ and $\chi^{\mathrm{THEORY}}$ are respectively the experimental and theoretical $k$-depending signals weighted for a $k^n$ term (where $n$ is not necessary an integer). The $\varepsilon_i$ quantity is the uncertainty associated to each point of the experimental spectrum composed by $N$ values. Typically, the EXAFS data are quite over-sampled compared to the information content justifying the weighting for $N_{\mathrm{ind}}$. The fitting procedure can be realised in the $k$-space but also in the Fourier (direct -$R$) space. In this last case, the theoretical and the reconstructed signal are expressed in their FT form: $\tilde{\chi}(R)^{\mathrm{DATA}}$ and $\tilde{\chi}(R)^{\mathrm{THEORY}}$. The residuals appearing in (1.8) are provided as the list composed joining together the real and the imaginary part of the difference between experimental and the theoretical curve: $\Re[\tilde{\chi}_i(R)^{\mathrm{DATA}} - \tilde{\chi}_i(R)^{\mathrm{THEORY}}] + \Im[\tilde{\chi}_i(R)^{\mathrm{DATA}} - \tilde{\chi}_i(R)^{\mathrm{THEORY}}]$. On this basis, the sum appearing in equation (1.8) will be extended up to $N = 2M$ points, where $M$ is the number of sampling points of the real and imaginary part of the experimental EXAFS FT representation. An extension of the EXAFS fit to a higher dimensional space, offered by the Wavelet Transform representation, is provided in **chapter 3**.

A brief note regarding the estimation of the uncertainties in the EXAFS region must be provided. As far as the author of this thesis know, the error estimation on the EXAFS (and more in general XAS) measurements do not have a very define protocol allowing their extraction. This subject is still a matter of study [37, 38]. In case of IFEFFIT the error estimation in the FT space is obtained following the method proposed by Newville et al in [39]. Herein, the starting point stands in the assumption that the FT associated to the $k^n\chi(k)^{\mathrm{DATA}}$ spectrum does not have any structural signal and it is only due to noise $\varepsilon_R$. Then the high $R$-potion of the $\tilde{\chi}(R)^{\mathrm{DATA}}$ is then substituted with the variance of the values within (15-25 Å) and it is used in the FT version of equation (1.8). This quantity is the same for the real and imaginary part of experimental spectrum $\tilde{\chi}(R)^{\mathrm{DATA}}$ since the imaginary part of the $k^n\chi(k)^{\mathrm{DATA}}$ is definitely zero. Dealing with the fit in the $k$-space, the options which can be used to estimate the measurements uncertainties are different. First at all, it is possible to realise several measurements of the same spectrum and take the $k^n\chi(k)^{\mathrm{DATA}}$ as the average spectrum and $\varepsilon_i^2$ as the variance affecting the mean values. The second procedure, employed in IFEFFIT, consists to evaluate the uncertainty in the $k$-space $\varepsilon_k$ by means of the knowledge of the error in the $R$-space. To this aim the Parseval's equality is exploited:

$$\int_{k_{\min}}^{k_{\max}} dk|k^n\varepsilon_k|^2 = 2\int_{k_{\min}}^{k_{\max}} dk|\varepsilon_R|^2 \tag{1.9}$$

Supposing $\varepsilon_k$ constant, equation (1.9) lead to:

$$\varepsilon_k = \varepsilon_R\sqrt{\frac{\pi(2n+1)}{\Delta k(k_{\max}^{2n+1} - k_{\min}^{2n+1})}} \tag{1.10}$$

Finally, the last method is the one implemented in GNXAS, which appear to be (for me), the most accurate. It is based on the technique described by Dent at al in [40]. The idea is the following. Given an EXAFS spectrum, it is possible to oversample it with a step lower than 0.02 Å$^{-1}$. The procedure continues in three steps: first of all, few points (from three to twenty) are selected in the spectrum around an experimental point. Secondly, a low order polynomial (degree one, two or three) is fitted on the selected data. Third, the root mean square (rms) deviation of all the data within the selected range, from the polynomial curve, is assigned to the signal point. This last procedure is then repeated on several narrow intervals along the total spectrum. Finally, all the extracted rms values are interpolated with a smooth function and its inverse is used as the error term in (1.8).

The minimization of equation (1.8) can be realised using different algorithms. The IFEFFIT code employees, for example the Leveremberg-Marquard routine [41]. The problem of this algorithm stands in the fact the minimization strongly depends on the values provided by the user. A second method, more robust, is the Nelder-Mead algorithm which exploits the simplex method [42] to identify the minimum of the target function, or the minimization routine provided by the CERN MINUIT library [43] as implemented in GNXAS. Finally, the global minima values can be reached using convex minimization approaches as the one used to minimize the target function associated to a generalised EXAFS equation as implemented in PyFitIt, which are indicated in **section 3.2.1.1** of **chapter 3**.

Looking at equation (1.8), it is possible to note that the $\Xi$ is equivalent to the chi-square ($\chi^2$) function and, for this reason, its minimum corresponds to the $\chi^2$ value associated to the fit. It follows that, under the hypothesis that the residual values ($\chi_i(k)^{DATA} - \chi_i(k)^{THEORY}$) are normally distributed, the confidence intervals associated to each parameter can be extracted using the $\chi^2$ or the Fisher test fixing a certain values of significance $\%\alpha$ (usually fixed to the 95%). Basically, imposing a number of degree of freedom $\nu = N_{ind} - p$, where $p$ is the number of parameters refined by the fit, for each fitting parameter the $\Xi$ function is evaluated moving it slightly from its minimum value (along the increasing and decreasing verse of variation) until the integral of the normal distribution between that value and $+\infty$ is lower than 95%. A similar methodology involving the Fisher test [44] is applied in **section 3.2.1.1** of **chapter 3**. This is, for example the approach employed by GNXAS or EXCURVE [34, 45]. Equivalently it can be shown that the probability $P$ of having certain $(p_1, \dots, p_n)$ values is proportional to: $P(p_1, \dots, p_n) \propto \exp\left[-\frac{1}{2}\Xi(p_1, \dots, p_n)\right]$.The region of parameter space delimited by the previous criteria, in the second-order approximation, is a $n$-dimensional ellipsoid, which becomes a circle in case of not correlating parameters. More in detail, the covariance matrix of $\Xi$ calculated in its minimum values, provides an insight into the correlation between the fitting parameters. It is possible, in fact to demonstrate that the diagonal elements of the correlation matrix corresponds to the uncertainties of the fitting parameters, while the diagonal off elements their correlations [24, 46].

Generally the best statistical estimator which can be used to express the goodness of a fit is the $\chi^2$ value or its reduced form $\chi^2_\nu = \chi^2/\nu$. Without executing any $\chi^2$-test, a good rule of thumb, which can be used to establish if the data are consistent with the fitting model, is to verify that $\chi^2_\nu \approx 1$. However, this relation is rarely satisfied. The reason is principally due to the uncertainty associated to the estimation of the errors $\varepsilon_i$ [30]. The tacit assumption behind this evaluation of $\varepsilon_i$ is that the noise is dominated by statistical variation. This is a poor hypothesis when a synchrotron source is used for the EXAFS measurement. Except for the most dilute samples measured in fluorescence, the flux incident upon the experiment, even from a second generation source, is so high that statistical variation is typically small compared to instrumental sources of uncertainty and to the error in the theoretical scattering factors. When the evaluation of $\varepsilon$ is too small, $\chi_\nu^2$ is too large, even for an obviously good fit [30]. This evidence implies that the $\chi_\nu^2$ parameter can be used just for a different purpose, such as to understand, through a Fisher test if the addition of a certain path or the choice of a determinate parametrization can increase the level of correspondence among the experimental and the theoretical curve.

A second term which can be used to evaluate the best agreement between the experiment and the best fit curve is the %R-factor ($\%\mathrm{R}_{\mathrm{factor}}$). This quantity is not uniquely defined. In all the results reported in this thesis work, it has been defined using the IXS standard formula [47] (only in the PCA section of **chapter 2**, this equation is slightly modified substituting the squared term with theie absolute value):

$$\%\mathrm{R}_{\mathrm{factor}} = 100 \times \frac{\sum_{i=1}^{N}[k^n(\chi_i(k)^{\mathrm{DATA}} - \chi_i(k)^{\mathrm{THEORY}})]^2}{\sum_{i=1}^{N}[k^n(\chi_i(k)^{\mathrm{DATA}}]^2} \tag{1.11}$$

In the hypothesis that the signal to noise (S/N) ratio of the data is good, the $\mathrm{R}_{\mathrm{IXS}}^2(\%)$ of an adequate fit can be expected to be in the order of few percent (not higher than 5%).

## 1.4 BASIC DETECTION METHODS AND EXPERIMENTAL SETUPS

The features of interest in XAFS spectra consist of small variations in the absorption coefficient. For this reason, to perform correctly an experiment, a good S/N ratio is required. This point is particularly critical for the energies appearing much higher than the edge since, at the end of the spectra, the oscillation amplitude is strongly damped because of the Debye-Waller effect. Therefore, an intense beam is required to obtain satisfactory data quality in a reasonable acquisition time. Moreover, a good energy resolution (lower than 1 eV) is necessary to resolve the XANES features and to have access to a wide range of energies in order to measure as many edges as possible. Synchrotron radiation sources [2], combined with the use of a monochromator crystal (see **Figure 1.1**) mounted on a high precision rotary motor, are optimal to fulfil these requirements and, in addition, they provide the possibility to exploit their spatial and temporal resolution for more challenging experiments [2, 48, 49].

The absorption coefficient (and consequently the XAFS spectrum) can be measured in several modes: directly by transmission or indirectly through secondary processes, such as fluorescence and electron detection mode... In the following sections, the descriptions concerning all the experimental methodologies employed to retrieve all the XAS spectra reported in this thesis work are provided.

### 1.4.1.1 *Transmission mode*

The photon fluxes $\Phi_0$ and $\Phi$ can be directly measured in front of and behind the sample, see **Figure 1.1**. In general, the two detectors are ionization chambers, with plane parallel electrodes, some tens of centimetres long [1]. The efficiency of the ionizations chambers can be tailored to different X-rays spectral regions by varying the atomic species and the pressure of the filling gas. The output of the ionization chambers consists in two electric currents $\mathrm{I}_0$ and $\mathrm{I}_1$ having a magnitude of the order of $10^{-10} - 10^{-8}$ A. The absorption coefficient: $\mu(E)$ will be related to these two quantities through the relation:

$$\mu(\hbar\omega) = \ln\left(\Phi_0/_{\Phi}\right) = \ln\left(I_0/_{I}\right) - \ln(C(E)) \qquad (1.12)$$

Where $C(E)$ is a smooth background, determined by the ionizations chambers response, which can be easily subtracted during the data analysis procedure [1]. The latter foresees to subtract the XAS pre-edge background through a spline curve. Afterwards, the spectrum is normalised to the absorption edge jump $\Delta E_0$. This quantity is evaluated interpolating a second spline function in the XAS post edge region and extrapolating the value of the absorption coefficient in correspondence of $E_0$. The value of $\mu(E_0)$, evaluated on the pre-edge subtracted XAS spectrum, provides the jump of absorption $\Delta\mu$ required for the normalization, see **Figure 1.5**. More information concerning the implementation of this procedure can be found in **chapter 4**.

Even if the transmission mode is the simplest and most direct way to measure a XAFS spectrum, it cannot be used in every case. In fact, it requires that the thickness of the sample and of the concentration of absorbing species are small enough to allow the beam passing through the sample, but high enough to obtain a satisfactory signal-to-noise ratio. The optimal combination of thickness and concentration should reflect into an edge jump close to 1 (e.g. 30% of difference in the transmitted beam before and after the edge) and a total absorption lower than 90%. If the sample is a powder or a solution, it is suggested to dilute it with a blank solvent (low Z atoms) to reach the optimal conditions. However, there will be many cases when the sample is too diluted, or too thick, or supported on a more absorbing material, where the transmission mode is not adequate and the fluorescence mode is usually preferred [1].

### 1.4.2 *Fluorescence mode*

Fluorescence is a secondary effect of X-ray absorption. Once the X-ray photon has extracted an electron from a core level of the absorbing atom, the core hole will be filled by one of the electrons in the outer levels. As a consequence, a fluorescence photon with energy equal to the difference between the two electronic levels will be emitted by the atom. In a fluorescence detection-mode experiment, such as the Partial Fluorescence Yield mode (PFY), the monitored quantity is represented by the intensity $I$ of the fluorescence emitted at a fixed frequency $\omega$ by the absorbing specie as a function of the incident X-ray energy $\hbar\omega$ having intensity $I_0$.

In fluorescence yield mode, $I_0$ is still measured by means of an ion chamber, but the flux of fluorescence photons $I$, emitted at the energies characteristic of the element (the so called region of interest or ROI), is measured by means of a multi-element semiconductor (based on e.g. Ge or Si) detector [2]. Usually the fluorescence detector is positioned at 90° with respect to the incoming X-ray beam and the sample is turned at 45° to minimize the signal due to elastic scattering. If the detector response is linear the signal is proportional to the flux and the absorption coefficient can be calculated considering the relation: $\mu(E) = \frac{I}{I_0}$. The fluorescence measurements can be applied to a large variety of diluted samples, whereas they are not appropriate for concentrated materials. Indeed, in the latter case, detector saturation may occur, causing a non-linear response. In addition, the measure could be affected by self-absorption phenomena [147], which depend on the different thickness of the sample probed by X-rays at the different energies of the scan.

### 1.4.3 *High-energy resolution fluorescence detected (HERFD) XANES mode*

In a conventional XANES experiment, one monitors either: (i) the transmitted photons or, (ii) the (partial) fluorescence yield (FY) (integrated over all the de-excitations related to the excited atomic species). In such experiments, besides the limits of the X-ray optics, there is a lower limit in the full width high maximum (FWHM) of the observed spectral features ($\Delta E_{FY}$) that is set by the life-time broadening of the core hole of the selected edge: $\Delta E_{FY} \approx \Gamma_{core} = \hbar/\tau_{core}$, where $\tau_{core}$ is the life time of the core hole created by the absorbed X-ray. The experimental setup requires a high flux, high brilliance synchrotron radiation X-ray source and a Rowland-type spectrometer equipped with analyser crystals or a polychromator based on cylindrically curved Bragg crystal in von Hamos geometry [2, 50]. In this condition, it is possible to follow the evolution of the fluorescence emission fixing $\hbar\omega$ (corresponding to a particular fluorescence decay channel) upon scanning the incident photon energy $\hbar\Omega$. In such a way, being the decay transition due to an electron coming from an higher level (HL-LUMO-), that has a core hole with a longer $\tau_{HL}$ life-time ($\tau_{HL} \gg \tau_{core}$) ,the resulting spectrum will be characterized by an intrinsic lower broadening $\Delta E_{HERFD} \approx ((\Gamma_{core})^{-2} + (\Gamma_{HL})^{-2})^{-1/2}$ where $\Gamma_{HL} = \hbar/\tau_{HL}$ [51]. This effectively leads to spectra with a higher energy resolution and sharper features named with the term high-energy resolution fluorescence detected (HERFD) XANES [52].

### 1.4.4 *Electrons Detection Mode*

In order to perform a deep study of the surface properties of a determined material, it is convenient to measure the flux of the photoelectrons and/or the Auger electrons emitted as a consequence of the atomic de-excitation after the X-ray absorption process [53]. It follows that as for the fluorescence case, the measure of the X-ray absorption intensity is not direct. The X-rays are absorbed through the excitations of core electrons to empty states above the vacuum or Fermi level. The created holes are then filled by Auger decay (dominant in the soft X-ray region over the X-ray fluorescence). The intensity of the emitted primary Auger electrons is a direct measure of the X-ray absorption process and is used in so called Auger electron yield (AEY) measurements, which are highly surface sensitive, similar to XPS. In the total electron yield detection mode (TEY) the total number of electrons (photoelectrons, Auger electrons, secondary electrons) delivered from the sample are counted. The secondary electrons are the electrons ejected after the interaction of the atoms of the sample with the fluorescence photons and/or the primary Auger electrons and photoelectrons [2, 53]. The number of emitted electrons is proportional to the number of holes created in the sample, which is proportional to the number of the absorbed photons. Since the mean free path of the electrons is very small, see **Figure 1.4**, the TEY mode is surface sensitive. Therefore, measurements in the TEY procedure require atomically clean surfaces without any contaminants. Assuming a X-ray penetration depth of ca. 10 Å, only the electron emitted over 3 Å of thickness have the possibility to be measured. Experimentally, the TEY signal can be measured monitoring, through a pico-amperometer, the intensity of drain current coming from the sample [54].

## 1.5 REFERENCES

[1] P. Fornasini, Introduction to X-ray absorption spectroscopy, in: B.F. Mobilio S., Meneghini C. (Ed.) Synchrotron Radiation, Springer, 2015, pp. 181-211.
[2] L. Mino, G. Agostini, E. Borfecchia, D. Gianolio, A. Piovano, E. Gallo, C. Lamberti, Low-dimensional systems investigated by x-ray absorption spectroscopy: a selection of 2D, 1D and 0D cases, J. Phys. D-Appl. Phys., 46 (2013) 72.
[3] M. Benfatto, C. Meneghini, A close look into the low energy region of the XAS spectra: the XANES region, in: B.F. Mobilio S., Meneghini C. (Ed.) Synchrotron Radiation, Springer, 2015, pp. 213-240.
[4] D. Koningsberger, R. Prins, X-ray absorption: principles, applications, techniques of EXAFS, SEXAFS, and XANES, (1988).
[5] F. de Groot, Multiplet effects in X-ray spectroscopy, Coord. Chem. Rev., 249 (2005) 31-63.
[6] F. de Groot, G. Vanko, P. Glatzel, The 1s x-ray absorption pre-edge structures in transition metal oxides, J. Phys.-Condes. Matter, 21 (2009) 7.
[7] E. Gorelov, A.A. Guda, M.A. Soldatov, S.A. Guda, D. Pashkov, A. Tanaka, S. Lafuerza, C. Lamberti, A.V. Soldatov, MLFT approach with p-d hybridization for ab initio simulations of the pre-edge XANES, Radiat. Phys. Chem., 175 (2020) 4.
[8] S. Sagmeister, C. Ambrosch-Draxl, Time-dependent density functional theory versus Bethe-Salpeter equation: an all-electron study, Phys. Chem. Chem. Phys., 11 (2009) 4451-4457.
[9] E.L. Shirley, Ab initio inclusion of electron-hole attraction: Application to x-ray absorption and resonant inelastic x-ray scattering, Phys. Rev. Lett., 80 (1998) 794-797.
[10] M.Y. Guo, L.K. Sorensen, M.G. Delcey, R.V. Pinjari, M. Lundberg, Simulations of iron K pre-edge X-ray absorption spectra using the restricted active space method, Phys. Chem. Chem. Phys., 18 (2016) 3250-3259.
[11] R.V. Pinjari, M.G. Delcey, M.Y. Guo, M. Odelius, M. Lundberg, Restricted active space calculations of L-edge X-ray absorption spectra: From molecular orbitals to multiplet states, J. Chem. Phys., 141 (2014) 11.
[12] K. Held, O.K. Andersen, M. Feldbacher, A. Yamasaki, Y.F. Yang, Bandstructure meets many-body theory: the LDA + DMFT method, J. Phys.-Condes. Matter, 20 (2008) 7.
[13] D. Nabok, A. Gulans, C. Draxl, Accurate all-electron G(0)W(0) quasiparticle energies employing the full-potential augmented plane-wave method, Phys. Rev. B, 94 (2016) 9.
[14] S. Dellalonga, A. Soldatov, M. Pompa, A. Bianconi, Atomic and electronic structure probed by X-ray absorption spectroscopy: Full multiple scattering scattering analysis with the G4XANES package, Comput. Mater. Sci., 4 (1995) 199-210.

[15] A.L. Ankudinov, B. Ravel, J.J. Rehr, S.D. Conradson, Real-space multiple-scattering calculation and interpretation of x-ray-absorption near-edge structure, Phys. Rev. B, 58 (1998) 7565-7576.
[16] S.A. Guda, A.A. Guda, M.A. Soldatov, K.A. Lomachenko, A.L. Bugaev, C. Lamberti, W. Gawelda, C. Bressler, G. Smolentsev, A.V. Soldatov, Y. Joly, Optimized Finite Difference Method for the Full-Potential XANES Simulations: Application to Molecular Adsorption Geometries in MOFs and Metal-Ligand Intersystem Crossing Transients, J. Chem. Theory Comput., 11 (2015) 4512-4521.
[17] M. Benfatto, S. Della Longa, C.R. Natoli, The MXAN procedure: a new method for analysing the XANES spectra of metalloproteins to obtain structural quantitative information, J. Synchrot. Radiat., 10 (2003) 51-57.
[18] G. Smolentsev, A. Soldatov, Quantitative local structure refinement from XANES: multi-dimensional interpolation approach, J. Synchrot. Radiat., 13 (2006) 19-29.
[19] A. Martini, S.A. Guda, A.A. Guda, G. Smolentsev, A. Algasov, O. Usoltsev, M.A. Soldatov, A. Bugaev, Y. Rusalev, C. Lamberti, A.V. Soldatov, PyFitit: The software for quantitative analysis of XANES spectra using machine-learning algorithms, Comput. Phys. Commun., 250 (2020) 15.
[20] F.W. Lytle, D.E. Sayers, E.A. Stern, Extended x-ray-absorption fine-structure technique. II. Experimental practice and selected results, Phys. Rev. B, 11 (1975) 4825-4835.
[21] D.E. Sayers, E.A. Stern, F.W. Lytle, New Technique for Investigating Noncrystalline Structures: Fourier Analysis of the Extended X-Ray---Absorption Fine Structure, Phys. Rev. Lett., 27 (1971) 1204-1207.
[22] E.A. Stern, Theory of the extended x-ray-absorption fine structure, Phys. Rev. B, 10 (1974) 3027-3037.
[23] E.A. Stern, D.E. Sayers, F.W. Lytle, Extended x-ray-absorption fine-structure technique. III. Determination of physical parameters, Phys. Rev. B, 11 (1975) 4836-4846.
[24] G. Bunker, Introduction to XAFS: A Practical Guide to X-ray Absorption Fine Structure Spectroscopy, Cambridge University Press, Cambridge, 2010.
[25] S. Calvin, XAFS for Everyone, 2013.
[26] B. Ravel, Muffin-tin potentials in EXAFS analysis, J. Synchrot. Radiat., 22 (2015) 1258-1262.
[27] L. Mattheiss, Energy bands for solid argon, Physical Review, 133 (1964) A1399.
[28] A.L. Fetter, J.D. Walecka, Quantum theory of many-particle systems, Courier Corporation, 2012.
[29] J.J. Rehr, R.C. Albers, SCATTERING-MATRIX FORMULATION OF CURVED-WAVE MULTIPLE-SCATTERING THEORY - APPLICATION TO X-RAY-ABSORPTION FINE-STRUCTURE, Phys. Rev. B, 41 (1990) 8139-8149.
[30] B. Ravel, Quantitative EXAFS Analysis, in: J.A. Van Bokhoven, C. Lamberti (Eds.) X-Ray Absorption and X-Ray Emission Spectroscopy, Wiley Online Books, 2016, pp. 281-302.
[31] J.J. Rehr, A.L. Ankudinov, Progress in the theory and interpretation of XANES, Coord. Chem. Rev., 249 (2005) 131-140.

[32] R. Haydock, The recursive solution of the Schrödinger equation, Comput. Phys. Commun., 20 (1980) 11-16.
[33] S.I. Zabinsky, J.J. Rehr, A. Ankudinov, R.C. Albers, M.J. Eller, MULTIPLE-SCATTERING CALCULATIONS OF X-RAY-ABSORPTION SPECTRA, Phys. Rev. B, 52 (1995) 2995-3009.
[34] A. Filipponi, A. DiCicco, X-ray-absorption spectroscopy and n-body distribution functions in condensed matter .2. Data analysis and applications, Phys. Rev. B, 52 (1995) 15135-15149.
[35] E.A. Stern, Number of Relevant Indipendent Points in X-ray Absorption Fine Structure Spectra, Phys. Rev. B, 48 (1993) 9825-9827.
[36] M. Newville, IFEFFIT: interactive XAFS analysis and FEFF fitting, J. Synchrot. Radiat., 8 (2001) 322-324.
[37] E. Curis, S. Benazeth, Propagation of statistical errors across EXAFS extraction and Fourier filtering, J. Synchrot. Radiat., 7 (2000) 262-266.
[38] G. Vlaic, D. Andreatta, A. Cepparo, P.E. Colavita, E. Fonda, A. Michalowicz, Estimation of the experimental standard deviations in EXAFS measurements, J. Synchrot. Radiat., 6 (1999) 225-227.
[39] M. Newville, B.I. Boyanov, D.E. Sayers, Estimation of uncertainties in XAFS data, J. Synchrot. Radiat., 6 (1999) 264-265.
[40] A.J. Dent, P.C. Stephenson, G.N. Greaves, The extraction of signal to noise values in X-Ray Absorption-Spectroscopy, Rev. Sci. Instrum., 63 (1992) 856-858.
[41] J.J. Moré, The Levenberg-Marquardt algorithm: Implementation and theory, in: G.A. Watson (Ed.) Numerical Analysis, Springer Berlin Heidelberg, Berlin, Heidelberg, 1978, pp. 105-116.
[42] J.A. Nelder, R. Mead, A Simplex Method for Function Minimization, The Computer Journal, 7 (1965) 308-313.
[43] F. James, M. Roos, Minuit - a system for function minimization and analysis of the parameter errors and correlations, Comput. Phys. Commun., 10 (1975) 343-367.
[44] R. Joyner, K. Martin, P. Meehan, Some applications of statistical tests in analysis of EXAFS and SEXAFS data, Journal of Physics C: Solid State Physics, 20 (1987) 4005.
[45] S. Gurman, N. Binsted, I. Ross, A rapid, exact curved-wave theory for EXAFS calculations, Journal of Physics C: Solid State Physics, 17 (1984) 143.
[46] W.H. Press, S.A. Teukolsky, W.T. Vetterling, B.P. Flannery, Numerical recipes 3rd edition: The art of scientific computing, Cambridge university press, 2007.
[47] I.S.a.C. Committee, Error Reporting Recommendations: A Report of the Standards and Criteria Committee, in, 2000.
[48] D. Gianolio, Combination of advanced X-ray techniques in understanding the structure and the electronic configuration of transition metal complexes: experiments vs calculations, in: Department of Chemistry Università degli Studi di Torino, Turin, 2011.
[49] Y.S. Li, F.Y. Liang, H. Bux, A. Feldhoff, W.S. Yang, J. Caro, Molecular Sieve Membrane: Supported Metal-Organic Framework with High Hydrogen Selectivity, Angew. Chem.-Int. Edit., 49 (2010) 548-551.
[50] M. Bauer, HERFD-XAS and valence-to-core-XES: new tools to push the limits in research with hard X-rays?, Phys. Chem. Chem. Phys., 16 (2014) 13827-13837.

[51] P. Carra, M. Fabrizio, B.T. Thole, HIGH-RESOLUTION X-RAY RESONANT RAMAN-SCATTERING, Phys. Rev. Lett., 74 (1995) 3700-3703.

[52] P. Glatzel, U. Bergmann, High resolution 1s core hole X-ray spectroscopy in 3d transition metal complexes - electronic and structural information, Coord. Chem. Rev., 249 (2005) 65-95.

[53] J. Stöhr, NEXAFS Spectroscopy, Springer-Verlag Berlin Heidelberg, Verlag Berlin Heidelberg, 1992.

[54] C. Castan-Guerrero, D. Krizmancic, V. Bonanni, R. Edla, A. Deluisa, F. Salvador, G. Rossi, G. Panaccione, P. Torelli, A reaction cell for ambient pressure soft x-ray absorption spectroscopy, Rev. Sci. Instrum., 89 (2018) 8.

# 2 XANES DATA ANALYSIS: METHODS AND IMPROVEMENTS

In this chapter a detailed description of the XANES data analysis methodologies, developed and employed, is provided. The first part (**section 2.1**) regards the description of the spectral decomposition procedure for an arbitrary XANES dataset. Particular attention is given to the examination of the methodologies exploited to extract and reconstruct the XANES profiles of the chemical species characterizing an experimental dataset, currently implemented in the PyFitIt code [1-3] (freely downloadable at https://pypi.org/project/pyfitit/) and in Thorondor [4], whose description will be provided in **chapter 4**. The second part (**section 2.2**) describes how it is possible, through a Machine Learning methodology, to fit the XANES part of the XAS spectrum and retrieving from it some quantitative and structural information about the molecular structure under investigation. Finally, the last part of this chapter (**section 2.3**) focuses on the ambiguities on the structural parameters emerging from the XANES fit and indicates how the principal component analysis can be employed to evaluate the accessibility of the information that can be retrieved from a quantitative XANES analysis.

## 2.1 SPECTRAL DECOMPOSITION OF A XANES DATASET

When a sample consists of a mixture of absorbing atoms forming different chemical species, or located in non-equivalent sites, the related XANES measurement represents an average of the single spectra corresponding to each species/site. It is worth noting that the XANES spectral features associated to a given absorbing atom will depend exclusively on the local geometry of the related species/site. This fact leads to the conclusion that the XANES spectra of each species characterizing the sample measurement, will be different to each other and, for this reason, they can be defined as pure spectra. It follows that an arbitrary XANES spectrum $\mu(E)$ can be expressed as the sum of these pure spectra weighted by their amount (fraction) inside the sample:

$$\mu(E) = \sum_{i=1}^{N} c_i \mathbf{s}_i(E) + \boldsymbol{\varepsilon} \tag{2.1}$$

Here, $N$ is the number of pure spectral compounds involved in the decomposition, $E = (E_1, \dots, E_m)$ is the energy vector, $\mathbf{s}_i$ is the energy dependent pure spectrum corresponding to the i$^{th}$ species/site, $c_i$ is a scalar value representing the fractional abundance or concentration of $\mathbf{s}_i$ inside the sample under study, while $\boldsymbol{\varepsilon}$ is a vector containing $m$ experimental noise values associated to the measure. Because of the element-selectivity of the XANES technique, it is possible to assert that, in general, the mass balance condition must be satisfied: $\sum_{i=1}^{N} c_i = 1$.

Equation (2.1) can be extended to the case of a dataset $\mathbf{X}$ containing multiple spectra collected during the variation of the physico-chemical system under study, caused by controlled modification of one or more external factors (i.e., temperature, gas feed composition, sampling time, sample position, …):

$$\mathbf{X} = \mathbf{S}\mathbf{C}^{\mathrm{T}} + \boldsymbol{\mathcal{E}} \tag{2.2}$$

where $\mathbf{X}$ is composed by $\mathrm{m}$ energy points and $\mathrm{n}$ spectra, i.e. $\dim(\mathbf{X}) = (\mathrm{m} \times \mathrm{n})$, $\mathbf{S}$ is the matrix of the pure spectral profiles having dimensions $\dim(\mathbf{S}) = (\mathrm{m} \times \mathrm{N})$ while $\mathbf{C}^{\mathrm{T}}$ is the transpose of matrix $\mathbf{C}$, with dimensions $\dim(\mathbf{C}^{\mathrm{T}}) = (\mathrm{N} \times \mathrm{n})$, containing on its rows the concentration profiles associated to each spectrum of $\mathbf{S}$. Finally, $\boldsymbol{\mathcal{E}}$ represents the noise matrix of dimensions $\dim(\boldsymbol{\mathcal{E}}) = (\mathrm{m} \times \mathrm{n})$ corresponding to dataset $\mathbf{X}$. A pictorial representation of the described spectral decomposition strategy is showed in **Figure 2.1**.

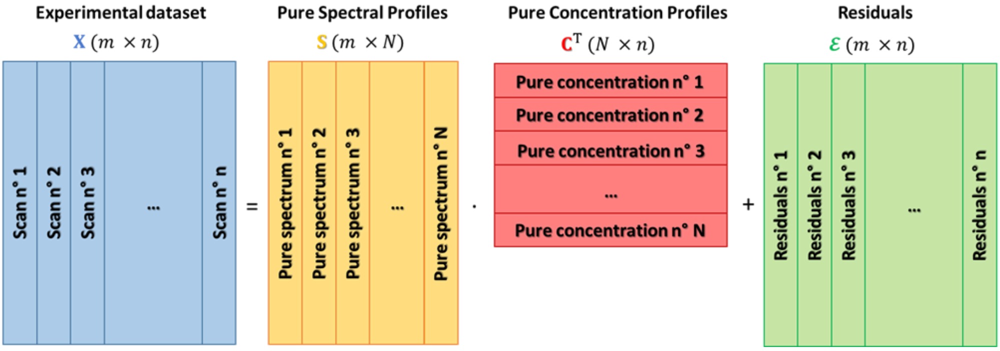

**Figure 2.1:** Schematic representation of the spectral decomposition regarding a XANES experimental dataset $\boldsymbol{X}$, composed by $n$ spectra (scans) and by $m$ energy points, in the product of a matrix $\boldsymbol{S}$, containing $N$ pure spectral profiles, and matrix $\boldsymbol{C}$, containing their related concentration values. The error in the proposed decomposition is represented by the residuals matrix $\boldsymbol{\mathcal{E}}$. It is worth noting that if the correct number of pure species characterizing the measurements is identified, matrix $\boldsymbol{\mathcal{E}}$ must contains on its columns only the contributions coming from the experimental noise.

The issue regarding the possibility to decompose a XANES dataset as showed in (2.2), usually called mixture analysis problem, has attracted great attention in the XANES community, especially for the analysis of data obtained from time-and space resolved experiments [5]. For this reason, several methods, based on the Principal Component Analysis (PCA), have been developed to realize it, which we will discuss in more details in the following sections.

### 2.1.1 *Principal Component Analysis (PCA) of a XANES dataset*

The first step towards the decomposition showed by equation (2.2) foresees the identification of the number of the $\mathrm{N}$ pure species characterizing the XANES dataset under study. Ideally, imaging that $\mathbf{X}$ could be a noise-free data matrix, it is possible to assert that each column (or spectra) of $\mathbf{X}$ can be properly expressed by the linear combination of a set of $\mathrm{N}$ independent spectra. It follows that the rank of matrix $\mathbf{X}$ (i.e. the number of irreducible columns or rows) must be equal to the number of pure species contributing to the dataset. Unfortunately, this statement is generally not true, because of the noise influencing the data, which makes the collected spectra independent to each other (i.e., the rank of $\mathbf{X}$ is equal to the number of spectra composing the dataset). However, the application of the Principal Components Analysis (PCA) procedure is able to provide deeper insights on how many components characterize a system and on the influence of the noise on the XANES data.

Generally speaking, PCA belongs to the family of unsupervised Machine Learning processing algorithms [6] and can be used in the analysis of a XANES dataset to correctly identify its rank. The PCA approach assumes that the XANES data mixture can be expressed as a linear combination of a fixed number of components weighted by their own fractions. The set of components employed in the spectral decomposition procedure must be independent to each other, moreover they must be able to account for the highest variance of the XANES dataset including the noise. While different techniques can be applied in order to decompose a set of spectroscopic data on the basis of its principal components, a standard matrix factorization technique called Singular Value Decomposition (SVD) is generally applied due to its robustness and accurateness. The SVD approach foresees the decomposition of the XANES data matrix in the product of three matrices:

$$\mathbf{X} = \mathbf{U\Sigma V}^{\mathrm{T}} \tag{2.3}$$

where $\mathbf{U}$ and $\mathbf{V}$ are two square unitary matrices ($\dim(\mathbf{U}) = (\mathrm{m} \times \mathrm{m})$ and $\dim(\mathbf{V}) = (\mathrm{n} \times \mathrm{n})$) while $\mathbf{\Sigma}$ is a diagonal rectangular matrix ($\dim(\mathbf{\Sigma}) = (\mathrm{m} \times \mathrm{n})$).

**Figure 2.2** shows schematically the output of the SVD procedure. It is worth noting that this kind of decomposition is not unique and that there are different ways to perform it; in some of them matrices $\mathbf{U}$ or $\mathbf{V}$ can be rectangular while $\mathbf{\Sigma}$ squared. More information about the different algorithms employed to realize the SVD can be found in [7].

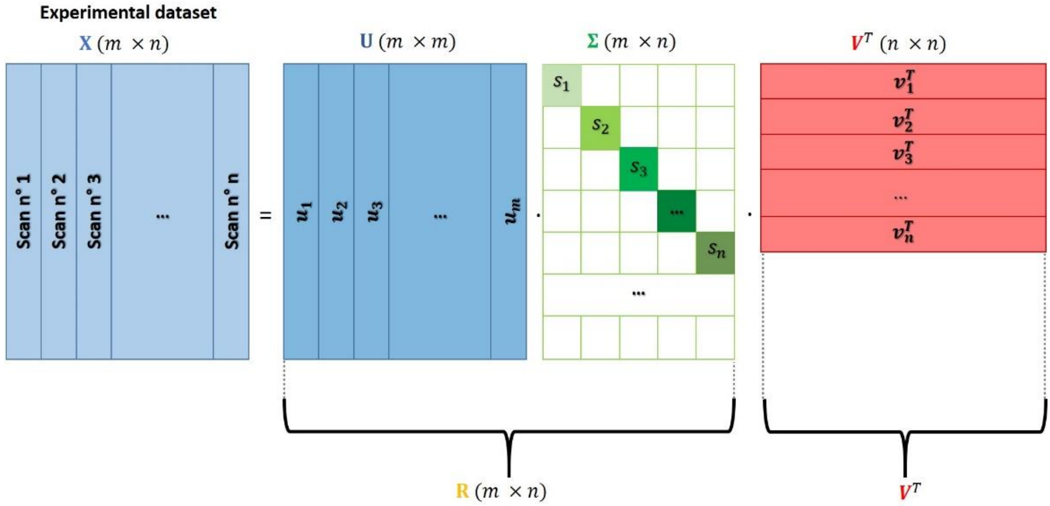

**Figure 2.2:** Schematic representation of the SVD procedure applied on the XANES dataset $\boldsymbol{X}$. The experimental spectra composing it are displaced on its columns. Matrix $\boldsymbol{X}$ is decomposed in three matrices: $\boldsymbol{U}$, $\boldsymbol{\Sigma}$ and $\boldsymbol{V}$, having dimensions equal to $(m \times m)$, $(m \times n)$ and $(n \times n)$, respectively. The quantities $m$ and $n$ indicate the number of energy points of each experimental spectrum and the number of spectra composing $\boldsymbol{X}$. The white squares and rectangles showed in $\boldsymbol{\Sigma}$ underline that this matrix only contains non-null values on its main diagonal, which are the so called singular values of $\boldsymbol{X}$: $s_i$. Matrices $\boldsymbol{U}$ and $\boldsymbol{\Sigma}$ can be multiplied together in order to provide a new matrix, $\boldsymbol{R}$, that, together with $\boldsymbol{V}^T$is able to realize a decomposition similar to the one showed in equation (2.2). As it will showed in **Figure 2.4**(b), the analysis of the spectra composing the new matrix $\boldsymbol{R}$ represents a fundamental step for the identification of the correct number of pure species characterising the dataset. Moreover, for some methods, it constitutes the initial step required to properly realize decomposition (2.2). More details about this topic will be provided in **2.1.3.**

Matrix $\mathbf{U}$ contains on its columns the eigenvectors of the covariance matrix associated to $\mathbf{X}$, i.e., $\mathbf{Z} = \mathbf{X}\mathbf{X}^{\mathrm{T}}$ which are the so-called principal directions or components. On the other hand, matrix $\mathbf{V}^{\mathrm{T}}$ shows on its rows the eigenvectors of the transpose of $\mathbf{Z}$ which, from a geometrical point of view, can be interpreted as the projection of dataset $\mathbf{X}$ over the entire set of principal directions contained in $\mathbf{U}$. These vectors can be also seen as the principal directions (or components) taken directly from the rows of $\mathbf{X}$ rather than from its columns. For sake of clarity, in this thesis, the name of principal components (PCs) will be used to indicate always the columns of matrix $\mathbf{U}$. As a didactic representation, the principal components associated to a bi-dimensional dataset composed by 200 points are reported in **Figure 2.3**.

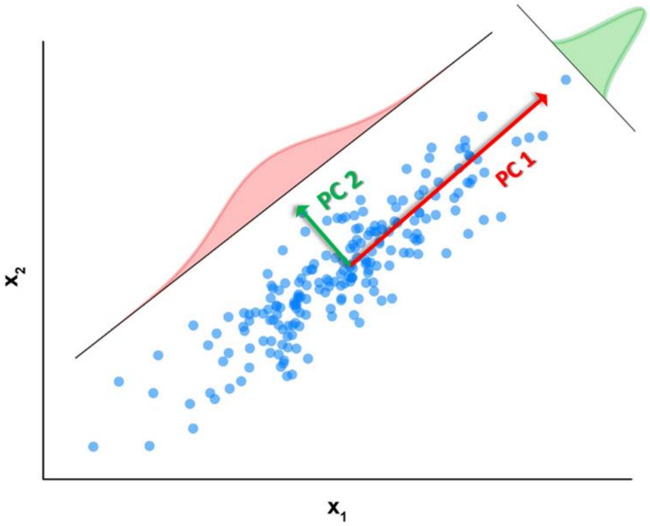

**Figure 2.3:** Pictorial representation of the principal directions or components (the red and the green arrows) of a bi-dimensional dataset composed by 200 points. With the red and green Gaussians are represented the fraction of the dataset variance expressed by the first and second component.

Finally, the diagonal elements of $\mathbf{\Sigma}$ are named as singular values and their magnitudes are connected to eigenvalues of the covariance matrix of $\mathbf{X}$ through the following formula:

$$\lambda_{\mathrm{i}} = \mathrm{s_i}^2/(\mathrm{m}-1) \tag{2.4}$$

where $\mathrm{s_i}$ and $\lambda_{\mathrm{i}}$ are the i^th^ singular value and eigenvalue corresponding to $\mathbf{\Sigma}$ and to the data covariance matrix, respectively. As already pointed out by Calvin in ref. [8], in the field of XANES analysis, the $\lambda_{\mathrm{i}}$ terms are usually referred to as the variances associated to the dataset principal components. However, this statement is true only if the XANES data are centered (i.e., the mean calculated over all the columns of $\mathbf{X}$ has been subtracted to every spectrum composing $\mathbf{X}$). Because in XANES analysis the dataset is usually not centered, the quantities retrieved by (2.4) cannot be properly interpreted as the true data variances, despite they follow the same decreasing trend as a function of the component number (see **section 2.1.2**). Nevertheless, the term variance is almost universally used in this context, even though the data mean centering condition is not satisfied [8].
The factors appearing in (2.3) can be grouped as follows:

$$\mathbf{X} = \mathbf{R}\mathbf{V}^{\mathrm{T}} \tag{2.5}$$

where $\mathbf{R} = \mathbf{U}\mathbf{\Sigma}$. The columns of $\mathbf{R}$ will correspond to the ones of $\mathbf{U}$ scaled by the correspondent singular values; the connection of this expression with equation (2.2) will be discussed in more detail in **section 2.1.3**.

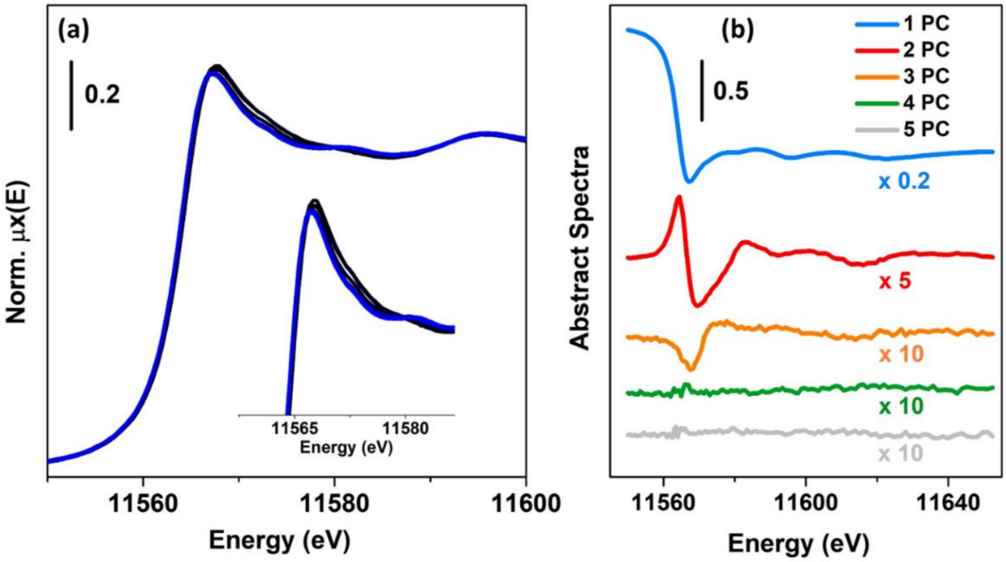

**Figure 2.4:** (a) Pt $L_3$-edge XANES dataset composed by 32 spectra acquired on a Pt/$Al_2O_3$ catalyst kindly provided by E. Groppo [9]. The XANES scans monitor the interaction of the catalyst with a flow of $H_2$/inert at 120 °C followed by a dehydrogenation process in inert atmosphere (He). More information about the sample and the experimental conditions can be found in ref. [9]. The inset reports a magnification of the energy range containing the white line (W.L.) peak, where the more evident spectral modifications are observed. (b) First five columns of matrix $\boldsymbol{R}$ for the dataset reported in part (a), plotted in the same energy range and scaled by the factors indicated in the figure for visualization purposes. These abstract spectral profiles do not have any chemical-physical meaning and they can be considered just as a mathematical solution of equation (2.2), as discussed more in detail in **section 2.2**. However, their visual/qualitative analysis is able to provide deeper insights about the number of chemical species present in the sample.

As an example, **Figure 2.4** reports a XANES dataset, in part (a), and the related first five columns of $\mathbf{R}$ (abstract spectra) in part (b), plotted in the same energy range. Because the first component is characterized by the highest variance, its contribution appears higher than the other components. In particular, it is interesting to note that its shape resembles an inverted XANES spectrum. The reason of the inversion depends on the output provided by the SVD decomposition (in some cases, it can be positive) while the similarity can be explained by the fact that $\mathbf{X}$ has not been centered. Because the first principal component needs to explain the highest variance of the dataset, it will assume a form resembling the mean of all the spectra composing the dataset. The second principal component captures the second highest spectral features of the XANES dataset while the third one appears to be connected to minor but not negligible variation of the spectra. Starting from the fourth component, it is possible to see that they appear featureless on the scale of the XANES spectra. In particular, the distribution of their values, as a function of the energy, appears to follow a trend typical of the instrumental noise [8]. A second validation of this result can be obtained trying to analyze the residuals and plotting the $\%\mathrm{R_{factor}}$ related to the reconstruction of each spectrum of the XANES dataset as a function of the number of principal component involved, see **Figure 2.5**(a-c). The $\%\mathrm{R_{factor}}$ here is defined as: $\%\mathrm{R_{factor}} = 100 \times \frac{\|\mathbf{X}-\mathbf{R}_\mathrm{k}\mathbf{V}_\mathrm{k}^\mathrm{T}\|^2}{\|\mathbf{X}\|^2}$, where the subscript $\mathrm{k}$ denotes the number of principal components considered to reconstruct matrix $\mathbf{X}$, while the symbol $\|\quad\|$ is the Frobenius norm. If the XANES dataset is not properly represented by the chosen number of PCs, it will show, for certain scans, a higher $\%\mathrm{R_{factor}}$ indicating that one (or more) additional components are required to describe them. Once that the correct number of PCs is found, the $\%\mathrm{R_{factor}}$ values associated to the reconstruction of each spectrum, must have comparable magnitudes, as showed by **Figure 2.5**(c).

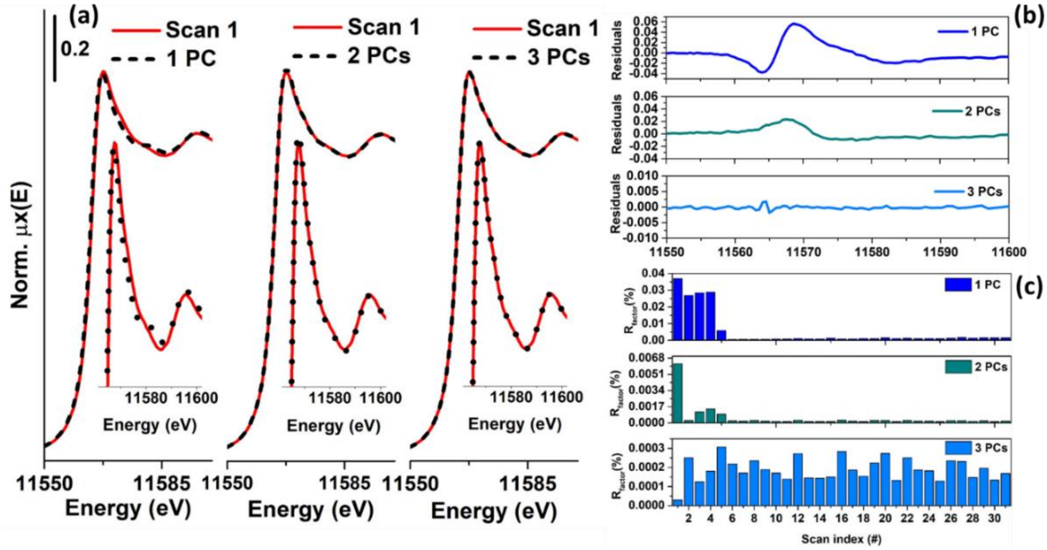

**Figure 2.5.** (a) Reconstruction of the first scan of the experimental dataset showed in **Figure 2.4**(a) using one, two and three components. The insets report magnifications of the WL feature. The level of misfit between the experimental spectrum and its reconstructed version diminish increasing the number of PCs. With two PCs there is a lack of reproduction connected with the WL, as showed by the inset and by the related residuals plotted in panel (b), while passing to three PCs the reproduction becomes excellent. (b) Plot of the residuals associated with the reconstruction showed in panel (a). These profiles have been calculated as the difference between the first experimental XANES scan and the first spectrum of the dataset reconstructed with one, two and three PCs, respectively. It is evident that with three PCs the residuals proper of the reconstruction of the first scan of the series resemble only the noise. (c) Trend of the $\%R_{factor}$ for each scan increasing the number of PCs involved in the representation. With three PCs the $\%R_{factor}$ appear distributed uniformly along all the scans of the dataset, indicating that the correct rank of the data matrix corresponds to three.

On the basis of the results showed in **Figure 2.4** and **Figure 2.5**, it is possible to conclude that the XANES dataset of **Figure 2.4**(a) can be properly described using only three principal components. Because each PC is independent to each other (i.e., they are orthogonal) their number represents a proper estimation of the rank of the XANES data matrix, corresponding to the number of chemical species associated to it. While the methods described above constitute a first, qualitative approach to the analysis, different techniques have been developed in the field of the PCA in order to establish quantitatively the correct rank of a dataset. Among them, in the field of XANES, the Scree Test, the Imbedded Error (IE), the Malinowsky Indicator factor (IND) and Fisher test (F-test) are widely applied and will be discussed in more details in the following section.

### 2.1.2 *Quantitative methods to extract the correct number of PCs*

The first widely used approach is named Scree Test (or Scree Plot) and it consists in plotting the variance or the singular values magnitudes associated to each principal component versus their number, as showed in **Figure 2.6**(a). As it is possible to see, after the first component, the variance associated to the components rapidly drops down, up to an elbow indicating the border between components having a real physical/chemical meaning (i.e., the number of species characterizing the dataset) from those related to the data noise. It is worth noting, in fact, that the components associated to the noise must contribute approximatively in the same way to the dataset variation and for this reason they usually lie on a flat line.

The Imbedded Error function (IE) is given by the following expression:

$$\mathrm{IE} = \sqrt{\frac{\mathrm{k}\sum_{\mathrm{i=k+1}}^{\mathrm{n}} \lambda_{\mathrm{i}}}{\mathrm{mn(n-k)}}} \tag{2.6}$$

where $\mathrm{k}$ represents the number of components used to reproduce the dataset $\mathbf{X}$. If the experimental errors are distributed randomly and uniformly along each spectrum of $\mathbf{X}$, then the sum of the squares of the projections of the residuals, defined as: $\boldsymbol{\mathcal{E}} = \mathbf{X} - \mathbf{R}_{\mathrm{k}}\mathbf{V}_{\mathrm{k}}^{\mathrm{T}}$ onto the noise-related PCs, should be approximately the same [10]. This means that the PCs representing the experimental noise must have approximately the same variances: $\lambda_{\mathrm{i}} \cong \lambda_{\mathrm{i+1}} \cong \cdots \cong \lambda_{\mathrm{n}}$ . Hence, for $\mathrm{k} > \mathrm{N}$ , equation (2.6) can be rewritten as:

$$\mathrm{IE} = \mathrm{n}^{1/2} \cdot \mathrm{h} \text{ ; with } \mathrm{h} = \left(\frac{\lambda_{\mathrm{i}}}{\mathrm{mn}}\right)^{1/2} \tag{2.7}$$

It follows that increasing the number of components, for $\mathrm{k} < \mathrm{N}$ the IE function progressively decreases until $\mathrm{k} = \mathrm{N}$, where it reaches a minimum corresponding to the proper number of PCs to consider. Then, for $\mathrm{k} > \mathrm{N}$, the IE assumes a slowly growing trend, as showed in **Figure 2.6**(b).

Malinowski discovered an empirical function called IND-function [10], which seems to be more sensitive than the IE function in its ability to pick-up the proper number of components [11]. The IND-function is defined as:

$$\mathrm{IND} = \frac{1}{(\mathrm{n-N})^2}\sqrt{\frac{\sum_{\mathrm{i=N+1}}^{\mathrm{n}} \lambda_{\mathrm{i}}}{\mathrm{m(n-N)}}} \tag{2.8}$$

Similarly to the IE functions, the IND estimator is calculated incrementally by increasing the number of PCs and, by definition, it reaches a minimum when the correct number of components is employed, see **Figure 2.6**(c). However, it has been observed that in this function the minimum is more pronounced and can appear in situations where the IE does not exhibit any valley. More details about the IE and IND estimators can be found in [10-12].

The Malinowski F-Test, reported in **Figure 2.6**(d) [10, 11], is the last statistical method applied to determine the true dimensionality of a dataset. It is based on the observation that the reduced eigenvalues $\mathrm{REV_i}$ are constant for non-significant PCs [13]:

$$\mathrm{REV_i} = \frac{\lambda_\mathrm{i}}{(\mathrm{m} - \mathrm{i} + 1)(\mathrm{n} - \mathrm{i} + 1)} \qquad (2.9)$$

Because the $\mathrm{REV_i}$ values are still proportional to a variance, a Fisher test can be applied. The test starts from the smallest $\mathrm{REV_i}$ term, clearly associated to the noise, and proceeds to those $\mathrm{REV_i}$ values, with higher magnitude, until the first significant one is found. The $\mathrm{k}^{\mathrm{th}}$ component is considered significant on the basis of the Fisher test applied on its related standardized F-variable:

$$\mathrm{F_{1,n-k}} = \left(\sum_{\mathrm{k-1}}^{\mathrm{n}} (\mathrm{m} - \mathrm{i} + 1)(\mathrm{n} - \mathrm{i} + 1)\right) \qquad (2.10)$$

If the percentage of significance level (%SL), associated with $\mathrm{k}^{\mathrm{th}}$ F variable, is lower than a pre-fixed value (usually fixed to 5%), then the $\mathrm{k}^{\mathrm{th}}$ extracted component is accepted as a pure component.

Although these estimators have been applied with success in several XANES studies [14-17], it is worth noting that the identification of the number of PCs connected with the existence of determined chemical species critically depends on the amount of noise affecting the data, as showed by Manceau et al. [13]. In fact, deviation from the correct number of chemical species notably occurs when the level of the experimental noise is close to the variation of the data. Another cause of uncertainty in the estimation of the correct number of PCs, must be found in an inconsistent normalization of the XANES dataset under analysis [13]. Moreover, if the concentration of some components is approximatively constant, or if the ratios of the concentration of some components are the same in the whole dataset, their independent contributions cannot be properly separated [5, 13, 18].

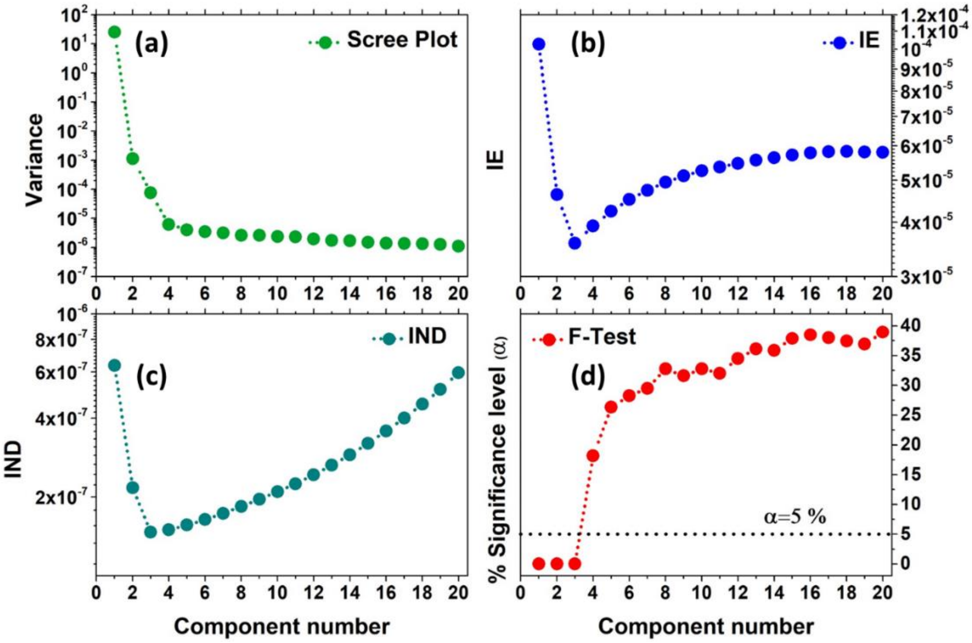

**Figure 2.6:** Statistical estimators used to evaluate the number of PCs contributing to the Pt $L_3$-edge XANES dataset showed in **Figure 2.4**(a). As it is possible to see, all the methods show a number of signal-related PCs equal to three. The elbow of the scree plot appears at the third component, in the Malinowsky F-test only three components are below the significance level of 5%, while both the IND and IE factors show a minimum sited at PC=3.

Finally, it is important to clarify the question regarding how many spectra are required for a proper identification of the significant components contributing to a XANES dataset. Because PCA is a statistical approach, one could think that, the higher the number of XANES spectra constituting a dataset, the higher would be the possibility to successfully identify all the contributing chemical species. That is ultimately not true, since PCA is a technique able to catch the highest independent variations of a dataset. It follows that it is preferable to have a lower amount of XANES spectra homogeneously sampling a chemical/physical process throughout its whole development, than a larger number of XANES spectra collected uniquely in determined moment of the reaction. Examples where the application of the PCA on a limited set of XANES spectra has been able to provide interpretable result can be found in the works by Beauchemin et al. [19], Lengke et al. [20] and Bugaev et al. [21], where the analyzed XANES datasets are composed by six, eight and ten spectra, respectively.

In PyFitIt is present a section designed specifically to help the user to identify properly the number of chemical species characterized the dataset. It posses a graphical user interface written exploiting the Jupyter notebook environment [22] in order to make accessible all the methodologies described before for a general user and it is reported here in **Figure 2.7**.

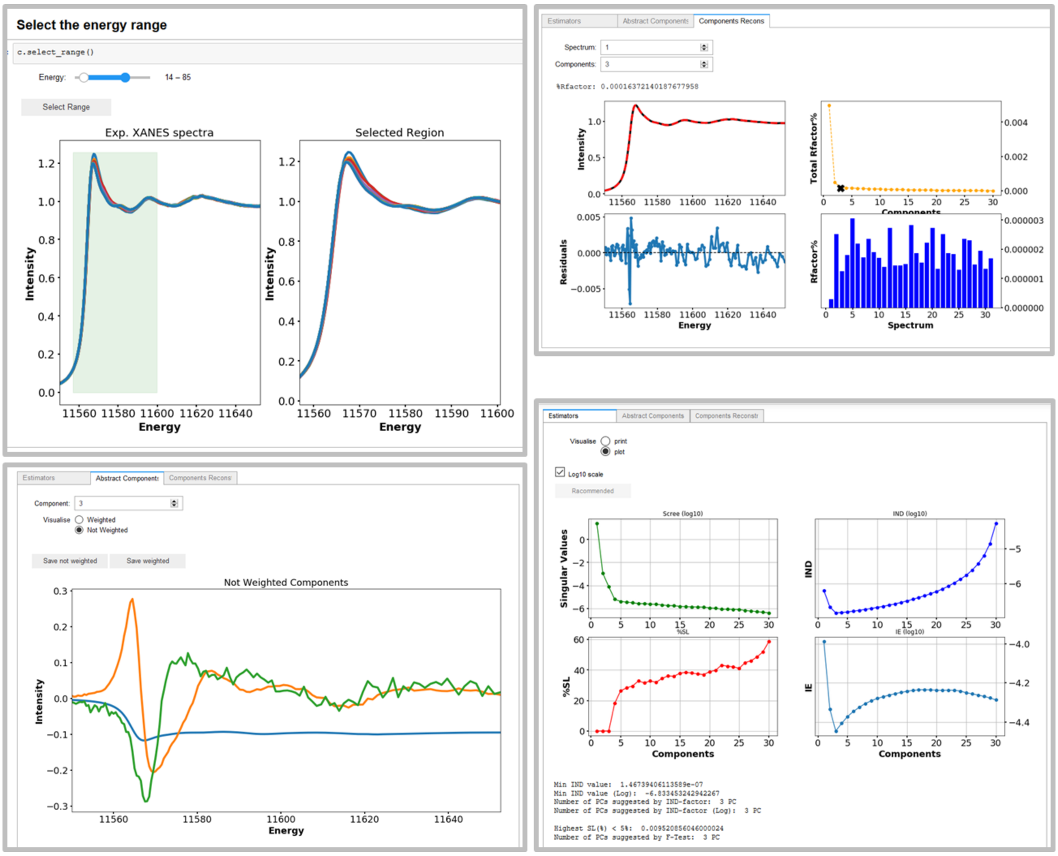

```
c.select_range()
```

Spectrum: 1
Components: 3

```
%Rfactor: 0.00016372140187677958
```

Component: 3

```
Min IND value:  1.46739406113589e-07
Min IND value (Log):  -6.833453242942267
Number of PCs suggested by IND-factor:  3 PC
Number of PCs suggested by IND-factor (Log):  3 PC

Highest SL(%) < 5%:  0.009520856046000024
Number of PCs suggested by F-Test:  3 PC
```

**Figure 2.7:** First four panels of the PCA Jupyter notebook notebook, showing the methods described before belonging to the PyFitIt code.

### 2.1.3 *Models used to decompose a XANES dataset*

As shown in **section 2.1.1**, PCA appears to be a fundamental tool to correctly understand the number of pure species characterizing a XANES dataset. Moreover, the PCA approach allows to decompose the set of data in a form resembling equation (2.2): if the PCA of a XANES dataset leads to the identification of $\mathrm{N}$ PCs, equation (2.5) can be rewritten as:

$$\mathbf{X} = \mathbf{R}_{\mathrm{N}}\mathbf{V}_{\mathrm{N}}{}^{\mathrm{T}} + \boldsymbol{\mathcal{E}} \tag{2.11}$$

where the subscript $\mathrm{N}$ indicates that only the first $\mathrm{N}$ column of $\mathbf{R}$ and $\mathbf{V}$ have been considered in the reconstruction of $\mathbf{X}$. If the number of PCs has been chosen correctly, each residual spectrum of $\mathcal{E}$ must resemble the white noise. It is interesting to note that among the various methods that can be adopted to decompose matrix $\mathbf{X}$ as (2.2), the one showed in (2.11) is able to guarantee the highest approximation of $\mathbf{X}$ (i.e. the lowest residual matrix), as stated by the Eckhart-Young theorem [23].

If analyzed, matrices $\mathbf{R}_{\mathrm{N}}$ and $\mathbf{V}_{\mathrm{N}}$ possess the same dimensionalities of $\mathbf{S}$ and $\mathbf{C}$, respectively. However, their set of spectra and concentration profiles do not have any spectroscopic meaning, as showed by **Figure 2.4**(b). For this reason $\mathbf{R}_{\mathrm{N}}$ and $\mathbf{V}_{\mathrm{N}}$ can be considered only as a mathematical solution of equation (2.2) and are usually named as the abstract set of spectra $\mathbf{S}_{\mathrm{abs}}$ and concentrations $\mathbf{C}_{\mathrm{abs}}$ of a dataset $\mathbf{X}$: $\mathbf{S}_{\mathrm{abs}} = \mathbf{R}_{\mathrm{N}}$ and $\mathbf{C}_{\mathrm{abs}} = \mathbf{V}_{\mathrm{N}}$. Despite this problem, it is worth noting that

the columns of $\mathbf{S}_{\mathrm{abs}}$ can be combined together linearly in order to construct one or more pure spectral profiles with a chemical/physical meaning. This procedure is at the basis of some approaches quite used in the field of XANES data analysis. These include, for example, the Transformation Matrix (TM) method currently employed in PyFItIt and described in **section 2.1.3.2.2**. On the other hand, several other methods been developed to realize equation (2.2) without making any kind of transformations on matrix $\mathbf{S}_{\mathrm{abs}}$ and $\mathbf{C}_{\mathrm{abs}}$, employing only some standard spectra or a set of selected spectral profiles for a single or multiple least-squares refinement. The most widely used are the Linear Combination Analysis (LCA) or Fit (LCF) (present in THORONDOR [4], see **chapter 4**), and the Alternating Least Squares (ALS) approach which will be added soon on PyFitIt.
In the following, each cited method will be described in detail.

### 2.1.3.1 *Linear Combination Analysis*

Given an experimental spectrum, if a set of $\mathrm{k}$ known reference spectra, named as standards, is supposed to correspond to the independent species present in the sample, they can be employed in (2.1) to retrieve the related fractions through the following minimization procedure:

$$\min_{\mathrm{c_i}}(\mu(\mathrm{E}) - \textstyle\sum_{\mathrm{i=1}}^{\mathrm{k}} \mathrm{c_i}\mathbf{s}_{\mathrm{i}}^{\mathrm{std}}(\mathrm{E})\,))^2 \text{ with } \textstyle\sum_{\mathrm{i=1}}^{\mathrm{k}} \mathrm{c_i} = 1 \tag{2.12}$$

where $\mathbf{s}_{\mathrm{i}}^{\mathrm{std}}(\mathbf{E})$ is the ith standard spectrum involved in the reconstruction. This method is the so-called Linear Combination Analysis (LCA) and it can be properly applied in the absence of non-linear effects, due to the sample thickness or fluorescence self-absorption, distorting the experimental data [24]. Equation (2.12) can undergo towards further modifications if one wants to optimize, besides the fraction estimations, secondary parameters such as the shifts in energy $\Delta\mathrm{E_i}$ of each reference. It is possible, in fact, to construct, in this case, a function returning each selected reference, interpolated over a fine energy grid, depending on $\Delta\mathrm{E_i}$ as: $\mathbf{s}_{\mathrm{i}}^{\mathrm{std}}(\mathrm{E};\Delta\mathrm{E_i}) = \mathbf{s}_{\mathrm{i}}^{\mathrm{std}}(\mathrm{E}+\Delta\mathrm{E_i})$. These quantities, together with each term $\mathrm{c_i}$ can then be refined minimizing (12) through a non-linear least squares approach [25, 26].
LCA can be clearly extended to the study of a dataset $\mathbf{X}$ once that the number of components has been defined by means of PCA. However, it is worth noting that the LCA of a series of XANES spectra can be performed properly only in the hypothesis that the selected set of standards is able to describe adequately each spectrum in the dataset. Moreover, how it was described by Giorgetti et al. [27], it is required to safely exclude secondary processes affecting the measure, such as the loss or the dissolution of some part of the sample, which can make the mass-balance condition constraint incorrect. These phenomena can be detected by analysing the XANES background of each spectrum; if it appears globally stable, it is possible to conclude that the modifications of the XANES features are only due to relevant physico-chemical processes and not to experimental artefacts. On these bases, the minimization procedure reported in (2.12) can be realized employing each spectrum composing $\mathbf{X}$, resulting in a set of concentrations profiles which describe, for each scan, the amount of each reference characterizing the experimental spectra composing the XANES dataset.

#### 2.1.3.2 *Multivariate Curve Resolution (MCR) Approaches Applied to XAS Data*

Multivariate curve resolution (MCR) is a generic denomination for a family of approaches aimed to realize the decomposition (2.2) from the sole information derived from the original data matrix, including the contributions coming from different chemical species [28]. Among the large number of methods which have been developed for this purpose [28], in the following sub-sections the main approaches designed and employed in my research project are described. These include: the transformation matrix approach (TM) and, finally, the alternating least squares method (ALS). The ALS approach can be employed to realize the so-called blind source separation of the dataset components [6], especially for the XAS datasets showing large variations of their spectral features. On the other hand, the TM method is mostly suitable for those datasets composed of spectra presenting limited variations in the XAS spectral features. However, the resulting set of spectra and concentrations require a careful a posteriori assessment by the user, who needs to discriminate the feasible solutions retrieved by (2.2) based on their physico-chemical and spectroscopic reliability. Generally speaking, although a priori knowledge is not mandatory in implementing such approaches, the availability of complementary information on the investigated systems and chemical processes often plays a crucial role in retrieving a meaningful solution.

In case of the MCR approaches, some rules of thumb should be followed to have higher possibilities to retrieve a feasible solution from equation (2.2). As in the PCA case, it appears more useful to have a lower amount of XAS spectra but homogeneously sampling the entire reaction process rather than a larger dataset contained several spectra acquired only in some specific moment of the experiment. The reason for this choice stands in the possibility to obtain a uniform distribution of the variations of the XAS spectral features during the entire measurement, thus increasing the probability to avoid a deficiency in the estimation of the rank of the dataset. Moreover, this methodology helps in identifying an initial set of spectra and concentration profiles as close as possible to the ideal, pure ones, leading the subsequent refinement towards a chemical/physical interpretable solution. Finally, it is worth to mention here a fundamental result obtained by Manne [29], who proposed two theorems aimed at defining when a dataset can be uniquely and correctly resolved. These states that: (i) the concentration profile of a determined compound can be correctly resolved if all the components inside the range of scans, where it is supposed to appear and evolve (i.e., its concentration window) are also present outside; (ii) the pure spectrum of a compound can be correctly recovered if its related concentration profile is not fully embedded into the range of existence of another component [28]. If these requirements are satisfied, a feasible solution can be identified using any MCR approach.

##### 2.1.3.2.1 *The Alternating Least Squares (MCR-ALS)*

The ALS approach, usually referred to as MCR-ALS, is a spectral un-mixing method introduced by Tauler and co-workers [30-32]. MCR-ALS has been largely used during the last two decades in different fields of research, ranging from chromatography to image analysis [28, 32]. This method was applied for the first time in the field of XAS data analysis by the pioneering work of Conti et al. [14]. Afterward, an increasing number of research groups have begun to use it in the analysis of XAS datasets relevant to different research areas, such as batteries [14], quantum-dots formation [33], solid-state chemistry [34] and heterogeneous catalysis [16, 35-38]. The main reasons behind the spread of this algorithm can be found in its simple implementation and robustness of the code as well as in the availability of practical Graphical user interface (GUI)s and packages which facilitate its application [39, 40].

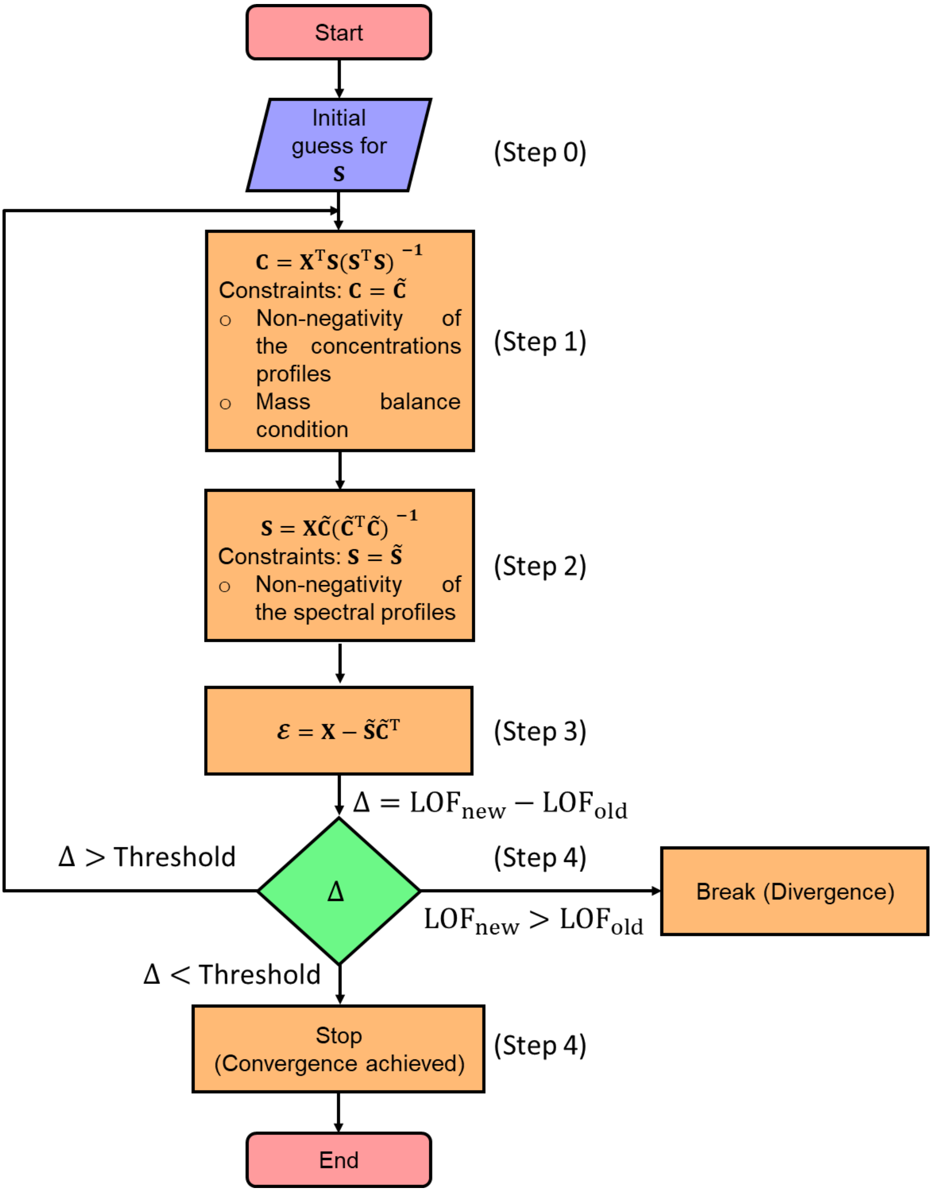

**Figure 2.8:** Flow diagram of the traditional ALS algorithm.

The flow diagram at the base of the MCR-ALS algorithm is showed in **Figure 2.8**. The first step of the algorithm consists in the estimation of a set of spectra or concentration profiles, whose number must correspond to the number of signal-related PCs. This step can be realized using different methods. For the analysis of XAS data the most widely used are the EFA and SIMPLISMA algorithms [41, 42].

Supposing that the MCR-ALS initialization has been realized using a set of spectra $\mathbf{S}_0$, the related concentration matrix $\mathbf{C}$ can be obtained, using a least squares approach, minimizing the square of residuals between the experimental XAS dataset $\mathbf{X}$ and the approximated one: $\min\limits_{\mathbf{C}}[(\mathbf{X}-\mathbf{S}_0\mathbf{C}^{\mathrm{T}})^2]$ which lead to the linear least squares solution: $\mathbf{C}=\mathbf{X}^{\mathrm{T}}\mathbf{S}\left(\mathbf{S}^{\mathrm{T}}\mathbf{S}\right)^{-1}$ (step 1). Afterwards, a set of constraints must be imposed on $\mathbf{C}$ to guarantee physico-chemical meaningfulness of the retrieved concentration profiles. As described in the precedent sections, dealing with XAS spectra it is possible to apply only two kind of constraints: the non-negativity of the spectra and concentration values and the mass balance condition (only if there are not phenomena involving the lost or dissolution of the sample under measurement). It follows that the negative elements of each column of $\mathbf{C}$ are set to zero while the row elements can be scaled by their related sum ensuring the condition $\sum_{\mathrm{j}}^{\mathrm{N}}\mathrm{c}_{\mathrm{ij}}=1$, where $\mathrm{c}_{\mathrm{ij}}$ is the element of matrix $\mathbf{C}$ sited in row $\mathrm{i}$ and column (scan) $\mathrm{j}$. Afterwards, the corrected matrix $\tilde{\mathbf{C}}$ is involved in the calculation of the new set of spectral profiles $\mathbf{S}$ minimizing, for a second time, the squared residuals between $\mathbf{X}$ and the reconstructed dataset: $\min\limits_{\mathbf{S}}[(\mathbf{X}-\mathbf{S}\tilde{\mathbf{C}}^{\mathrm{T}})^2]$, the solution of which is: $\mathbf{S}=\mathbf{X}\tilde{\mathbf{C}}(\tilde{\mathbf{C}}^{\mathrm{T}}\tilde{\mathbf{C}})^{-1}$. The negative values of $\mathbf{S}$ are then forced to be zero, converting $\mathbf{S}$ in $\tilde{\mathbf{S}}$ (step 2). It is worth noting that the alternating computation of matrices $\tilde{\mathbf{C}}$ and $\tilde{\mathbf{S}}$ in the linear least squares approach followed by setting negative values to zero and by imposing the concentrations closure is simple but very crude and can make the algorithm quite slows, especially if the XAS data matrix $\mathbf{X}$ is composed by several spectra. This problem can be solved employing some non-negative least squares algorithms (implemented in the most widely used codes for data analysis such as Python, MATLAB and Wolfram Mathematica) which provides, as solution, a positive set of spectra or concentration subjected to linear constraints criteria (i.e., the mass balance condition) [43].

The corrected version of $\tilde{\mathbf{S}}$ and $\tilde{\mathbf{C}}$ can be employed to generate $\mathbf{X}$ as: $\mathbf{X}=\tilde{\mathbf{S}}\tilde{\mathbf{C}}^{\mathrm{T}}+\boldsymbol{\mathcal{E}}$ (step 3). Finally, the residual matrix $\boldsymbol{\mathcal{E}}$ is used for the calculation of the so-called lack of fit parameter (LOF) (step 4):

$$\mathrm{LOF}=100\times\frac{||\boldsymbol{\mathcal{E}}||}{||\mathbf{X}||} \tag{2.13}$$

After the calculation of the LOF parameter, using Equation (2.13), for the first iteration (i.e., $\mathrm{LOF}_1$), the ALS routine is re-started deriving a new set of concentration profiles from step 1 using the corrected spectral profiles $\tilde{\mathbf{S}}$ obtained from step 2 of the first cycle. The procedure then continues as described before until the LOF parameter for the second cycle is calculated ($\mathrm{LOF}_2$). Once this step is completed, the difference within $\mathrm{LOF}_1$ and $\mathrm{LOF}_2$ is evaluated. If this quantity is lower than a user defined value or threshold (usually 0.1%) the convergence is achieved and the ALS routine is stopped, otherwise the spectral profiles $\tilde{\mathbf{S}}$ are employed in step 1 of the third cycle and so on. It is possible that among two or more cycles the LOF parameter starts to increase, indicating the divergence of the routine; in this case the algorithm is automatically stopped.

The main weakness of the MCR-ALS algorithm stands in this poor convergence and in the so-called *rotational ambiguity*. This phenomenon expresses the fact that there is not a unique solution for the task of decomposing the XAS matrix $\mathbf{X}$ into the product of two positive matrices $\mathbf{S}$ and $\mathbf{C}$ [44]. In fact, as showed for the TM approach, it is always possible to decompose $\mathbf{X}$ as: $\mathbf{X} = \mathbf{S}\mathbf{T}\mathbf{T}^{-1}\mathbf{C}^{\mathrm{T}} + \boldsymbol{\mathcal{E}}$ . This evidence indicates that sets of spectra and concentration profiles with different shapes can reproduce the original dataset with the same fit quality. It follows that the final result retrieved by by the ALS approaches strongly depends on the initialisation of the routine, especially when the spectra composing the experimental dataset are similar to each other [28]. Different ways to assess the ambiguity of a solution can be found in references [45-48]. A common way to decrease or suppress this phenomenon foresees the usage of further constraints in the algorithm. These can involve, for example, the requirement that a pure spectrum or concentration profile could correspond to a determinate XAS standard or concentration values retrieved by other techniques (e.g., UV spectroscopy [49]). A second method requires that different datasets, supposed to be characterised by the same components, could be merged and analysed together in order to increase the probability to have a certain region of the data matrix where a particular species is dominant over the others. This procedure helps the initialization of the algorithms to identify, from the analysis of the dataset, a proper initial set of spectral and concentration profiles closer to the real solution. An example where this strategy provided good results is described in details in **chapter 5**, where multiple XANES datasets collected on Cu-Zeolites samples with different Si/Al and Cu/Al ratios, during thermal pre-treatment process carried out under consistent conditions, were joined in one larger dataset.

In order to clarify the concept of rotational ambiguity, an example is reported in the following. Herein two spectra corresponding to Cu K-edge XANES for CuO and $Cu_2O$ oxides have been considered. A theoretical XAS dataset composed by 30 spectra, see **Figure 2.9**(a), was generated on the basis of two concentration profiles following the kinetics curves: $\mathbf{c}_{\mathrm{Cu2O}}(\mathrm{t}) = \exp(-0.1\mathrm{t})$ and $\mathbf{c}_{\mathrm{CuO}}(\mathrm{t}) = 1 - \exp(-0.1\mathrm{t})$, where $\mathrm{t}$ denotes the scan number (or time). A noise matrix composed of 30 vectors, having their values selected following a normal distribution with mean 0 and standard deviation equal to 0.005, was added to the noise-free theoretical dataset in order to simulate the effect of the instrumental error in the measurement. The MCR-ALS routine, shown in **Figure 2.8**, was initialized using the EFA algorithm. Without any constraints, the algorithm converged after 21 iterations. The set of pure spectra and concentrations profiles are reported in **Figure 2.9**(b,c) (dotted black and grey curves). Focusing on the spectral profiles, small differences appear among the ALS retrieved spectra and the reference ones. These are localized around the rising-edge (approximately 8982 eV), the white line (W.L.) (approximately 8995 eV) and the post edge (approximately 9028 eV) features and refer exclusively to the first component, while the second is approximatively equal to the spectrum of $Cu_2O$. On the other hand, bigger differences appear analysing the concentration profiles. It is possible to see, in fact, that the concentrations of the pure spectra retrieved without any constraint slightly deviated from the real values. As described before, the deviations involving the extracted spectra and concentrations were connected with the rotational ambiguity affecting the solution of (2.2). Indeed, the ALS routine converged towards one of the several minima. The requirement that one pure spectrum corresponds perfectly to the $Cu_2O$ reference drives the algorithm to identify the correct solution (convergence after 19 iterations), as shown in **Figure 2.9**(b,c), where the constrained pure spectral and concentration profiles (orange and azure dashed curves) coincided with the standards.

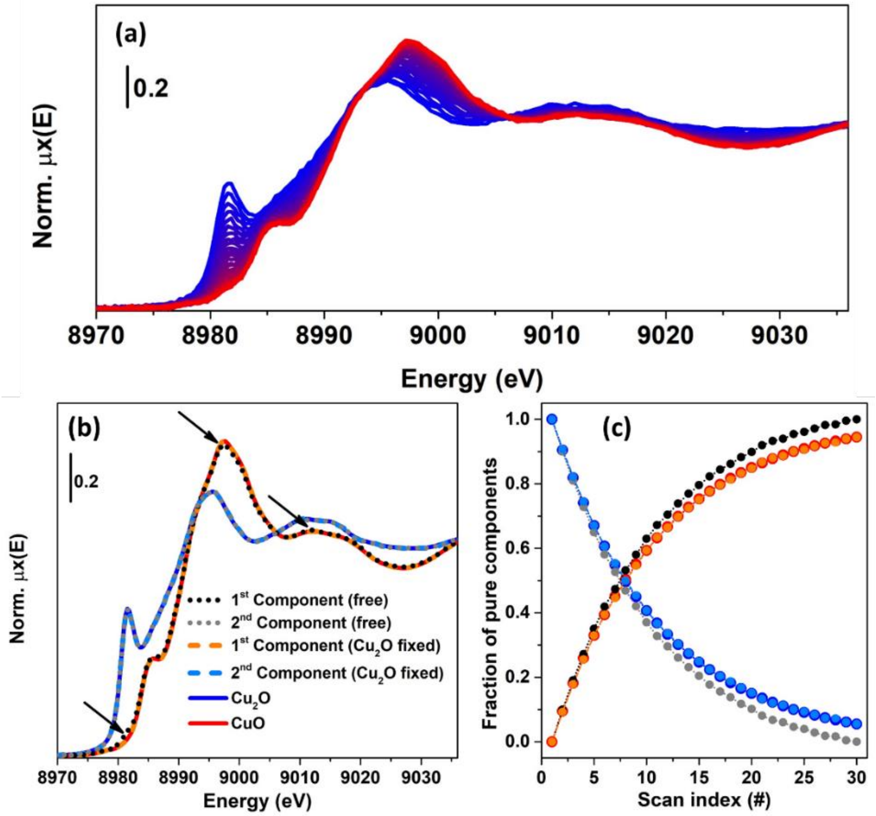

**Figure 2.9:** (a) Theoretical dataset (30 spectra), generated combining two spectra referring to $Cu_2O$ and CuO compounds using the following kinetic equations for the concentrations: $\mathbf{c}_{\mathrm{Cu2O}}(\mathrm{t}) = \exp(-0.1\mathrm{t})$ and $\mathbf{c}_{\mathrm{CuO}}(\mathrm{t}) = 1 - \exp(-0.1\mathrm{t})$, where the variable $t$ denotes the scan number (or time). (b,c) Set of spectral and concentration profiles retrieved from the MCR-ALS algorithm using unconstrained and constrained optimizations. The arrows in part (b) highlight the main differences between the spectrum retrieved by the unconstrained refinement (1st component) and the CuO reference.

The example showed before demonstrated that under a proper set of constraints, the ALS algorithm can provide a solution approximatively equal to the real one. However, it worth noting that the possibility of reaching a meaningful result depends also on the initial estimation of the spectral or concentration profiles. In the case illustrated in **Figure 2.9**, the theoretical dataset was characterised by two species, which, at scan 0, had a relative fraction set to 1 ($Cu_2O$):0 (CuO). This fact, as stated before, helps the EFA algorithm (and the SIMPLISMA algorithm as well) to identify a set of spectral profiles closer to the real ones.

#### 2.1.3.2.2 *Transformation Matrix Approach (TM)*

The transformation matrix (TM) approach was introduced by Smolentsev et al. [17] and then improved by me, A. A. Guda and S. A. Guda (The Smart Materials Research Institute, Southern Federal University, Rostov on Don). It is currently implemented in the PyFitIt software for the quantitative analysis of XANES spectra.

This method is based on the observation that the decomposition shown in Equation (2.11) is not unique. In fact, it can be rewritten as:

$$\mathbf{X} = \mathbf{S}_{\mathrm{abs}}\mathbf{T}\mathbf{T}^{-\mathbf{1}}\mathbf{C}_{\mathrm{abs}}^{\mathrm{T}} + \boldsymbol{\mathcal{E}} \tag{2.14}$$

where $\mathbf{T}$ is a is a square invertible matrix, called transformation matrix. Because the matrix product $\mathbf{T}\mathbf{T}^{-\mathbf{1}}$ is equal to the identity matrix $\mathbf{I}$, the variation of each element $\mathrm{T}_{\mathrm{ij}}$ of $\mathbf{T}$ does not have any kind of impact on the decomposition shown by equation (2.11). However, the abstract spectra and concentration profiles can be grouped in the following way: $\mathbf{S} = \mathbf{S}_{\mathrm{abs}}\mathbf{T}$ and $\mathbf{C}^{\mathrm{T}} = \mathbf{T}^{-\mathbf{1}}\mathbf{C}_{\mathrm{abs}}^{\mathrm{T}}$. Afterwards, the elements of $\mathrm{T}_{\mathrm{ij}} \in \mathbf{T}$ can be properly moved in order to retrieve a set of pure spectra and concentration profiles spectroscopically interpretable and to find a solution to equation (2.2). From a practical point of view, this step is realized in PyFitIt through the usage of a set of sliders which can be directly moved by the user. Because matrix $\mathbf{T}$ is a squared matrix with dimensions $\mathrm{N} \times \mathrm{N}$, the general number of sliders that could be moved would be equal to $\mathrm{N}^2$. While for the simplest case (i.e., $\mathrm{N} = 2$) four sliders can still be moved without large difficulties; however, when the number of species in the dataset starts to increase, this approach appears to be not so practical. Nevertheless, the possibility to impose a set of physical constraints can substantially reduce the number of sliders to move, together with their range of variation. As already stated in sections **2.1.3.1** and **2.1.3.2.1**, it is possible to include the non-negativity of the spectral and concentration profiles and the mass balance condition. While the first two constraints can be implemented looking for a set of parameters, $\mathrm{T}_{\mathrm{ij}}$ of $\mathbf{T}$ is able to provide absorption coefficients and concentration values that are non-negative, the mass balance condition is less straightforward to realize. In general, one should move the sliders in order to guarantee for each scan that the sum of all the concentration values is equal to one. If the XANES profiles, composing the dataset, only show small variations in their spectral shapes and intensities, it is possible to impose the normalization of the spectral profiles through the following formula:

$$\sigma_{\mathbf{i}}^{\mathbf{2}} = \frac{1}{\mathrm{E}_{\mathrm{max}} - \mathrm{E}_{\mathrm{min}}}\int_{\mathrm{E}_{\mathrm{min}}}^{\mathrm{E}_{\mathrm{max}}} \mathrm{dE}\ \mu_{\mathrm{i}}(\mathrm{E})^2 \tag{2.15}$$

where $\sigma_{\mathrm{i}}$ is the normalization factor used to scale the i^th spectrum determining $\sigma_{\mathrm{i}}^2 = 1$, while $\mathrm{E}_{\mathrm{min}}$ and $\mathrm{E}_{\mathrm{max}}$ are the minimum and maximum energy values of the XANES range, respectively. If the absorption edge region does not undergo towards abrupt changes, the normalizations factors remain almost unvaried from spectrum to spectrum: $\sigma_{\mathrm{i}} \cong \sigma = \mathrm{constant}$ (based on our experience, the variations of $\sigma$ involve usually the third decimal digit), allowing to maintain the same jump of absorption normalization (i.e., $\mu_{\mathrm{i}}(\mathrm{E}_0) \cong 1/\sigma$, where $\mathrm{E}_0$ is the energy edge position) approximatively constant for each XANES in the dataset. The requirement of the dataset normalization ensures the equality between each element of the first abstract concentration of (2.11) (i.e., $\mathrm{v}_{\mathrm{i}1}$) and the normalization coefficient related to the first abstract spectrum: $\mathrm{v}_{\mathrm{i}1} = \sigma_{\mathrm{u}}$, where $\sigma_{\mathrm{u}} = \sqrt{\frac{1}{\mathrm{E}_{\mathrm{max}}-\mathrm{E}_{\mathrm{min}}}\int_{\mathrm{E}_{\mathrm{min}}}^{\mathrm{E}_{\mathrm{max}}} \mathrm{dE}\mathbf{r}_1(\mathrm{E})^2}$ while $\mathbf{r}_1$ is the first vector columns (i.e., the first abstract spectrum) of matrix $\mathbf{R}_{\mathrm{N}}$. This result can be used to guarantee the condition $\sum_{\mathrm{j}=1}^{\mathrm{N}} \mathrm{c}_{\mathrm{ij}} = 1$. In fact, it is possible to show that the normalization of the components reduces the number of matrix transformation elements from $N^2$ to $N^2 - N$ and determines the following simplification:

$$\sum_{j=1}^{N} c_{ij} = \sum_{j=1}^{N} {t_{ik}}^{-1} v_{kj} = v_{i1}/\sigma_u = 1 \tag{2.16}$$

The presence of these constraints obviously limits the range of variation of the elements of $\mathbf{T}$ and only the construction of a proper set of strongly selective constraints can lead to the isolation of a series of XANES components extremely close to the real physical/chemical solution. These can foresee, for example, the requirement that a particular spectrum in the dataset could be considered as pure. It follows that a selected column of $\mathbf{T}$ could be recovered using a least squares approach as in (2.12) in order to allow the equality between the pure spectrum and the experimental one. The number of sliders to move is then reduced to $N^2 - 2N + 1$. Furthermore, other constraints can be clearly implemented and imposed in order to reduce the number of free sliders, as described in [50].

$$N_{param}: \begin{cases} N^2 - N: \ \text{Norm. imposed;} \\ N^2 - 2N + 1: \ \text{Norm. i and first/ last spectrum fixed;} \\ N^2 - 3N + 2: \ \text{Norm. and both first and last spectrum fixed;} \end{cases} \tag{2.17}$$

The output of the PyFitIt software concerning the TM method, is reported in the following picture, **Figure 2.10**.

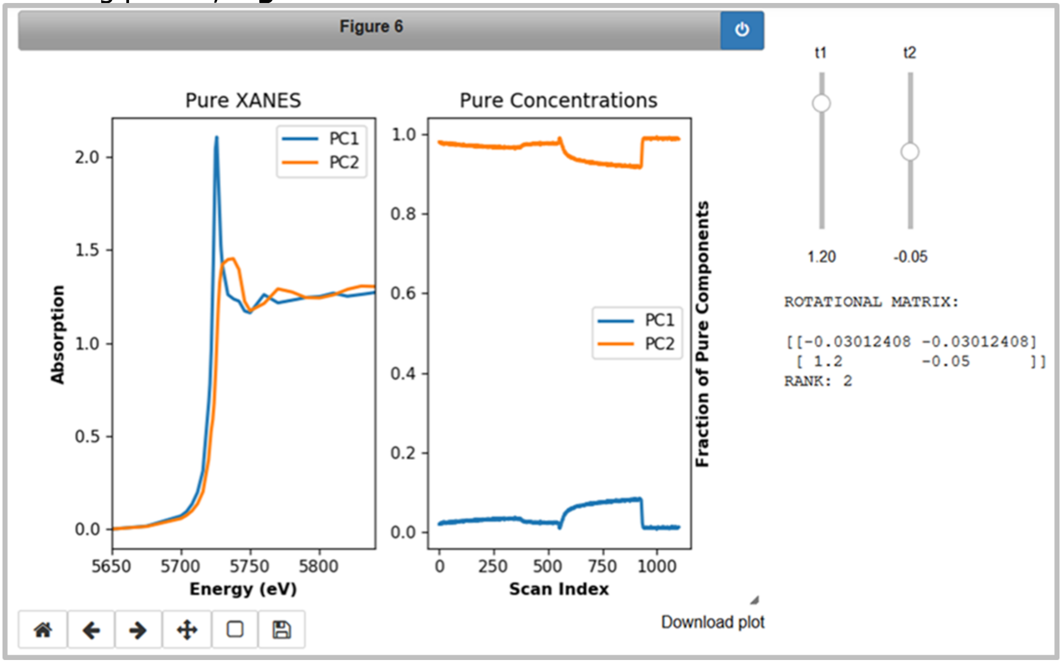

```
ROTATIONAL MATRIX:

[[-0.03012408 -0.03012408]
 [ 1.2         -0.05       ]]
RANK: 2
```

**Figure 2.10:** Output of the TM approach provided by the PyFitIt code. On the lest are present the set of sliders whose variation is able to change the weights related to the linear combination of the PCs involved in the data mixture. Here it is worth noting that the labels PC 1 and PC 2 do not stands for Principal Component n° 1 and 2 but for Pure Component 1 and 2. A similar notation will be used also in **chapter 5**.

As an example, in **Figure 2.11**, it is reported t the solution is found by applying this approach to the set of Pt $L_3$-edge XANES spectra shown in **Figure 2.4**(a).

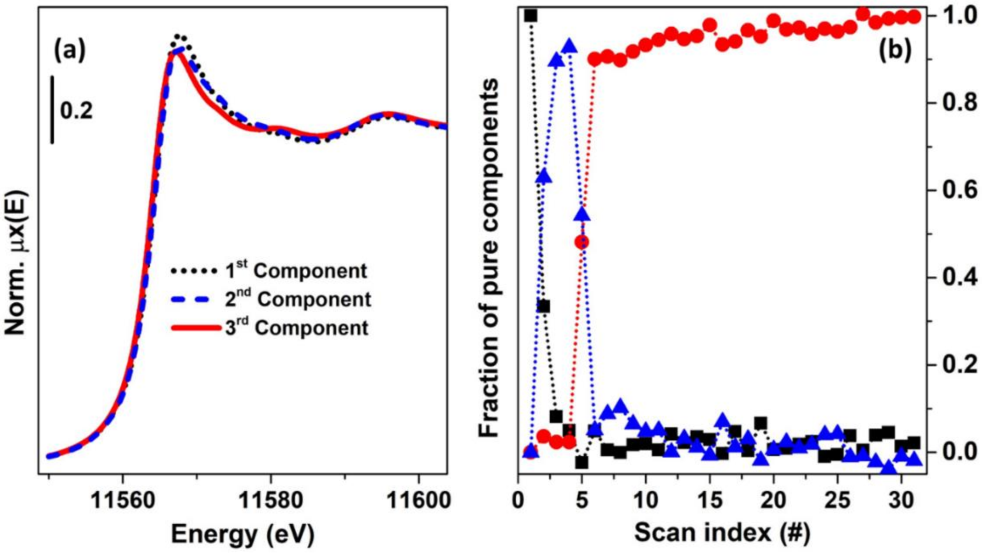

**Figure 2.11:** The result of the TM approach applied to the set of data reported in **Figure 2.4**(a). Herein, the normalization constraint together with the requirement that the first spectrum of the XANES dataset corresponds to a pure specie have been imposed. The method shows that the process involves a three-step mechanism. The 1st component corresponds to partially oxidized Pt nanoparticles (NPs). The 2nd component corresponds to the maximum hydrogen coverage upon interaction of Pt NPs with the $H_2$/He mixture at 120 °C. Finally, the 3rd component, forming during the dehydrogenation step, corresponds to the minimum hydrogen coverage over the supported Pt NPs. More information about the analysed process and complementary characterisation results for this system can be found in Reference [9].

#### 2.1.3.2.3 *A remarkable application of the TM approach: Tracking the Ce-Speciation in Pt/$CeO_2$ Catalysts under Redox Conditions*

Noble metals on redox-active $CeO_2$ supports are largely employed in the automotive sector to clean vehicles exhaust gases from polluting products such as CO, $NO_x$ and unreacted hydrocarbons. In relation with their application in gas after treatment systems, these catalysts naturally operate under rapid oscillations of the gas feed composition [51], making transient XAS experiments particularly suited to determine and correlate reduction/oxidation kinetics of both noble-metal NPs and ceria support.

Herein the data concerning an experiment performed at the SuperXAS beamline of the SLS are provided. The experimental setup consisted in a for fluorescence-detected XAS with sub-second time resolution employed to track Ce-speciation in 1.5 wt% Pt/$CeO_2$ catalysts while cycling CO and $O_2$ gas feeds. The sample was sieved to 100–150 μm grain size and placed into an in situ plug-flow reactor cell [52]. Afterwards, the reactor was connected to gas lines devoted to reductive (5% CO in argon) and oxidative (21% $O_2$ in argon) gas feeds; fast electro-valves allowed quick switching between these two mixtures. The study involved XAS data collection at both Pt $L_3$- and Ce $L_3$-edge; hereafter, only the latter dataset is considered, addressing the response of the $CeO_2$ support. **Figure 2.12**(a) shows the set of experimental spectra, recorded during two redox cycles at 26 °C and 90 °C, consisting into 120 s of reduction by CO gas flow followed by 60 s of oxidation in $O_2$. These cycles were repeated for every energy point of the spectrum, selected by the monochromator; in each point, the Ce $L_3$ fluorescence signal was recorded with 0.3 s time resolution, ultimately resulting in 1103 Ce $L_3$ XANES spectra.

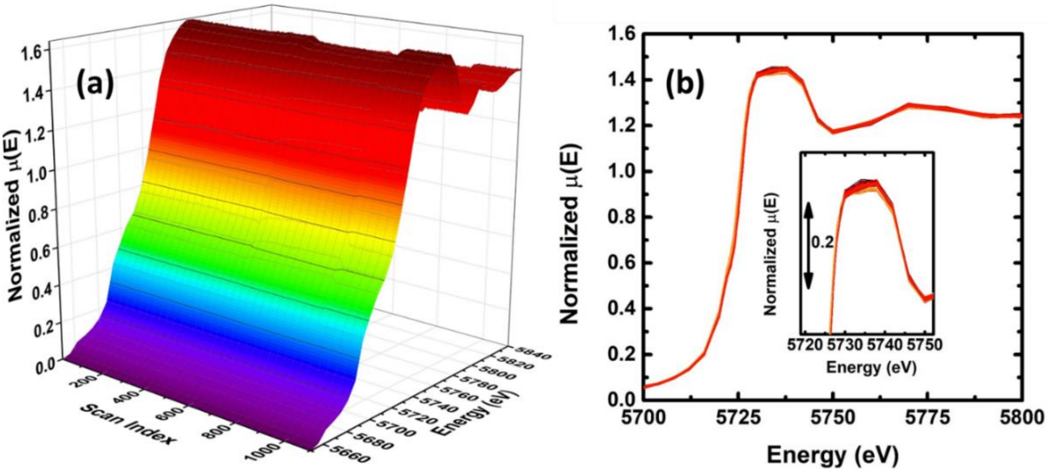

**Figure 2.12:** (a) 3D (energy, scan index vs μ(E)) and (b) 2D (energy vs μ(E)) representation of 1103 Ce $L_3$ XANES spectra. This dataset was used further as input for the analysis of the principal component and the following spectral and concentration decomposition.

The differences between subsequent spectra are hardly visible from simple qualitative analysis of the dataset, as it can be noted in **Figure 2.12**(b). Thus, quantitative analysis of the PCs was applied to clarify the number of pure components in the set of spectra and their concentrations profiles. PCA performed on the raw fluorescence-detected data indicated the presence of two components affecting the dataset; all the statistical estimators (scree plot, IE, IND, and F-test) suggested the same number of PCs. Similar to what was done in the previously discussed example, also in this case the TM approach was employed to model the abstract spectra and concentrations, starting from an initial transformation matrix consisting of four elements. Imposing the normalization of the components, the number of its free parameters was reduced to two. Afterwards, these elements were moved in the range between -2 and 2 with a step of 0.05 guaranteeing the non-negativity of the spectra and concentration values. A chemical/physical meaningful solution was found with the following matrix:

$$\mathbf{T}_{\mathrm{Ceria}} = \begin{pmatrix} -0.03 & -0.03 \\ 1.20 & -0.05 \end{pmatrix}$$

The possible solution is reported in **Figure 2.13**(a) and (b).

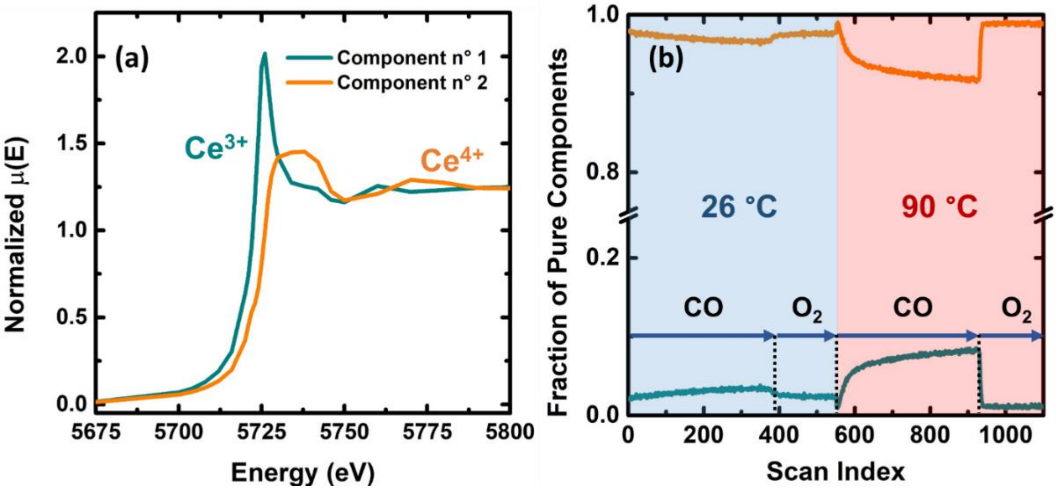

**Figure 2.13:** Pure Spectra (a) and Concentration profiles (b) recovered from the Ce $L_3$ XANES spectra shown in **Figure 2.9**. With the blue and orange lines are represented, respectively, the spectra and the related concentration profiles of $Ce^{4+}$ and $Ce^{3+}$ species.

Kinetic curves obtained in **Figure 2.13**(b) contain important information about catalytical system. First, it is possible to estimate directly the concentration of active oxygen atoms which are released from ceria lattice at two temperatures: 26 and 90 °C. Indeed, each released oxygen leave two electrons in the system which reduce two ceria atoms from $Ce^{4+}$ to $Ce^{3+}$. The amount of lattice oxygen that can be extracted in CO atmosphere from the $CeO_2$/Pt increases six times upon temperature increase. Another important feature is that at 26 °C ceria is not fully oxidized in the $O_2$ atmosphere and some fraction of $Ce^{3+}$ atoms is constantly present in the lattice which was also indicated by another methods [53]. Finally, the time dependant concentrations reported in **Figure 2.13**(b) can be further used to calculate kinetic constants of the system which are important to understand the microscopical origin of the catalytic behaviour of the ceria-based system [54].

It is worth noting that, in general, an original dataset can be reconstructed with the same quality fit using spectra and concentration profiles, with different shapes, by varying each element of the corresponding transformation matrix $\mathbf{T}_{\mathrm{Ceria}}$. In order to reduce it, different further constraints can be imposed. In the case of the Ce dataset, the transformation matrix is constituted by two free parameters. This means that the areas of feasible solutions (AFS) can be represented graphically (i.e. a 2D plot) and limited by further specific constraints. In this case, the study was restricted considering only the couples of $(\mathrm{T}_1, \mathrm{T}_2)$ able to isolate only the *pure* non-negative spectra, with a white line lower than 2.5, and characterized by concentration values between 0 and 1. The results of this calculation are reported in **Figure 2.14**(a,b).

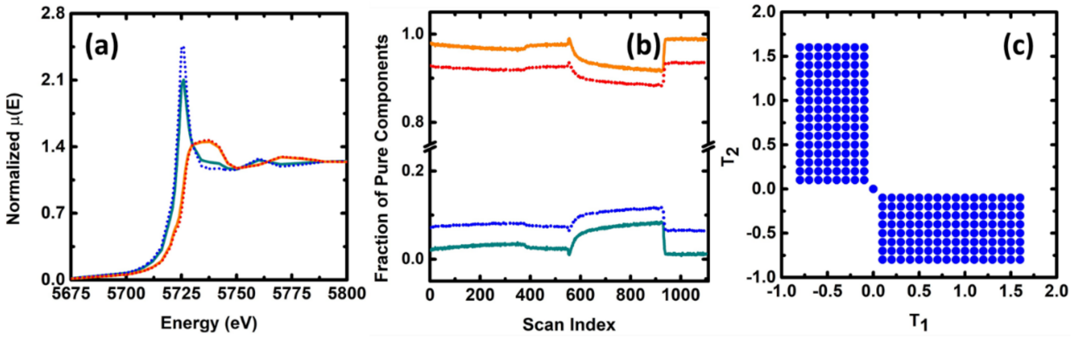

**Figure 2.14:** Pure spectral (a) and concentration profiles (b) obtained by setting both the free elements of matrix $\boldsymbol{T}_{Ceria}$ respectively to: 1.20 and -0.05 (continuous lines) and to 1.60 and -0.15 (dotted lines) .(c) Related area of the feasible solution obtained selecting a range of variation for variables $T_1$ and $T_2$ between -2 and 2 with a step of 0.1. The following constraint have been considered: 1) non-negativity of the spectral profiles; 2) maximum intensity of the spectral white line fixed to 2.5; 3) concentration values included in the region between 0 and 1.

From **Figure 2.14** (c) it is possible to see the presence of a general *symmetry* in the AFS representation. This behaviour can be explained on the basis that there is no inherent order on the columns of the pure spectral matrix $\mathbf{S}$ and the corresponding rows of $\mathbf{C}$. The interchanging the two columns of $\mathbf{S}$ and rows of $\mathbf{C}$ is realized by permuting the two columns of the transformation matrix (i.e. swapping the two free elements of $\mathbf{T}_{\text{Ceria}}$). From this example it is possible to understand that, without a set of appropriate constraints, it is literally impossible to identify a unique solution.

#### 2.1.3.2.4 *Retrieving the Area of Feasible solutions associated to the TM approach*

In the following, an experimental case regarding the identification of the AFS associated to a XAS dataset is provided. The XANES spectra regards the evolution of Cu K-edge associated to determined Cu-complexes, forming during the direct conversion of methane ($CH_4$) to methanol ($CH_3OH$) (DMTM) catalysed by a particular kind of Cu-zeolite (ferrierite (FER)). The intent here is not to provide a detailed description of the process and of the Cu speciation (which will be discussed in details in **chapters 5** and **6**) but it wants to underlie a method to visualize and analyse the AFS associated to a three component mixture. The XAS test data were collected during the DMTM conversion at beamline BM31 [55] of the European Synchrotron Radiation Facility (ESRF, Grenoble, France). The followed protocol is reported in **Figure 2.15**. Technical details concerning the XAS data acquisition can be found in **section 5.8.1** (*Operando* XAS measurements) of the appendix in **chapter 5**.

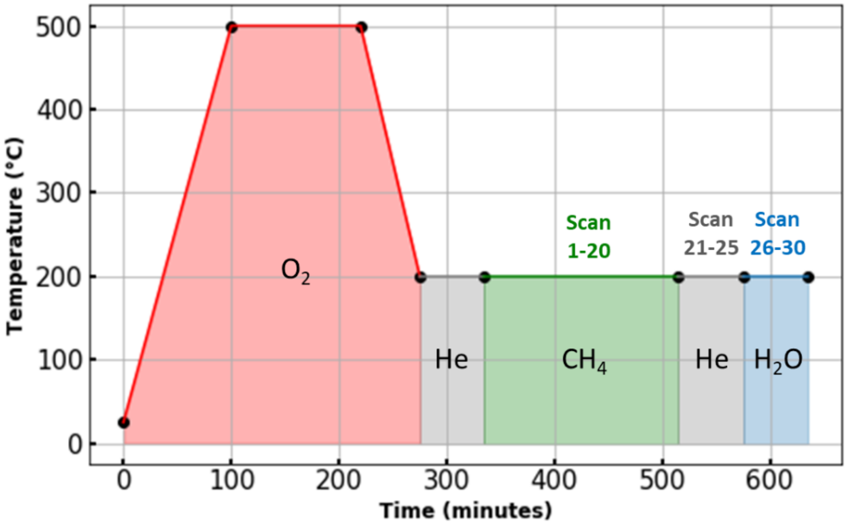

**Figure 2.15:** Graphical representation of the protocol followed: 120 min $O_2$ activation at 500 °C (red), 180 min $CH_4$ loading at 200 °C (green), steam-assisted $CH_3OH$ extraction at 200 °C for ca. 60 min (blue). The sample and the lines were flushed with He (grey segments) after $O_2$ activation and $CH_4$ loading for ca. 60 min.

In order to obtain more insights into the conversion mechanism of $CH_4$ to $CH_3OH$ mediated by Cu-FER, the set of data acquired after the $O_2$ activation (see **Figure 2.15**) starting from the He flushing till to the extraction of $CH_3OH$ by means of steam have been selected for the MCR analysis. The collected dataset shown in **Figure 2.16** is composed by 30 XANES spectra properly normalized to the unity edge jump using the Athena software from the Demeter package [56].

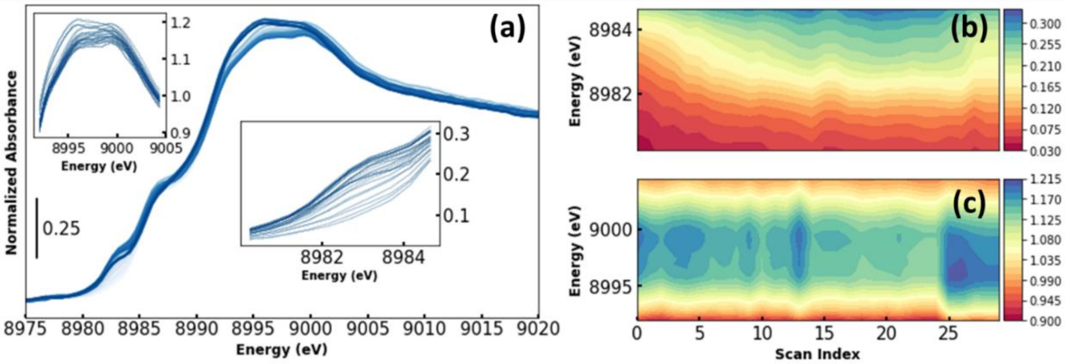

**Figure 2.16:**(a) Plot of the analysed time-resolved XANES dataset: the insets contain the magnification of the spectral regions showing the highest variations during the followed experimental protocol: W.L. variations (upper left inset), rising-edge peak variation (central inset). (b) Contour maps associates to the insets reported in Figure (a).

As it is possible to see from **Figure 2.16**(a), during the entire DMTM process, only small variations in the XANES spectra occur. In particular, these variations involve the intensities of the XANES WL and the rising-edge transitions (see the insets of **Figure 2.16**(a)). Analysing these spectral modifications together with the variation of the scan index (that can be imagined as a temporal variable, being the adopted sampling time in our experiment 5 min/scan) some interesting trends appear. By sending $CH_4$, scans 1-20, the energy edge is shifted progressively towards lower values, the XANES white line magnitude becomes lower, while the intensity of the 1s→4p dipolar transition at ca. 8983 eV (characteristic of the Cu(I) ions) increases, as showed in **Figure 2.16**(b). This phenomenon can be interpreted as the reduction of a certain quantity of framework-coordinated Cu(II) sites, previously formed during the activation process in the presence of $O_2$, to Cu(I) sites, always coordinated to the zeolite lattice oxygens [57-59]. During the extraction of $CH_3OH$ with water, scans 26-30, the edge energy is re-shifted towards higher energy, the intensity of the Cu(I) 1s→4p transition is abated and the XANES white line feature grows up again (see **Figure 2.16**(c)). These evidences underline the presence of a higher abundance of Cu(II) sites in the chemical mixture, plausibly encompassing both Cu(II) aquo-complexes and framework-coordinated Cu(II) ions.

The TM approach was applied on the experimental dataset showed in **Figure 2.16**(a). Each spectrum was initially normalised using equation (2.15). Then, employing the TM method for three PCs, a 3×3 transformation matrix was defined. Thanks to the normalization constraint, the number of sliders was adjusted from nine to six. The elements of the matrix were then moved according to the non-negativity of the spectra and concentration profiles.

A retrieved solution of equation (2.2) having a well-defined chemical/physical meaning is given by matrix $\mathbf{T} = \begin{pmatrix} 1/\sigma & 1/\sigma & 1/\sigma \\ 3.40 & -1.05 & -0.70 \\ 0.45 & 1.50 & -0.30 \end{pmatrix}$, with $1/\sigma = -0.18$ and it is showed in **Figure 2.17**(a,c).

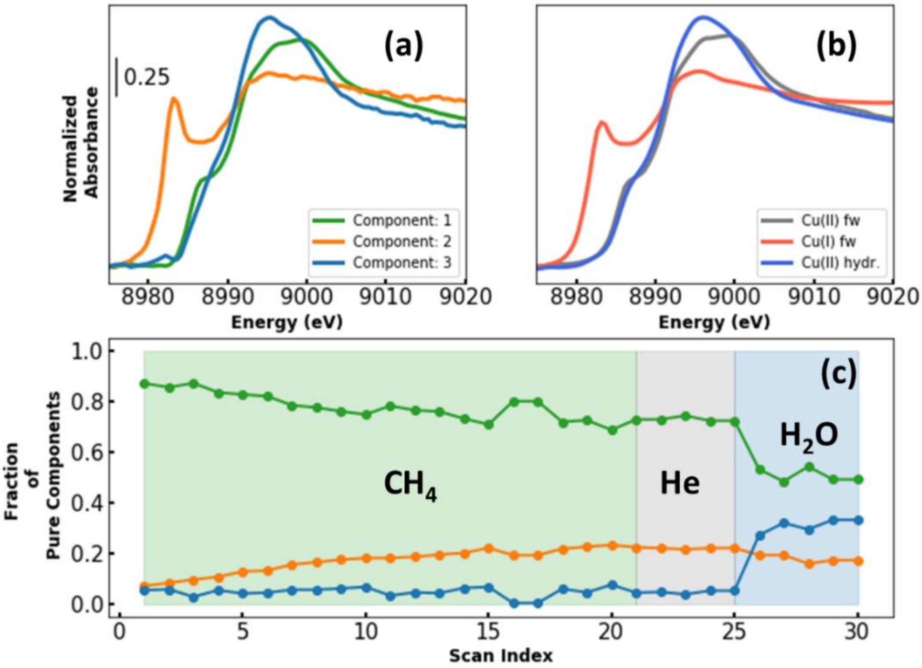

**Figure 2.17:** (a,c) Spectral and concentration profiles retrieved using the transformation matrix approach. (b) Cu-references used to test visually the goodness of the spectral decomposition.

It is possible to see that the identified spectral profiles are extremely similar to a set of references showed in **Figure 2.17**(b). These include a pseudo-octahedral

Cu(II) aquo-complex (Cu(II) hydr.) as well as two framework-coordinated Cu(II) and Cu(I) species referred to as Cu(II) and Cu(I) fw, respectively. The Cu(II) hydr. was obtained measuring a Cu(II) acetate aqueous solution at RT. The Cu(I) fw reference was collected at RT after heating the sample up to 400 °C in vacuum. Finally the XANES acquired in He at 200 °C, just before the $CH_4$ loading step, was used as a Cu(II) fw reference.

The extracted profiles seem to be affected by a small amount of noise. This fact can be explained remembering that if the correct number of components is chosen, the PCA acts as a filter removing the highest amount of noise characterizing the dataset. However, as described by Malinowsky [10], there is always a fraction of residual noise depending on the quality of the measurement mixed in the pure spectral and concentration profiles which cannot be removed deleting the unnecessary components.

The analysis of the concentration profiles associated to the pure spectra extracted showed in **Figure 2.17**(c) and can lead to the following interpretation. A fraction of the Cu(II) sites (green profile) formed after that activation at high temperature of the catalyst are converted, in presence of $CH_3OH$, in Cu(I) sites (orange) still interacting with the framework. During the water extraction, the framework-coordinated Cu(II) fraction diminution can be explained by the hydrolysis mechanism involving the methoxide group of the $Z[Cu(II)(OCH_3)]$ complex with the consequent formation of Cu(II) fully hydrated complexes (blue profile), while the small abatement of the Cu(I) concentration values can be associated with $H_2O$-mediated re-oxidation pathways. It is worth noting that a precise assessment on the nature of this Cu(II) site is not straightforward. As it will be showed in **chapter 5**, depending on the zeolite topology, a number of Cu(II)-oxo species potentially active towards DMTM have been proposed to form during the high-temperature activation in $O_2$ and their structures are still debated in the literature [57-60].

As previously discussed in **section 2.1.3.2.2**, the solution obtained by the matrix transformation method depends on the values of the elements of $T_{ij}$ and it is not unique. In order to quantify the maximum and minimum values of the spectral and concentration profiles for the solutions of (2.2), having a chemical/physical meaning, the following protocol can be followed:

First, an objective function $P$ can be defined as [61]:

$$P(T_{21}, T_{22}, T_{23}, T_{31}, T_{32}, T_{33}) = \sum_{i=1}^{m}\sum_{j=1}^{N} H_s(s_{ij}){s_{ij}}^2 + \sum_{k=1}^{n}\sum_{j=1}^{N} H_c(c_{kj}){c_{kj}}^2 \quad (2.18)$$

Due to the normalization constraint, $P$ does not depend on the first row of $\mathbf{T}$, fixed to $1/\sigma$. In (2.18) $H_s$ is a Heaviside function that returns 0 if the spectral values $s_{ij}$ are higher or equal to zero and 1 for their negative values, while $H_c$ is a second function, associated with the concentrations profiles, that returns 0 for concentrations within 0 and 1 while it is equal to 1 if this last condition is not satisfied. Initializing randomly function $P$ and minimizing it for a considerable number of iterations (i.e. 1000 or more) it is possible to obtain a graphical representation of all the combination of the elements of matrix $\mathbf{T}$ satisfying the AFS conditions, see **Figure 2.18**. The ensemble of spectra associated to every minimum point of (2.18) is showed in the bottom of this last picture.

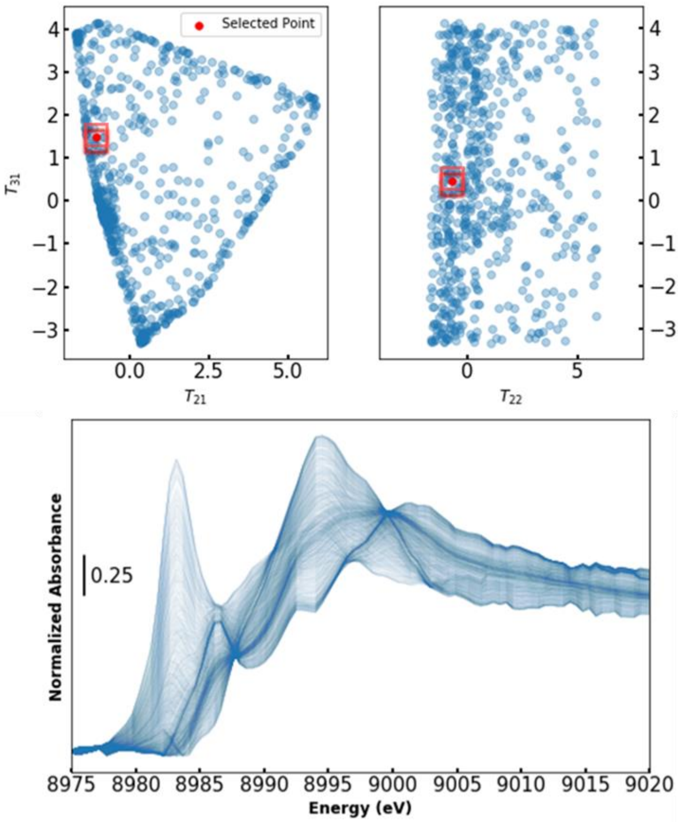

**Figure 2.18:** Graphical representation of two of the fifteen AFS, related to dataset showed in **Figure 2.16**, for the couples of variables: $(T_{21}, T_{31})$ and $(T_{22}, T_{23})$. These distributions have been obtained using a brute force approach, initializing and minimizing equation (2.18) for 1000 times. The initialization has been realized generating random numbers between -10 and 10, while for the minimization process, the Nelder-Mead algorithm has been employed [26]. With the red points are represented the sets of parameters able to provide the solution of **Figure 2.17**, while the red cubes indicates, pictorially, the projections of a six-dimensional hypercube with a side of 0.3 over the 2D plane defined by these couples of parameters. The bottom plot represents all the spectra associated to the points $T_{ij}$ reported on the top figure and satisfying equation (2.18).

The geometric shapes of the obtained AFS can be explained taking into account the portions of a $\mathbb{R}^6$ space enclosed in a subspace limited by the conditions $s_{ij} \geq 0$ and $0 \leq c_{ij} \leq 1$ [61]. Despite the large range of variation of the elements of the transformation matrix, only a small number of combinations of these parameters are acceptable. The retrieved spectra must satisfy the imposed constraints as showed by **Figure 2.18**, but, at the same time, they must be characterized by determined spectral features physically and chemically interpretable. This fact reduces drastically the number of spectra and the related AFS of **Figure 2.18**. Unfortunately, at the moment, there is no technique available able to automatedly assess if a XANES spectrum, generated by a determined combination of parameters $\mathrm{T_{ij}}$, has a physical/chemical meaning. As already stressed in **2.1.3.2.2**, the transformation matrix approach is not able to realize the so-called *blind source separation* of the experimental signal and only the user's intuition and the knowledge of the system under study can lead to a meaningful solution. Probably, the creation of a large dataset of reference XANES (experimental and simulated) spectra together with a solid Machine Learning algorithm for spectral comparison could improve the quality of the results. However, it is possible to select a region surrounding a feasible point and try to identify the maximum and minimum band boundaries of the feasible solutions having a physical/chemical meaning. To do this, the following scalar function can be defined:

$$f_k(T_{ij}) = \frac{\|\mathbf{S}(\mathbf{T})\mathbf{C}^T(\mathbf{T})\|}{\|\mathbf{X}\|} \tag{2.19}$$

This function gives the ratio between the contribution of a particular $k^{th}$ specie with respect to the total contribution coming from all the components $\mathbf{X}$. The optimization of this objective function, either maximized or minimized under the constraints, will give respectively the maximum and the minimum boundary for each chemical specie present in the dataset. In this case, it has been considered a subspace of the AFS consisting of a six-dimensional hypercube having a side equal to 0.3 (six times the step variation used as a standard values in PyFitIt) surrounding the point which provides the spectra and concentrations of **Figure 2.17**. Afterwards, equation (2.19) has been minimized and maximized changing progressively the components. This step was realised under constraints using the Sequential Least Squares Programming method [43].

The obtained results are showed in **Figure 2.19**.

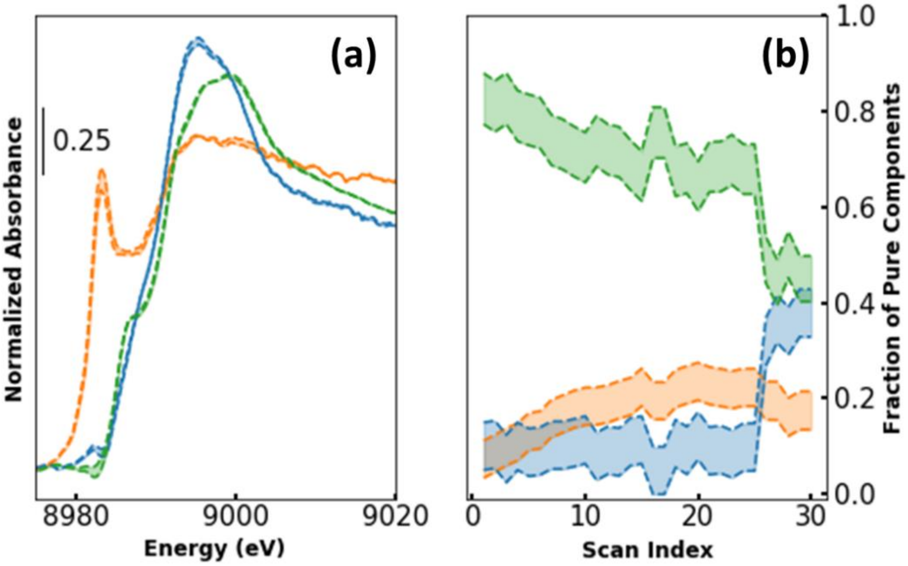

**Figure 2.19:** Spectral (a) and concentration (b) band boundaries calculated for the profiles of **Figure 2.17** minimizing and maximizing for six times equation (2.19).

Analysing this picture, it is interesting to see that the lines constituting the spectral variation bounds are extremely close to each other. Some small differences appear in the rising-edge region (especially for the 1s→4p peak of the Cu(I) component) and for the WL peak. Vice-versa, larger variations are observable for the related concentration profiles. The explanation must be found in the selection of the subspace of the $T_{ij}$ parameters used for the minimization procedure [62]. The chosen hypercube has been defined in order to incorporate only the spectral profiles characterized by interpretable spectroscopic features. This *user-based* constraint limited the shape of the pure spectral profiles that can be isolated but not their concentrations that, in the selected range of variation of the $T_{ij}$ can undergo significant variations. Possible strategies to reduce the concentration band boundaries amplitude could rely on the introduction of additional concentration constraints or by fixing a reference spectrum as a *pure* component in the analysed system.

### 2.1.4 *Extending the Spectral Decomposition procedures to an EXAFS dataset*

So far, an overview on the principal methods used to decompose a XAS data matrix has been provided. It is worth noting that in the previous sections, the description of the methodologies has been focused only on the XANES part of the XAS signal. However, it is worth mentioning that there are articles which use the XAS term instead of XANES. This choice is attributable to the fact that in the field of XAS data analysis, there are works applying these spectral decomposition methods not only in the XANES region but also in the EXAFS part. However, it is possible to verify that, at the moment, the number of articles connected with the analysis of the XANES region is higher than ones related to EXAFS. The reasons are multiple. First of all, it is worth noting that the XANES part of a XAS spectrum is usually collected faster than the EXAFS part; moreover, the spectral features affecting a XANES spectrum are always more distinguishable than in the EXAFS. The second reason is more conceptual, and it is still debated. Various works have been written dealing with the application of PCA and MCR approaches on EXAFS spectra [63, 64]. However, considering the application of the PCA analysis on a set of EXAFS spectra, some ambiguities on the retrieved result can appear. As stated by Klementiev in [65], the EXAFS region is described by a sum of modulated sine functions. These form a complete set of vectors and, for this reason, they can be linearly combined to reproduce any kind of function. Moreover, the functional shape of EXAFS makes each spectrum strongly correlated with any others, regardless of spatial structural correlations, possibly translating into ambiguities in the PCA solution. A clever solution to this problem is the one provided by Rochet et al. [37], and it consists in processing by PCA the entire XAS spectra as they are (XANES + EXAFS), exploiting the dominant fingerprints of the XANES part to drive the PCA algorithm to suggest a reasonable number of pure species characterising the dataset. This result is made also possible thanks to the usage of a Quick-EXAFS monochromator, offering unique capabilities for the sub-second time-resolved characterisation of catalysts under working conditions [66, 67]. Afterwards the MCR approaches can be applied to decompose the XAS dataset and, once a feasible set of pure spectra and concentration has been retrieved from each XAS pure spectrum, the EXAFS part can be extracted according to standard procedures in the field, and properly analysed in the direct space, after e.g., Fourier Transform.

A further problem influencing the spectral decomposition of an EXAFS dataset can emerge when the EXAFS spectra are collected following a process as a function of the temperature. In fact, while the XANES region is substantially unaffected by thermal effects, the same is not true for the EXAFS part. Indeed, the Debye-Waller factor $\sigma_{DW}^2$ strongly depends on the temperature [68] and can cause the rise of misleading components during the PCA analysis of the EXAFS spectra.

Finally, it is not recommended to use the PCA with derivative or difference spectra since they show sharpened features and even small misalignments in energy will have a substantial impact on the analysis [8].

## 2.2 THE FIT OF THE XANES ENERGY REGION THROUGH A MACHINE LEARNING APPROACH

In this section, a description concerning the possibility to retrieve quantitative structural information through a XANES fit procedure is provided. In particular, the discussion verts on the XANES fitting part of the PyFitIt code, designed by S. A. Guda and A. A. Guda (Southern Federal University-Rostov on Don-), in which I had the possibility to contribute to its development and testing. The PyFitIt code is able to provide an estimation of a set of structural parameters (i.e. distances, angles, coordinates and different deformations) characterizing a XANES spectrum through two machine learning (ML) approaches: the direct and the indirect methods. Both the approaches foresee to generate, as initial step, a training dataset. In the direct approach, the following reciprocal correspondence is defined: XANES → geometry. The input features for the ML algorithms are then the data points of the XANES spectra (or some particular XANES features characterising the spectrum named descriptors, e.g. the energy edge, the pre-edge peaks position …etc. ). Once the algorithm is trained, the experimental spectrum is submitted as input of the algorithm and the corresponding geometry is predicted as the output of the process. On the contrary in the indirect approach, the ML algorithms are used to approximate the XANES between different molecular geometries. In this case, the inverse correspondence: geometry → XANES is established. Once a general XANES function, depending on the set of input parameters has been defined, the discrepancy between the experimental XANES curve and the new theoretical one can be minimized. This approach is the analogous of the polynomial interpolation method realised by the Smolentsev's code FitIt [2, 3] with the difference that the latter is substituted with different ML algorithms, providing a higher level of reproducibility of the interpolated XANES spectrum. It is worth to underlie, in fact, that high order interpolation polynomials exhibit large oscillations, known as Runge's phenomena, while low order interpolation polynomials have a poor approximation quality. Because my work has been focused uniquely on this last method, the following discussion will regard jus it.

In general, a XANES spectrum $\mu(E, \mathbf{P})$ can be considered as a multi-variable function of $k$-structural parameters $\mathbf{P} = (p_1, p_2, \dots, p_k)$ (i.e. distances, angles, coordinates and different deformations). The starting point of the Indirect method of fitting consists to create an interpolation grid where each point corresponds to a set of structural parameters obtained deforming determined part of the molecular complex under study (i.e. the crystallographic or DFT optimized structure). Different topologies of grid can be created; some examples are represented in **Figure 2.20**.

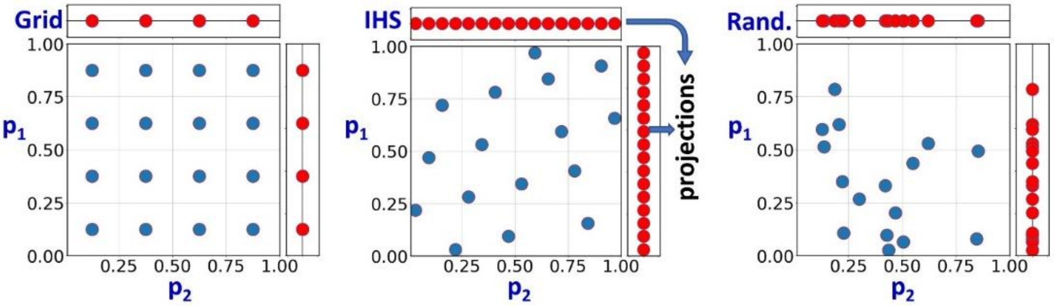

**Figure 2.20:** 16 sampling points distributed in the two-dimensional space of parameters ($p_1$, $p_2$) according to the Grid, IHS and Random methods. Red points are the projections of the sampling points on corresponding axes.

Among them the most performant in terms of projected inter-points distances over a selected deformation is the improved Latin Hypercube Sampling scheme (IHS). In case of a grid characterized by several sampling points, the performances between the IHS and random sampling topologies becomes comparable.

Each point of a grid must be associated to a XANES spectrum. Each theoretical profile can be calculated by various XAS software such as FDMNES or FEFF [69-71]. The entire set of XANES calculation related to the defined grid constitutes the training dataset. To predict a spectrum, consisting of many energy points, regression models with multiple target variables can be applied. Among these regressors, the most popular is the ridge regression which foresees to construct an approximation $\hat{\mu}$ of spectrum $\mu$ linearly with respect to set of parameters $\mathbf{P}$.

$$\hat{\mu}(E,\mathbf{P}) = w_0(E) + \mathbf{w}(E)\cdot\mathbf{P} = w_0(E) + \sum_{j=1}^{k} w_j(E)p_j \tag{2.20}$$

When the linear regression is used, the unknown coefficients $w_j$ are obtained minimizing the sum of squares (usually known also with the name of Euclidean or $L_2$-norm) between the approximated and the theoretical-one:

$$\min_{\mathbf{w}}\left(\sum_{i=1}^{N}\left(\hat{\mu}(E,\mathbf{P_i}) - \mu^{THEORY}(E,\mathbf{P})\right)^2\right) \tag{2.21}$$

In such approach, the coefficients $\mathbf{w} = (w_1, w_2, \dots, w_k)$ are usually large and thus they decrease the quality of the XANES prediction between the points of the training set. To avoid such large values, a regularization term is added to the minimization function. In eq. (2.22) this term is written as sum of squares of coefficients for the linear approximation multiplied by a constant factor $C$.

$$\min_{\mathbf{w}}\left(\sum_{i=1}^{N}\left(\hat{\mu}(E,\mathbf{P_i}) - \mu(E,\mathbf{P})\right)^2 + C\|\mathbf{w}\|^2\right) \tag{2.22}$$

The regularization procedure avoids the overfitting phenomenon and the best value of factor $C$ is obtained via cross validation procedure [72]. Approximation (2.20) can be further improved by extending the structural parameters with their pairwise products, i.e. using the quadratic regression:

$$\hat{\mu}(E,\mathbf{P}) = w_0(E) + \sum_{j=1}^{k} w_j(E)p_j + \sum_{j=1}^{k}\sum_{m=1}^{j} w_{jm}(E)p_jp_m \tag{2.23}$$

where $w_{jm}$ is a coefficient for the quadratic term $p_j p_m$. Several other approximations, including also non-linear models such us Radial Basis Functions (RBF), can be applied with success to construct the interpolating function $\hat{\mu}$. In particular, this interpolation function is a well-proven mesh-free method [73]. In this case, the unknown function $\hat{\mu}(E, \mathbf{P})$ is represented in terms of a set of basis functions characterised by certain factors and polynomial terms as follow:

$$\hat{\mu}(E, \mathbf{P}) = \sum_{i=1}^{N} w_i(E) K(\|\mathbf{P} - \mathbf{P}_i\|) + \mathrm{Polynomial}_E(\mathbf{P}) \tag{2.24}$$

where $K(r)$ – is the radial basis function. The term $\mathrm{Polynomial}_E(\mathbf{P})$ – is a polynomial function of $k$-structural parameters $(p_1, p_2, \ldots, p_k)$ with energy dependent coefficients. The unknown factors $w_i$ and the polynomial coefficients are obtained by least squares method. Every basis function is a function of distance from the training set point $\mathbf{P}_i$. For the XANES interpolation task, some good results were obtained using linear basis functions and a second-order polynomial (extracted by the ridge quadric regression method).

Finally, a second class of ML methods are those based on decision trees. Basically, they divide the space of geometric parameters into non-intersecting rectangles. In each of them the objective function $\mu(E, \mathbf{P})$is approximated by a linear expression $\hat{\mu}_j(E, \mathbf{P})$ (where $j$ is rectangle index) using the least squares method. Each node of the decision tree contains a condition $p_j < t$ for one of the geometrical parameters $p_j$which divides the training subset into parts (see **Figure 2.21**).

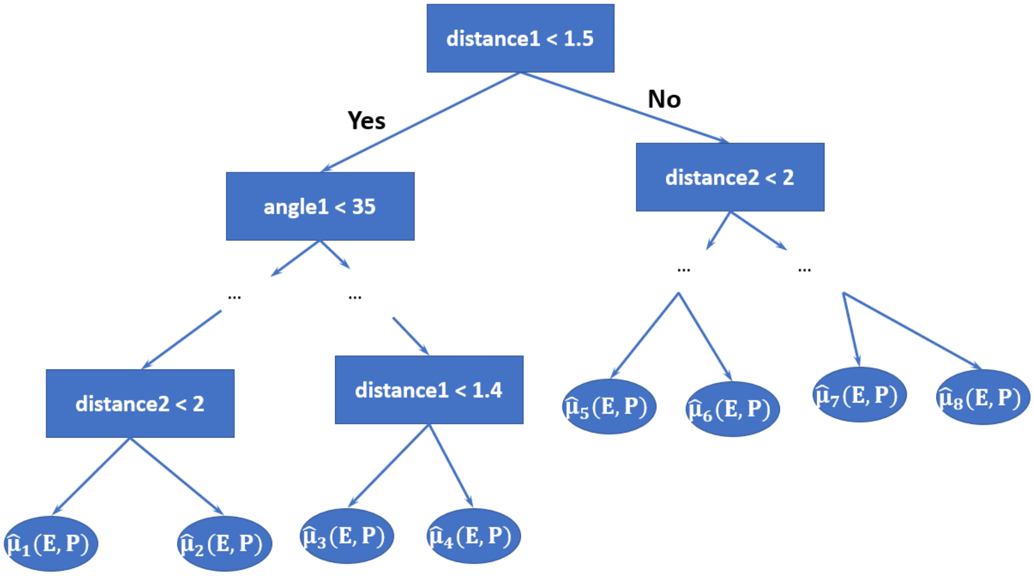

**Figure 2.21:** Illustration of a decision tree for dividing set of theoretical spectra in groups (ellipses, called leaves) corresponding to the combination of restriction on structural parameters (rectangles, called nodes). While tree is constructing, the branching process continues until the sample size of a node is more than 10 spectra.

Initially the overall training set $\mathbf{P}$ is randomly divided into training and test subsets $\mathbf{P}_1$, $\mathbf{P}_2, \ldots,$ $\mathbf{P}_N$ which are used to construct and evaluate the quality of the tree correspondingly. Each leaf of the tree (ellipses in the **Figure 2.21**) contain the linear approximations of the XANES functions $\hat{\mu}_1(E, \mathbf{P}) \ldots \hat{\mu}_l(E, \mathbf{P})$, which are constructed based on the training subset for a given leaf ($l -$ is the number of leaves in the tree). Thus, a single tree is a specific form of piecewise linear function of geometric parameters $(\mathrm{p}_1, \mathrm{p}_2, \ldots, \mathrm{p}_\mathrm{k})$. The values of $t$, for each node, are selected from a random set based on the comparison of the approximation $\hat{\mu}_i(\mathrm{E}, \mathbf{P})$ with the exactly known values for the test subset. In the Extra Trees method [74] several random trees are constructed, on the basis of a random subsample of the training set. The results of the approximation from all the trees are then averaged. Such method of combining machine learning models is called bagging.

Once that the interpolating function $\hat{\mu}(\mathrm{E}, \mathbf{P})$ has been created on the basis of a XANES dataset characterized by the same convolution parameters, the fitting of the experimental spectrum can be realized minimizing the following (modified) $L_2$ norm of the difference between the experiential profile and the fitting function as follow:

$$\Xi(\mathbf{P}) = \sqrt{\frac{1}{\mathrm{E}_{\mathrm{max}} - \mathrm{E}_{\mathrm{min}}} \int_{\mathrm{E}_{\mathrm{min}}}^{\mathrm{E}_{\mathrm{max}}} \mathrm{dE} \left(\mu_{\mathrm{exp}}(\mathrm{E}) - \hat{\mu}(\mathrm{E}, \mathbf{P})\right)^2} \tag{2.25}$$

Where the integration is realized numerically using the trapezoidal integration technique. It is worth noting the experimental and the theoretical curve must be properly normalized in order to be properly compared. To do so both of them can be divided for their variance defined as: $\sqrt{\frac{1}{\mathrm{E}_{\mathrm{max}} - \mathrm{E}_{\mathrm{min}}} \int_{\mathrm{E}_{\mathrm{min}}}^{\mathrm{E}_{\mathrm{max}}} \mathrm{dE}(\mu)^2}$, where $\mu$ is $\mu_{\mathrm{exp}}(\mathrm{E})$ or $\hat{\mu}(\mathrm{E}, \mathbf{P})$.

Different algorithm can be used to minimize this function. Among them, it is worth citing the classical gradient and coordinates descendent approaches already cited in **chapter 1**.

### 2.2.1 *An application of the indirect approach: The structural refinement of the Fe(terpy)$_2$ excited state*

Spin-crossover 3d metal complexes are potential candidates for molecular switches, novel data storage devices and optical displays [75]. Iron complexes with octahedral coordination can exist either in a low-spin (LS) or a high-spin (HS) state, depending on the temperature or pressure. Green light pulse can trigger LS to HS transition in solution of $[\mathrm{Fe(terpy)_2}]^{2+}$ (terpy: 2,2′:6′,2″-terpyridine) already at room temperature [76]. To understand the fundamental processes upon electron transitions and improve the photo-switching parameters, a detailed characterisation of the excited state is required. In particular, the spin state and its lifetime should be determined at first. Recently, high spin state of Fe(terpy)$_2$ was characterized by ultrafast time-resolved XANES [77] and the $^5$E quintet state was identified after irradiation through the laser pulse. Later, Vanko et al. [78] discussed the difficulty in the selection between $^5$E and $^5$B$_2$ candidate quintet states. One of the difficulties was that the standard DFT predicted $^5$B$_2$ to be the more stable while the more sophisticated CASPT2 approach predicted $^5$E state to be at 150 meV lower in energy. However, geometry optimization is almost impossible at such high level of theory. The quantitative fitting of the time-resolved XANES data offers a new independent source of structural information complementary to the EXAFS fit and quantum chemistry simulations. The problem of the structural analysis of the HS state of Fe(terpy)$_2$ is here selected as a demonstration of the capabilities of this method.

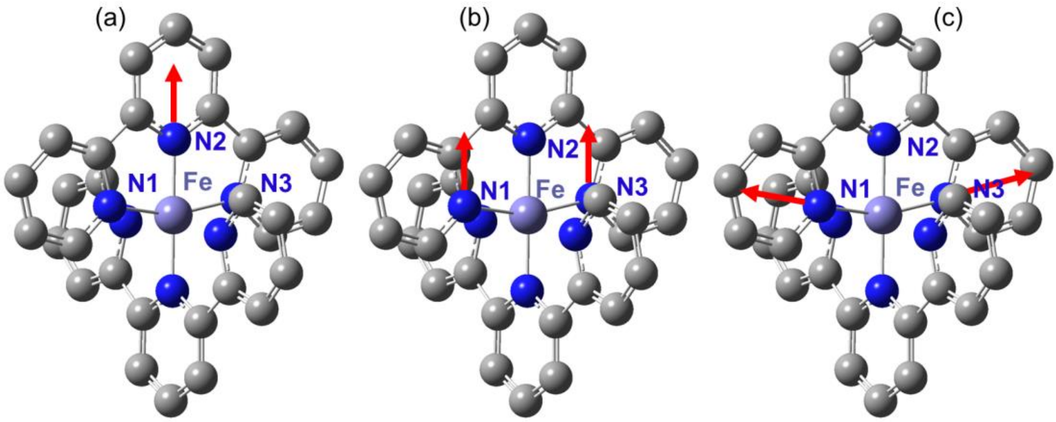

**Figure 2.22:** Three structural deformations for one terpy ligand of Fe(terpy)$_2$ molecule. (a) shift of the axial ring along the Fe-N2 axis. (b) Shift of two equatorial rings along the direction of Fe-N2 bond. (c) shift of two equatorial rings along Fe-N1 and Fe-N3 bonds correspondingly. Total number of structural parameters for fitting equals 6 – three for each ligand. Atoms are plotted with spheres only for the upper terpy ligand. Colour code: azure: Fe, blue: N, grey: C.

**Figure 2.22** shows the Fe(terpy)$_2$ molecule. The distortions of the structure upon spin transition were performed splitting the terpy ligand into three rings which are moved independently. Six degrees of freedom were considered in the fit. Three of them for one terpy are shown in the **Figure 2.22** and the rest are identical but for another terpy ligand. The first deformation, shown in panel (a) corresponds to the translation of the axial ring along Fe-N2 axis. The second deformation is the translation of two equatorial rings along the same Fe-N2 direction. Third deformation is the simultaneous symmetric elongation of Fe-N1 and Fe-N3 bonds for equatorial rings. The amplitude of all deformations was set equal to 0.8 Å in the range -0.3 Å … 0.5 Å relative to the crystallographic low spin structure. These values correspond to distances 1.58 Å … 2.38 Å for axial Fe-N bond and 1.68 Å … 2.48 Å for equatorial Fe-N bonds.

In the 6-dimensional space of parameters 729 sampling points were fixed according to IHS scheme. In case of the *classical* grid method for sampling, such number corresponds to three points along each deformation, i.e. $3^6 = 729$ points. Despite the large values of deformation along each parameter (0.8 Å) the quality of approximation was sufficient for the analysis even for such low number of points.

**Figure 2.23** shows the resulting fit obtained in the inverse approach. The experimental data used was kindly provided by W. Gawelda from [78]. The red curve is the theoretical spectrum which fits best the experimental one. The theoretical spectrum quantitatively reproduces the energy position and the intensities of maxima A-D in the experimental spectrum. During the fitting procedure, several close minima were found in terms of different combinations of the structural parameters. Therefore, the region near the global minimum was analyzed in more details by means of two-dimensional contour maps shown in **Figure 2.24**.

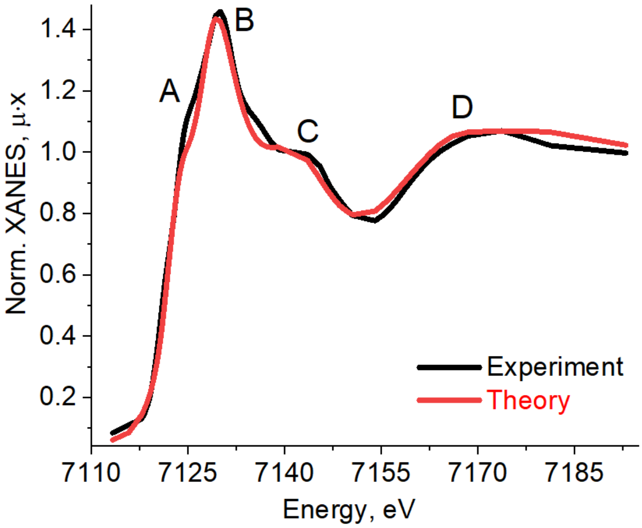

**Figure 2.23:** XANES best fit obtained from the indirect method.

Contour plots for the fit index indicate an obvious correlation between the interatomic distances in the first coordination sphere of iron. As clear from **Figure 2.24**(a), small increment of Fe-N$_{axial}$ distance in one terpy ligand can be compensated by the analogous decrease in the length of Fe-N$_{axial}$ bond in the second terpy ligand. Similar behavior of the fit index is observed for the Fe-N equatorial distances in the two ligands as shown in **Figure 2.24**(c) where the minimum valley is located along the line $y = -x + b$. An interesting observation can be made from **Figure 2.24**(b). Herein it is plotted the contour plot for the variation of the fit index in the plane of Fe-N$_{axial}$ and Fe-N$_{equatorial}$ distances averaged over the two ligands. Since the equatorial distortion involves two nitrogen atoms, the valley of minimum of the fit index is located along the line $y = -0.5x + b$ (i.e. the shift on one axial nitrogen by 0.1 Å is compensated by 0.05 Å shift of two equatorial nitrogen atoms).

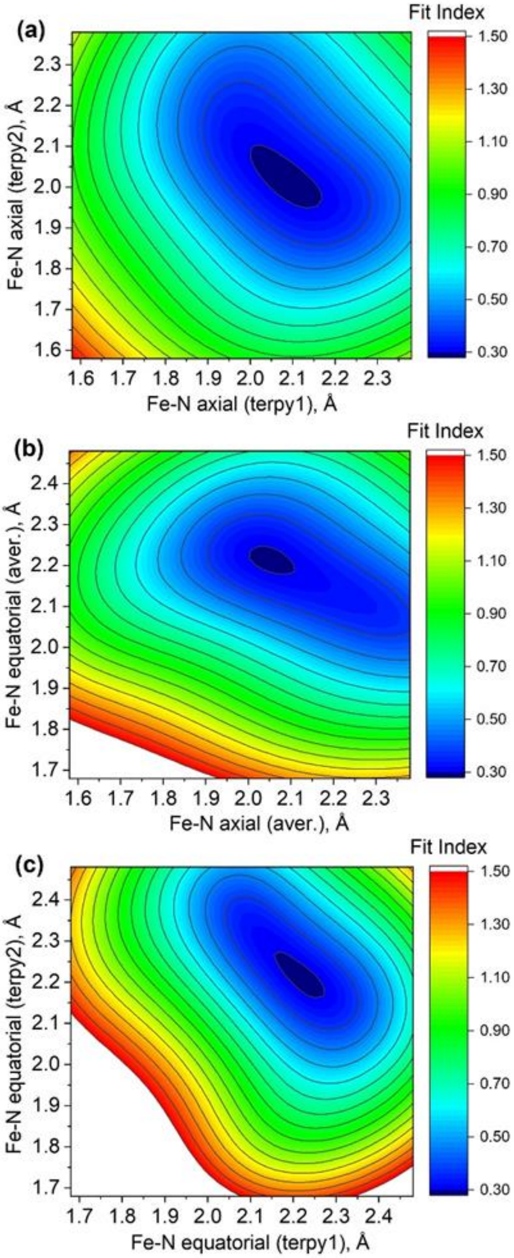

**Figure 2.24:** Contour plots for the fit index as a function of two selected structural parameters. The rest parameters were fixed in the position of the best minimum. (a)

Due to the correlations indicated in **Figure 2.24**, the averaged Fe-N distances over the two terpy ligands is reported. In **Table 2.1** the values obtained in the fit of the XANES spectrum are compared with the structural parameters obtained in DFT simulations. The latter predict the difference between Fe-N axial and equatorial distances equal to 0.1 Å in $^5$E state and only 0.03 in $^5B_2$ state. The results of the fit agree better with the $^5$E model of the excited state, which also follows from CASPT2 simulations of Vanko et.al. [78]. However, from statistical point of view the $^5$E state is difficult to distinguish from $^5B_2$ state in the XANES fit. The valley of minima in the multidimensional space of parameters contains many structures with similar fit indices but representing both $^5E$ and $^5B_2$ excited spin states. The global minimum depends on the choice of the parameters used for the FDMNES convolution, energy region for calculating $L_2$ norm and energy shift between theoretical and experimental spectrum.

| | **Fe-N Axial (Å)** | **Fe-N Equatorial (Å)** |
|---|---|---|
| XANES fit | 2.05 | 2.23 |
| Exafs fit [78] | 2.08 | 2.20 |
| DFT $^5E$ [78] | 2.10 | 2.20 |
| DFT $^5E$ [77] | 2.12 | 2.22 |
| DFT $^5B_2$ [78] | 2.16 | 2.19 |
| DFT $^5B_2$ [77] | 2.18 | 2.21 |

**Table 2.1:**Structural parameters obtained in the inverse approach. Due to correlations between distances in two terpy ligands (**Figure 2.24**(a-c)) herein are showed the averaged values for axial and equatorial distances.

## 2.3 MACHINE LEARNING POWERED BY PRINCIPAL COMPONENT DESCRIPTORS

In the following, a novel theoretical method combining supervised and unsupervised (PCA) ML algorithms is presented. It aims to provide to the user the possibility to understand which is the combination of parameters able to influence more a XANES spectrum. At the same time, it constitutes a tool which can be exploited to visualize and understand the level of uncertainty associated on the structural parameters that can be estimated through the indirect approach of fitting described in **section 2.2** of this thesis work.

Given a molecular structure, it is possible to select a set of $k$-structural parameters characterizing it, and perform, for each of them, a series of deformations under some reasonable ranges of variation. Each combination of these parameters (e.g. $\mathbf{p}^i = (p_1^i, \dots, p_k^i)$, where the apex $i$ denotes the i^th^ combination), can be considered as a multidimensional point of a space of structural parameters, here indicated as $\mathbf{P}$. In order to sample it uniformly, different multidimensional sampling schemes can be applied, such as the IHS topology.

Once that this procedure has been realized, it is possible to calculate, for each sampling point, the corresponding XANES spectrum using different multiple scattering (MS) codes (e.g. FDMNES [69], FEFF [79] and G4XANES [80]), generating, in this way, a theoretical XANES dataset $\mathbf{X}$. The latter can be considered as a classic spectral matrix of dimensions $(m \times n)$, where $m$ is the number of XANES energy points while $n$ is the number of theoretical spectra constituting it. Furthermore, the dataset $\mathbf{X}$ is centered (the mean spectrum is subtracted from all the spectra composing the theoretical dataset) and processed through the SVD decomposition. As a consequence, an expression identical to equation (2.3) is clearly found. The main differences among this approach and the one described in **section 2.1.1** regard, first at all, the nature of the dataset, which is here theoretical and then the main aim of the decomposition. The SVD approach is used here not to perform a spectral decomposition (all the spectra are pure because they are theoretical) but to understand which are the main spectral features characterizing the XANES dataset as a function of the variation of the selected set of parameters. The centering procedure is then required to delete the first components, which would coincide with the mean of the dataset, and it does not posses any relation with the parameters.

Matrix $\mathbf{U}$ contains on its columns the main directions of the dataset (the PCs) common to each spectrum of the theoretical series of spectra. On the other hand, matrix $\mathbf{\Sigma V}$ provides the weights which need to be employed to reconstruct each spectrum of $\mathbf{X}$ from $\mathbf{U}$. It follows that the i^th^ XANES element $\mu_i$of $\mathbf{X}$, it can be rewritten as:

$$\mu_i\left(E, \mathbf{p}^i\right) = \sum_{j=1}^{m} w_{ij}(\mathbf{p}^i)\mathbf{u}_j(E) \tag{2.26}$$

Where $E = (E_1, \dots E_m)$ is the XANES energy array, $\mathbf{u}_j$ represents the j^th^ column vector of $\mathbf{U}$ while $w_{ij}$ is the fraction of the j^th^ component owning to the i^th^ spectrum provided by matrix $\mathbf{\Sigma V}$. It follows that each coefficient $w_{ij}$, here named as XANES multipliers, can be intended as the projection of $\mu_i$ over $\mathbf{u}_j$. Because in equation (2.26) the dataset components are common for every spectrum in $\mathbf{X}$, it is possible to assert that the parameters dependence of each XANES, resides in its multipliers, constituting, in this way, a new class of XANES descriptors. The main difference between equation (2.26) and (2.5) stands in the fact that the dataset singular values weight matrix $\mathbf{\Sigma}$ instead of $\mathbf{U}$.

Given an experimental XANES spectrum $\mu^{\exp}$ and supposing that it can be properly reproduced by a XANES simulation performed over the same molecular structure used to generate each profile contained in $\mathbf{X}$, it is possible to retrieve, for it, the related set of multipliers. Firstly, the mean of the dataset needs to be subtracted from the experimental spectrum. Afterwards the main PCs, describing the highest variations of the dataset and supposed to characterize also the corrected experimental profile within the experimental error, have to be isolated from the pool of components constituting $\mathbf{U}$. The latter can be easily realized analyzing the trend of the singular values associated to each dataset component. Finally, once this step is completed, the XANES PCA-multipliers, proper of the experimental spectrum, can be extracted through the scalar product among the mean-corrected spectrum $\tilde{\mu}^{\exp}$ and each of the selected columns $(\mathbf{u}_i)$ of $\mathbf{U}$: $w_i^{\exp} = \tilde{\mu}^{\exp} \cdot \mathbf{u}_i$. On this basis, the first weight: $w_{i=1}^{\exp}$, constituting the first PCA-multiplier, will be the most intense and it will be associated to the highest XANES features of the experimental spectrum, while the subsequent PCA-multipliers $w_{i+1}^{\exp}$ will be responsible for the lower spectral features in descending order of intensity (i.e. the second PCA-multiplier will be associated to the second highest XANES features, the third PCA-multiplier to the third-ones and so on…). On this basis, the sum of the PCs, weighed for their related multipliers coefficients, will be able to reproduce as close as possible the experimental spectrum, making possible to realize in in the PCs space, a novel XANES fitting procedure.

The inner relation between the PCA derived XANES multipliers and the set of structural parameters affecting an arbitrary XANES spectrum, appears to be intriguing. It must be able to explain the connection of the highest variations of the

XANES features with a certain combination of molecular deformations. Clearly, the comprehension of this dependence is not straightforward, especially because it can be non-linear. However, the usage of a supervised machine learning (ML) approach demonstrated to be extremely useful to explore it. This method offers, in fact, for each component, the possibility to construct a function that maps the space of structural parameters $\mathbf{P}$ into its related multipliers space. In order to clarify this concept, the results obtained analysing, two theoretical XANES datasets retrieved from relatively simple molecules: the $[Cu(I)(NH_3)_2]^+$ and the $[Cu(II)(NH_3)_4]^{2+}$ are provided in the next section.

### 2.3.1 *Two dimensional space of parameters*

In this section, the analysis described in the precedent section is applied on the $[Cu(I)(NH_3)]^+$ complex, represented in the inset of **Figure 2.25**.

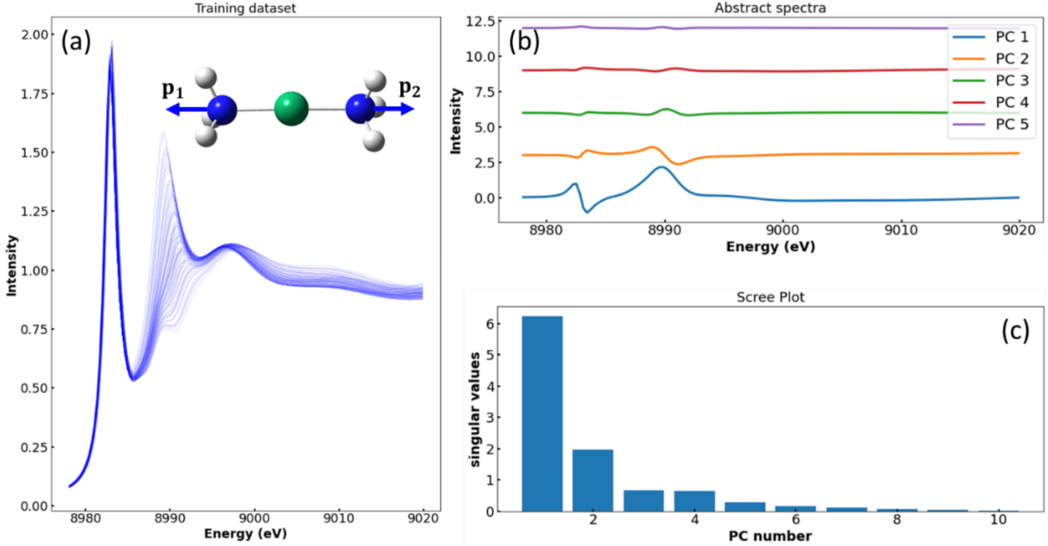

**Figure 2.25:** (a) Plot of the theoretical Cu K-edge XANES spectra calculated employing the structural deformations $(p_1, p_2)$ on the $[Cu(I)(NH_3)_2]^+$ molecule showed in in the inset. The DFT optimized complex structure comes from [81, 82]. Color legend: green: Cu, blue: N, white: H. (b) Plot of the first six columns of $\mathbf{U}$ (abstract components), weighted for their related singular value, associated to the XANES dataset (centered) (a) *vs* the dataset energy. (c) Trend of the first ten singular values plotted *vs* the component numbers.

Herein the independent deformations of the $NH_3$ groups distances along the Cu-$NH_3$ bond-directions (contraction and elongation) were considered. This kind of parametrization lead to the identification of two parameters, as reported by the colored blue arrows in **Figure 2.25**. Accordingly with the IHS method, 100 deformed structures for the $[Cu(I)(NH_3)_2]^+$ model were generated, varying each parameter in the range within $-0.2$ and $+0.2$ Å. The resulting simulated Cu K-edge XANES spectra, retrieved exploiting the FDMNES code for each model-deformation, constituted the dataset showed in **Figure 2.25**(a).

The analysis of the abstract spectra and of the singular values associated to the dataset, represented in **Figure 2.25**(b) and (c) reveals the existence of two dominant PCs: the first and the second-one. This result implies the presence of two main combinations of structural parameters able to describe the most intense XANES features of every spectrum in the theoretical dataset. On the contrary, the

remaining components will be associated to combinations of deformations generating only smaller XANES spectral variations, some of them even negligible.
For each XANES dataset, the radial basis functions (RBF) regressor, described in **section 2.2**, was employed to establish a functional relation between the XANES multipliers and the selected set of deformations. On the basis of the scree plot analysis, the study is restricted to only to those multipliers corresponding to the first and second PCs. It is worth noting that the selected RBF regressor allows to generate, for each dataset, two functions returning the values of the first and second PC multipliers depending on the set of deformations provided as input: $f_{1PC}(p_1, p_2) = w_{1PC}$ and $f_{2PC}(p_1, p_2) = w_{2PC}$. The first and second multipliers functions are reported in **Figure 2.26**(a,b) as two surfaces contour plot.

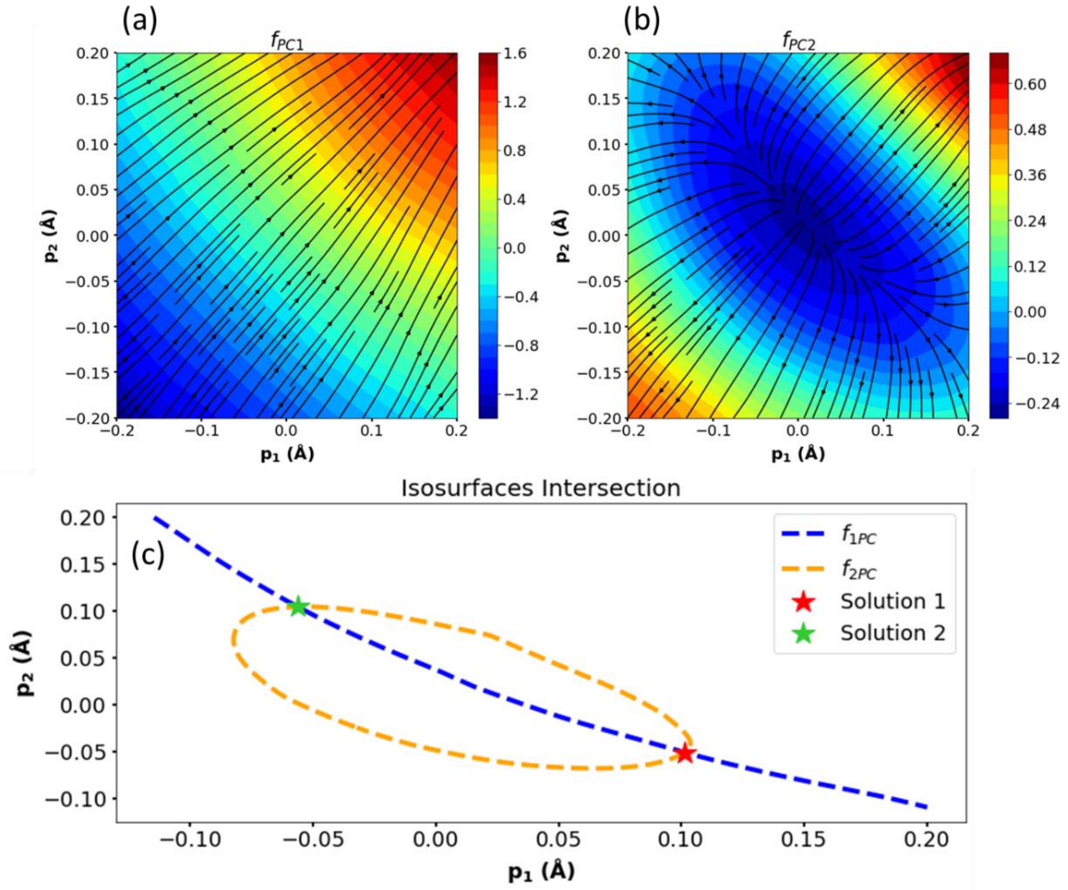

**Figure 2.26:** Contour plot of the first (a) and second (b) XANES multipliers functions associated to the $[Cu(I)(NH_3)_2]^+$ model, corresponding to the first and second PC, respectively. The arrows showed in each plot represent the direction and the verse of the gradient field emerging from the multipliers surfaces. (c) Plot of the parameters isosurfaces (indicated here with dashed lines) solutions of the equations: $f_{1PC}(p_1, p_2) = w_{1PC}$ (blue curve) and $f_{2PC}(p_1, p_2) = w_{2PC}$ (orange curve). The red and green stars indicates the intersection of the two isosurfaces showing directly the number of couples of parameters $(p_1, p_2)$ able to reproduce properly the XANES spectrum.

Analysing **Figure 2.26**(a) it is interesting to note that the functional-form of the multiplier associated to PC 1 ($f_{1PC}$) is extremely close to a plane while its gradient field is characterized by a set of flow lines almost parallel. It follows that for a given arbitrary XANES spectrum depending on of $p_1$and $p_2$, its most intense features will be explained by a quasi-linear combination of these structural parameters. On the contrary, the multiplier function connected to PC 2 ($f_{2PC}$) is clearly non-linear in $p_1$ and $p_2$, as showed by **Figure 2.26**(b). In particular, its isosurfaces are comparable to ellipses, indicating that the second highest XANES features can be properly described by a quasi-quadratic relation of the selected set of deformations. An important insight can be extracted from the joined analysis of these plots. It regards the possibility to establish if the chosen parametrization could appear suitable to describe an experimental XANES spectrum avoiding the multivaluedness phenomena. It is worth noting, in fact, that once that a specific set of parameters have been defined, there could be different combination of them able provide the same XANES spectrum. This fact, clearly, strongly affect the quality of their estimation provided by the direct or by the indirect approach of fitting [1, 83, 84]. Because all the set of deformations generating an arbitrary spectrum, must be common to all the related set of multiplier isosurfaces, their intersections becomes very important because they can provide all possible combinations of parameters characterizing it. Given an experimental XANES spectrum supposed to be described by the parameters $p_1$and $p_2$, its first and second PC isosurfaces can be obtained in the following way. First, it is necessary to extract the first and second PC multipliers as described before. Afterwards their related isosurfaces can be retrieved numerically minimizing for $p_1$ and $p_2$ (in the range within $-0.2$ and $+0.2$ Å) the system composed by the square of residuals: $(f_{1PC}(p_1, p_2) - w_{PC1})^2$ and $(f_{2PC}(p_1, p_2) - w_{PC2})^2$, where $w_{PC1}$ and $w_{PC2}$ are the projection of the experimental spectrum over the first and second PC. This procedure is repeated for a large number of times (i.e. $2 \times 10^3$ in this case). The result of this approach, applied on a XANES synthetic spectrum is reported in **Figure 2.26**(c). The latter was generated considering the XANES spectrum associated to the test combination $(p_1, p_2) = (0.1, -0.05)$ Å and assuming negligible the effect of the instrumental noise on the XANES profile.

This result is curious because it graphically indicates that there is not just one couple of parameters able to reproduce the given spectrum. The solutions consist in points $(p_1, p_2) = (0.1, -0.05)$ Å (solution 1: red star) and $(p_1, p_2) = (-0.056, 0.105)$ Å (solution 2: green star). Their symmetry clearly depends on the chosen parametrization: $p_1$ and $p_2$ are in fact symmetric respect to the Cu site. The small differences occurring in solution 2, if compared to solution 1, are explained considering that the DFT optimized distances of the two $NH_3$ from the Cu site are slightly different [81, 82].

### 2.3.2 *N>2 dimensional space of parameters*

Similarly to the $[Cu(I)NH_3]^+$ case, a XANES dataset can be obtained for the $[Cu(II)(NH_3)_4]^{2+}$complex moving independently within $-0.2$ and $0.2$ Å all the $NH_3$ groups along their related Cu-N directions, see the inset in **Figure 2.27**(a). The resulting dataset, obtained for a set of 250 deformations is reported in **Figure 2.27**(a).

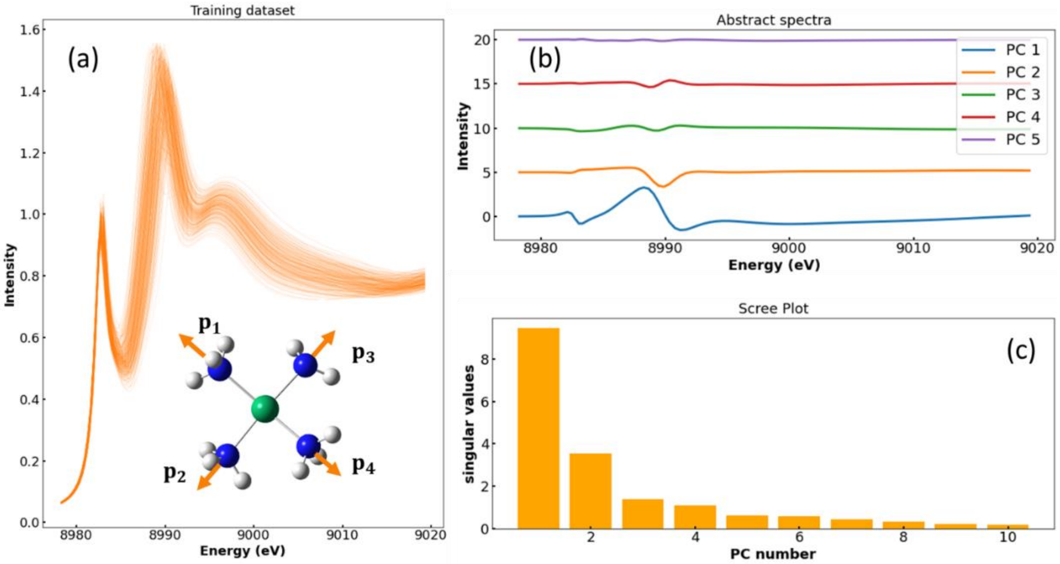

**Figure 2.27:** (a) Plot of the theoretical Cu K-edge XANES spectra calculated employing the structural deformations $(p_1, p_2, , p_3, , p_4)$ on the [Cu(II)(NH$_3$)$_4$]$^{2+}$ molecule showed in in the inset. The DFT optimized complex structure comes from [81, 82]. Color legend: green: Cu, blue: N, white: H. (b) Plot of the first six columns of $\mathbf{U}$ (abstract components), weighted for their related singular value, associated to the XANES dataset (centered) (a) *vs* the dataset energy. (c) Trend of the first ten singular values plotted *vs* the component numbers.

As for the [Cu(I)NH$_3$]$^+$ complex, also in this case the analysis of the abstract spectra and of the related scree plot suggests the presence of two main components describing the highest features of all the spectra. It follows that it is possible to define two new multipliers functions able to described the highest XANES variation: $\mathrm{g_{1PC}(p_1, p_2, p_3, p_4) = w'_{1PC}}$ and $\mathrm{g_{2PC}(p_1, p_2, p_3, p_4) = w'_{2PC}}$.
However, due to the presence of a number of structural parameters higher than two, the representation of the XANES multipliers functions proper of the [Cu(II)(NH$_3$)$_4$]$^{2+}$ structure deserve a deeper study. First at all, it is not possible to represent them as in **Figure 2.26**(a) and (b). An an alternative visualization has been obtained considering the multipliers sections retrieved varying only two of them and fixing the remaining parameters to a null variation. Due to the high degree of similarity among the [Cu(I)(NH$_3$)$_2$]$^+$ and the [Cu(II)(NH$_3$)$_4$]$^{2+}$ complexes, in terms of geometry and parametrization, these last pair of plots appear very similar to the ones showed in **Figure 2.26** and for this reason are here neglected The second problem concerns the identification of all possible intersection of the multipliers curves. As it has been done through the approach described in the precedent section, it is possible to see that the intersection of the functions: $\mathrm{g_{PC1}}$ and $\mathrm{g_{PC1}}$ provides a four dimensional surface, see **Figure 2.28**(a) and (b). In particular, **Figure 2.28** shows that the range of possible solutions becomes narrower increasing the number of PC used to describe the spectrum under study.

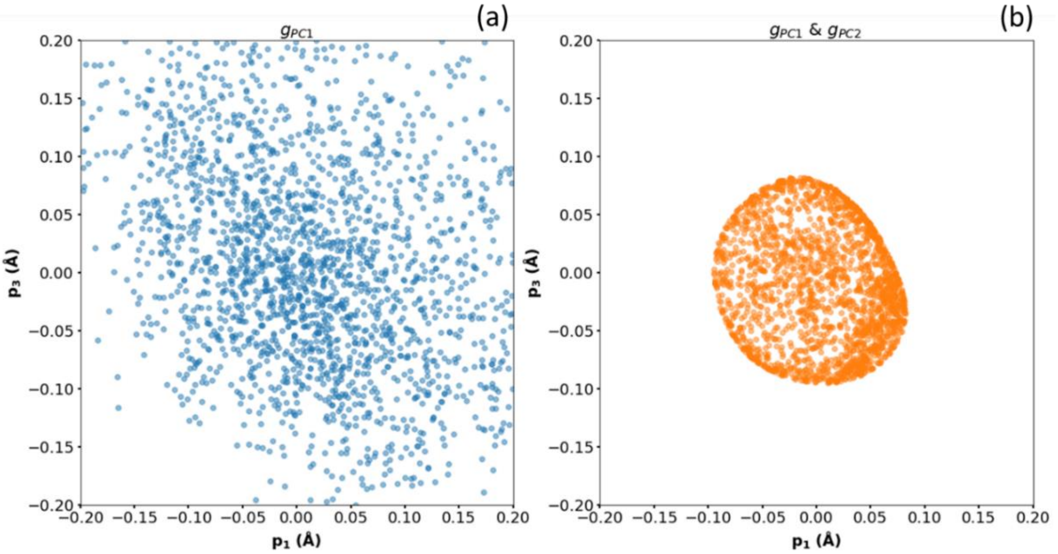

**Figure 2.28:** (a) Plot of the sections here reported as dispersion of points, for the variables $p_1$ and $p_3$ of the PC 1 and PC 2 multiplers function associated to the equation: $g_{PC1}(p_1, p_2, p_3, p_4) = w'_{PC1}$ (blue points) and to the system of equations (b) $g_{PC1}(p_1, p_2, p_3, p_4) = w'_{PC1}$ and $g_{PC1}(p_1, p_2, p_3, p_4) = w'_{PC2}$ (orange points). The quantities $w'_{PC1}$ and $w'_{PC2}$ have been obtained projecting a synthetic representative spectrum (generated using the touple of parameters: $(p_1, p_2, p_3, p_4) = (0.1, -0.05, -0.08, 0.02)$) over the first and second PCs respectively.

In general, given a XANES spectrum described by the tuple $(p_1, p_2, p_3, p_4)$, all the possible solution could by identified numerically considering the further less relevant XANES multipliers, involving PC 3 and PC 4 (i.e. $g_{PC3}$ and $g_{PC4}$). However, the level of precision provided by this approach strongly depends first on the quality of the estimation provided by the ML-regressor for these multipliers, second on the matching among the theoretical profiles and the experiment, which can be also affected by some noise artifacts characterizing the experiment. For this reason, the study is conducted here considering only the first two PCs and limiting, in this way the amount of information which can be extracted through this technique. Herein the four independent parameters solutions of $g_{PC1}$ and $g_{PC2}$ were rearranged in two new-derived linear variables (possessing an interpretable geometrical meaning) employing the following procedure.

The new parametrization can be obtained directly looking at the isosurfaces of the first and second PCs multipliers function. As already described above, these functions describe the highest XANES variations and it appears interesting trying to derive from them a new combination of parameters which could be predicted with the lowest uncertainty. Because the first multiplier function $g_{PC1}(p_1, p_2, p_3, p_4)$ is basically linear, it can be approximated using a linear function of the parameters, whose coefficients are obtained through the classic ridge regression, see **Table 2.2**. This represent the first combination of parameters or direction, which can be estimated. Looking at this expression, it is interesting to note that all the four coefficients have a similar magnitude and sign, indicating that the first major variations of the XANES features are connected to an equal contribution coming from each structural parameter, resembling a mean. On the other hand, the second multiplier function is close to a four dimensional ellipsoid. This fact implies that it can be properly approximated using a quadric expression whose coefficient are derived through a ridge quadric method. The four axis of this ellipsoid are linear function of the structural parameters and are reduced to three imposing the condition that the parameters must be related to each other through the equation $\mathrm{g_{PC1}(p_1, p_2, p_3, p_4) = w'_{PC1}}$, where here $\mathrm{g_{PC1}}$ is approximated using the linear function (average function) showed in **Table 2.2**. In particular, starting from the normalized coefficient characterizing the linear expression of $\mathrm{g_{PC1}}$, it is possible to considered other three new vectors of coefficient enabling to constitute an orthonormal basis in $\mathbb{R}^4$. The set of coefficients defines a 4×4 transformation matrix which is employed to convert the old variables/structural parameters $\mathrm{(p_1, p_2, p_3, p_4)}$ in the new-ones $\mathrm{(l_1, l_2, l_3, l_4)}$. Afterwards the new variables are used to rewrite the second multiplier (quadric) function $\mathrm{g_{PC2}}$. The requirement that $\mathrm{g_{PC1}(p_1, p_2, p_3, p_4) = w'_{PC1}}$ lead to the following relation: $\mathrm{q_1 = w'_{PC1}/\|\mathbf{k}\|}$, where $\mathbf{k} = \mathrm{(k_1, k_2, k_3, k_4)}$ are the coefficient multiplying the linear terms $\mathrm{(p_1, p_2, p_3, p_4)}$ in $\mathrm{g_{PC1}}$. As introduced before, this constraint reduces of one dimension the ellipsoidal equation of the second multiplier function. The latter is furthermore expressed in canonical form and the equation of its three axis are rewritten again as a function of $\mathrm{(p_1, p_2, p_3, p_4)}$, identifying three new directions for the $\mathrm{g_{PC2}}$ function, see **Table 2.2** together with their geometrical interpretation.

| | **New parameters combination** | **Geometry Interpretation** |
|---|---|---|
| $\mathbf{g_{PC1}}$ **direction** | $\mathrm{0.46p_1 + 0.53p_2 + 0.51p_3 + 0.48p_4}$ | Average Cu distance Cu-N |
| $\mathbf{g_{PC2}}$ **direction 1** | $\mathrm{-0.07p_1 + 0.03p_2 - 0.67p_3 + 0.74p_4}$ | Asymmetry in $\mathrm{p_3}$ and $\mathrm{p_4}$ bond lengths |
| $\mathbf{g_{PC2}}$ **direction 2** | $\mathrm{-0.78p_1 + 0.62p_2 + 0.08p_3 - 0.03p_4}$ | Asymmetry in $\mathrm{p_1}$ and $\mathrm{p_2}$ bond lengths |
| $\mathbf{g_{PC2}}$ **direction 3** | $\mathrm{-0.42p_1 - 0.57p_2 + 0.53p_3 - 0.47p_4}$ | Center of mass between 3 nitrogen atoms versus 1 nitrogen |

**Table 2.2**: Combination of parameters obtained directly from the first $g_{PC1}$ and second $g_{PC2}$ multipliers functions and employed in **Figure 2.29**. In the last column is indicated their geometrical interpretation. The test spectrum used to derived these relations corresponds to the touple of parameters: $\mathrm{(p_1, p_2, p_3, p_4) = (0.1, -0.05, -0.08, 0.02)}$

These new combination of parameters, extracted from the first and second multiplier function, can be employed to represent the tuples of points extracted from the RBF approach solving the system of equations: $\mathrm{g_{PC1}(p_1, p_2, p_3, p_4) = w'_{PC1}}$ and $\mathrm{g_{PC1}(p_1, p_2, p_3, p_4) = w'_{PC2}}$ and showed for $\mathrm{(p_1, p_3)}$ in **Figure 2.28**(b). The mapped touples of points in the 2D plots are reported in **Figure 2.29**.

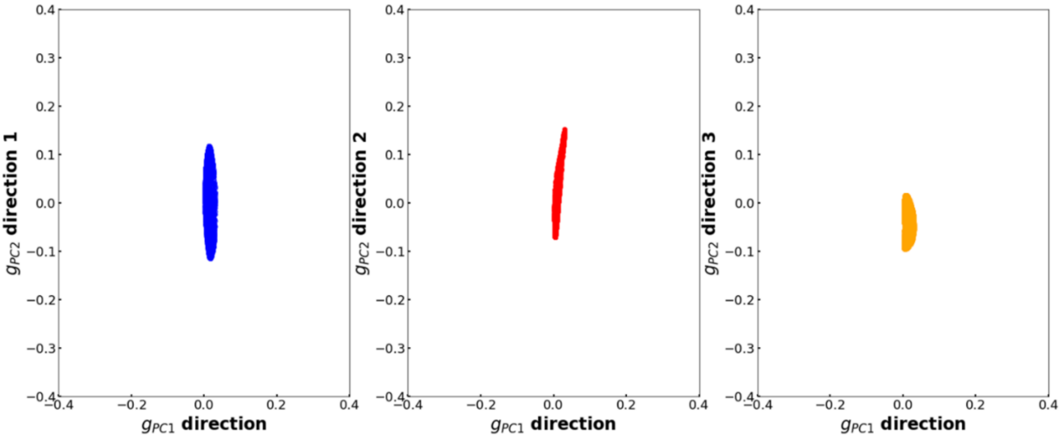

**Figure 2.29:** Plot of the $g_{PC_1}$ direction vs the three new linear combination of parameters given by $g_{PC_2}$ direction 1 (a), 2 (b) and 3 (c) reported in **Table 2.2**.

Herein it is possible to see that among the three main direction of $g_{PC2}$, the one characterized by the narrower variations of the touples along the new combination of parameters (or direction) is represented by the third direction which is also affected by the highest coefficients. It follows that the new parameters function represented by the $g_{PC1}$ direction and $g_{PC2}$ *direction 3* constitutes a new set of parameter which can be estimated with lowest uncertainty limiting the knowledge of the system to two PCs. In the ideal case, a general user would be able to find in **Figure 2.29** just a point. This result would imply the minimal variation of the solutions over the two axis and a perfect prediction of the two new variables. While this condition appears to be almost satisfied for the first new variable (the average or $g_{PC1}$ direction is almost equal to zero) the same is not valid for $g_{PC2}$ *direction 3* which shows a larger variation. A possible solution could involve the introduction of a non-linear relation of the parameter, which could make however their interpretation difficult to understand.

## 2.4 REFERENCES

[1] A. Martini, S.A. Guda, A.A. Guda, G. Smolentsev, A. Algasov, O. Usoltsev, M.A. Soldatov, A. Bugaev, Y. Rusalev, C. Lamberti, A.V. Soldatov, PyFitit: The software for quantitative analysis of XANES spectra using machine-learning algorithms, Comput. Phys. Commun., (2019) 107064.
[2] G. Smolentsev, A. Soldatov, Quantitative local structure refinement from XANES: multi-dimensional interpolation approach, J. Synchrot. Radiat., 13 (2006) 19-29.
[3] G. Smolentsev, A.V. Soldatov, FitIt: New software to extract structural information on the basis of XANES fitting, Comput. Mater. Sci., 39 (2007) 569-574.
[4] D.H. Simonne, A. Martini, M. Signorile, A. Piovano, L. Braglia, P. Torelli, E. Borfecchia, G. Ricchiardi, THORONDOR: a software for fast treatment and analysis of low-energy XAS data, J. Synchrot. Radiat., 27 (2020).
[5] A. Martini, E. Alladio, E. Borfecchia, Determining Cu-Speciation in the Cu-CHA Zeolite Catalyst: The Potential of Multivariate Curve Resolution Analysis of In Situ XAS Data, Top. Catal., 61 (2018) 1396-1407.

[6] J. Timoshenko, A.I. Frenkel, "Inverting" X-ray Absorption Spectra of Catalysts by Machine Learning in Search for Activity Descriptors, ACS Catal., 9 (2019) 10192-10211.
[7] J. Demmel, M. Gu, S. Eisenstat, I. Slapnicar, K. Veselic, Z. Drmac, Computing the singular value decomposition with high relative accuracy, Linear Alg. Appl., 299 (1999) 21-80.
[8] S. Calvin, XAFS for Everyone, CRC Press, 2013.
[9] M. Carosso, E. Vottero, A. Lazzarini, S. Morandi, M. Manzoli, K.A. Lomachenko, M.J. Ruiz, R. Pellegrini, C. Lamberti, A. Piovano, E. Groppo, Dynamics of Reactive Species and Reactant-Induced Reconstruction of Pt Clusters in Pt/Al2O3 Catalysts, ACS Catal., 9 (2019) 7124-7136.
[10] E.R. Malinowski, Factor analysis in chemistry, Wiley, 2002.
[11] R.G. Brereton, Chemometrics: data analysis for the laboratory and chemical plant, John Wiley & Sons, 2003.
[12] E.R. Malinowski, Determination of the number of factors and the experimental error in a data matrix, Anal. Chem., 49 (1977) 612-617.
[13] A. Manceau, M. Marcus, T. Lenoir, Estimating the number of pure chemical components in a mixture by X-ray absorption spectroscopy, J. Synchrot. Radiat., 21 (2014) 1140-1147.
[14] P. Conti, S. Zamponi, M. Giorgetti, M. Berrettoni, W.H. Smyrl, Multivariate Curve Resolution Analysis for Interpretation of Dynamic Cu K-Edge X-ray Absorption Spectroscopy Spectra for a Cu Doped V2O5 Lithium Battery, Anal. Chem., 82 (2010) 3629-3635.
[15] M. Fernandezgarcia, C.M. Alvarez, G.L. Haller, XANES-TPR Study of Cu-Pd Bimetallic Catalysts - Application of Factor-Analysis, J. Phys. Chem., 99 (1995) 12565-12569.
[16] A. Martini, E. Borfecchia, K.A. Lomachenko, I.A. Pankin, C. Negri, G. Berlier, P. Beato, H. Falsig, S. Bordiga, C. Lamberti, Composition-driven Cu-speciation and reducibility in Cu-CHA zeolite catalysts: a multivariate XAS/FTIR approach to complexity, Chem. Sci., 8 (2017) 6836-6851.
[17] G. Smolentsev, G. Guilera, M. Tromp, S. Pascarelli, A.V. Soldatov, Local structure of reaction intermediates probed by time-resolved x-ray absorption near edge structure spectroscopy, J. Chem. Phys., 130 (2009) 9.
[18] J. Timoshenko, A. Shivhare, R.W.J. Scott, D.Y. Lu, A.I. Frenkel, Solving local structure around dopants in metal nanoparticles with ab initio modeling of X-ray absorption near edge structure, Phys. Chem. Chem. Phys., 18 (2016) 19621-19630.
[19] S. Beauchemin, D. Hesterberg, M. Beauchemin, Principal component analysis approach for modeling sulfur K-XANES spectra of humic acids, Soil Sci. Soc. Am. J., 66 (2002) 83-91.
[20] M.F. Lengke, B. Ravel, M.E. Fleet, G. Wanger, R.A. Gordon, G. Southam, Mechanisms of gold bioaccumulation by filamentous cyanobacteria from gold(III) - Chloride complex, Environ. Sci. Technol., 40 (2006) 6304-6309.
[21] A.L. Bugaev, O.A. Usoltsev, A.A. Guda, K.A. Lomachenko, I.A. Pankin, Y.V. Rusalev, H. Emerich, E. Groppo, R. Pellegrini, A.V. Soldatov, J.A. van Bokhoven, C. Lamberti, Palladium Carbide and Hydride Formation in the Bulk and at the Surface of Palladium Nanoparticles, J. Phys. Chem. C, 122 (2018) 12029-12037.

[22] F.a.G. Perez, B. E., IPython: A System for Interactive Scientific Computing, Computing in Science Engineering, 9 (2007) 21-27.

[23] I. Markovsky, Structured low-rank approximation and its applications, Automatica, 44 (2008) 891-909.

[24] L. Mino, G. Agostini, E. Borfecchia, D. Gianolio, A. Piovano, E. Gallo, C. Lamberti, Low-dimensional systems investigated by x-ray absorption spectroscopy: a selection of 2D, 1D and 0D cases, J. Phys. D-Appl. Phys., 46 (2013) 72.

[25] J.J. Moré, The Levenberg-Marquardt algorithm: Implementation and theory, in: G.A. Watson (Ed.) Numerical Analysis, Springer Berlin Heidelberg, Berlin, Heidelberg, 1978, pp. 105-116.

[26] J.A. Nelder, R. Mead, A Simplex Method for Function Minimization, The Computer Journal, 7 (1965) 308-313.

[27] M. Giorgetti, S. Mukerjee, S. Passerini, J. McBreen, W.H. Smyrl, Evidence for reversible formation of metallic Cu in Cu0.1V2O5 xerogel cathodes during intercalation cycling of Li+ ions as detected by X-ray absorption spectroscopy, J. Electrochem. Soc., 148 (2001) A768-A774.

[28] C. Ruckebusch, Resolving Spectral Mixtures: With Applications from Ultrafast Time-Resolved Spectroscopy to Super-Resolution Imaging, Elsevier, 2016.

[29] R. Manne, On the resolution problem in hyphenated chromatography, Chemometr. Intell. Lab., 27 (1995) 89-94.

[30] A. de Juan, R. Tauler, Chemometrics applied to unravel multicomponent processes and mixtures - Revisiting latest trends in multivariate resolution, Analytica Chimica Acta, 500 (2003) 195-210.

[31] A. de Juan, R. Tauler, Multivariate curve resolution (MCR) from 2000: Progress in concepts and applications, Critical Reviews in Analytical Chemistry, 36 (2006) 163-176.

[32] R. Tauler, Multivariate curve resolution applied to second order data, Chemometr. Intell. Lab., 30 (1995) 133-146.

[33] B.L. Caetano, V. Briois, S.H. Pulcinelli, F. Meneau, C.V. Santilli, Revisiting the ZnO Q-dot Formation Toward an Integrated Growth Model: From Coupled Time Resolved UV–Vis/SAXS/XAS Data to Multivariate Analysis, J. Phys. Chem. C, 121 (2017) 886-895.

[34] H.W.P. Carvalho, S.H. Pulcinelli, C.V. Santilli, F. Leroux, F. Meneau, V. Briois, XAS/WAXS Time-Resolved Phase Speciation of Chlorine LDH Thermal Transformation: Emerging Roles of Isovalent Metal Substitution, Chem. Mat., 25 (2013) 2855-2867.

[35] W.H. Cassinelli, L. Martins, A.R. Passos, S.H. Pulcinelli, C.V. Santilli, A. Rochet, V. Briois, Multivariate curve resolution analysis applied to time-resolved synchrotron X-ray Absorption Spectroscopy monitoring of the activation of copper alumina catalyst, Catal. Today, 229 (2014) 114-122.

[36] J.P. Hong, E. Marceau, A.Y. Khodakov, L. Gaberova, A. Griboval-Constant, J.S. Girardon, C. La Fontaine, V. Briois, Speciation of Ruthenium as a Reduction Promoter of Silica-Supported Co Catalysts: A Time-Resolved in Situ XAS Investigation, ACS Catal., 5 (2015) 1273-1282.

[37] A. Rochet, B. Baubet, V. Moizan, E. Devers, A. Hugon, C. Pichon, E. Payen, V. Briois, Intermediate Species Revealed during Sulfidation of Bimetallic Hydrotreating

Catalyst: A Multivariate Analysis of Combined Time-Resolved Spectroscopies, J. Phys. Chem. C, 121 (2017) 18544-18556.

[38] A. Voronov, A. Urakawa, W.v. Beek, N.E. Tsakoumis, H. Emerich, M. Rønning, Multivariate curve resolution applied to in situ X-ray absorption spectroscopy data: An efficient tool for data processing and analysis, Analytica Chimica Acta, 840 (2014) 20-27.

[39] C.H. Camp, pyMCR: A Python Library for Multivariate Curve Resolution Analysis with Alternating Regression (MCR-AR), J. Res. Natl. Inst. Stand. Technol., 124 (2019) 10.

[40] J. Jaumot, A. de Juan, R. Tauler, MCR-ALS GUI 2.0: new features and applications, Chemometr. Intell. Lab., 140 (2015) 1-12.

[41] P.J. Gemperline, A priori estimates of the elution profiles of the pure components in overlapped liquid chromatography peaks using target factor analysis, Journal of Chemical Information and Computer Sciences, 24 (1984) 206-212.

[42] W. Windig, J. Guilment, Interactive self-modeling mixture analysis, Anal. Chem., 63 (1991) 1425-1432.

[43] D. Kraft, A software package for sequential quadratic programming, DFVLR, Köln, 1988.

[44] M. Maeder, Practical Data Analysis in Chemistry, 1st ed., 2007.

[45] A.G. Martini, A.; Guda, S.; Dulina, A.; Tavani, F.; D'Angelo, P.; Borfecchia, E.; Soldatov, A., Estimating a set of pure XANES spectra from multicomponent chemical mixtures using a transformation matrix-based approach, Springer Proceedings in Physics, Submitted (2020).

[46] J. Jaumot, R. Tauler, MCR-BANDS: A user friendly MATLAB program for the evaluation of rotation ambiguities in Multivariate Curve Resolution, Chemometr. Intell. Lab., 103 (2010) 96-107.

[47] A. Jurss, M. Sawall, K. Neymeyr, On generalized Borgen plots. I: From convex to affine combinations and applications to spectral data In memory of Odd S. Borgen (1929-1994), J. Chemometr., 29 (2015) 420-433.

[48] R. Rajko, K. Istvan, Analytical solution for determining feasible regions of self-modeling curve resolution (SMCR) method based on computational geometry, J. Chemometr., 19 (2005) 448-463.

[49] F.M. Tavani, A.; Capocasa, G.; Di Stefano, S.; Lazalunga, O.; D'Angelo, P., Direct mechanistic evidence for a non-heme complex reaction through a multivariate XAS analysis, Inorganic Chemistry, Submitted (2020).

[50] A. Martini, S.A. Guda, A.A. Guda, G. Smolentsev, A. Algasov, O. Usoltsev, M.A. Soldatov, A. Bugaev, Y. Rusalev, C. Lamberti, A.V. Soldatov, PyFitit: The software for quantitative analysis of XANES spectra using machine-learning algorithms, Comput. Phys. Commun., 250 (2020) 107064.

[51] A. Trovarelli, P. Fornasiero, Catalysis by Ceria and Related Materials, Imperial College Press, 2013.

[52] G.L. Chiarello, M. Nachtegaal, V. Marchionni, L. Quaroni, D. Ferri, Adding diffuse reflectance infrared Fourier transform spectroscopy capability to extended x-ray-absorption fine structure in a new cell to study solid catalysts in combination with a modulation approach, 85 (2014) 074102.

[53] R. Kopelent, J.A. van Bokhoven, J. Szlachetko, J. Edebeli, C. Paun, M. Nachtegaal, O.V. Safonova, Catalytically Active and Spectator Ce3+ in Ceria-Supported Metal Catalysts, Angew. Chem.-Int. Edit., 54 (2015) 8728-8731.

[54] A.A. Guda, A.L. Bugaev, R. Kopelent, L. Braglia, A.V. Soldatov, M. Nachtegaal, O.V. Safonova, G. Smolentsev, Fluorescence-detected XAS with sub-second time resolution reveals new details about the redox activity of Pt/CeO2 catalyst, J. Synchrot. Radiat., 25 (2018) 989-997.

[55] P.M. Abdala, O.V. Safonova, G. Wiker, W. van Beek, H. Emerich, J.A. van Bokhoven, J. Sa, J. Szlachetko, M. Nachtegaal, Scientific Opportunities for Heterogeneous Catalysis Research at the SuperXAS and SNBL Beam Lines, Chimia, 66 (2012) 699-705.

[56] B. Ravel, M. Newville, ATHENA, ARTEMIS, HEPHAESTUS: data analysis for X-ray absorption spectroscopy using IFEFFIT, J. Synchrot. Radiat., 12 (2005) 537-541.

[57] K.A. Lomachenko, A. Martini, D.K. Pappas, C. Negri, M. Dyballa, G. Berlier, S. Bordiga, C. Lamberti, U. Olsbye, S. Svelle, P. Beato, E. Borfecchia, The impact of reaction conditions and material composition on the stepwise methane to methanol conversion over Cu-MOR: An operando XAS study, Catal Today, 336 (2019) 99-108.

[58] D.K. Pappas, E. Borfecchia, M. Dyballa, I.A. Pankin, K.A. Lomachenko, A. Martini, M. Signorile, S. Teketel, B. Arstad, G. Berlier, C. Lamberti, S. Bordiga, U. Olsbye, K.P. Lillerud, S. Svelle, P. Beato, Methane to Methanol: Structure Activity Relationships for Cu-CHA, J. Am. Chem. Soc., 139 (2017) 14961-14975.

[59] D.K. Pappas, E. Borfecchia, K.A. Lomachenko, A. Lazzarini, E.S. Gutterod, M. Dyballa, A. Martini, G. Berlier, S. Bordiga, C. Lamberti, B. Arstad, U. Olsbye, P. Beato, S. Svelle, Cu-Exchanged Ferrierite Zeolite for the Direct CH4 to CH3OH Conversion: Insights on Cu Speciation from X-Ray Absorption Spectroscopy, Top. Catal., 62 (2019) 712-723.

[60] E.M.C. Alayon, M. Nachtegaal, A. Bodi, J.A. van Bokhoven, Reaction conditions of methane-to-methanol conversion affect the structure of active copper sites, ACS Catal., 4 (2014) 16-22.

[61] K. Sasaki, S. Kawata, S. Minami, Constrained nonlinear method for estimating component spectra from multicomponent mixtures, Appl. Opt., 22 (1983) 3599-3603.

[62] A.C. Olivieri, R. Tauler, The effect of data matrix augmentation and constraints in extended multivariate curve resolution-alternating least squares, J. Chemometr., 31 (2017) 10.

[63] A.I. Frenkel, O. Kleifeld, S.R. Wasserman, I. Sagi, Phase speciation by extended x-ray absorption fine structure spectroscopy, J. Chem. Phys., 116 (2002) 9449-9456.

[64] S.R. Wasserman, P.G. Allen, D.K. Shuh, J.J. Bucher, N.M. Edelstein, EXAFS and principal component analysis: a new shell game, J. Synchrot. Radiat., 6 (1999) 284-286.

[65] K. Klementiev, XANES dactyloscopeA program for quick and rigorous XANES analysis for Windows, (2012).

[66] E. Fonda, A. Rochet, M. Ribbens, L. Barthe, S. Belin, V. Briois, The SAMBA quick-EXAFS monochromator: XAS with edge jumping, J. Synchrot. Radiat., 19 (2012) 417-424.

[67] C. La Fontaine, L. Barthe, A. Rochet, V. Briois, X-ray absorption spectroscopy and heterogeneous catalysis: Performances at the SOLEIL's SAMBA beamline, Catal. Today, 205 (2013) 148-158.

[68] E. Sevillano, H. Meuth, J.J. Rehr, Extended x-ray absorption fine structure Debye-Waller factors. I. Monatomic crystals, Phys. Rev. B, 20 (1979) 4908-4911.

[69] S.A. Guda, A.A. Guda, M.A. Soldatov, K.A. Lomachenko, A.L. Bugaev, C. Lamberti, W. Gawelda, C. Bressler, G. Smolentsev, A.V. Soldatov, Y. Joly, Optimized Finite Difference Method for the Full-Potential XANES Simulations: Application to Molecular Adsorption Geometries in MOFs and Metal-Ligand Intersystem Crossing Transients, J. Chem. Theory Comput., 11 (2015) 4512-4521.

[70] J.J. Rehr, J.J. Kas, M.P. Prange, A.P. Sorini, Y. Takimoto, F. Vila, Ab initio theory and calculations of X-ray spectra, C. R. Phys., 10 (2009) 548-559.

[71] J.J. Rehr, J.J. Kas, F.D. Vila, M.P. Prange, K. Jorissen, Parameter-free calculations of X-ray spectra with FEFF9, Phys Chem Chem Phys, 12 (2010) 5503-5513.

[72] R. M. Rifkin, R. A. Lippert, Notes on Regularized Least-Squares, Computer Science and Artificial Intelligence Laboratory, Technical Report, (2007) 8.

[73] G.E. Fasshauer, Meshfree Approximation Methods with Matlab, WORLD SCIENTIFIC, 2007.

[74] P. Geurts, D. Ernst, L. Wehenkel, Extremely randomized trees, Machine Learning, 63 (2006) 3-42.

[75] J.A. Real, A.B. Gaspar, M.C. Munoz, Thermal, pressure and light switchable spin-crossover materials, Dalton Transactions, (2005) 2062-2079.

[76] F. Renz, H. Oshio, V. Ksenofontov, M. Waldeck, H. Spiering, P. Gutlich, Strong field iron(II) complex converted by light into a long-lived high-spin state, Angewandte Chemie-International Edition, 39 (2000) 3699-3700.

[77] S.E. Canton, X.Y. Zhang, L.M.L. Daku, A.L. Smeigh, J.X. Zhang, Y.Z. Liu, C.J. Wallentin, K. Attenkofer, G. Jennings, C.A. Kurtz, D. Gosztola, K. Warnmark, A. Hauser, V. Sundstrom, Probing the Anisotropic Distortion of Photoexcited Spin Crossover Complexes with Picosecond X-ray Absorption Spectroscopy, J. Phys. Chem. C, 118 (2014) 4536-4545.

[78] G. Vanko, A. Bordage, M. Papai, K. Haldrup, P. Glatzel, A.M. March, G. Doumy, A. Britz, A. Galler, T. Assefa, D. Cabaret, A. Juhin, T.B. van Driel, K.S. Kjaer, A. Dohn, K.B. Moller, H.T. Lemke, E. Gallo, M. Rovezzi, Z. Nemeth, E. Rozsalyi, T. Rozgonyi, J. Uhlig, V. Sundstrom, M.M. Nielsen, L. Young, S.H. Southworth, C. Bressler, W. Gawelda, Detailed Characterization of a Nanosecond-Lived Excited State: X-ray and Theoretical Investigation of the Quintet State in Photoexcited Fe(terpy)(2) (2+), J. Phys. Chem. C, 119 (2015) 5888-5902.

[79] A.L. Ankudinov, B. Ravel, J.J. Rehr, S.D. Conradson, Real-space multiple-scattering calculation and interpretation of x-ray-absorption near-edge structure, Phys. Rev. B, 58 (1998) 7565-7576.

[80] S. Dellalonga, A. Soldatov, M. Pompa, A. Bianconi, Atomic and electronic structure probed by X-ray absorption spectroscopy: Full multiple scattering

scattering analysis with the G4XANES package, Comput. Mater. Sci., 4 (1995) 199-210.
[81] F. Giordanino, E. Borfecchia, K.A. Lomachenko, A. Lazzarini, G. Agostini, E. Gallo, A.V. Soldatov, P. Beato, S. Bordiga, C. Lamberti, Interaction of NH3 with Cu-SSZ-13 Catalyst: A Complementary FTIR, XANES, and XES Study, J. Phys. Chem. Lett., 5 (2014) 1552-1559.
[82] K.A. Lomachenko, E. Borfecchia, S. Bordiga, A.V. Soldatov, P. Beato, C. Lamberti, Iop, Active sites in Cu-SSZ-13 deNO(x) catalyst under reaction conditions: a XAS/XES perspective, in: 16th International Conference on X-Ray Absorption Fine Structure, Iop Publishing Ltd, Bristol, 2016.
[83] A.A. Guda, S.A. Guda, K.A. Lomachenko, M.A. Soldatov, I.A. Pankin, A.V. Soldatov, L. Braglia, A.L. Bugaev, A. Martini, M. Signorile, E. Groppo, A. Piovano, E. Borfecchia, C. Lamberti, Quantitative structural determination of active sites from in situ and operando XANES spectra: From standard ab initio simulations to chemometric and machine learning approaches, Catal. Today, 336 (2019) 3-21.
[84] A.A. Guda, S.A. Guda, A. Martini, A.L. Bugaev, M.A. Soldatov, A.V. Soldatov, C. Lamberti, Machine learning approaches to XANES spectra for quantitative 3D structural determination: The case of CO2 adsorption on CPO-27-Ni MOF, Radiat. Phys. Chem., (2019) 108430.

# 3 EXAFS DATA ANALYSIS: METHODS AND IMPROVEMENTS

This chapter covers some recent developments related to the 2D representation of the EXAFS signal realised through the Wavelet Transform. After the definition of this topic and the description of the benefits that it can bring to the EXAFS analysis, the discussion will proceed focusing on a new variation of this technique and it will be showed how it is possible to realise the EXAFS fit in the joined $k$-$R$ space (2D dimension). Finally, a new methodology of fit of the EXAFS region, based on the usage of Machine Learning algorithms (which will be soon added to the PyFitIt code) is proposed and discussed.

## 3.1 WAVELET TRANSFORM ANALYSIS OF AN EXAFS SPECTRUM: A QUALITATIVE AND QUANTITATIVE APPROACH

It is possible to assert that if two or more groups of different atoms are localized at close distances around the absorber, their contributions in the direct space $R$ overlap, becoming often indistinguishable [1]. This fact makes the classical Fourier transform (FT) analysis of the EXAFS spectrum rather uninformative. However, from a detailed analysis of the EXAFS equation, it is possible to observe that contributions, coming from the different scatterers surrounding the absorbing atom, are localized in the $k$-space, principally because of their related backscattering amplitude factor $F(k)$, as showed in **Figure 3.1**.

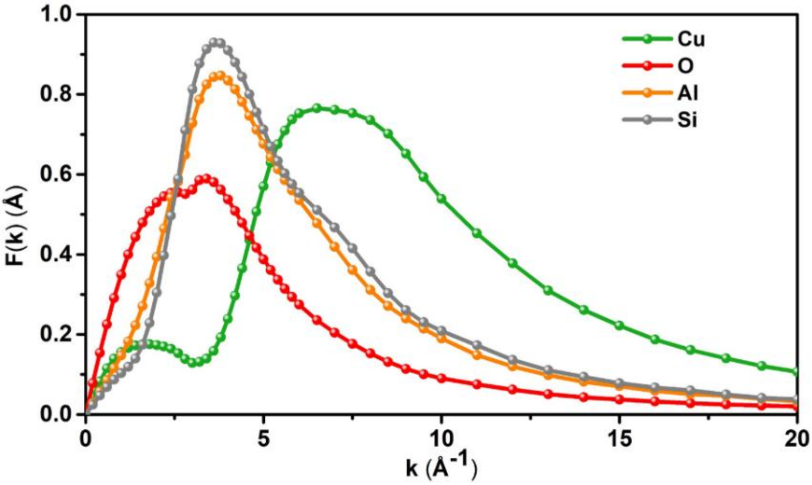

**Figure 3.1:** Backscattering amplitude factor calculated using FEFF, for the Cu-Cu (green) Cu-O (red), Cu-Al (orange) and Cu-Si (grey) SS paths evaluated for the Cu-Cu dimeric structure reported in [2]. As it is possible to see the contributions of Si and Al are completely overlapped (similar Z), making impossible to discriminate their contribution through the WT representation. At the same time, also the O backscattering amplitude is almost completely overlapped under the ones of the Si and Al atoms Its discrimination in presence of these elements result, also in this case, difficult to realise. On the other hand, the Cu backscattering amplitude function is well separated from the precedent contributions making the Cu-Cu interaction possible to be visualised through the WT analysis.

The $F(k)$ term depends strongly on the atomic number Z. In particular it is possible to observe that signals produced by heavy atoms, being characterized by large values of $F(k)$, are usually localized at higher wavenumbers than lighter atoms [3]. This evidence can be exploited by a modern technique of spectral processing called Wavelet Transform (WT) [4], which can efficiently replace the classical FT representation of the EXAFS spectrum. The WT is able to provide a 2D representation of the EXAFS, revealing, in this way, the signal features both in $k$ and $R$-spaces simultaneously, see **Figure 3.2**.

The WT of a general $k^n$-weighted EXAFS spectrum is defined as:

$$W^{\psi}(a,b) = \frac{1}{\sqrt{a}} \int_{-\infty}^{+\infty} dk' \, k'^{n} \chi(k') \psi^{*}\left(\frac{k'-b}{a}\right) \tag{3.1}$$

This equation can be seen as the inner product between the $k^n$-weighted EXAFS spectrum $\chi(k)$ and a defined window function $\psi$, called mother wavelet or simply wavelet (where the apex $\psi^*$ denotes the complex conjugate of $\psi$), which must decay at zero for higher values of $|k'|$. Here, the signal $\chi(k)$ is analysed through a set of train-waves (wavelets) that are shifted by $b$ units in the $k$-space and distorted by a factor $a$ in order to take account of the local frequencies of the signal [2]. The variables $a$ and $b$ are connected to $k$- and $R$-space by the following relations: $a = \eta/2R$ and $b = k$.

In mostly of the treated examples, the Morlet mother function, expressed in the following form, was used:

$$\psi(k) = \frac{1}{\sqrt{2\pi}\sigma} \exp(i\eta k)\exp(-k^2/2s^2) \tag{3.2}$$

Where $i$ denotes the complex unit while $\eta$ and $s$ are two parameters regulating the wavelet resolution in $R$ and $k$ spaces [5]. The selection of an appropriate set of these two parameters is critical and must be optimized in order to have the best visualization of the desired spectral features. In fact, it is worth mentioning that the WT distributes the signal information over some $k$-$R$ cells, usually named as uncertainty or Heisenberg boxes [6], which are expressed for the Morlet wavelet as:

$$\left[k \pm \frac{\eta s}{\sqrt{2}R}\right] \times \left[R \pm \frac{R}{\sqrt{2}\eta s}\right] \tag{3.3}$$

On this basis, it is possible to see that the resolution in $k$ and $R$ space are inversely proportional; this means that a good resolution in $k$-space always implies a loss of information in the related $R$-space, and vice versa.

The basic condition, regarding the possibility to process properly the EXAFS signal through the WT approach, consists to guarantee a good localization of the signal in the $k$-space and and in $R$-space (i.e., $\psi$ has well defined characteristic frequency /*distance* $R_0$). On this basis, the interpretation of the obtained wavelet image is rather straightforward: the absolute value of wavelet image of spectrum $\chi(k)$ at some point $(k_1, R_1)$ is large, if in this spectrum, around a wavenumber point $k = k_1$, the amplitude of the spectral component that corresponds to frequency $R = R_1$ is significant. Note that if the first condition is neglected and the mother-wavelet is localized only in $R$-space, the wavelet transform becomes, actually, equivalent to the Fourier transform [7].

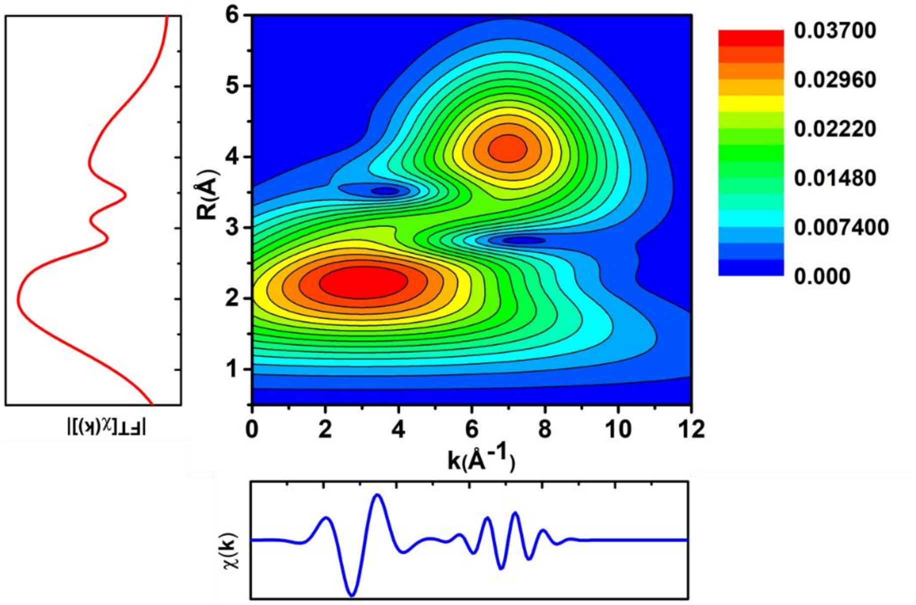

**Figure 3.2:** Graphical representation of the theoretical signal: $\chi_1(k) = 2sin(4k)e^{-(k-3)^2} + sin(8k)e^{-(k-7)^2}$ in the indirect $(k)$, direct $(R)$ and WT space. How it is possible to see from the expression, the two Gaussians act as the EXAFS backscattering amplitudes and localise the two sine contributions at different $k$-values: $k = 3$ and $7$ Å. Despite the two signals are properly separated in the $k$-space, the same is not true in the $R$ -space, where the two contributions are overlapped. In this scenario the WT representation appear extremely useful because it is able to provide a 2D representation of the signal in the $k$ and $R$ space simultaneously, allowing to have a higher level of discrimination of the EXAFS features.

In the case one would employ the WT representation to identify the presence of a contribution coming from a particular scatterer, the WT resolution parameters can be optimised easily allowing to gain the highest resolution in both the spaces. As told before, the magnitude of the integral transform, showed in equation (3.1), has a maximum if the agreement of the integral kernel (wavelet) and the signal is at a maximum. Because the EXAFS spectrum is given by a sum of sinusoidal functions, it is possible to select a particular value of the frequency of the wavelet mother function in order to enhance a particular contribution in the total EXAFS signal. This requirements is easy to be satisfied and can be realised, considering a Morlet function, just setting the wavelets parameters to $\mathrm{s} = 1$ and $\eta = 2\mathrm{R}_{\mathrm{path}}$, where $\mathrm{R}_{\mathrm{path}}$ is the effective half path length of the SS involving the scattering atom that one wants to visualize in the best way. This criterion has been exploited intensively in the cases described in **chapters 5** and **6**.

As an example, the WT representation applied on an experimental spectrum is reported in **Figure 3.3**. The EXAFS spectrum acquired in a precise step proper of a low-temperature SCR protocol, described in **chapter 6**, is analyzed through a Morlet Wavelet transform having the following resolution parameters: $\mathrm{s} = 1$ and $\eta = 7$. The choice of this last value is determined by the necessity to enhance the Cu-Cu contribution of the Cu-complex (showed in **Figure 3.3** ) which is assumed to be responsible of the acquired signal and supposed to contribute at ca. 3.4 Å. As it is possible to see from the graph, the different WT lobes has been associated to determined scatterers on the basis on the position of the maximum of their related $\mathrm{F}(\mathrm{k})$ function. The low $\mathrm{k}$-value lobe within 1.75 and 3.25 Å has been connected to the mixed contribution of the N atoms (having a $\mathrm{F}(\mathrm{k})$ close to the oxygen one) of the molecule but also to the O, Si, Al atoms composing the framework of the zeolite (CHA framework) which can influence the EXAFS signal coming from the dimeric specie.

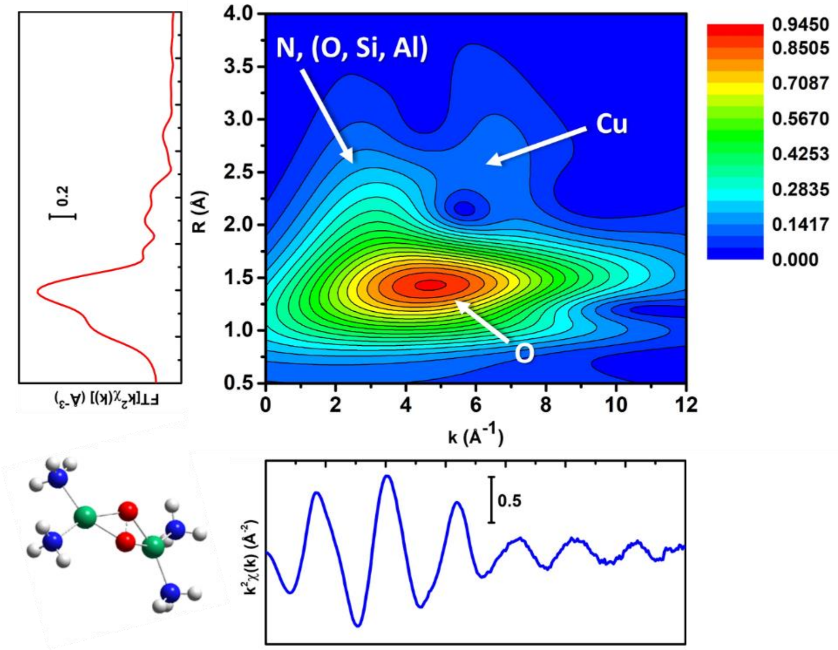

**Figure 3.3:** WT and FT magnitudes representation of the $k^2\chi(k)$ signal associated to the Cu-complex reported in the figure. Colour legend: H: white, N: blue, O: red, Cu: green. In order to enhance the Cu-Cu interaction, the following resolution parameters have been adopted: $s = 1$ and $\eta = 7$.

Looking at the WT representation showed in **Figure 3.3**, some questions could arise about the attribution of the main lobe to the O contribution. It is in fact evident that the ridges of the main lobe extend till to high $\mathrm{k}$-values. The reason of this behavior, present also in the theoretical example showed in **Figure 3.2**, is attributable to a broadening effect characterizing the low $\mathrm{R}$-values WT features. It is possible to demonstrate, in fact, (evaluating the ratio among the second moment of an arbitrary WT representation along $\mathrm{k}$ and $\mathrm{R}$ axis) that if for low $\mathrm{R}$-values, the relation $\frac{1}{\mathrm{a}} \ll \eta$ is satisfied, the wavelet lobes are distorted in the $\mathrm{k}$-space showing a profile similar to the one in the low $\mathrm{R}$ region of **Figure 3.2** and **Figure 3.3**.

### 3.1.1 *Increasing the EXAFS WT resolution through a FEFF-based wavelet representation*

As described in **paragraph 2.3.1** if one or more groups of atoms are localized at low distances from the absorber, their contributions in the $\mathrm{R}$-space can overlap. The WT representation of the EXAFS spectrum can be a good tool to overcome this problem thanks to its ability to provide a two dimensional representation of the EXAFS signal (in $\mathrm{k}$ and $\mathrm{R}$ spaces). However, when the absorbing atom is surrounded in the first, second or third shell by scatters having comparable $\mathrm{F(k)}$ values, their features tend to be undistinguishable in the $\mathrm{k \times R}$ plane too. In order to overcome this problem, a novel method of analysis based on the construction of a wavelet mother function, suitable to maximize the possibility to visualize a determined absorber-scatterer path, has been developed on the basis of the work realized by Funke et al [8].

A FEFF input file is written with one back-scatterer atom at the distance of interest. The global Debye–Waller (DW) factor and the distance can be taken from first fit estimations or from earlier results (for example the distance can be fixed from DFT). The resulting *feffNNNN*.dat file is used to reconstruct the theoretical, $\mathrm{k}^\mathrm{n}$ (n=1,2,3) weighted spectrum: $\chi(\mathrm{k})^{\mathrm{Theo}}$. The full spectrum has to be restricted to its left-hand slope, i.e. the $\mathrm{k}$ interval that contains information on the amplitude function. The reason of this choice is due to the fact that the right part of the $\chi(\mathrm{k})^{\mathrm{Theo}}$ spectrum is attenuated substantially by the DW factor and the typical amplitude information is suppressed. Therefore, the maximum of the envelope of the theoretical spectrum is chosen as the upper limit of the relevant $\mathrm{k}$ range, $\mathrm{k_{max}}$, while lower limit, $\mathrm{k_{min}}$, is taken from the spectrum showed **Figure 3.4**.

The construction of the FEFF based Morlet wavelet (FM) is based on three main step. In the following all of them will be described. The method is tested on the experimental spectrum showed in **Figure 3.3**. Although its classic WT representation provides a good discrimination of the Cu-Cu feature, this novel approach demonstrates the possibility to gain a level of resolution even higher.

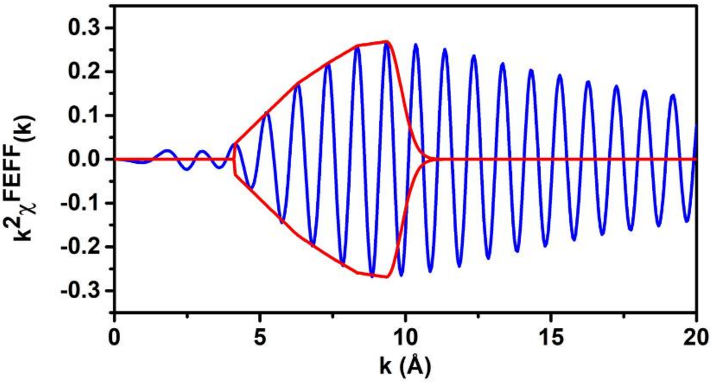

**Figure 3.4:** ($k^2$ weighted) FEFF Cu-Cu SS path EXAFS signal (blue spectrum) and the related convolution profile (in red) used to isolate the modulated spectral part ($\chi(k)^{mod}$) containing the highest information about the SS contribution. The FEFF SS path has been extracted from FEFF using as input structure the one showed in **Figure 3.3**.

- *Adjustment of the amplitude information*.

The envelope $\mathrm{E(k)}$ is built by a spline procedure connecting the maxima of the oscillations of the spectrum (see **Figure 3.4**) between $\mathrm{k_{min}}$ and $\mathrm{k_{max}}$. To avoid truncation effects in the wavelet transform, the envelope is smoothed by adding the right-hand half part of a Gaussian curve with a half maximum (FWHM) set to $1/2$ Å. The resulting model spectrum, included in the range within $\mathrm{k_{min}}$ and $\mathrm{k_{max}}$ by the total envelope, is called as $\chi(\mathrm{k})^{\mathrm{mod}}$.

- *Adjustment of the phase information of* $\chi(\mathrm{k})^{\mathrm{mod}}$.

Knowing the envelope $\mathrm{E(k)}$, the real part of a complex function $\psi(\mathrm{k})$ (the future FEFF–Morlet wavelet) is defined as:

$$\Re[\psi(\mathrm{k})] = \mathrm{E(k)}\cos(2\mathrm{kR} + \varphi) \tag{3.4}$$

The values of the parameters in the cosine function, distance $\mathrm{R}$ and phase $\varphi$, are adapted from $\chi(\mathrm{k})^{\mathrm{mod}}$ by means of a correlation procedure, see **Figure 3.5**. The correlation function $\mathrm{C(R,\varphi)}$ is calculated between the functions $\Re[\psi(\mathrm{k})]$ and $\chi(\mathrm{k})^{\mathrm{mod}}$ varying $\mathrm{R}$ and the phase $\varphi$:

$$\mathrm{C(R,\varphi)} = \int_{\mathrm{kmin}}^{\mathrm{kmax}} \mathrm{dk\,E(k)}\cos(2\mathrm{kR} + \varphi)\,\chi(\mathrm{k})^{\mathrm{mod}} \tag{3.5}$$

Thereby the values of $\mathrm{R}$ and $\varphi$ are perturbed in the ranges of $\mathrm{R} \in [\mathrm{R} - \Delta\mathrm{R}, \mathrm{R} + \Delta\mathrm{R}]$ and $\varphi \in [0,2\pi]$ requiring to find a couple of values $(\mathrm{R},\varphi)$ satisfying the condition: $\max_{\mathrm{R},\varphi}(\mathrm{C})$, which can be realised minimizing the correlation function multiplied for -1. The result of the minimization process provides the following parameters: $\mathrm{R} = 3.20$ Å and $\varphi = 0.28$ rad.

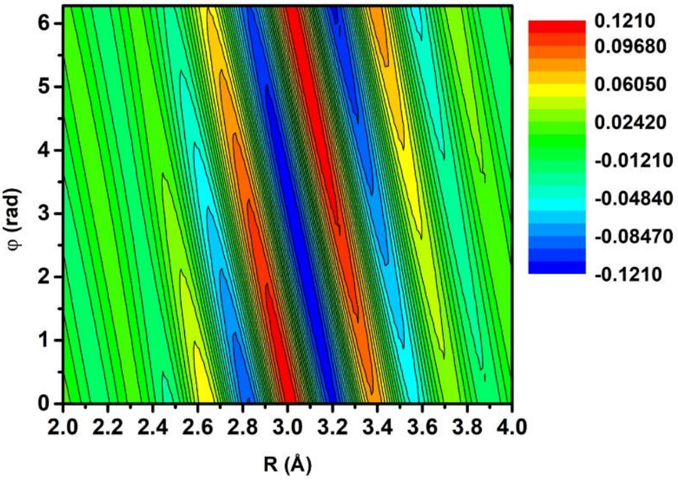

**Figure 3.5:** Correlation plot between the distance and the theoretical phase used to correct the phase and the frequency ($R_{\mathrm{eff}}$ of the path absorber-scatterer) of the FEFF-based wavelet.

The imaginary part of the wavelet is then simply built by the addition of a phase shift of $\pi/2$ to the phase of $\Re[\psi(\mathrm{k})]$ with the implicit assumption that $\mathrm{E(k)}$ is a real function:

$$\Im[\psi(\mathrm{k})] = \mathrm{E(k)}\sin(2\mathrm{kR} + \varphi) \tag{3.6}$$

- *Fulfilling the zero-mean condition.*

The complex function $\psi(\mathrm{k})$ has to be converted into a mother wavelet, fulfilling the zero mean condition. This requires to translate the $\psi(\mathrm{k})$ function on the $\mathrm{k}$ axis by a correction $\mathrm{k_{grav}}$ defined as: $\mathrm{k_{grav}} = \frac{\int_{\mathrm{k_{min}}}^{\mathrm{k_{max}}} \mathrm{dk'k'}\psi(\mathrm{k'})}{\int_{\mathrm{k_{min}}}^{\mathrm{k_{max}}} \mathrm{dk'}\psi(\mathrm{k'})}$. With this final step, the FM wavelet is fully defined, see **Figure 3.6**:

$$\begin{aligned} \Re\left[\psi\left(\mathrm{k} + \mathrm{k_{grav}}\right)\right] &= \mathrm{E}\left(\mathrm{k} + \mathrm{k_{grav}}\right)\cos\left(2(\mathrm{k} + \mathrm{k_{grav}})\mathrm{R} + \varphi\right) \\ \Im\left[\psi\left(\mathrm{k} + \mathrm{k_{grav}}\right)\right] &= \mathrm{E}\left(\mathrm{k} + \mathrm{k_{grav}}\right)\ \sin(2(\mathrm{k} + \mathrm{k_{grav}})\mathrm{R} + \varphi) \end{aligned} \tag{3.7}$$

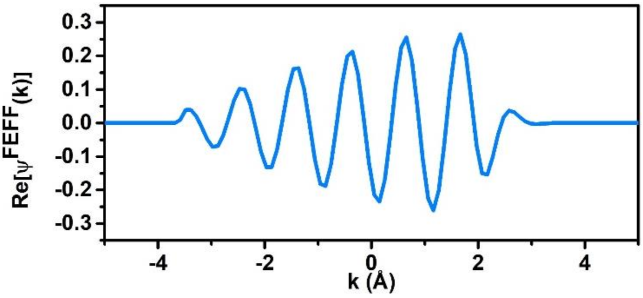

**Figure 3.6:** Final morphology of the modified FEFF-based Wavelet mother function (real part) generated from the FEFF the Cu-Cu path.

The retrieved FEFF-modified mother wavelet can then be applied on the experimental EXAFS spectrum of **Figure 3.3**. The result is reported in **Figure 3.7**.

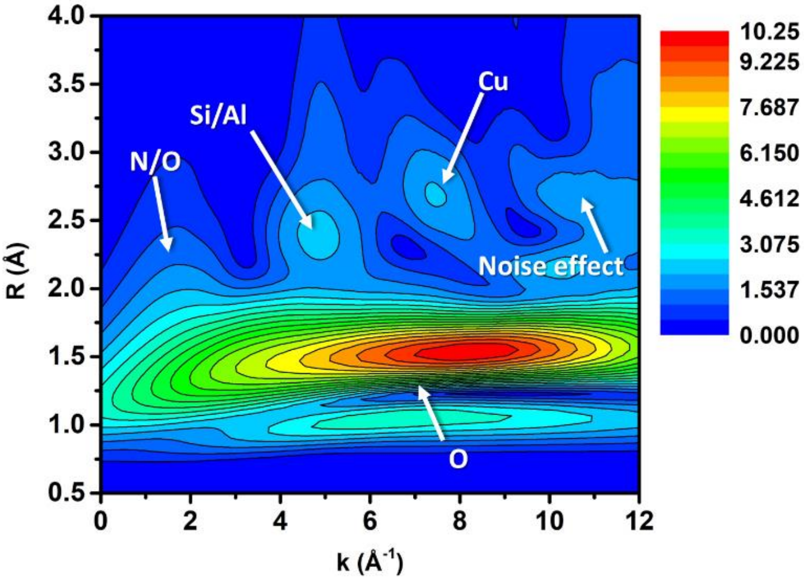

**Figure 3.7:** FEFF modified WT representation of the EXAFS signal reported in **Figure 3.3**.

The morphology of the wavelet mother function, causes a distortion of the features proper of the Fourier transform magnitude, attributable to the O contributions, and enhances the noise effects present at high $k$-values. This can be easily demonstrated by varying the envelope-range enclosing the FEFF signal: reducing or increasing it the Cu-Cu feature remain stable while the high $k$-values ridges change position in $k$. On the other hand, the Cu-Cu, Cu-Si/Cu-Al features (proper of the zeolite framework) are well divided from the other contributions, maintaining a position corresponding to a maximum of their own $F(k)$ functions. This evidences indicate that the dimeric structure showed in **Figure 3.3** is sited in the cage of the zeolite close to the framework, as it will be described in **chapter 6**.

### 3.1.2 *Retrieving quantitative information from the WT representation: from the power density function plot till to the WT fit*

Up to now, the WT representation has been used to have just a qualitative representation of the EXAFS signal. Clearly, the possibility to extract from the WT representation a set of quantitative information acquires a certain importance as an alternative to the classical EXAFS fit in the $k$ or $R$ space. Generally, there are three directions which can be followed. The first-one derives from the signal theory and it is almost unknown to the XAS community. It consists in a procedure which can be employed to enhance the presence of some typologies of scatteres, similarly to what has been discussed in **section 3.1.1**. Basically, it consists to calculate the power density function of the modulus of the WT representation of an EXAFS spectrum as follow:

$$\Phi^{\Psi}(k) = \int_{R_{min}}^{R_{max}} dR \left| W^{\Psi}(k,R) \right|^2 \tag{3.8}$$

Through this equation, it is possible to obtain the representation of the modulus of the WT limited to the $k$-dimension. If plotted vs $k$, the $\Phi^{\Psi}(k)$ function (due to $F(k)$ term) will show a series of peaks distributed along the $k$-axis as a function of the atomic number of the scattering elements affecting the EXAFS signal. As an example, the experimental spectrum introduced in **Figure 3.3** is processed through this technique, see **Figure 3.8**. As it is possible to see, the $\Phi^{\Psi}(k)$ function, obtained evaluating the integral among 2 and 4 Å shows two main peaks. Considering , it is possible to attribute the first one to the contribution coming from O/N, Al and Si, while the second-one shows a maximum around 7 Å, that is where the Cu-Cu SS backscattering amplitude shows a maximum, demonstrating, in this way, the existence of a multimeric Cu site (a Cu-Cu interaction) in the sample. This approach has been used to establish (qualitatively) the existence of Cu-Cu dimers inside different typologies of Cu-zeolites during various working conditions. A more detailed description of the results obtained using it can be found in **chapter 5** and **6**.

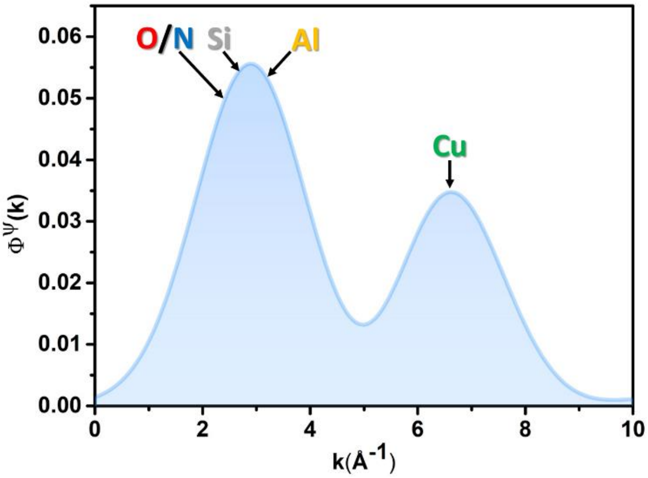

**Figure 3.8:** Power density function of the wavelet transform showed in **Figure 3.3** integrated within 2 and 4 Å. It is possible to identify two main peaks. The first one can be assigned to the mixed contributions coming from the Si, Al and O atoms of the zeolite

framework and from the N atoms (they are indistinguishable from the oxygens because they have comparable Z) composing the complex. The second peak has a maximum around 7 Å and can be attributed to the existence of a Cu-Cu dimeric interaction, as demonstrated by the WT fit showed in **Figure 3.9**.

The second method is the one developed by Timoshenko et al. [9]. It consists to perform, given an initial structure, the EXAFS fit of an experimental spectrum following a Reverse Monte Carlo (RMC) scheme. The WT of the theoretical spectrum, evaluated for each iteration of the process (based on a genetic algorithm), is compared with the WT representation of the experiment following a Monte Carlo scheme. The letter is realised calculating the norm of the discrepancy among the two representation and normalise it for the norm of the experimental signal. More information about this approach (here just mentioned), which has been applied largely by Kuzmin and Puran's group (University of Latvia) to study the thermal properties of rare-earth oxides, can be found here [7, 9-11].

The last method has been introduced by me to shed light on the different EXAFS contributions coming from the $Cu_xO_y$ moieties forming during the $O_2$ activation of various Cu-zeolites, see **chapter 5** and **6**. In particular, this last approach was used to reinforce quantitatively the evidences of the existence of a Cu-Cu contribution emerging from the first method described above.

For the fitting procedure, the scheme exploited by IFEFFIT [12, 13] was followed. Herein, for a determined structure, a FEFF input file is created selecting an atom as the absorber. Afterwards, the FEFF6.0l [14, 15] software is used to generate the *feffNNN.dat* file for each path. Finally, for all of them, the $\mathrm{k}$-depended arrays obtained by FEFF, (whose description is reported in **chapter 1**), are linearly interpolated on the $\mathrm{k}$-grid of the experimental EXAFS spectrum and then used to build up the single path contribution $\chi_i(k)$, which is given by the following expression:

$$\begin{aligned}\chi_i(k) &= \frac{S_{0i}^2 N_i F_i(k)}{k(\Delta R_i + R_i)^2}\exp\{\, i[2kR_i + \delta_i(k)]\} \\ &\times \exp[i(2p\Delta R_i - 4p\sigma_i^2/R_i)] \times \exp[-\frac{2R_i}{\lambda(k)} - 2p^2\sigma_i^2]\end{aligned} \tag{3.9}$$

This is the equation used in all the versions of IFEFFIT to realise a fit (in absence of higher order cumulants). As it is possible to see, it shows some differences from the classical EXAFS fit discussed in **chapter 1**, in particular it shows some additional terms. Here, the path length variation is represented by the $\Delta R_i$ and it constitutes, together with the DW term $\sigma_i^2$, the first cumulant of the atomic pair distribution for the $i^{th}$ path. Finally, $p$ is the complex values wavelength, introduced to take account for the thermal or configurational disorder [12]. More information about this quantity can be found in [14]. It is worth to underlie, that this equation is suitable to deal with systems characterized by a higher level of disorder (especially thanks to the variable $p$), however the result of the fitting procedure are identical with those deriving form the *classical* MS EXAFS equation showed in (3.16). Considering (3.9), the fitting parameters are, in this way: $S_{0i}^2$, $N_i$, $\sigma_i^2$, $\Delta E_0$ and $\Delta R_i$. Once that for each selected path the relative EXAFS signal has been calculated using (3.9), the theoretical total signal is generated summing all the contributions together:

$$\chi^{\mathrm{THEORY}}(\mathrm{k}) = \sum_{\mathrm{i}} \chi_{\mathrm{i}}(\mathrm{k}) \tag{3.10}$$

The theoretical signal $\chi^{\mathrm{THEORY}}(\mathrm{k})$ can be involved in the calculation of the residual complex function for the wavelet transformed data using the following formula:

$$\mathrm{f}(\mathrm{k},\mathrm{R}) = \Re\left[\mathrm{W}^{\psi}_{\chi_{\mathrm{DATA}}}(\mathrm{k},\mathrm{R}) - \mathrm{W}^{\psi}_{\chi_{\mathrm{THEORY}}}(\mathrm{k},\mathrm{R})\right] + \Im\left[\mathrm{W}^{\psi}_{\chi_{\mathrm{DATA}}}(\mathrm{k},\mathrm{R}) - \mathrm{W}^{\psi}_{\chi_{\mathrm{THEORY}}}(\mathrm{k},\mathrm{R})\right] \tag{3.11}$$

The output of equation (3.11), calculated in the $\Delta\mathrm{k}$ and $\Delta\mathrm{R}$ ranges of interest, is a two dimensional grid which can be arranged to a one dimensional array, indicated here as $\mathrm{f_i}$, including the real and imaginary parts, having in this way a length equal to two times the length of the product of the $\mathrm{k}$ and $\mathrm{R}$ lists. On this basis, it is possible to define a metric function $\Xi$, similar to the one employed by Kuzmin in the EDA XAS code [16], which is defined as:

$$\Xi = \frac{1}{2\times(\mathrm{M}\times\mathrm{N})} \sum_{\mathrm{i}=1}^{2\times(\mathrm{M}\times\mathrm{N})} [\mathrm{f_i}(\mathrm{k},\mathrm{R})]^2 \tag{3.12}$$

This equation is a variation to the metric function showed in equation (1.8) of **chapter 1**. The errors are uniformly set to 1 and the residuals are normalised for the list length. However, the nucleus of the equation remain always the same, i.e. the minimization of the sum of squares of the residuals. Both the equations must provide, in fact, the same minimum value. The letters $\mathrm{M}$ and $\mathrm{N}$ indicate, respectively, the lengths of the $\mathrm{k}$ and $\mathrm{R}$ arrays. Function $\Xi$ can be properly minimized using different algorithms. In all the examples described in this thesis, the classical Levemberg-Marquard method [17] used also in IFEFFIT was adopted, however it is possible also to employ more robust algorithms such as the Nelder-Mead simplex scheme [18]. Finally, the errors and the correlation values associated to the best-fit derived parameters, are obtained by the inverse of the Hessian ($\mathrm{H}^{-1}$), calculated for $\Xi$, in correspondence of its minimum valueas, how described by Kuzmin in [16].

As an example, the fit of the EXAFS spectrum, showed in **Figure 3.3**, using the molecular structure depicted in the same graph, is reported in **Figure 3.9**. The discussion about the number of EXAFS paths employed to realised the fit, together with their parameterization is postponed in **chapter 6**. A summary table, indicating the refined distances, is inserted after the comparison plot of **Figure 3.9**.

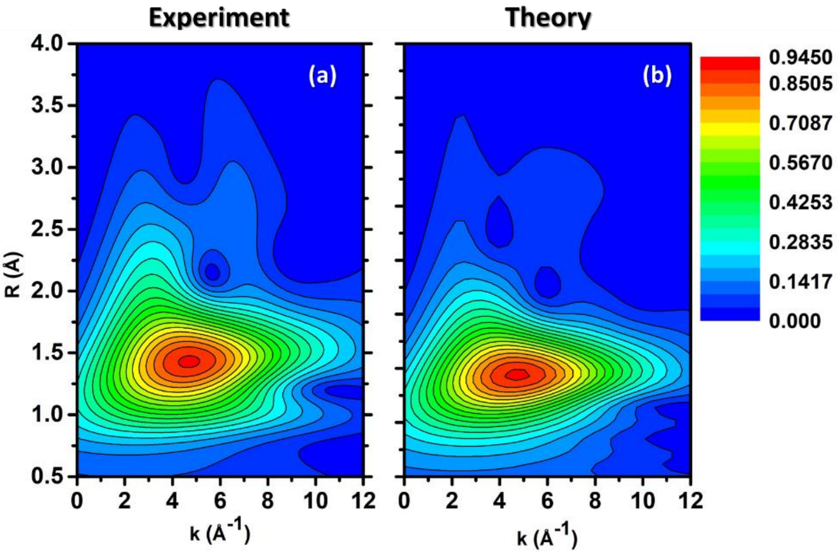

**Figure 3.9:** EXAFS fit executed in the WT space. (a) Experiment. (b) Best-fit. The fit was realise using for both the representation the same resolution parameters: $s = 1$ and $\eta = 7$.

| Best Fit Parameters | |
|---|---|
| $S_0^2$ | 0.806 ± 0.003 |
| $\Delta E$ (eV) | -0.22 ± 0.07 |
| $\Delta R_O$ (Å) | -0.053 ± 0.001 |
| $\Delta R_N$ (Å) | 0.022 ± 0.001 |
| $\Delta R_{Cu}$ (Å) | 0.048 ± 0.003 |
| $\sigma_O$ (Å$^2$) | 0.002 ± 0.0001 |
| $\sigma_N$ (Å$^2$) | 0.0041 (fixed) |
| $\sigma_{Cu}$ (Å$^2$) | 0.0139 ±0.0004 |

**Table 3.1:** Best fit parameters associated to the EXAFS spectrum showed in **Figure 3.9** and obtained starting from the structure reported in **Figure 3.3**. The $\sigma_N$ has been fixed to a reference value obtained from the fitting procedure involving the [Cu(I)(NH$_3$)$_2$]$^+$ complex. More details about the fitting strategy are reported in **chapter 6**.

## 3.2 FIT OF THE EXAFS ENERGY REGION THROUGH A FEFF-BASED MACHINE LEARNING APPROACH

As already introduced in **chapter 1**, within the Multiple Scattering (MS) theory, the total EXAFS signal can be described through a sum of an infinite number of scattering events $\chi_i(k)$ as follow [1]:

$$\chi(k) = \sum_{i=1}^{\infty} \chi_i(k) \tag{3.13}$$

Equation (3.13) involves different contributions coming from Single Scattering (SS) and Multiple scattering (MS) paths. For both of the cases, their signal can be properly expressed as the product of an amplitude factor for an oscillating function [14]:

$$\chi_i(k) = A_i(k, \{\mathbf{r}\}_i)\sin(2kR_i + \phi_i(k, \{\mathbf{r}\}_i)) \tag{3.14}$$

The quantity $\{\mathbf{r}\}_i$ represents all the set of vector positions characterising the $i^{th}$ path contribution: $\{\mathbf{r}\}_i = (\mathbf{r}_1, \dots, \mathbf{r}_n)$, where $\mathbf{r}_n$ is vector coordinates of the $n^{th}$ atom involved in the scattering process. The amplitude $A_i$ and the phase $\phi_i$ appearing in (3.14) depends on the scattering properties of the neighbouring atoms interacting with the excited photoelectron before it returns to the absorbing site, while the $2R_i$ term is the total scattering path length. Equation (3.14) can be properly rewritten in the more conventional form as:

$$\chi_i(k) = S_{0i}^2 \frac{N_i}{kR_i^2} |F_i(k, \{\mathbf{r}\}_i)| \sin(2kR_i + \varphi_i(k, \{\mathbf{r}\}_i) + 2\delta_i(k, \{\mathbf{r}\}_i)) \exp\left(-\frac{2R_i}{\lambda_i(k, \{\mathbf{r}\}_i)}\right) \tag{3.15}$$

Where the parameters appearing in equation (3.15) are the same as the ones of equation (3.9) and have been already introduced in **chapter 1**. The main difference among the classic FEFF derived EXAFS equation (written in the MS formalism) and the one reported in equation (3.15) is represented by the geometry dependence of the backscattering amplitude factor $F_i(k, \{\mathbf{r}\}_i)$, of the effective total phase shift $\phi_i(k, \{\mathbf{r}\}_i) = \varphi_i(k, \{\mathbf{r}\}_i) + 2\delta_i(k, \{\mathbf{r}\}_i)$ and of the energy-dependent free mean path $\lambda_i(k, \{\mathbf{r}\}_i)$, which here is made explicit.

Although the series reported in equation (3.13) is infinite, it is possible to assert that only the first few $\ell$ elements are able to produce a significant contribution to the total EXAFS signal. The reason of this behaviour must be found in the finite lifetime of the electron excitation, in the scattering path lengths and in the cancellation effects [19]. Under these conditions equation (3.13) con be expressed as the ordinary EXAFS equation:

$$\chi(k) = \sum_{i=1}^{\ell} S_{0i}^2 \frac{N_i}{kR_i^2} |F_i(k, \{\mathbf{r}\}_i)| \sin(2kR_i + \phi_i(k, \{\mathbf{r}\}_i)) \exp\left(-\frac{2R_i}{\lambda_i(k, \{\mathbf{r}\}_i)}\right) \exp(-2{\sigma_i}^2 k^2) \tag{3.16}$$

With $\ell < \infty$. Equation (3.16) can be considered as a good candidate to perform the fit of an experimental EXAFS signal. However it can undergo towards further modifications involving the cumulant expansion technique, which is sometimes needed to take account for the large disorder affecting a system [20, 21]. Focusing on (3.16), for each paths, the fitting parameters will be represented by the variables: $S_{0i}^2$, $N_i$, $R_i$ and $\Delta E_i$. The main difference among this fitting function and the one reported in equation (3.9) consist in the fact that here the half paths length is optimized instead of its variation$\Delta R_i$ and the classical electron wave number $k$ is used instead of the complex variable $p$. Finally, the Debye-Waller ${\sigma_i}^2$ can be refined during the fitting procedure or evaluated using a semi-empirical correlated Einstein or Debye models [19, 22-25].

Despite this approach has been widely employed, for several years, from a large part of the XAFS community and lead to a considerable number of successful results in different areas of Physics and Chemistry [19, 26-29], some problem still remain partially unsolved. As already pointed out by Ravel in [30], it is worth noting, in fact, that contributions coming from scattering geometries not present in the input cluster cannot be computed. Only small changes of the inter-atomic spacings can be accommodated by the parametrization of $R_i$ during the fitting procedure, while for large changes their estimation becomes unreliable. This evidence is clearly attributable to the geometry dependence of the effective scattering amplitudes and phases shift profiles calculated by FEFFF that, from the classic codes employed in the EXAFS fitting (e.g. IFEFFIT), is usually neglected. In addition, it is worth mentioning that these functions show also, for the MS paths, a strong non-linear angular dependence and are even sensitive to small variations of the angles along the scattering path, especially in the case of linear atomic chains [19, 31]. This problem has been addressed in the GNXAS code employing the first order terms of the Taylor expansion for the amplitude and phase shift [32, 33] while other valid alternatives can be found in advanced approaches regarding the classical molecular dynamic [34, 35] and the reverse Monte Carlo technique [9, 36]. A second problem often encountered during an EXAFS fit, is represented by the choice of the set of variables, appearing in equation (3.16), which can be properly refined through the fitting procedure. As described in **chapter 1**, the superior limit on the number of fitting parameters is given by the Nyquist criterion, however as the number of parameters involved in the fit increase, the correlation among all the couples of the fitting variables can become higher. These two facts, clearly requires to express some variables (e.g. $R_i, \sigma_i{}^2, \dots$) appearing in equation (3.16) as a function of the pool of parameters usually associated to the SS paths, which can be further refined through the EXAFS fit. Clearly, this approach is characterised by some complications related to the definition of a corrected expression that needs to be used to represent each of these EXAFS variables without introducing any new guess parameter. In particular, there is not a common modus operandi, which can be followed by all the users. Some empirical rules are used, for example, to constrain the MS half path length on the basis of the path typology (e.g. focused, double, conjoined …) [37] or using a general expression containing the volumetric lattice expansion term $\alpha$ [38]. Another methodology requires to represent the path length associated to each MS path through the so called *cosine theorem*. However, all these methods, assume fixed the angles among the path legs, moreover the application of the *cosine theorem* can lead to long expressions when the number of involved scatterers starts to be higher than four [39].

In the following, a new method of fitting which aims to solve these problems is proposed. This new approach has been already used, with some changings, on the XANES fitting procedure provided by the PyFitIt code [40] described in **chapter 2**. It is based on the generation of a set of Machine-Learning-based interpolation functions, which are employed to approximate each $\chi_i(k)$ path signals under the variation of a set of user-defined structural parameters. Using this new implementation, equation (3.16) is generalised to take account of any kind of deformations: from the bond stretching till to the variation of multiple angles of the selected molecular structure. Moreover, the effective path lengths associated to each scattering process are obtained directly as a function the selected molecular deformations without recurring to any elaborated formula.

### 3.2.1 *Method description*

The basic idea, behind this approach, stands in the construction, for each scattering process, of a signal path functions $\chi_i$ that, under the variation of a user-defined set of $h$ structural parameters: $\mathbf{p} = (p_1, \dots, p_h)$, is able to return an accurate approximation for the $i^{th}$ scattering signal. This contributions needs to be as close as possible to the one obtained through an *ab initio* calculation involving the molecular complex affected by $\mathbf{p}$.

The perturbation of each element of $\mathbf{p}$ is reflected automatically in the change of the each vector distances $\{\mathbf{r}\}_i(\mathbf{p}) = (\mathbf{r}_1(\mathbf{p}), \dots, \mathbf{r}_n(\mathbf{p}))$ , from whom the $F_i(k, \{\mathbf{r}\}_i)$, $\phi_i(k, \{\mathbf{r}\}_i)$ and $\lambda_i(k, \{\mathbf{r}\}_i)$ depend. These terms, in turn, determine a modification of the correspondent path signal $\chi_i$, whose dependence from $\mathbf{p}$ can be then reported as: $\chi_i(k, \mathbf{p})$. The variations of the scattering amplitudes and the total phase shifts, for a SS and MS path, from the bond distances angle of a test-structure are represented, for sake of comprehension, in **Figure 3.10**.

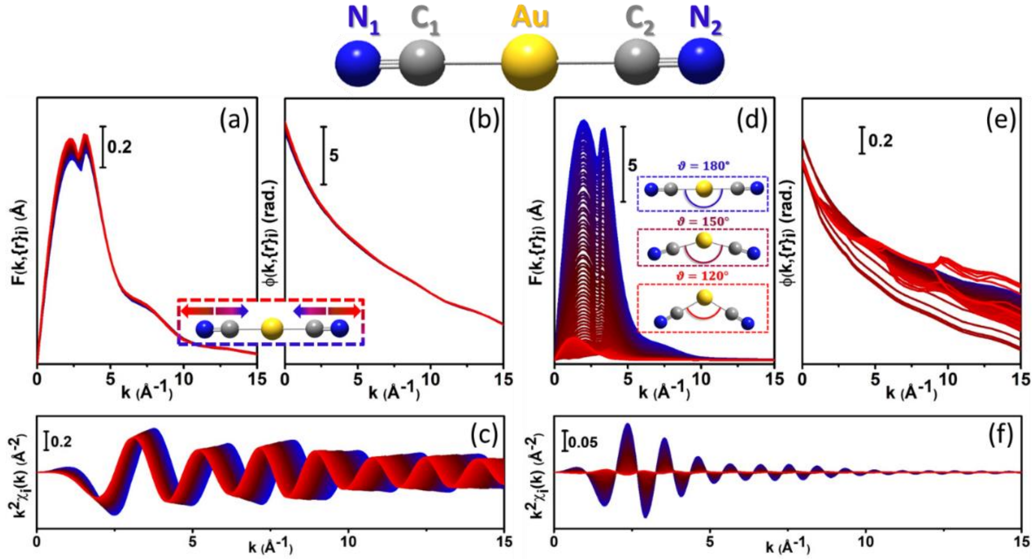

**Figure 3.10:** Plot of the scattering amplitudes, of the effective phase shifts and of the related single path EXAFS signals as a function of the deformations regarding the Au(CN)$_2$ molecule. Panels (a), (b) and (c) refers to a SS process involving the paths $\mathrm{Au}\rightarrow\mathrm{C_1}\rightarrow\mathrm{Au}$ and $\mathrm{Au}\rightarrow\mathrm{C_2}\rightarrow\mathrm{Au}$ proper of the carbon first shell. The curves have been generated extending the CN groups along the Au-C bond directions of a quantity varying from $-0.12$ Å (blue profile) till to $+0.12$ Å (red profile) respect to the unperturbed structure. How already discussed in **section 3.2**, small variation characterize these profiles, in particular, the most evident seems to affect the scattering amplitudes. On the other hand, the profiles showed in panels (d), (e) and (f) are connected to the evolution of a three legs MS paths: $\mathrm{Au}\rightarrow\mathrm{C_1}\rightarrow\mathrm{C_2}\rightarrow\mathrm{Au}$ and $\mathrm{Au}\rightarrow\mathrm{C_2}\rightarrow\mathrm{C_1}\rightarrow\mathrm{Au}$, which evolves from a configuration almost collinear: $\vartheta = 180°$ to a new one where the scattering geometry becomes triangular: $\vartheta = 120°$. The progressive diminution of $\vartheta$ is responsible of an abrupt diminution of the scattering amplitude, which causes the abatement of the signal intensity, and of a non-linear variation of the effective total phase trend.

### 3.2.1.1 *Generation of a set of ML-based $\chi_i$ functions and fit of the experimental EXAFS signal*

The first step of this approach consists to identify those scattering paths able to contribute more in a selected region of the experimental spectrum where the fit must be performed. In the *classical* (geometry independent) EXAFS fit this requirement can be satisfied considering only those SS and MS paths having a curve-wave amplitude $C_{cw}$ higher than a certain user defined value. In case of a geometry-variable molecular complex, this step is not straightforward and it requires a well defined methodology if the most relevant EXAFS path are not known beforehand. The main reason is due to the strong geometry dependence of some MS paths. The gradual evolution of a collinear MS path to a triangular-one can cause, for example, the abatement of its intensity, expressed in terms of $C_{cw}$ [15]. It follows that there could be some molecular configurations, involving the same atoms, where a MS path is significant while in the others its fitting contribution is completely negligible.

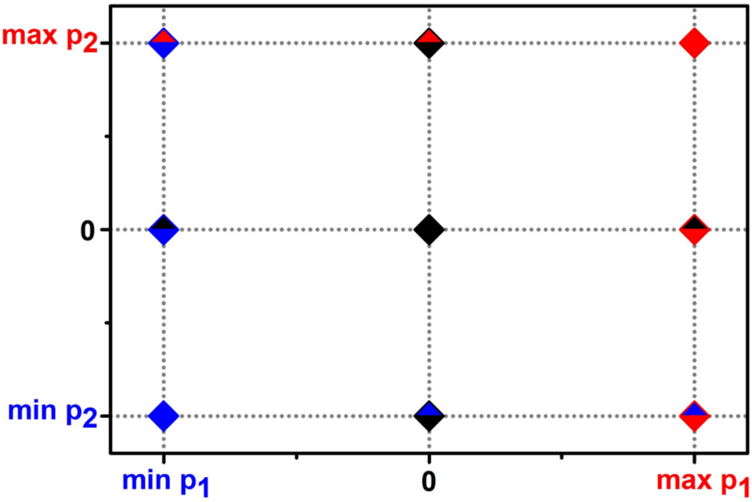

**Figure 3.11:** First multidimensional grid (here 2-dimensional) used to identify those scattering paths which can assume a significant role in the total EXAFS signal representation as a function of the variation of a user-defined set of structural parameter (i.e. $p_1$ and $p_2$). The grid includes all the combinations among the maxima (red) and minima (blue) deformations plus the null (black) combination

In order to take account of this behavior, the following procedure can be proposed.

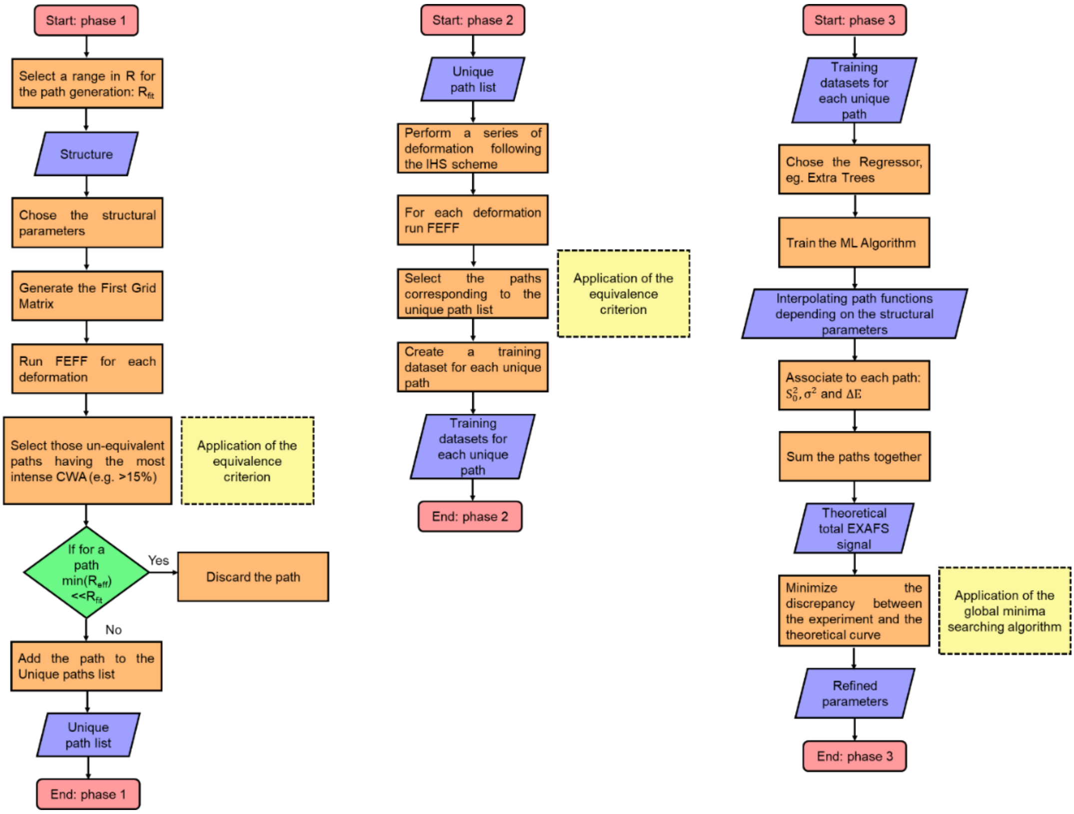

**Figure 3.12:** Flow diagram reporting the procedure followed to fit, through the indirect method fitting, the experimental EXAFS signal.

The first step (phase 1 of **Figure 3.12**), clearly, consists to identify a set of structural parameters which needs to be further refined through the fitting routine, and a certain fitting range in the $\mathrm{R}$ space extending till $\mathrm{R_{fit}}$. Then, a first multidimensional grid constituted by all possible combinations, involving the maxima and minima values of each selected structural parameter plus the null deformations (i.e $\mathbf{p} = (\mathrm{p}_1 = 0, \ldots, \mathrm{p_h} = 0)$), is generated, see **Figure 3.11**. For each grid-point, a FEFF input file employing the relative deformed input structure, is created and runned. Afterwards, for each molecular configuration, the $\mathrm{C_{cw}}$ terms associated to each path, are extracted and analyzed. A good rule of thumb for a first screening, foresees to consider only those paths possessing a $\mathrm{C_{cw}}$ equal or higher than 15% and a maximum half path length (RMAX) around 6 Å. Afterwards, the fit can be improved including the lower intensity and farer paths . This approach is fundamental, in fact it allows to take in consideration all the possible paths having a strong impact on the fitting routine independently from the considered geometry. Clearly, the first grid can be made finer evaluating also the combination of the deformations corresponding to half of their variation, ensuring a more detailed analysis of the generated paths. The employment of a grid having a different topology (i.e. the IHS, see later) from the one showed in **Figure 3.11** is advised for a number of structural parameters higher than 2. At the same time, further user-defined filtering criteria can be introduced in order to limit even more their number. For example, if a relevant path ($\mathrm{C_{cw}}$>15%) shows a $\mathrm{R_{eff}}$ >> $\mathrm{R_{fit}}$ for the combination of deformed parameters corresponding to their minima, it can be properly excluded. Once this step is completed, it is necessary to consider those significant scattering paths associated to an arbitrary distorted geometry and compare them progressively with the ones related to the remaining molecules, trying to establish, in this way, if they can be assumed equivalent or not. The term of comparison, here adopted, foresees to consider equivalent two paths if they have the same kind of scattering atoms and if they show the same half path length and scattering angles evaluated taking as reference the unperturbed molecule, within an error sited on the fourth decimal digit. The time-reversal symmetry [41] is taken in consideration too. In fact, in case of disagreement of the scattering angles between two paths presenting the same half path length and atoms type, the comparison can be repeated inverting the order of the atoms involved in one of the scattering processes. The final path-list, that from now will be named as *unique list*, will be composed by a series of scattering geometries, not equivalent to each other, which will be further approximated as a function of the variation of the selected set of structural parameters through the employment of a regression approach. The letter is realized by means of a Machine Learning algorithm, which must undergo towards a training procedure. The next step of this technique, see (phase 2 of **Figure 3.12**), foresees to construct, in fact, a training set used for this purpose. Herein the multidimensional space of the structural parameters $\mathbf{P}$,generated by the combination of the variations of each parameter (i.e. $p_1 \otimes \dots \otimes p_h$ ), is sampled uniformly using the Improved Latin Hypercube Sampling (IHS) method, which ensures the narrowest distance among the projections of each multidimensional point along every dimension of $\mathbf{P}$ [3]. The result will be a second larger multidimensional grid. Similarly to the first grid construction, also in this case, for every point of $\mathbf{P}$, a distorted molecular complex is generated and used to compose a FEFF input file which is subsequently runned. Afterwards the path equivalence criterion, described above and depicted in **Figure 3.13**, can be exploited to discriminate, among all the FEFF scattering contributions, those contained in the unique list. It is worth noting that every path contained in this list must be found among all the ones generated by FEFF for each sampling point of $\mathbf{P}$. As already discussed before, it is possible that some paths, because of the molecular geometry, can have a very low contribution in term of EXAFS signal and, for this reason, they can be neglected by FEFF. Because some of them can correspond to some path present in the unique list, it appears necessary to avoid their removal by the code. This purpose can be easily realized inserting, in each FEFF file, the CRITERIA 0 0 command. Through this key-word no cut-off criteria based on the evaluation of $\mathrm{C_{cw}}$ and of the path plane wave amplitude approximation ($\mathrm{C_{pwa}}$) [15] will be used by FEFF to reduce the number of paths found by the pathfinder. The contraindication of this choice is represented by the large amount of scattering paths that can be generated by FEFF. However, this problem can be easily bypassed including in each FEFF input file the RMAX and NLEG key-words, limiting, in this way, the number of FEFF generated paths on the basis of the maximum path length parameter and of the maximum number of legs proper of the ones belonging to the unique list. Herein it is worth mentioning that it necessary to set the RMAX keyword to a value not lower than the half path length of the relevant path present in the unique list assumed during the highest deformation of the molecular structure.

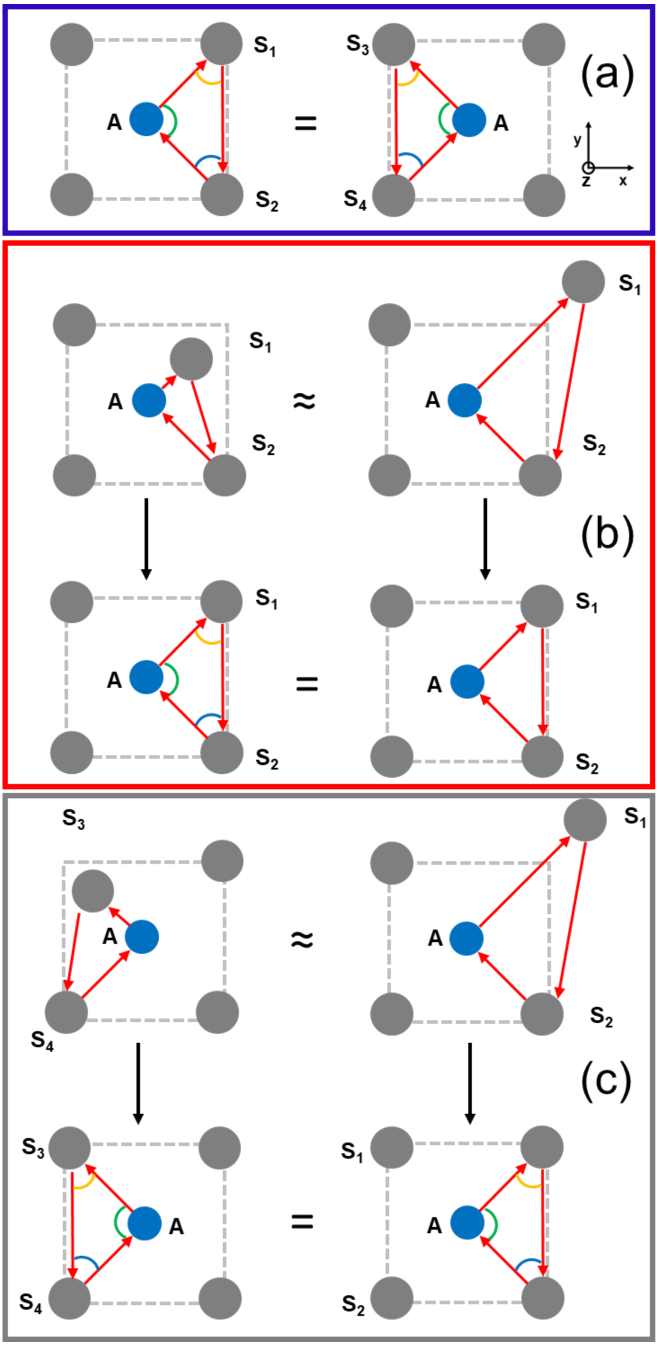

**Figure 3.13:** Schematic representation of the equivalence principle employed to identify the equivalent paths corresponding here to a 3 leg scattering process. (a) The paths $A \rightarrow S_1 \rightarrow S_2 \rightarrow A$ and $A \rightarrow S_3 \rightarrow S_4 \rightarrow A$ possess the same half path length and the same kind of atoms. The two processes are symmetric over the axis y=A and for these reason are equivalent. (b) The two scattering process define to two distinct processes. However, if referred to the unperturbed molecule, the atoms order, the angles and the half path lengths of the two paths are the same and for these reason they can be considered equivalent. (c) The two path refers to different atoms type and are characterized by incompatible half path length and angles. However, as in the precedent case (b) if referred to the unperturbed structure, they identifies two paths equivalent for symmetry around the y=A axis.

For each distorted molecule, in case of matching of a path with one owning to the unique list, it is necessary to extract from the related FEFF output files its scattering amplitude, its effective phase shifts and finally its electron mean-free path. These arrays will be then interpolated over a wave-vector, finer than the one provided by FEFF grid, within 0 and 20 Å$^{-1}$ (a common step can be, for example 0.05 Å$^{-1}$) and then included together with their own $R_i$, in the corresponding EXAFS single contribution equation given by (3.15). Once calculated, this signal will be inserted in a table containing all the single EXAFS contributions, associated to the selected path present in the unique list, for every distorted molecule. This table constitutes the dataset used to train a ML based regressor, providing as output an interpolating function approximating the selected path, see (phase 3 of **Figure 3.12**). As a result, each path proper of the unique list will be associated with a function returning its single EXAFS contribution depending on the value of the structural parameters given in input. Among the huge variety of regressors, which are employed, at the moment, in the filed of the Machine Learning, the Extra-Trees regressor with a number of leafs set to 200 was found suitable for this application [3]. Afterwards, each interpolating path function can be weighted by its related Debye-Waller parameter and then summed with the others as showed by equation (3.16). Similarly to the fit by sliders method, described for the XANES spectra in **chapter 2**, also here the same approach can be employed. In particular, through the Jupyter ipywidgets class [42] it is possible to associate a slider to each parameter involved in the fit and move it until the best qualitative agreement among the experiment and the theoretical spectrum is obtained. This step is qualitative but instructive because it allows to understand which are the structural parameters influencing more the fit and to fix their related range of variation. As an example, two Jupyter notebook prototypes of interface, designed for the *fit the EXAFS by sliders* notebook (soon available in PyFitIt), are showed in **Figure 3.14** (fit in the $k$-space) and **Figure 3.15** (fit in the $R$-space). Both of them refer to the EXAFS spectrum of the $Au(CN)_2$ complex represented in **Figure 3.10**.

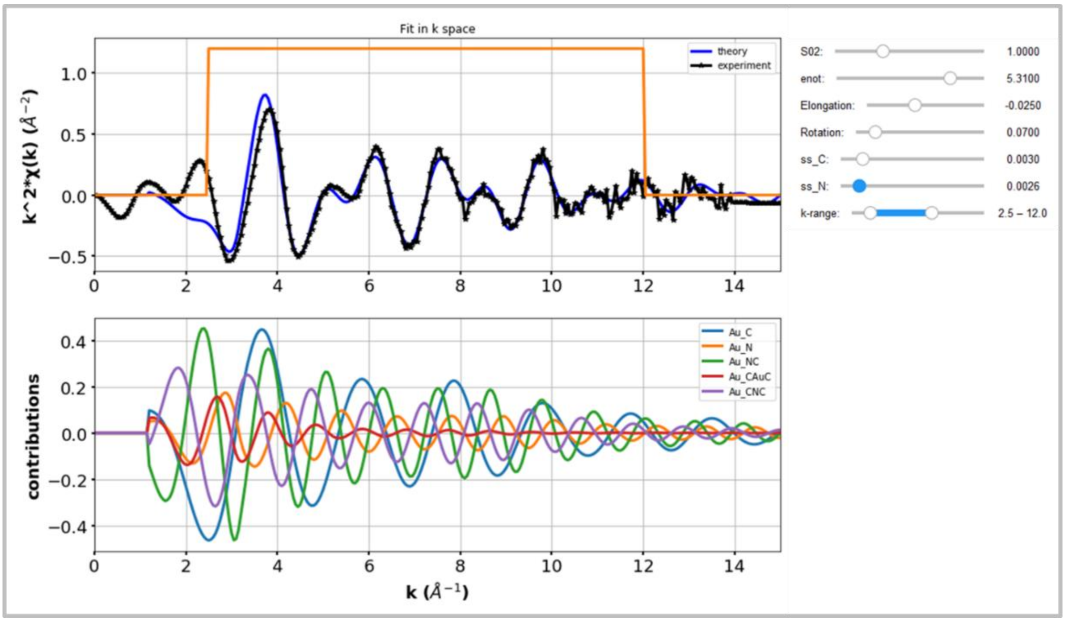

S02: 1.0000
enot: 5.3100
Elongation: -0.0250
Rotation: 0.0700
ss_C: 0.0030
ss_N: 0.0026
k-range: 2.5 – 12.0

**Figure 3.14:** Fit by sliders interface reporting on the top graph the $k^2$ weighted experimental and theoretical EXAFS spectrum. The latter is obtained summing all the SS and MS contributions, reported in the bottom panel, resulting to be Au→$C_1$→ Au, Au→$N_1$→Au, Au→$C_1$→ $N_1$→Au, Au → $C_1$→$N_1$→ $C_1$→ Au and Au → $C_1$→Au→ $C_2$→ Au . The orange square window is used to select the range in $k$ for the fitting procedure.

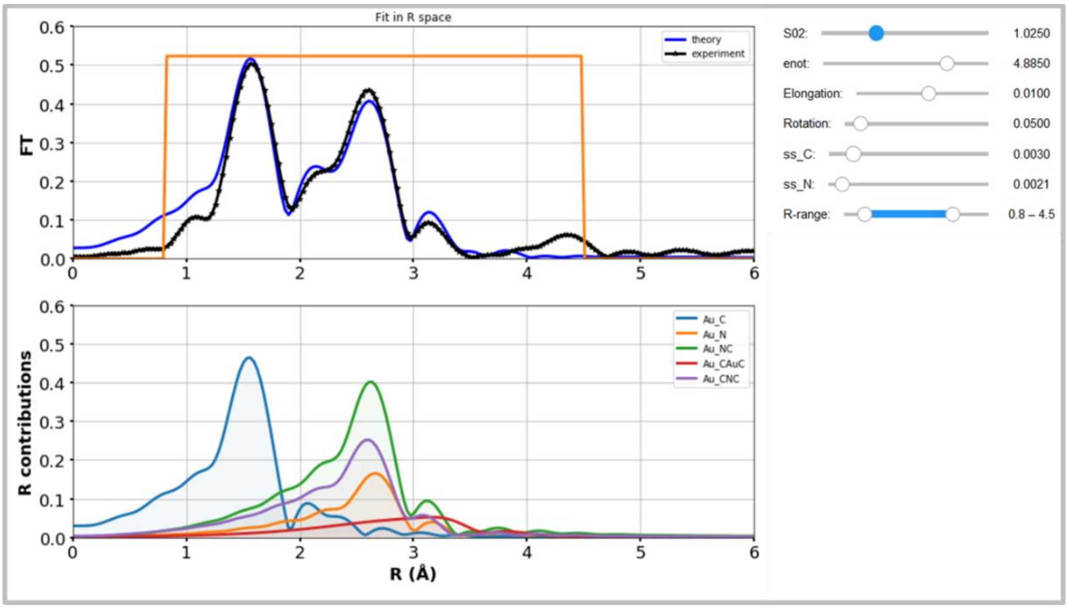

S02: 1.0250
enot: 4.8850
Elongation: 0.0100
Rotation: 0.0500
ss_C: 0.0030
ss_N: 0.0021
R-range: 0.8 – 4.5

**Figure 3.15:** Fit by sliders interface reporting on the top graph the FT magnitude representation of the $k^2$ weighted experimental and theoretical EXAFS spectrum. The latter is obtained summing all the SS and MS contributions, reported in the bottom panel, resulting to be the same employed in **Figure 3.14**. The orange square window is used to select the range in $R$ for the fitting procedure.

For the sake of clarification, a detailed description concerning how the paths functions involved in the slider plots of **Figure 3.14** and **Figure 3.14** are obtained is now provided.

The EXAFS experimental spectrum at the Au $L_3$-edge (11919 eV) was performed at the BM23 beamline of the European Synchrotron Radiation Facility (ESRF, Grenoble, France). An EXAFS cell, specifically devoted to liquid samples, was filled with a 5 x $10^{-4}$ M ethanolic solution of $\{Zn(L_1)_2[(\mu\text{-}CN)Au(CN)](H_2O)\}[Au(CN)_2]$ with few drops of $H_2O$ to enhance the solubility of $K[Au(CN)_2]$. The XAS data have been collected at room temperature. Due to low concentration of the complex, EXAFS spectra were acquired in fluorescence mode, using a Si(111) double crystal monochromator to select the incident X-ray energy and a single-element silicon drift detector.

Starting from the crystallographic $Au(CN)_2$ structure showed in **Figure 3.10**, obtained through a SC-XRD refinement of $Zn(L_1)_2[(\mu\text{-}CN)Au(CN)](H_2O)\}[Au(CN)_2]$ in solid state, two structural parameter have been selected for their refinement. These are the two bond distances $\Delta R$: Au-(CN), indicted in **Figure 3.14** and **Figure 3.15** by the parameter *elongation*, and the variation of the angle $\Delta\theta$ defined by the bond directions Au-$C_1$ and Au-$C_2$ respect to the initial position, and named *Rotation*, see **Figure 3.16**. The first grid associated to these parameters is equivalent to the one showed in **Figure 3.11** and it was generated assuming a range of variation for $\Delta R$ within $-0.12$ and $0.12$ Å, and for $\Delta\vartheta$ within 0 and $\pi/6$ rad. .

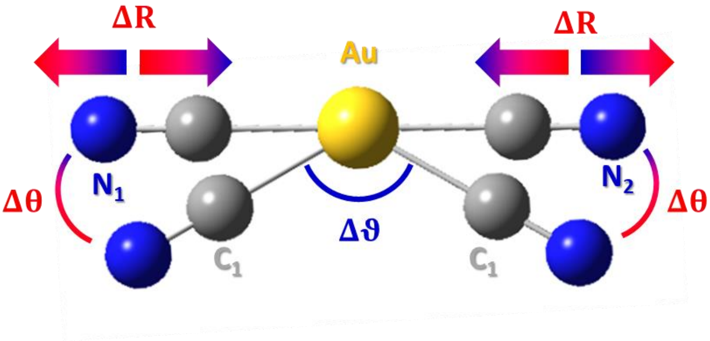

**Figure 3.16:** Picture representing the first set of structural deformations applied to the molecule of $Au(CN)_2$. These involve the common contraction/expansion of the Au-CN bond lengths ($\Delta R$) and the variation $\Delta\theta$ from the crystallographic position. As already showed in **Figure 3.10**, $\Delta\vartheta$ is the variation of the angle defined by the two carbon bond lengths. Color code: Au: yellow, C: grey, N: blue.

The criterion used for the selection of the most relevant paths was based on the curve wave amplitude $C_{cw}$ associated to each path: $C_{cw} > 15\%$. The equivalence criteria were then employed to determine, among all the most intense paths, the unique list, which appeared composed by the following five terms: Au→$C_1$→ Au (SS), Au→$N_1$→Au (SS), Au→$C_1$→ $N_1$→Au (MS with 3 legs), Au → $C_1$→$N_1$→ $C_1$→ Au (MS with 4 legs) and finally Au → $C_1$→Au→ $C_2$→ Au (MS with 4 legs). It is worth to underlie here that these paths are the most representative for each extreme deformation (see **Figure 3.11**). Clearly, it is possible that, for some perturbed geometry, the FEFF pathfinder could provided, for example, the path Au→$C_2$→ Au with degeneration 2 instead of Au→$C_1$→ Au, or in case of asymmetrical deformations (not considered here because, in this example, the parameter $\Delta R$ is the same for each bond lengths) even both of them: Au→$C_1$→ Au and Au→$C_2$→ Au with path degeneration equal to 1. Independently of the atoms enumeration, these paths are catalogued under the same path typology, in this case: Au→$C_1$→ Au. The similar approach can be extended to every MS path. Once that the unique SS and MS paths were found, the interpolation grid was built varying the quantities $\Delta R$ and $\Delta \theta$ for 300 times following the IHS scheme. For each couple of deformations the related structure was generated and the correspondent input file has been employed in the execution of the FEFF routine. Afterwards, for each perturbed geometry, the equivalence criteria were applied and only the paths satisfying them were considered and stored in the related matrix. In case of presence of two (or more) equivalent paths for the same molecular deformation, for example Au→$C_1$→ Au and Au→$C_2$→ Au with degeneration 1, both of signals are extracted, summed and saved in the corresponding matrix named, in this case Au→$C_1$→ Au matrix. This approach can be followed, if and only if, it is supposed that both the paths are characterized by the same DW parameter. If this condition is not satisfied the Au→$C_2$→ Au must be decoupled from the Au→$C_1$→ Au paths. It follows that if for one deformation, it is just present the Au→$C_1$→ Au path with degeneration 2, this signal must by cloned, associated to the Au→$C_2$→ Au paths and its degeneration must be then reduced of one term. The same procedure must be pursued for any other kind of path if the decoupling is needed.

At the end of the selection procedure, the five data matrices (Au→$C_1$→ Au, Au→$N_1$→Au, Au→$C_1$→ $N_1$→Au, Au → $C_1$→$N_1$→ $C_1$→ Au and Au → $C_1$→Au→ $C_2$→ Au), containing the related equivalent paths deriving from each IHS geometry, were used for the training procedure of the ML algorithm (extra-trees). The algorithm returned, for each matrix, the correspondent path function depending from $\Delta R$ and $\Delta \theta$. Afterwards, these functions were weighted for their own DW factor. This is the only parameterization required by this method. The DW factors associated to the SS paths: Au→$C_1$→ Au and Au→$N_1$→Au, were defined using the quantities $\sigma_C$ and $\sigma_N$. On the other hand, the MS DW terms were parametrized as the square root of the sum of squares of the DW factors associated to the atoms involved in each path. For all the paths, the terms $S_0^2$ and $\Delta E$ (enot) were assumed common.

The fit by sliders procedure showed in the precedent figures, is clearly a qualitative approach. In order to extract quantitative structural information it is required to perform a fit. How described in **chapter 1**, the EXAFS fit is usually realized in $k$ or $R$ space. However, it is worth noting that a good agreement, for instance, in the Fourier space only, does not necessarily mean a good agreement in $k$-space. Thus, the WT representation is a natural way to take into account features of signal both in $k$- and Fourier space simultaneously. Additionally, the advantage of the WT over the FT and over the representation of the spectra in $k$-space, can be seen in the case when the agreement between two spectra is not good: in this situation the WT, provides the information on the misfit of spectra both in $k$- and $R$-space simultaneously, allowing to identify the problem more easily. The WT fit can be realised employing the equation (3.12) or minimising the R-factor between the experimental spectrum and the theoretical one as follow:

$$\Xi = \frac{\sum_{i=1}^{2\times(M\times N)}[f_i(k,R)]^2}{\sum_{i=1}^{2\times(M\times N)}[g_i(k,R)]^2} \tag{3.17}$$

Where $f_i(k,R)$ corresponds to equation (3.11) while $g_i(k,R)$ is the mono-dimensional list containing the real and the imaginary part of the WT representation of the experimental signal: $g(k,R) = \Re\left[W_{\chi^{DATA}}^{\psi}(k,R)\right] + \Im\left[W_{\chi^{DATA}}^{\psi}(k,R)\right]$. Equation (3.12) and (3.17) must bring to the same solution. The main difference stands in the normalization of the residuals. In equation (3.17) the target function $\Xi$ can varies between 0 and 1. This choice can in fact improve the convergence algorithms towards a global minimum and, for this reason, equation (3.17) is suggested over (3.12).

The minimization of equation (3.17) was performed using the coordinated descended approach. The fitting parameters were: $\Delta R, \Delta\theta, \sigma_C$, $\sigma_N, S_0^2$ and $\Delta E$. The fitting ranges ware set to $\Delta k = (2.6{:}\,12)\ \text{Å}^{-1}$ and $\Delta R = (1{:}\,3.5)\ \text{Å}$, determining a number of independent points equal to $N_{ind} \approx \frac{2\Delta k \Delta R}{\pi} + 1 = 10$.

The fit was realized in the 2D range $\Delta k \times \Delta R = (2.6{:}\,12)\ \text{Å}^{-1} \times (1{:}\,3.5)\ \text{Å}$ setting the following bounds: $\Delta R \in [-0.12{:}\,0.12]$ Å, $\Delta\theta \in \left[0{:}\frac{\pi}{6}\right]$ rad., $\sigma_C$ and $\sigma_N \in [0.001, 0.015]$ Å$^2$, $S_0^2 \in [0.8, 1.8]$ and $\Delta E \in [-10, 10]$ eV, while the WT parameters, chosen for both the experimental and theoretical 2D plot, were: $s = 1$ and $\eta = 5$. The result of the minimization (global minimum of (3.17)) is shown in the following table:

| Best Fit Parameters | | Confidence Intervals (95%) |
|---|---|---|
| $S_0^2$ | 0.89 | 0.8 : 1.1 |
| $\Delta E$ (eV) | 9 | 7.4 : 10 |
| $\Delta R$ (Å) | 0 | -0.02 : 0.02 |
| $\Delta\vartheta$ (rad.) | 0.14 | 0 : $\frac{\pi}{6}$ |
| $\sigma_C$ (Å$^2$) | 0.002 | 0.01 : 0.007 |
| $\sigma_N$ (Å$^2$) | 0.001 | 0.001 : 0.06 |

**Table 3.2**: Best Fit Parameters obtained minimising the target function of equation (3.17) considering the set of deformations reported in **Figure 3.16**. The confidence intervals has been evaluated using the F-test map considering a number of independent points equal to 16.

The R-factor, evaluated as the minimum value of (3.17) multiplied for a factor 100, is equal to 1.9%, demonstrating that the molecular complex can be associated to the experimental signal. The confidence intervals, for each parameter, were evaluated using the F-test. Herein the following statistical variable was evaluated:

$$F_{N_{ind}-p,p}^{\alpha} = \frac{N_{ind} - p}{p}\left(\frac{\chi_0^2}{\chi^2} - 1\right) \tag{3.18}$$

The $F_{N_{ind}-p,p}^{\alpha}$ is a Fisher variable evaluated assuming the presence of six fitting parameters: $p = 6$. Fixing a significance level of $\alpha = 95\%$, every parameter is varied within its related interval until the integral of the Fisher distribution between $F_{N_{ind}-p,p}^{\alpha}$ and $+\infty$ becomes higher of 0.95, see **Figure 3.17**(a). Considering a determined parameter, the ration among the two chi-squares variables $\frac{\chi_0^2}{\chi^2}$ is obtained calculating the division of the target function $\Xi_0$ (evaluated in the global minimum) for the same function calculated fixing all the parameters to the best fit values and varying the selected one within the defined boundaries. Function (3.17) can be interpreted, in fact, as a sort of $\chi^2$ function, normalized for the constant quantity $\sum_{i=1}^{2\times(M\times N)}[g_i(k,R)]^2$ and weighted for a uniform error factor set to 1.

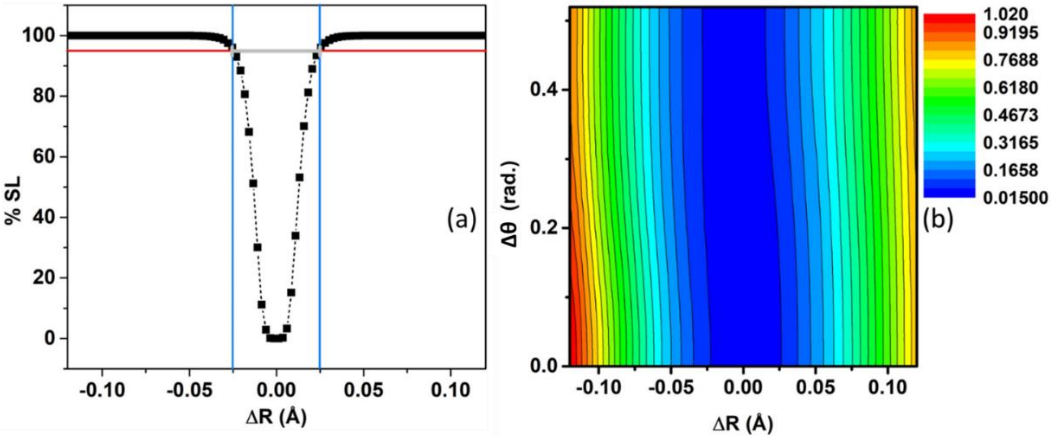

**Figure 3.17:** (a) Plot of the significance level associated to the $\Delta R$ parameter. The red horizontal line correspond to the %S.L. of 95% while the vertical blue lines are the values of ΔR allowing to obtain this significance level. (b) Plot of the section of $\Xi$ obtained varying $\Delta R$ and $\Delta\vartheta$ and maintaining fixed to the best fit values all the remaining parameters.

Analyzing the retrieved confidence intervals for each parameter of **Table 3.2**, it is possible to see that most of them are not symmetric. One of the main difference between the minimization of equation (3.17) with equation (3.10) stands in the fact that the latter employs a minimization algorithm over a set of parameters without bounds. It is possible to verify, in fact, that the error estimation retrieved using the covariance matrix often fails in presence of bounds [43]. The usage of the F-test (or equivalently of the $\chi^2$-maps) is able to provide a more reliable estimation of the uncertainties proper of the parameters refined through the WT fit. It is interesting to note from **Table 3.2** that the variation of the each angle $\Delta\theta$ from the initial configuration is found to be by the fit equal to ca. 8°. However, the error associated to the estimation of this parameter is extremely large, extending over all its variation range. The reason of this evidence is explained considering the curve wave amplitude associated to the $Au \rightarrow C_1 \rightarrow Au \rightarrow C_2 \rightarrow Au$ contribution. This is the only path having, in fact, a connection with the angle $\vartheta$ between the two carbon atoms ($\vartheta = \widehat{C_1AuC_2}$). However, if compared with all the other paths constituting the total EXAFS signal, it is also the one with the lowest intensity (see in **Figure 3.15** the red FT profile) and the highest half path length (independently from the performed deformation). It follows that during the minimization routing its influence on the variation of $\Xi$ is overpowered by the $\Delta R$ effect, see **Figure 3.17**(b). A second interesting results is represented by the DW value associated to the SS Au→N path. It is possible to see that this value coincides with the lowest bound for the $\sigma_N$ range of variation. This evidence can be understood remembering that the DW factor is a measure of the mean square displacement of the atoms from their equilibrium position. Because the each N atom is connected to their related C atom through a triple bond ("robust" connection), this result appears justified.

The main conclusions emerging from this fitting routine is that it is possible to estimate from the EXAFS analysis the bond distances with an uncertainty of ca. 2% but not the bond angles among the two carbon atoms. Similarly to the XANES fitting case discussed in **chapter 2**, this result implies that the number of parameters with can be estimated is lower than the number of independent points given by the Nyquist criterion.

As it has been demonstrated, the estimation of the $\vartheta$ angle is impossible because of the low intensity curve wave amplitude of the Au → $C_1$→Au→ $C_2$→ Au path. However, it is possible to estimate properly a second kind of angle $\varrho$, which is the one defined by the bonds: $\mathrm{Au}-\mathrm{C}$ and $\mathrm{C}\equiv\mathrm{N}$, ie. $\varrho=\widehat{\mathrm{AuCN}}$, where C and N are $C_1$, $N_1$ and $C_2$, $N_2$, respectively.

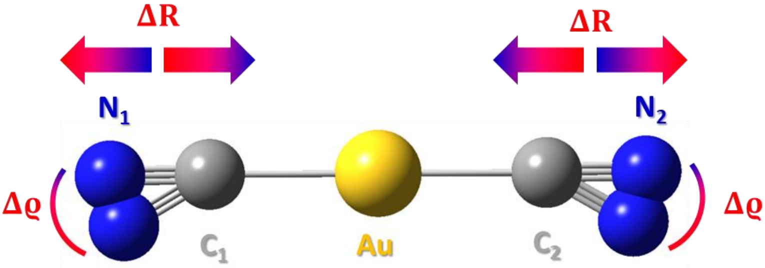

**Figure 3.18:** Picture representing the second set of structural deformations applied to the molecule of $Au(CN)_2$. These involve the common contraction/expansion of the Au-CN bond lengths (ΔR) and the variation $\Delta\varrho$ of the $\widehat{AuCN}$ angles. Colour code: Au: yellow, C: grey, N: blue.

Herein the procedure described above is repeated. However the parameters estimated by the fit are, this time: $\Delta\mathrm{R}, \sigma_\mathrm{C}$, $\sigma_\mathrm{N}, \mathrm{S}_0^2$, $\Delta\mathrm{E}$ an, $\Delta\varrho$ instead of $\Delta\theta$. The $\Delta\mathrm{R}$ structural parameter represents always the common contraction/expansion of the Au-C bonds within the range of $[-0.12{:}\,0.12]$ Å, while $\Delta\varrho$ consists in the synchronous tilting of the N atoms from their initial position: $\varrho=0$ rad. As in the case of $\Delta\theta$, the rage of variation of $\Delta\varrho$ was fixed to $\left[0{:}\frac{\pi}{6}\right]$ for both the angles. The unique list appeared composed by the same paths described for the precedent fitting routine. The result of the WT fit executed through this new parametrization is showed in **Table 3.3** and in **Figure 3.19**.

| **Best Fit Parameters** | | **Confidence Intervals (95%)** |
|---|---|---|
| $\mathrm{S}_0^2$ | 0.89 | 0.8 : 1.06 |
| $\Delta\mathrm{E}$ (eV) | 8.463 | 6.8 : 10 |
| $\Delta\mathrm{R}$ (Å) | -0.002 | -0.02 : 0.02 |
| $\Delta\varrho$ (rad.) | 0.024 | 0 : 0.26 |
| $\sigma_\mathrm{C}$ (Å$^2$) | 0.002 | 0.001 : 0.07 |
| $\sigma_\mathrm{N}$ (Å$^2$) | 0.001 | 0.001 : 0.07 |

**Table 3.3:** Best Fit Parameters obtained minimising the target function of equation (3.17) considering the set of deformations reported in **Figure 3.18**. The confidence intervals has been evaluated using the F-test map.

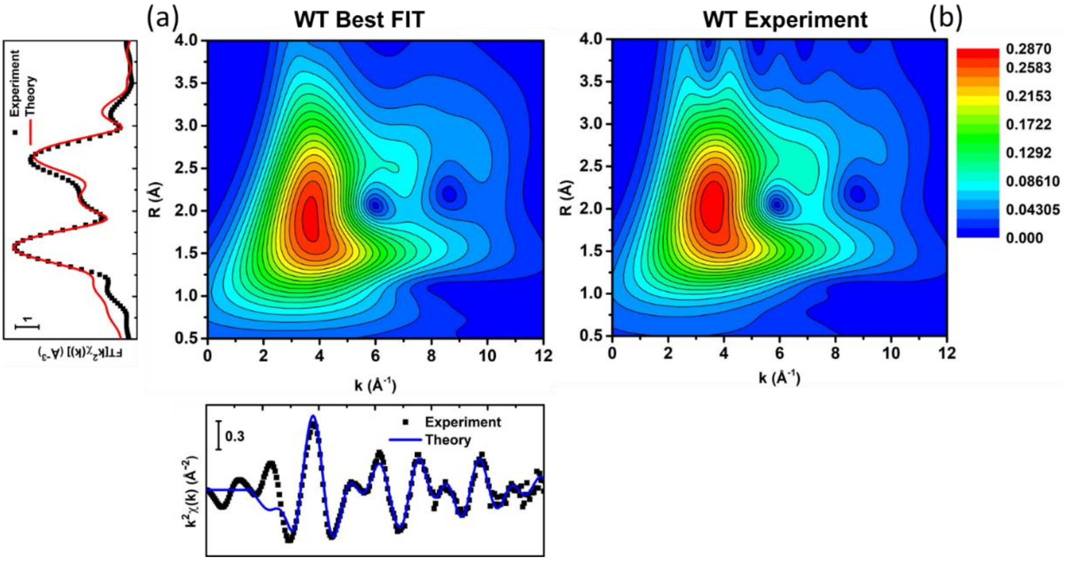

**Figure 3.19:** (a) Plot of the best fit WT representation. In the bottom and right panels are compared reported the best-fit curves EXAFS curves in the $k$ ad $R$ pace. The fit has been realised in the $\Delta k \times \Delta R = (2.6-12)\ \text{Å}^{-1} \times (1-3.5)\ \ \text{Å}$ 2D space. (b) WT representation of the experimental signal. As for the precedent case, the same WT parameters were employed here too: $s = 1$ and $\eta = 5$.

The quality of the fit, measured through the R-factor parameter indicates, also here, an good agreement between the experiment and the theoretical model: $\%\mathrm{R_{factor}} \approx 2\%$. Looking at **Table 3.3**, it is possible to note that the variation $\Delta\varrho$ is comparable with zero and its confidence interval is narrower indicating that for the EXAFS fit it is possible to obtain a proper estimation of the $\varrho$ angle. This is also evident analyzing the contour plot of $\Xi$ associated to the variation of $\Delta\mathrm{R}$ and $\Delta\varrho$.

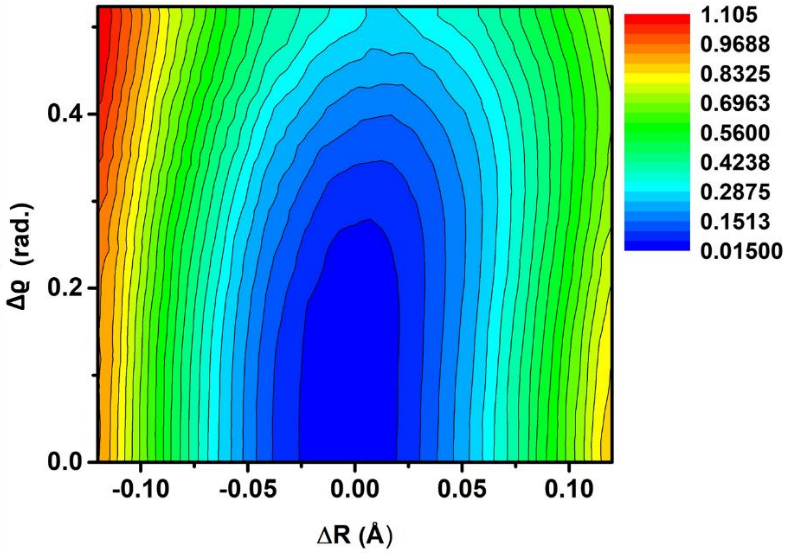

**Figure 3.20:** Plot of the section of $\Xi$ obtained varying $\Delta R$ and $\Delta\varrho$ and maintaining fixed to the best fit values all the remaining parameters.

## 3.3 REFERENCES

[1] J. Timoshenko, A. Kuzmin, Wavelet data analysis of EXAFS spectra, Computer Physics Communications, 180 (2009) 920-925.

[2] A. Martini, I.A. Pankin, A. Marsicano, K.A. Lomachenko, E. Borfecchia, Wavelet analysis of a Cu-oxo zeolite EXAFS simulated spectrum, Radiation Physics and Chemistry, 175 (2020) 108333.

[3] I.A. Pankin, A. Martini, K.A. Lomachenko, A.V. Soldatov, S. Bordiga, E. Borfecchia, Identifying Cu-oxo species in Cu-zeolites by XAS: A theoretical survey by DFT-assisted XANES simulation and EXAFS wavelet transform, Catalysis Today, 345 (2020) 125-135.

[4] M. Munoz, P. Argoul, F. Farges, Continuous Cauchy wavelet transform analyses of EXAFS spectra: A qualitative approach, Am. Miner., 88 (2003) 694-700.

[5] H. Funke, A.C. Scheinost, M. Chukalina, Wavelet analysis of extended x-ray absorption fine structure data, Phys. Rev. B, 71 (2005) 7.

[6] T.J. Penfold, I. Tavernelli, C.J. Milne, M. Reinhard, A. El Nahhas, R. Abela, U. Rothlisberger, M. Chergui, A wavelet analysis for the X-ray absorption spectra of molecules, J. Chem. Phys., 138 (2013) 7.

[7] J. Timoshenko, A. Anspoks, A. Kalinko, A. Kuzmin, Analysis of extended x-ray absorption fine structure data from copper tungstate by the reverse Monte Carlo method, Physica Scripta, 89 (2014).

[8] H. Funke, M. Chukalina, A.C. Scheinost, A new FEFF-based wavelet for EXAFS data analysis, J. Synchrot. Radiat., 14 (2007) 426-432.

[9] J. Timoshenko, A. Kuzmin, J. Purans, Reverse Monte Carlo modeling of thermal disorder in crystalline materials from EXAFS spectra, Computer Physics Communications, 183 (2012) 1237-1245.

[10] J. Timoshenko, A. Anspoks, A. Kalinko, A. Kuzmin, Temperature dependence of the local structure and lattice dynamics of wurtzite-type ZnO, Acta Mater., 79 (2014) 194-202.

[11] J. Timoshenko, A. Kuzmin, J. Purans, EXAFS study of hydrogen intercalation into ReO3 using the evolutionary algorithm, Journal of Physics-Condensed Matter, 26 (2014) 15.

[12] M. Newville, IFEFFIT: interactive XAFS analysis and FEFF fitting, J. Synchrot. Radiat., 8 (2001) 322-324.

[13] M. Newville, EXAFS analysis using FEFF and FEFFIT, J. Synchrot. Radiat., 8 (2001) 96-100.

[14] J.J. Rehr, R.C. Albers, Theoretical approaches to x-ray absorption fine structure, Rev. Mod. Phys., 72 (2000) 621-654.

[15] S.I. Zabinsky, J.J. Rehr, A. Ankudinov, R.C. Albers, M.J. Eller, MULTIPLE-SCATTERING CALCULATIONS OF X-RAY-ABSORPTION SPECTRA, Phys. Rev. B, 52 (1995) 2995-3009.

[16] A. Kuzmin, EDA - EXAFS DATA-ANALYSIS SOFTWARE PACKAGE, Physica B, 208 (1995) 175-176.

[17] J.J. Moré, The Levenberg-Marquardt algorithm: Implementation and theory, in: G.A. Watson (Ed.) Numerical Analysis, Springer Berlin Heidelberg, Berlin, Heidelberg, 1978, pp. 105-116.

[18] J.A. Nelder, R. Mead, A Simplex Method for Function Minimization, The Computer Journal, 7 (1965) 308-313.

[19] A. Kuzmin, J. Chaboy, EXAFS and XANES analysis of oxides at the nanoscale, IUCrJ, 1 (2014) 571-589.

[20] G. Bunker, Introduction to XAFS: A Practical Guide to X-ray Absorption Fine Structure Spectroscopy, Cambridge University Press, Cambridge, 2010.

[21] P. Fornasini, Study of lattice dynamics via extended x-ray absorption fine structure, Journal of Physics-Condensed Matter, 13 (2001) 7859-7872.

[22] G. Beni, P.M. Platzman, Temperature and polarization dependence of extended x-ray absorption fine-structure spectra, Phys. Rev. B, 14 (1976) 1514-1518.

[23] G. Bunker, Application of the ratio method of EXAFS analysis to disordered systems, Nucl. Instrum. Methods Phys. Res., 207 (1983) 437-444.

[24] A. Kuzmin, G. Dalba, P. Fornasini, F. Rocca, O. Sipr, X-ray absorption spectroscopy of strongly disordered glasses: Local structure around Ag ions in g-Ag2O center dot nB(2)O(3), Phys. Rev. B, 73 (2006) 12.

[25] E. Sevillano, H. Meuth, J.J. Rehr, Extended x-ray absorption fine structure Debye-Waller factors. I. Monatomic crystals, Phys. Rev. B, 20 (1979) 4908-4911.

[26] V.L. Aksenov, M.V. Koval'chuk, A.Y. Kuz'min, Y. Purans, S.I. Tyutyunnikov, Development of methods of EXAFS spectroscopy on synchrotron radiation beams: Review, Crystallogr. Rep., 51 (2006) 908-935.

[27] S. Bordiga, E. Groppo, G. Agostini, J.A. van Bokhoven, C. Lamberti, Reactivity of Surface Species in Heterogeneous Catalysts Probed by In Situ X-ray Absorption Techniques, Chem. Rev., 113 (2013) 1736-1850.

[28] A.I. Frenkel, Applications of extended X-ray absorption fine-structure spectroscopy to studies of bimetallic nanoparticle catalysts, Chem. Soc. Rev., 41 (2012) 8163-8178.

[29] L. Mino, G. Agostini, E. Borfecchia, D. Gianolio, A. Piovano, E. Gallo, C. Lamberti, Low-dimensional systems investigated by x-ray absorption spectroscopy: a selection of 2D, 1D and 0D cases, J. Phys. D-Appl. Phys., 46 (2013) 72.

[30] B. Ravel, Path aggregation techniques for EXAFS visualization and analysis, in: Z.Y. Wu (Ed.) 15th International Conference on X-Ray Absorption Fine Structure, Iop Publishing Ltd, Bristol, 2013.

[31] A. Kuzmin, J. Purans, THE INFLUENCE OF THE FOCUSING EFFECT ON THE X-RAY-ABSORPTION FINE-STRUCTURE ABOVE ALL THE TUNGSTEN-L EDGES IN NONSTOICHIOMETRIC TUNGSTEN-OXIDES, Journal of Physics-Condensed Matter, 5 (1993) 9423-9430.

[32] A. Filipponi, A. DiCicco, X-ray-absorption spectroscopy and n-body distribution functions in condensed matter .2. Data analysis and applications, Phys. Rev. B, 52 (1995) 15135-15149.

[33] A. Filipponi, A. DiCicco, C.R. Natoli, X-ray-absorption spectroscopy and n-body distribution functions in condensed matter .1. Theory, Phys. Rev. B, 52 (1995) 15122-15134.

[34] P. Dangelo, A. Dinola, A. Filipponi, N.V. Pavel, D. Roccatano, AN EXTENDED X-RAY-ABSORPTION FINE-STRUCTURE STUDY OF AQUEOUS-SOLUTIONS BY EMPLOYING MOLECULAR-DYNAMICS SIMULATIONS, J. Chem. Phys., 100 (1994) 985-994.

[35] A. Kuzmin, R.A. Evarestov, Quantum mechanics-molecular dynamics approach to the interpretation of x-ray absorption spectra, Journal of Physics-Condensed Matter, 21 (2009).
[36] A. Di Cicco, A. Trapananti, Reverse Monte Carlo refinement of molecular and condensed systems by x-ray absorption spectroscopy, Journal of Physics-Condensed Matter, 17 (2005) S135-S144.
[37] E.A. Hudson, P.G. Allen, L.J. Terminello, M.A. Denecke, T. Reich, Polarized x-ray-absorption spectroscopy of the uranyl ion: Comparison of experiment and theory, Phys. Rev. B, 54 (1996) 156-165.
[38] B. Ravel, Composing complex EXAFS problems with severe information constraints, in: A. DiCicco, A. Filipponi (Eds.) 14th International Conference on X-Ray Absorption Fine Structure, Iop Publishing Ltd, Bristol, 2009.
[39] E. Groppo, C. Prestipino, C. Lamberti, P. Luches, C. Giovanardi, F. Boscherini, Growth of NiO on Ag(001): Atomic environment, strain, and interface relaxations studied by polarization dependent extended X-ray absorption fine structure, J. Phys. Chem. B, 107 (2003) 4597-4606.
[40] A. Martini, S.A. Guda, A.A. Guda, G. Smolentsev, A. Algasov, O. Usoltsev, M.A. Soldatov, A. Bugaev, Y. Rusalev, C. Lamberti, A.V. Soldatov, PyFitit: The software for quantitative analysis of XANES spectra using machine-learning algorithms, Computer Physics Communications, 250 (2020) 15.
[41] B. Ravel, Path degeneracy and EXAFS analysis of disordered materials, J. Synchrot. Radiat., 21 (2014) 1269-1274.
[42] F.a.G. Perez, B. E., IPython: A System for Interactive Scientific Computing, Computing in Science Engineering, 9 (2007) 21-27.
[43] M. Newville, Stensitzki, Till, Allen, Daniel B., & Ingargiola, Antonino., LMFIT: Non-Linear Least-Square Minimization and Curve-Fitting for Python (Version 0.8.0). Zenodo, (2014).

# 4 A NEW CODE FOR THE NEXAFS DATA ANALYSIS

In this chapter is presented a detailed description of a software, named THORONDOR [1], realised for the analysis and treatment of low energy XAS spectra (NEXAFS). The code has been completely designed by me and by my friend and colleague D. Simonne (University of Turin, now at SOLEIL, France) and can be downloaded freely at: https://pypi.org/project/THORONDOR/.
After a brief discussion about the NEXAFS data analysis issues, which brought to the development of this code, the chapter will focus on the different approaches designed to manipulate, correct and visualise the experimental NEXAFS data. Finally, the last section is devoted to explain the functionalities of the peak-fitting toolbox embedded in the code.

## 4.1 THORONDOR A SOFTWARE DESIGNED FOR A FAST TREATMENT AND ANALYSIS OF NEXAFS SPECTRA

As introduced in **chapter 1**, XAS is a fundamental tool for the characterization of a large variety of materials thanks to its chemical selectivity and high sensitivity in determining interatomic distances [2]. These fact render this technique powerful to study surface/interface phenomena such as those found in heterogeneous catalysis, fuel cells or batteries [3, 4]. In these contexts, the usage of soft X-rays below 2.0 keV is extremely useful to study the oxidation state and the coordination geometry of both light element (at K-edges) and transitions metals (at e.g. L-edges), which play a fundamental role in these fields [5].
In the soft X-ray energy regime, the high X-ray absorption coefficients make it often necessary to work under low-pressure environments [6]. Although the high-vacuum condition produces an ideally clean environment for the sample under study, a multitude of chemically relevant phenomena only take place under ambient pressure [7, 8]. In an effort to bridge the pressure gap in this context, different gas and liquid cells were designed in recent years, enabling to carry out soft X-ray studies of different reactions under in situ conditions [5, 7-17]. In general, their design implies that the X-ray beam penetrates inside the reaction volume through a $Si_3N_4$ membrane of few tens of nanometres of thickness [7]. These membranes have sufficient mechanical resistance to resist the difference of pressure between the vacuum of the chamber, where the cell is situated, and the gas environment inside it, at atmospheric pressure [8]. Because of the high yield of the photoelectric effect in the soft X-ray range and pushed by the experimental simplicity, the so called Total Electron Yield measured by the replacement current (or drain current) has emerged as the most popular way to perform XAS in the soft X-ray range (below 2 keV). This technique combines surface sensitivity, resulting from the short escape depth of photoelectrons in this energy range, and the practical advantage of minimizing the alignment problems with the detector [8]. The standard way to acquire the absorption spectrum is realised by moving the monochromator with a discrete step, recording the TEY intensity at the selected energy, and repeating this operation for the entire energy range of interest. Recently, the experimental practice has been improved by continuously scanning the grating monochromator through the desired energy range (and sometimes also

the undulator gap) while collecting the signal in a streaming mode. This last methodology, sometimes known as *fast-scan* or *on the fly scan*, significantly improves the time resolution of the NEXAFS measurements, allowing to follow under in situ conditions different dynamic processes (e.g. chemical reactions) [6,7]. Although several software packages have been developed for the analysis of hard-XAS data (e.g. GNXAS [18, 19], ATHENA [20], VIPER [21], EDAXAFS [22], SIXPACK [23] …), only a few of them have been specifically designed for the data treatment of soft X-ray absorption spectra such as QANT [24], Blueprint XAS [25] or KKCalc [26]. The critical features necessary for accurate and efficient treatment of NEXAFS data are a user-friendly interface, a quick and straightforward installation of the program on any machine, and a versatile range of functions covering the whole data treatment, from the subtraction of the background until the fit of the spectrum. THORONDOR aims to be a software for the analysis of multiple NEXAFS spectra, flexible enough to manage data collected both in conventional ultra-high vacuum (UHV) measurements and during more challenging experiments in environmental conditions. Equipped with an intuitive graphical user interface (GUI), this program, developed in Python, allows a fast data treatment and the visualization of several spectral profiles collected under different working conditions, ranging from UHV to ambient pressure atmosphere. Similarly to PyFitIt [27], one of its strengths stands in the possibility to quickly perform the conventional XAS data-handling procedures, such as the spectral background subtraction and normalization, using an approach based on sliders and cursors. A peak-fitting toolbox characterized by a high variety of peak functions and ionizations step potentials is also included for in-depth studies. Herein, it is worth noting that users can exploit different minimizations algorithms to perform the peak fitting of a defined NEXAFS spectrum and evaluate, using different statistical criteria, the quality of the chosen model and the uncertainties associated to the parameters retrieved by the fit. THORONDOR has been designed principally for the analysis of TEY measurements. However, its multiple functions can also be applied for spectra collected using alternative detection modes such as Partial Fluorescence Yield (FY).

## 4.2 STRUCTURE OF THE SOFTWARE

THORONDOR is based on two Python objects: the classes Dataset and GUI. During the initialisation procedure, a new instance of the class GUI, containing only temporary information, is generated.

Here, the user can provide several datasets as input to the GUI, as long as they focus on the same absorption edge.

The term *dataset* herein refers to the n-columns contained in a single experimental data-file, saved directly from the beamline with a minimum of two columns: the incoming photon energy, and the corresponding NEXAFS intensity. The remaining columns can contain supplementary data, such as the intensity of the incoming beam or the NEXAFS spectrum of a reference compound. At the moment, despite an important effort coming from several scientists, that consists in defining a common data exchange and archival format for X-ray experiments named NeXus-NXxas [28], for the soft X-rays absorption measurements, there is not a well-established conventional protocol describing how an output file containing raw data should be properly formatted and designed. The number of columns characterizing a dataset thus varies depending on the beamline where the measurements are taken.

If the datasets do not possess the same exact energy range and/or number of points, all the contained spectra will automatically be interpolated on the common energy range, with a step fixed by the user.

Once that one or more datasets have been selected, a new instance of the class Dataset, having as its first attribute the raw data, is created for each of them, see **Figure 4.1**. If a logbook was compiled during the experiment and saved in an .xlsx format (common excel file), it can be imported in the program too. Specific experimental parameters, such as the temperature, can then be extracted from it, saved as classes attributes and used by the program. This method drastically simplifies the data analysis procedure that every scientist needs to follow after an experiment, allowing to rapidly visualize and manipulate several datasets together.

The Pandas package [29] is employed to transform any common format of data into a DataFrame: a Python object that allows a quick manipulation and visualisation of the data as array (provided by the NumPy package [30]).

It is worth noting that each new variable, parameter or model that is specific to one dataset, will be automatically saved as an attribute of the associated class. Hence, the user can always come back to resume his work, or to alternate between different datasets without losing his progress.

The THORONDOR interface is based on the Jupyter widgets package [31]. The displayed GUI window is divided in multiple tabs. Each of them is built exploiting the ipywidgets.HBox and ipywidgets.VBox objects, containing several widgets. The functions proper to the GUI class are used to perform the entire data analysis. They are called interactively by the ipywidgets.interact and displayed. The result is a user-friendly interface, allowing a quick data visualisation, analysis and fitting in a Jupyter notebook environment. Each function can also be used outside the GUI for users that possess a deeper knowledge of Python and of the class-objects functionalities.

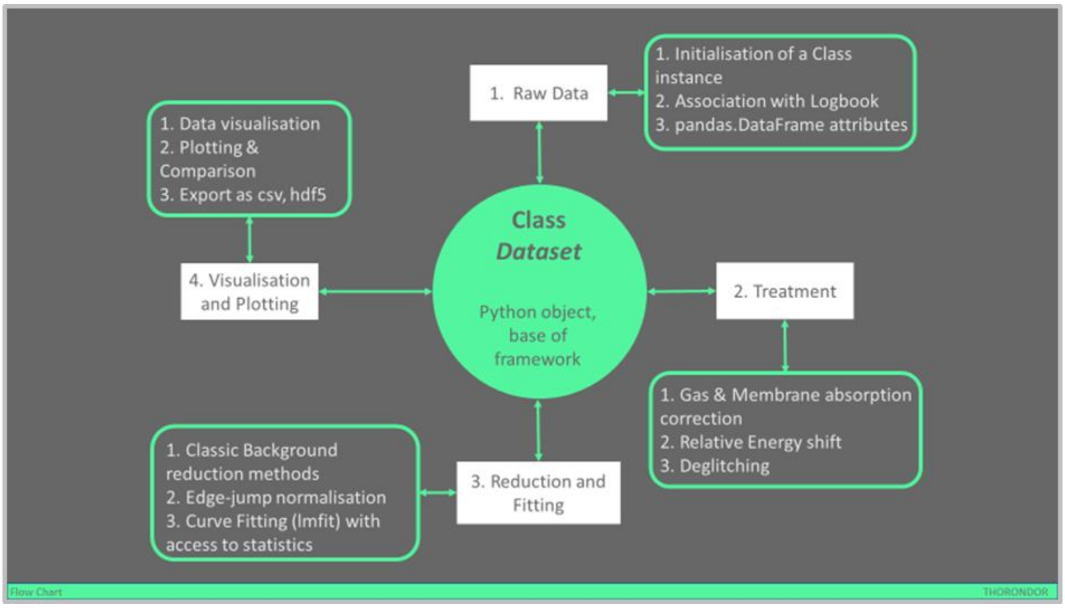

**Figure 4.1:** Flowchart of THORONDOR. A Python graphical user interface (GUI) is provided to help the user for each step of the analysis.

## 4.3 IMPORTING AND HANDLING RAW DATA

The experimental data files, in .txt or .dat format, directly retrieved from the beamline, must be located inside a data folder, in the same directory as the Jupyter notebook working file, where the THORONDOR package is imported. It is supposed that the experimental files are stored in the same data folder and refer to the same energy edge. The spectral profiles coming from different experiments and belonging to different datasets can be processed only in the condition that they refer to the same absorbing element and that they share the same file architecture. As introduced in **section 4.2**, the raw data files can be accompanied by a logbook from which the user can extract, through a filtering method provided by THORONDOR, specific experimental information associated to each dataset, such as the data collection temperature or the composition of the gas feed. These working parameters play a fundamental role in the gas X-ray absorbance correction (see **section 4.4.2**) and in the analysis of the XAS features.

To initialize the data treatment, the user needs to provide a name for each column of every dataset contained in the working directory. Each spectrum recorded during the experiment is imported inside a pandas.Dataframes object under a specific column. This operation is realized thanks to the use of practical dropdown-widgets. Once that all the columns of a dataset have been re-named, the same nomenclature is applied directly to all the other columns of the remaining files. It is worth noting that THORONDOR requires that at least two columns for each dataset correspond to two specific channels: the photon energy ($\mathrm{E}$), and the NEXAFS intensity ($\mu$). The latter can be computed as the ratio of the intensity of the signal coming from the sample ($\mathrm{I_S}$) over the incident flux beam intensity ($\mathrm{I_0}$) , see **Figure 4.2**. The nature of $\mathrm{I_0}$ and $\mathrm{I_S}$ depends, clearly, on the kind of measurement. In case of a TEY experiment, they consist of a current signal on the pA range [7]. This procedure (i.e. recording the beam intensity before the incidence on the sample) is due to the non-constant intensity of the beam in the spectrum energy range (due to the shape of the harmonic of the undulator and the transmission of the beamline optics [6]), moreover the beam in the ring can present variation in time (e.g. due to the top-up filling mode of the modern synchrotrons). Thus, the division of the absorption signal, coming from the sample, by the beam intensity, measured typically on a fine wire mesh of some noble metal, removes those artifacts from the $\mu$ shape and has become very popular among the beamline experimental stations. In addition, if present as part of the experimental data file, the user may also specify a reference column useful for energy-alignment purposes (see section **4.4.1**) and a column containing the experimental uncertainties associated to the measurement, which can be used during the peak fitting routine. It is worth noting that sometimes the flux monitor mesh can be contaminated by some elements, which are present in the sample under study too. This problem is usually addressed by normalising $\mu$ for the quantity $\mu_{\mathrm{ref}}$ obtained as the ratio among the NEXAFS signal of a reference sample free of that target element $\mathrm{I}_{\mathrm{ref}}$ for the intensity of the beam collected on the mesh $\mathrm{I}_0^{\mathrm{ref}}$: $\mu_{\mathrm{ref}} = \mathrm{I}_{\mathrm{ref}}/\mathrm{I}_0^{\mathrm{ref}}$. This approach, named as stable monitor method [32], is realised in THORONDOR selecting the so-called check box after the creation of the working datasets. Once that this option is activated, the user can declare which columns of the dataset (i.e. $\mathrm{I}_{\mathrm{ref}}$ and $\mathrm{I}_0^{\mathrm{ref}}$) can be considered to evaluate the $\mu_{\mathrm{ref}}$ spectrum. Afterwards the new normalised spectrum $\mu_{\mathrm{S}} = \mu/\mu_{\mathrm{ref}}$ is added to the dataframe and can undergo towards further corrections.

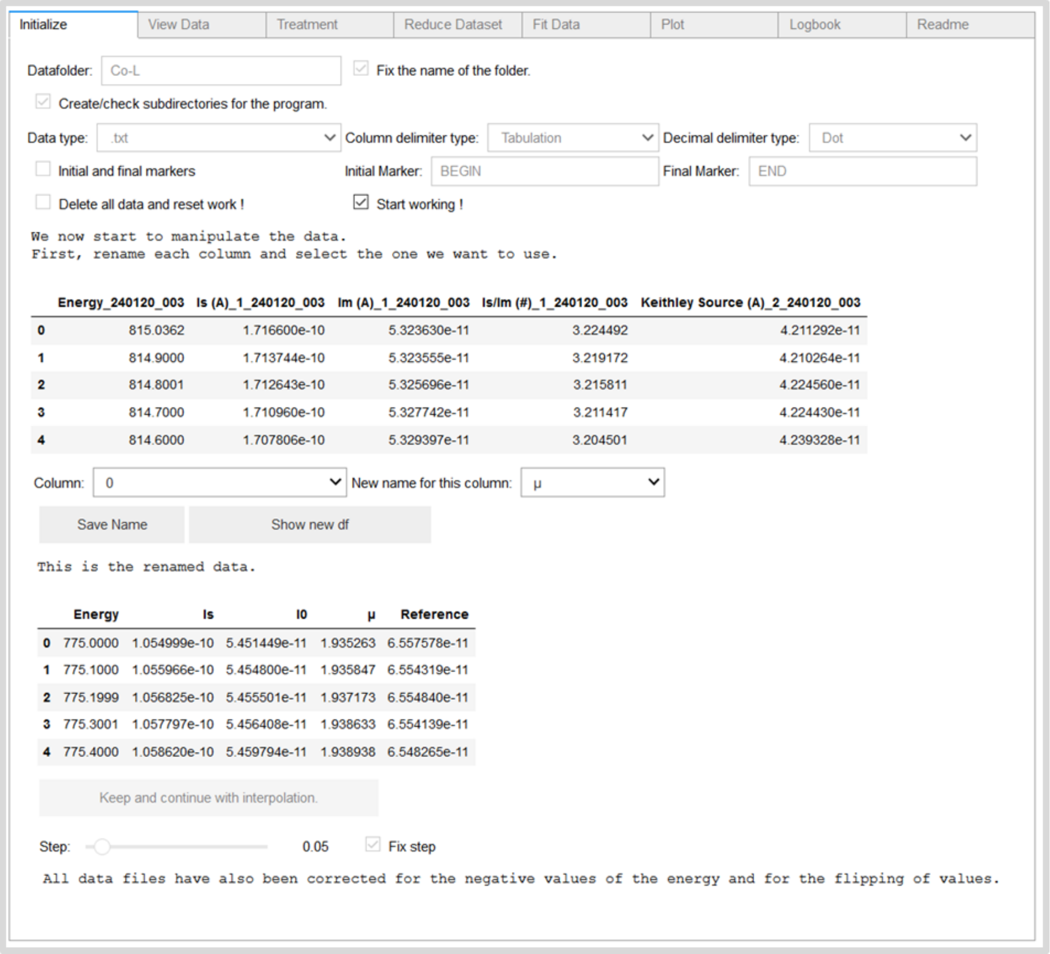

Datafolder: Co-L

☑ Fix the name of the folder.

☑ Create/check subdirectories for the program.

Data type: .txt

Column delimiter type: Tabulation

Decimal delimiter type: Dot

☐ Initial and final markers

Initial Marker: BEGIN

Final Marker: END

☐ Delete all data and reset work !

☑ Start working !

```
We now start to manipulate the data.
First, rename each column and select the one we want to use.
```

| | Energy_240120_003 | Is (A)_1_240120_003 | Im (A)_1_240120_003 | Is/Im (#)_1_240120_003 | Keithley Source (A)_2_240120_003 |
|---|---|---|---|---|---|
| 0 | 815.0362 | 1.716600e-10 | 5.323630e-11 | 3.224492 | 4.211292e-11 |
| 1 | 814.9000 | 1.713744e-10 | 5.323555e-11 | 3.219172 | 4.210264e-11 |
| 2 | 814.8001 | 1.712643e-10 | 5.325696e-11 | 3.215811 | 4.224560e-11 |
| 3 | 814.7000 | 1.710960e-10 | 5.327742e-11 | 3.211417 | 4.224430e-11 |
| 4 | 814.6000 | 1.707806e-10 | 5.329397e-11 | 3.204501 | 4.239328e-11 |

Column: 0

New name for this column: μ

```
This is the renamed data.
```

| | Energy | Is | I0 | μ | Reference |
|---|---|---|---|---|---|
| 0 | 775.0000 | 1.054999e-10 | 5.451449e-11 | 1.935263 | 6.557578e-11 |
| 1 | 775.1000 | 1.055966e-10 | 5.454800e-11 | 1.935847 | 6.554319e-11 |
| 2 | 775.1999 | 1.056825e-10 | 5.455501e-11 | 1.937173 | 6.554840e-11 |
| 3 | 775.3001 | 1.057797e-10 | 5.456408e-11 | 1.938633 | 6.554139e-11 |
| 4 | 775.4000 | 1.058620e-10 | 5.459794e-11 | 1.938938 | 6.548265e-11 |

Step: 0.05

☑ Fix step

```
All data files have also been corrected for the negative values of the energy and for the flipping of values.
```

**Figure 4.2:** The pandas.DataFrame object allows the quick visualisation and treatment of the dataset. Each spectrum of a dataset is recorded on the same energy range and is represented as a column in the dataframe. Here the first table shows the raw data read from the dataset referring to the first scan, while the second one reports the dataset columns selected by the user. The column $\mu$ contains here the ratio of $I_s$ over $I_0$, resulting from the first normalization procedure.

In THORONDOR, the signals coming from channel $I_s$ are firstly normalized by $I_0$, if such a procedure has not been performed beforehand, to produce $\mu$. This procedure is called here first normalization and the related spectral intensities will be indicated in the text as $\mu$. At the end of this scaling process, each dataframe will possess an extra column containing the first normalized signal $\mu$. The description of the signal background subtraction followed by a further data normalization is provided in **section 4.5**. Finally, the plotting window tool of THORONDOR allows the user to graphically represent the information contained in each dataframe. Each NEXAFS spectrum can be plotted singularly or together with the other signals collected during an experiment. Herein, in order to gain a better visualization, the colour of each spectrum can be personalized by the user together with the energy range of plotting. A sketch of the program window is showed in **Figure 4.3**.

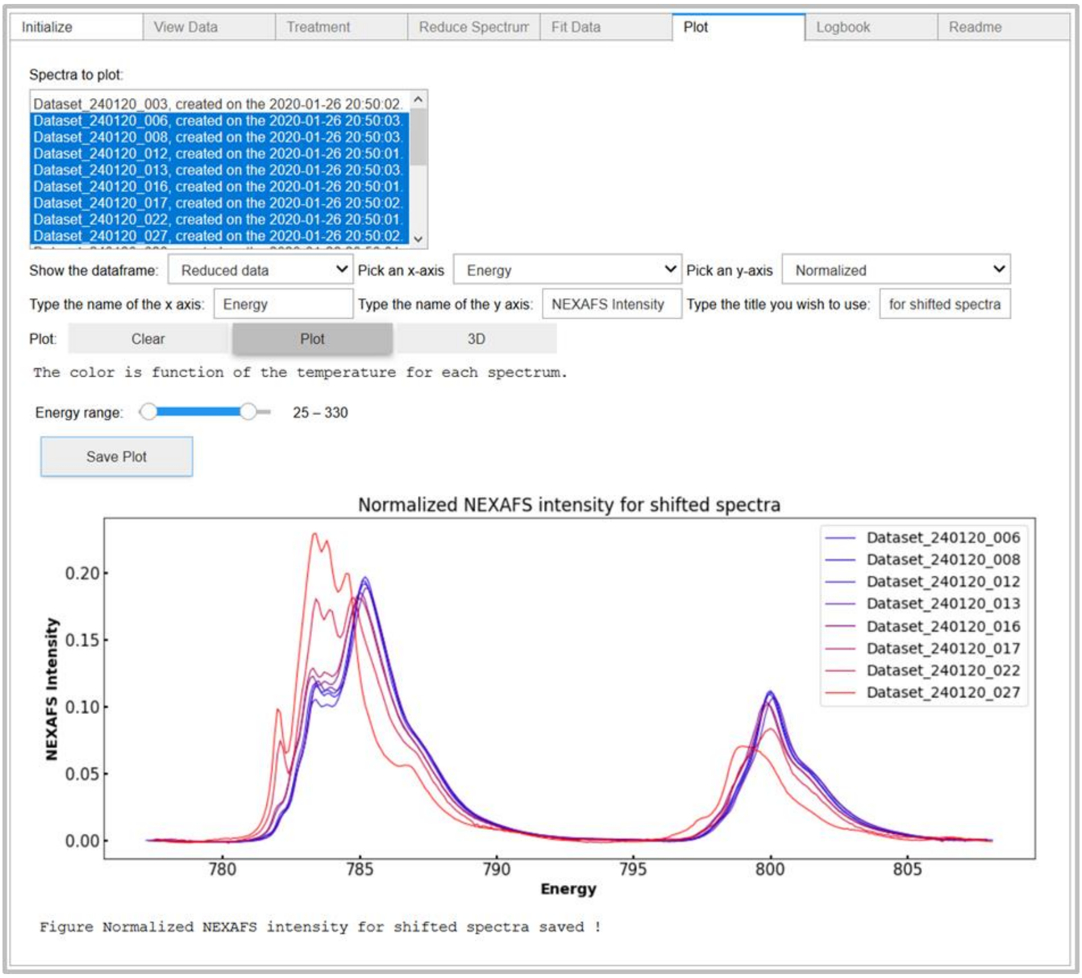

Spectra to plot:

Dataset_240120_003, created on the 2020-01-26 20:50:02.
Dataset_240120_006, created on the 2020-01-26 20:50:03.
Dataset_240120_008, created on the 2020-01-26 20:50:03.
Dataset_240120_012, created on the 2020-01-26 20:50:01.
Dataset_240120_013, created on the 2020-01-26 20:50:03.
Dataset_240120_016, created on the 2020-01-26 20:50:01.
Dataset_240120_017, created on the 2020-01-26 20:50:02.
Dataset_240120_022, created on the 2020-01-26 20:50:01.
Dataset_240120_027, created on the 2020-01-26 20:50:02.

Show the dataframe: Reduced data
Pick an x-axis: Energy
Pick an y-axis: Normalized
Type the name of the x axis: Energy
Type the name of the y axis: NEXAFS Intensity
Type the title you wish to use: for shifted spectra
Plot:

```
The color is function of the temperature for each spectrum.
```

Energy range: 25 – 330

```
Figure Normalized NEXAFS intensity for shifted spectra saved !
```

**Figure 4.3:** A sketch of the THORONDOR GUI. It is possible to display it in both Jupyter notebook and Jupyter-lab under proper builds.

## 4.4 DATA TREATMENT

In general, an acquired NEXAFS scan requires some corrections in order to be converted from a raw measure to an interpretable absorption spectrum. These spectral modifications, in THORONDOR, can be realised in four steps. These consist in: (i) the alignment of the measured spectrum to a determined reference and its subsequent calibration; (ii) the removal of eventual glitches affecting the measure; (iii) the membrane and gas transmittance correction; (iv) the spectral background subtraction and second normalization. In the following sections, each of these steps and their implementation in the software will be described in detail.

### 4.4.1 *Data energy alignment*

It is quite common that monochromators do not retain a perfect energy calibration over the course of multiple measurements. It follows that in some cases there could be some drift or jump effects in energy within a range of a few electronvolts [33]. THORONDOR offers the possibility to align all datasets with respect to a common spectral feature.

If along each scan, a reference spectrum of a well-known compound (containing the same selected absorbing element) is collected simultaneously with the sample measurement, it can be used for the energy alignment procedure. The reference spectrum must be imported during the data-importing step as described in **section 2.1**. Afterwards, the user, by means of a cursor, can select the position of the same spectral feature for each reference spectrum per dataset. This yields to a list containing the position of the same feature, perchance slightly shifted, for each dataset.

Once this step is completed all the references will be shifted in energy of a quantity equal to the difference among their features and the one of the selected reference. The shifts in energy accompanying each aligned reference are automatically exported to each spectrum of every dataset, realizing, in this way, their alignment. Finally, it may happen that the reference spectrum is not acquired during the measurement. In this case, the user can align the NEXAFS spectra over a feature belonging to the $\mathrm{I_s}$ or $\mu$ channel.

### 4.4.2 *Treating the effect of the window and gas X-ray absorption*

Under UHV condition, it is possible to measure the photon flux $\mathrm{I_0}$ impinging on the sample surface. This can be realized, for example, by measuring the TEY from a highly transparent metal grid intercepting a fraction of the incoming beam, localized, typically, before the entrance of the experimental chamber [7]. In case of ambient pressure measurements, this important part of the XAS acquisition in UHV cannot be done because of the presence of both the cell membrane and gas layer, which act as photon absorbers. However, considering these limitations, the photon flux hitting the sample $\mathrm{I_0^{eff}}$ can be estimated from a standard $\mathrm{I_0}$ measurement before the entrance in the reaction volume and the window and gas slabs transmittances, as follow:

$$\mathrm{I_0^{eff} = I_0 exp[-(k_w l_w + k_g l_g)]} \tag{4.1}$$

Where $\mathrm{k_w}$ and $\mathrm{l_w}$ together with $\mathrm{k_g}$ and $\mathrm{l_g}$ are respectively the X-ray attenuation lengths and thickness of the membrane and of the gas. The attenuation length for an element in a given material (in the solid or gas state) is calculated as the product of the atomic density $\rho_a$ by the atomic *photo-absorption cross section* $\sigma^{\mathrm{abs}}$ given by:

$$\sigma^{\mathrm{abs}}(\mathrm{E}) = 2\mathrm{r_0}\lambda \mathrm{f_{im}} \tag{4.2}$$

Where $\mathrm{r_0}$ is the classical electron radius, λ is the X-ray wavelength and $\mathrm{f_{im}}$ is the imaginary part of the atomic scattering factor of the element under analysis [34]. In THORONDOR, the attenuation length for the membrane refers to the $Si_3N_4$ compound and has been taken from the tabulated value in [34]. The only free parameter that, in this case, can be managed by the user is the window thickness $\mathrm{l_w}$ (in µm). Regarding the X-rays absorption phenomena due to the gases inside the cell, the user can easily calculate the transmittance factor for any gas mixture with THORONDOR, see **Figure 4.4**. In particular, given the working pressure p (in Pa) and the temperature T (in K) of one molecular component of a N-gas mixture, the related $\mathrm{k_g}$ term used in (4.1) is derived, using the following formula:

$$\mathrm{k_g} = \sum_{\mathrm{j=1}}^{\mathrm{N}} \frac{\mathrm{h_j p}\sigma^{\mathrm{abs}}}{\mathrm{k_B T}} \tag{4.3}$$

Where $h_j$ is the stoichiometric index of the $j^{th}$ element composing the molecule, while $k_B$ is the Boltzmann constant. Once recovered, the X-ray transmittances for each gas component are multiplied by their percentual volume fraction, their final product is then equal to the total gas-mixture transmittance. It is worth noting that the described correction is not suitable if the measurement is performed at the energy edge of the elements constituting the gas phase present in the cell.

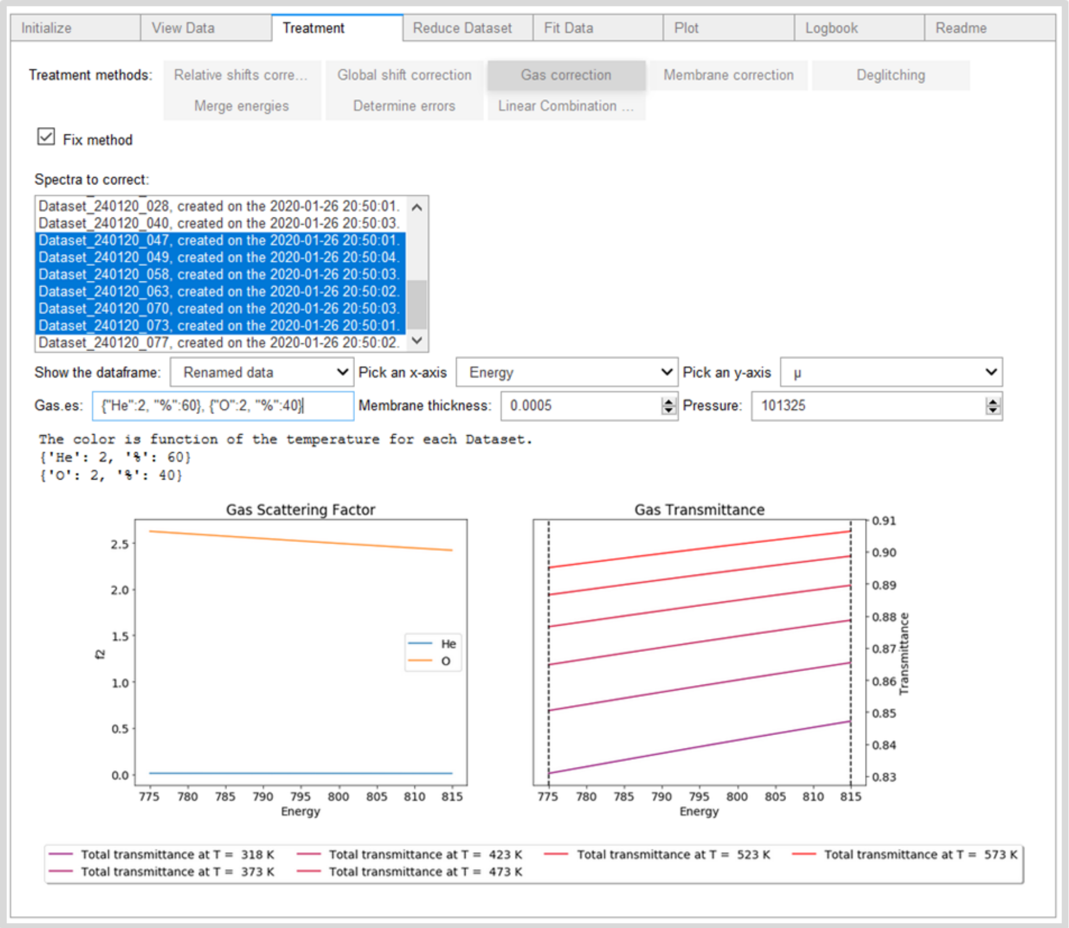

☑ Fix method

Spectra to correct:

Dataset_240120_028, created on the 2020-01-26 20:50:01.
Dataset_240120_040, created on the 2020-01-26 20:50:03.
Dataset_240120_047, created on the 2020-01-26 20:50:01.
Dataset_240120_049, created on the 2020-01-26 20:50:04.
Dataset_240120_058, created on the 2020-01-26 20:50:03.
Dataset_240120_063, created on the 2020-01-26 20:50:02.
Dataset_240120_070, created on the 2020-01-26 20:50:03.
Dataset_240120_073, created on the 2020-01-26 20:50:01.
Dataset_240120_077, created on the 2020-01-26 20:50:02.

Show the dataframe: Renamed data
Pick an x-axis: Energy
Pick an y-axis: μ
Gas.es: {"He":2, "%":60}, {"O":2, "%":40}
Membrane thickness: 0.0005
Pressure: 101325

```
The color is function of the temperature for each Dataset.
{'He': 2, '%': 60}
{'O': 2, '%': 40}
```

**Figure 4.4:** Plot of the gas transmittances calculated for four spectra as a function of the composition (60% He and 40% $O_2$) and of the temperature (showed in K for each scan in the box on the bottom part of the graph). The dashed vertical lines indicate the working energy range where the signal has been acquired (in this case within 775 eV and 815 eV).

### 4.4.3 *Deglitching*

At certain orientations, the diffraction peak being utilized by the monochromator can interfere with multiple reflections associated with another set of crystal planes [33], resulting in a glitch in $I_0$. Thermal (especially at high temperatures) and electrical noise can also cause some spikes in the $I_s$ signal. The presence of glitches can distort some fundamental procedures in the program such as the background subtraction and the spectral normalization [33]. In THORONDOR, it is possible to select, through a single slider, the energy region surrounding a glitch and to replace it with a set of points obtained using a spline interpolating function (linear, quadratic and cubic). This curve is generated considering a user-defined number of points, situated before and after the glitch, as showed in **Figure 4.5**.

☑ Fix method

Select the Dataset: Dataset_230120_007, cre

Show the dataframe: Renamed data

Nb of extra ...: 5

Pick an x-axis Energy

Pick an y-axis μ

Choose an order: Linear

Range (indi... 325 – 340

**Figure 4.5:** Picture of the deglitching module of THORONDOR. Moving the energy slider, it is possible to select a spectral region surrounding the glitch. Through the Deglitch button, these points will be replaced by values extrapolated by a user defined interpolating function (linear, quadratic or cubic).

## 4.5 BACKGROUND SUBTRACTION AND SECOND NORMALIZATION

The background removal procedure for XAS with hard X-rays, in transmission mode (excluding phenomena of self-absorption), is well established and relatively easy. It aims to subtract a pre-edge background contribution $\mu_b$, that is usually approximated by a spline function represented by a Victoreen polynomial curve $p(E; a, b) = aE^{-3} + bE^{-4}$, whose coefficients $(a, b)$ are obtained via least squares methods [21]. Afterwards, the XAS normalization is performed employing the scaling for the edge-step defined by the following formula:

$$\mu_N(E) = \frac{\mu(E) - \mu_b(E)}{\Delta\mu_0} \tag{4.4}$$

Where $\mu(E)$ is the raw XANES spectrum, while the normalization constant $\Delta\mu_0$, showed in (4.4), is the edge-step parameter. This last term is computed as the difference between the pre-edge and post-edge curves (approximated with a spline too), at the absorption edge energy $E_0$. This energy value is usually identified taking the maximum of the first derivative of the XANES spectrum.

The application of the procedure to a NEXAFS spectrum may be problematic in some cases. A limitation of this method can be found when dealing with a spectrum that possess a low ionization potential edge or when two edges are situated at close distances from each other, therefore limiting the pre and post-edge energy ranges used to define the spline functions, see **Figure 4.6**. The estimation of the edge jump will contain, in this case, a larger uncertainty.

Further problems can emerge also if the spectra have been acquired outside the UHV conditions. In particular, the NEXAFS background can increase with the gas absorption of the X-ray beam and, at the same time, some signal features can be distorted if the gas concentration quickly changes during a spectrum acquisition [7].

Beside these particular cases, the problem is caused by the electron detection mode so popular in the soft X-ray range. In fact, for one absorbed photon, n electrons are generated, a number depending from a high number of parameters that are not always constant in the energy range of the spectrum. This effect give rise to slopes that are superimposed to the NEXAFS spectrum (often called background) and that alter the shape of the spectrum thus making difficult the extrapolation of the meaningful information.

THORONDOR offers five different techniques which can be exploited to subtract the NEXAFS background. In the GUI, these methods are indicated as: Splines, Single spline, Polynomial curves, Asymmetric Least Squares and Chebyshev polynomials. The first method, Splines, has been described earlier for hard X-rays. It is recommended only for those spectra which have been acquired in ultra-high vacuum (UHV) or referring to samples with a high concentration of the absorber element. The Single spline method is the fastest to execute and allows a quick visualization of the data quality during an experiment. The last three approaches are suitable for NEXAFS data characterized by a non-linear variation of the background and by an extremely small edge jump, as the ones reported in **Figure 4.6**. Each of these techniques, excluding the Chebyshev polynomials (resulted to be unstable), is described in detail in the following section.

In THORONDOR, for each method, the parameters regulating the generation of the background curves are completely accessible to the user through sliders. In particular, the program allows, for a user-defined energy range, the simultaneous visualization of the original (untreated) spectrum and the background subtracted spectrum on two separated graphic windows. Once defined for a spectrum (e.g. $\mu$) in a first dataset, the same background subtraction parameters can be applied to the other spectra for all the acquired datasets. This is an important feature of THORONDOR that allows the user to define a set of parameters on one dataset, and to then, if satisfactory, to use the same parameters on the other datasets. Thereby quickly correcting the background for all datasets and allowing a quick visualisation of the corrected data.

In case of a NEXAFS signal treated using the Splines method, the second normalization procedure is realised using equation (4.4). For the other cases, the intensity of each NEXAFS point is divided by the total area under the background subtracted curve.

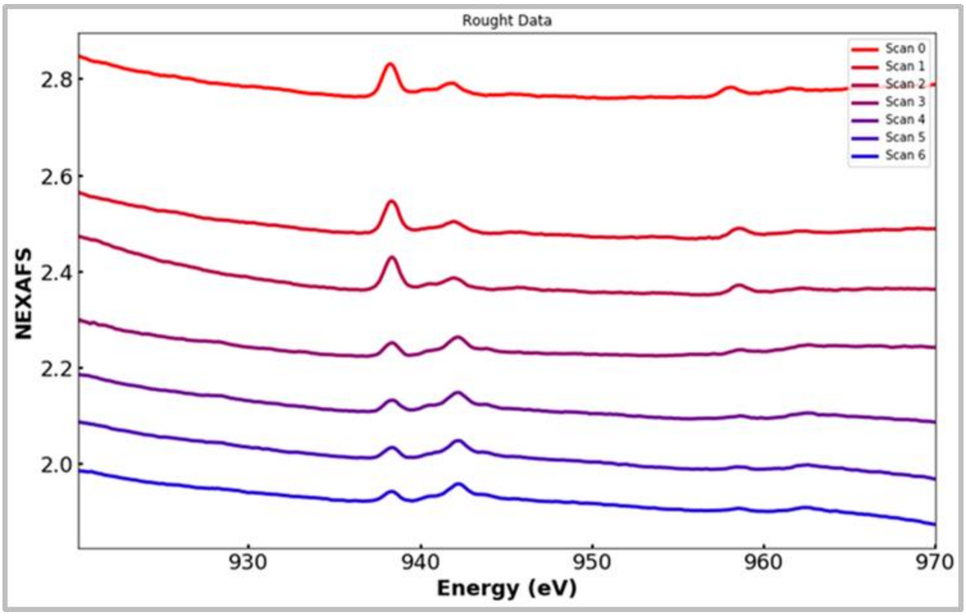

**Figure 4.6:** Plot of seven NEXAFS (μ) scans referring to the Cu $L_2$ and $L_3$ edges acquired during the cooling ramp (from 135 °C to 100 °C) in presence of CO for a Cu-exchanged CHA zeolite (Cu/Al=0.5, Si/Al=15; Cu 2.6 wt%: typical example of diluted absorbing element). It is evident from the graph that the classical background subtraction and normalization procedure typical of the hard-XAS here cannot be applied because of low edges absorption jump and due to non-linear background.

### 4.5.1 *Splines method*

The first step of this technique consists in the identification of the absorption energy edge ($\mathrm{E}_0$) for the spectrum under analysis. This is done, in the program, by calculating the first order derivative of the NEXAFS spectrum and taking the energy value of its maximum. The selection of the maximum of the derivative is done automatically by the program. However, the user has the possibility, through a cursor, to select a specific point of the derivative curve and to save the related energy value as $\mathrm{E}_0$. Once that the value of the edge energy position has been defined, the user can start to manipulate two sliders controlling the number of energy points situated, respectively, in the pre-edge and post-edge part of the NEXAFS spectrum. These two set of points are used to define the pre-edge and post-edge spline functions which are subsequently employed to remove the background and normalize the spectrum in accordance to equation (4.4). THORONDOR offers also different kind of interpolating functions which can be used instead of the classical splines introduced in **4.5**. These include linear, quadratic and cubic polynomial models realised exploiting the numpy.polyfit method [30]. An example where this method is applied with success is showed in **Figure 4.7**.

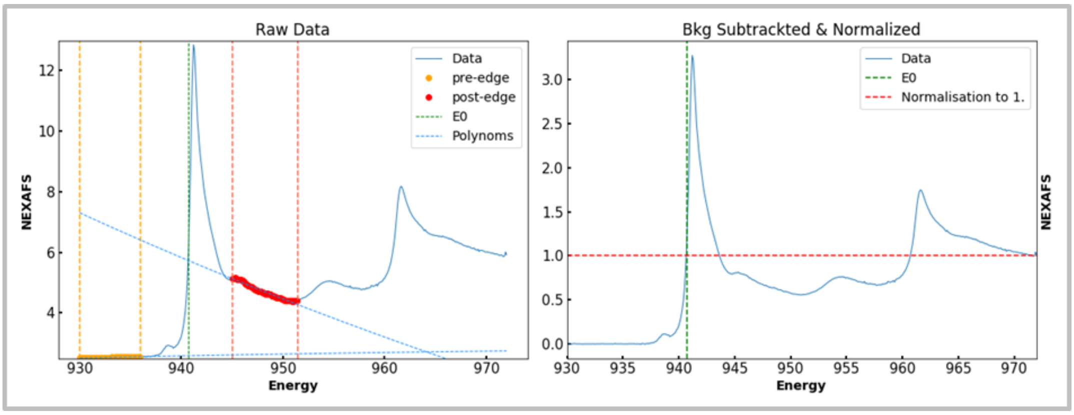

**Figure 4.7:** Cu $L_3$ and $L_2$ edge NEXAFS spectra for $Cu_2O$ (representative example of highly concentrated absorbing element), before (left panel) and after (right panel) the background subtraction and normalization provided by the splines method. The yellow and red vertical lines and the colour-related points indicate the selected pre-edge and post-edge regions, respectively. The green dashed line denotes in both graphs the position of the energy position of the absorption edge ($E_0$).

### 4.5.2 *Single Spline method*

This method can be used as an alternative normalization procedure for a NEXAFS spectrum whose background has been subtracted with the same kind of interpolating curves (splines or polynomials) employed in the Splines method described in section **4.5.1**. Through a single slider, the user can select the number of points situated in the pre-edge of the NEXAFS spectrum. Once this step is completed, this range of points is fitted by a spline or a polynomial function, which is subsequently subtracted to the raw NEXAFS spectrum. Contrary to the classic Splines method, which foresees the edge-step normalization, this procedure is realised by scaling the background subtracted NEXAFS spectrum to the magnitude of a point in the curve (e.g. the maximum peak intensity of the NEXAFS white-line (W.L.) or a point corresponding to the maximum value of the energy range [35]), which is selected through the usage of a proper slider. A demonstrative representation of this approach is showed in **Figure 4.8**.

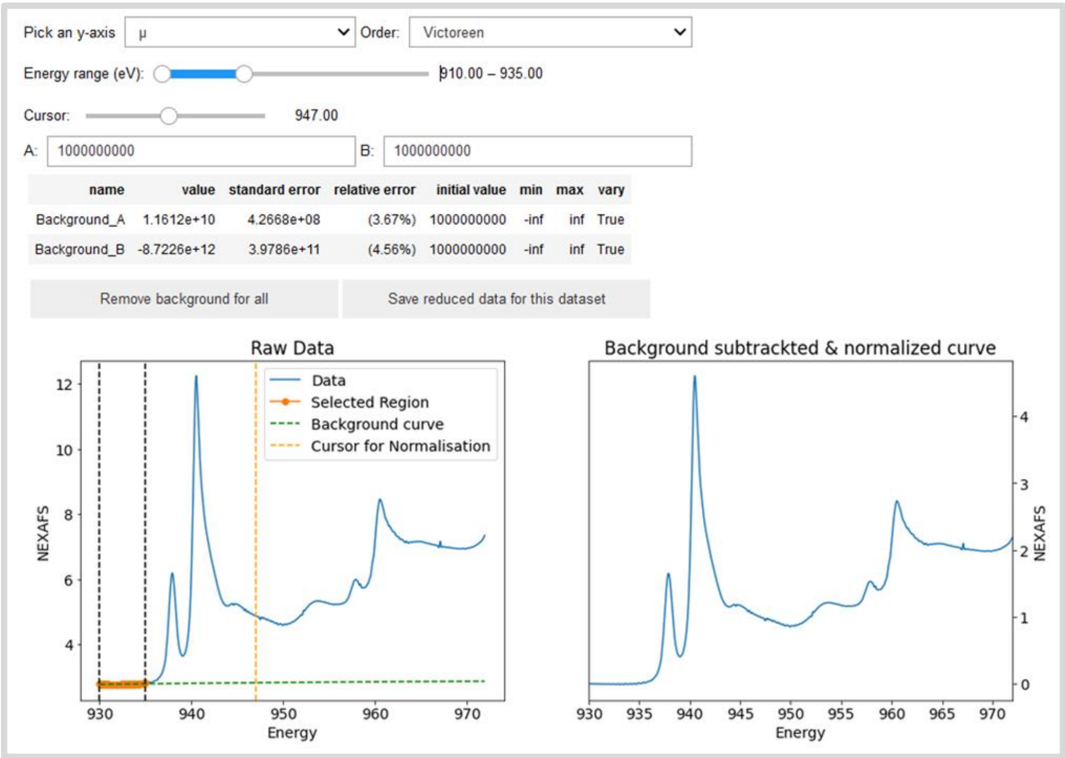
Pick an y-axis μ
Order: Victoreen
Energy range (eV): 910.00 – 935.00
Cursor: 947.00
A: 1000000000
B: 1000000000

| name | value | standard error | relative error | initial value | min | max | vary |
|---|---|---|---|---|---|---|---|
| Background_A | 1.1612e+10 | 4.2668e+08 | (3.67%) | 1000000000 | -inf | inf | True |
| Background_B | -8.7226e+12 | 3.9786e+11 | (4.56%) | 1000000000 | -inf | inf | True |

**Figure 4.8:** Sketch of the THORONDOR single spline method tab window. The orange points enclosed within the two dashed black vertical lines represent the NEXAFS values in the pre-edge employed to generate the green spline curve, which is then subtracted to the experimental spectrum. The vertical orange dashed curve identifies a NEXAFS point whose intensity is used to scale the entire NEXAFS spectrum.

### 4.5.3 *Polynomial curves method*

Given an experimental spectrum, a background curve is generated based on a determined number of points $\mu(E_i)$ belonging to the NEXAFS signal. The amounts of points and position in energy are user defined. Through sliders, the user can distribute them along the entire spectrum selecting specific energy positions which are not characterized by real spectral features but uniquely by the signal background (e.g. some region of the spectrum without any peak), see **Figure 4.9**. Once that this step is completed, the related background function, consisting in a third order spline, is generated, using the splrep method of the SciPy package [36], and directly subtracted to the raw data.

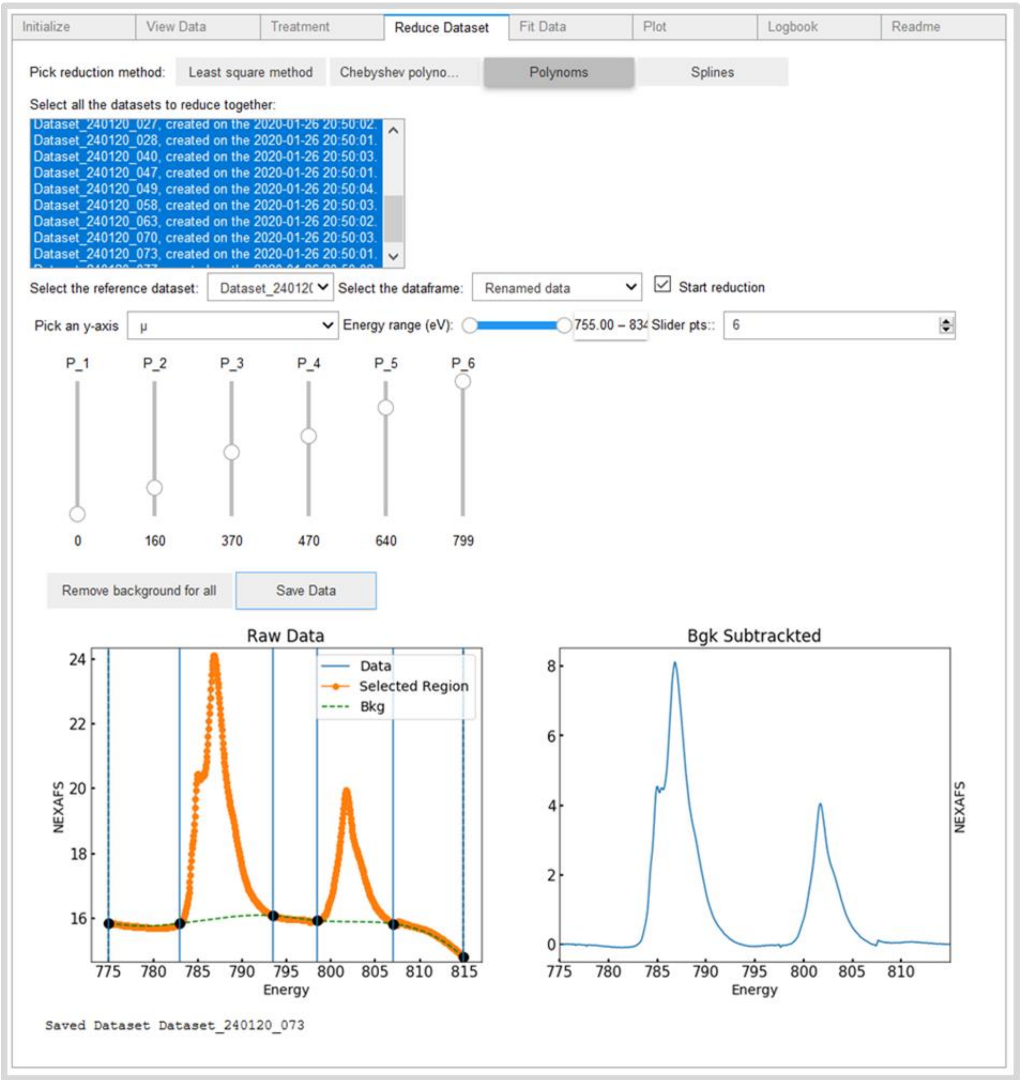

Pick reduction method: Polynoms

Select all the datasets to reduce together:

Dataset_240120_027, created on the 2020-01-26 20:50:02.
Dataset_240120_028, created on the 2020-01-26 20:50:01.
Dataset_240120_040, created on the 2020-01-26 20:50:03.
Dataset_240120_047, created on the 2020-01-26 20:50:01.
Dataset_240120_049, created on the 2020-01-26 20:50:04.
Dataset_240120_058, created on the 2020-01-26 20:50:03.
Dataset_240120_063, created on the 2020-01-26 20:50:02.
Dataset_240120_070, created on the 2020-01-26 20:50:03.
Dataset_240120_073, created on the 2020-01-26 20:50:01.

Select the reference dataset: Dataset_24012(
Select the dataframe: Renamed data
☑ Start reduction
Pick an y-axis μ
Energy range (eV): 755.00 – 834
Slider pts:: 6

```
Saved Dataset Dataset_240120_073
```

**Figure 4.9:** Application of the polynomial curves method to remove the background from a representative NEXAFS spectrum at Co L-edge (orange points, left panel) containing both the $L_2$ and $L_3$ edges. After having selected the working energy range and the number of spectral points needed to generate the background function, the user can move them along the spectral profile through sliders while simultaneously observing their effect on the background subtracted spectrum (blue curve, right panel).

### 4.5.4 *Asymmetric Least Squares method*

Among all the approaches, the Asymmetric Least Squares method has proven to be the fastest and most accurate. This baseline subtraction approach was introduced by Eilers and Boelens and it has been extensively used in the field of Raman spectroscopy [37, 38]. It exploits an asymmetric least squares (AsLS) method. The method aims at fitting a smooth background $f$ to an experimental spectrum $\mu(E)$. To do so, it is necessary to minimize the following objective function:

$$\underset{f}{\operatorname{argmin}}\left\{\sum_{i=1}^{N} w_i(\mu(E_i) - f_i) + \lambda \sum_{i=1}^{N} (\Delta^2 f_i)^2\right\} \tag{4.5}$$

The first term of equation (4.5) expresses the fitness to the data while the second one is related to the smoothness of $f$. Herein $\mu(E_i)$ and $f_i$ are respectively the $i^{th}$ value of the experimental NEXAFS spectrum ($\mu$ having $N$ values) and the smoothed function $f$ evaluated at the $i^{th}$ energy point. The $\Delta^2 f_i$ term is a difference operator defined as: $\Delta^2 f_i = (f_i - f_{i-1}) - (f_{i-1} - f_{i-2}) = f_i - 2f_{i-1} + f_{i-2}$, $\lambda$ is a regularization parameter while $w_i$ represents a set of weights chosen asymmetrically: $w_i = p$ if $\mu(E_i) > f_i$ and $w_i = 1 - p$ otherwise. In THORONDOR, the user can have direct access to $\lambda$ and $p$ and consequently move them in the recommended ranges within $10^7 - 10^9$ for $\lambda$ and $0.001 - 0.1$ for $p$ [37]. Once that the parameters have been chosen, the background function is automatically generated and subtracted to the experimental spectrum. The THORONDOR tab window designed for this approach is reported in **Figure 4.10**.

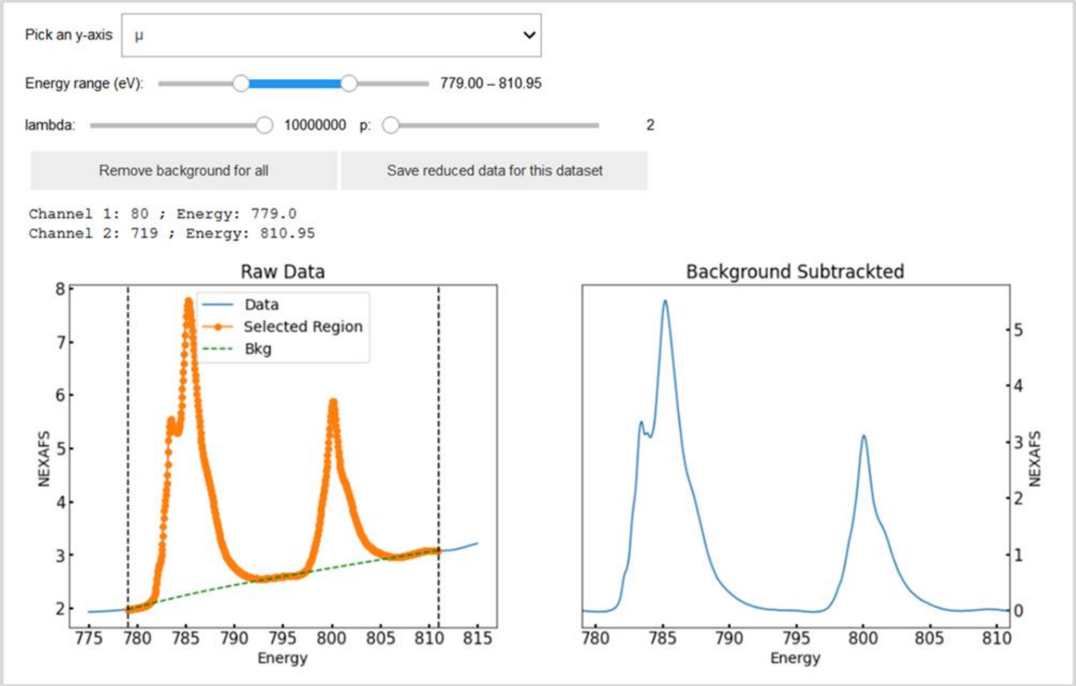

Pick an y-axis μ

Energy range (eV): 779.00 – 810.95

lambda: 10000000 p: 2

```
Channel 1: 80 ; Energy: 779.0
Channel 2: 719 ; Energy: 810.95
```

**Figure 4.10:** Application of the asymmetric least squares method to remove the background from a representative region of a NEXAFS spectrum, corresponding to the Co L-edge (orange points, left panel), containing both the $L_2$ and $L_3$ edges. The parameters lambda and p, controlled by sliders, are the ones appearing in equation (5) and modify directly the shape of the background subtracting curve.

## 4.6 PEAK FITTING

Once that the data treatment procedure (described in **section 4.4)** is completed**,** a NEXAFS spectrum can be further processed using the THORONDOR peak-fitting toolbox.

In general, a NEXAFS spectrum is always characterized by resonances corresponding to different transitions from an occupied core state to an unfilled final state [24]. These resonances can be usually modelled as peak shapes, properly reproduced by Lorentzian peak-functions [6, 32, 39, 40]. The procedure of peak decomposition becomes extremely important when someone wants to decompose a NEXAFS spectrum into a set of peaks where each of them can be assigned to an existing and physically reasonable electronic transition. Finally, spectral energy shifts for a set of scans can be recovered from the fitting procedure too. They correspond to inflection points in the absorption edge step function (i.e. the maximum of their first derivatives). The evaluation of these quantities is extremely important because they properly indicate the presence of reduction or oxidation phenomena involving the absorber atoms in the system under study.

THORONDOR offers a large class of peak functions including Gaussian, Lorentzian, Voigt and pseudo-Voigt profiles. The signal absorption edge step can be properly modelled using an arc-tangent function [41] as well as an error function, which have been proven to be suitable for this usage too [40, 42]. In general, the user should pick a step-function according to his knowledge prior to the fitting, since it has been shown that the width of the error function is related to the instrumental resolution [42], whereas the width of the arc-tangent is connected with the life-time of the excited state. The step localization depends on the quality of the spectrum, usually several eV below the core level ionization energy [42]. Sometimes, the background in the pre-edge can slightly differ from the step function due to features linked to transition to the bound states in the system [39]. In THORONDOR, if one wishes to focus on that energy range, it is possible to use splines of different order to fit the baseline for those energy values and then pass to fit and normalize the pre-edge peaks [43].

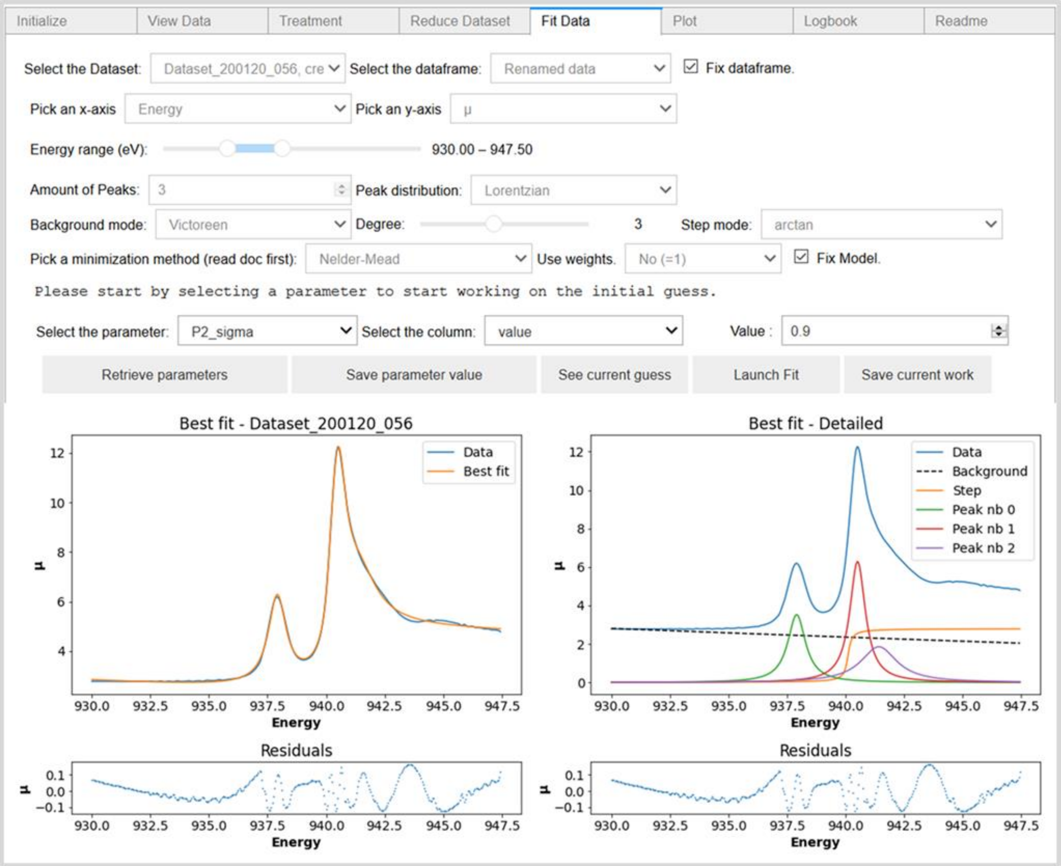

Select the Dataset: Dataset_200120_056, cre
Select the dataframe: Renamed data
☑ Fix dataframe.
Pick an x-axis: Energy
Pick an y-axis: μ
Energy range (eV): 930.00 – 947.50
Amount of Peaks: 3
Peak distribution: Lorentzian
Background mode: Victoreen
Degree: 3
Step mode: arctan
Pick a minimization method (read doc first): Nelder-Mead
Use weights: No (=1)
☑ Fix Model.

```
Please start by selecting a parameter to start working on the initial guess.
```

Select the parameter: P2_sigma
Select the column: value
Value : 0.9

**Figure 4.11:** Screenshot of the THORONDOR peak-fitting toolbox. In the graph on the left is reported the comparison between the experimental spectrum and the best fit referring to a $Cu_2O$ sample, while on the right are showed all the optimized profiles. The associated R-factor, quantifying the misfit among the experiment and the best fit is $R^2_{IXS}(\%) = 0.15\%$.

In THORONDOR, the parameters associated with the peak and step profiles (i.e. the number of peaks and their energy position, their FWHM, the peak function amplitudes, the number of step functions and their slopes …) are defined by the user via cursors and text-boxes, see **Figure 4.11**. After the definition of a fitting model, the user needs to provide an initial guess to initialise the fitting routine. The sum of all the user-defined functions with the current guess for the parameters is plotted along the experimental spectrum by clicking on the button *See current guess*. Therefore, by tuning the initial guess, the user can visualise the agreement between the experimental curve and the reconstructed one. Once that this step is performed, the user-defined parameters are employed to initialize the fitting routine.

The fitting routine is based on the minimization of a square residual objective function Ξ, defined as:

$$\Xi(\mathbf{p}) = \sum_{i=1}^{N} \frac{(\mu^{\mathrm{exp}}(E_i) - \mu^{\mathrm{theo}}(E_i, \mathbf{p}))^2}{\varepsilon_i^2} \tag{4.6}$$

Where $\mathbf{p} = (p_1, \dots, p_M)$ is the set of $M$ parameters characterizing the selected peak and step functions, N is the number of the energy points, $\mu^{exp}(E_i)$ and $\mu^{theo}(E_i, \mathbf{p})$ are respectively the i<sup>th</sup> value of the experimental and the theoretical spectrum, while $\varepsilon_i$ is the uncertainty weighting related to the i<sup>th</sup> experimental point. Equation (4.6) assumes that the experimental signal is only affected by random Gaussian noise with standard deviation equal to $\varepsilon_i$ around the true signal [18].

Thanks to the use of the lmfit packaged [44], THORONDOR provides different minimizations algorithm that can be applied to minimize equation (4.6). In particular, the Levenberg-Marquardt algorithm [45] is recommended for the fitting procedure if the user decides to start the analysis with a good initial guess. Indeed, this method is quite fast and converges quickly towards a local minimum. If the fitting routine does not succeed, some additional algorithms are provided, such as the Nelder-Mead method [46] which has been demonstrated to be more robust than the precedent one [44].

### 4.6.1 *Estimating the experimental uncertainties*

As it is possible to see from (4.6), the definition of $\Xi$ requires the evaluation of the experimental errors $\varepsilon_i$. If these are not provided by the user, THORONDOR offers three different alternatives.

The first procedure has been inspired by the work by Dent et al. [47] and it is employed in the GNXAS software to estimate the error associated to an experimental EXAFS spectrum [18].The second method simply uses the errors from the user, imported along with the data, as uncertainty weights for equation (4.6). Finally, in case the errors provided by the first method seem under- or over-estimated and if the user is unable to quantify the uncertainty on the measure, the errors can either be equalled to the inverse of the background subtracted data or to one, resulting in a non-weighted fitting routine for the latter.

### 4.6.2 *Evaluation of the goodness of a fit*

Mismatch between data and fit can be measured in a number of ways [33]. One of the common methods implemented in THORONDOR is the XAFS R-factor. Similarly to the one showed for the EXAFS analysis in of **chapter 1**, it is defined as:

$$R^2_{IXS}(\%) = 100 \times \frac{\sum_{i=1}^{N}\left(\mu^{exp}(E_i) - \mu^{theo}(E_i, \mathbf{p})\right)^2}{\sum_{i=1}^{N}(\mu^{exp}(E_i)^2)} \tag{4.7}$$

In the hypothesis that the S/N ratio of the data is good, the $R^2_{IXS}(\%)$ of an adequate fit can be expected to be in the order of few percent [33, 48].

Because of the presence of M parameters in the fit, the quantity $\Xi(p_1^0, \dots, p_M^0)$, where the vector $\mathbf{p}^0 = (p_1^0, \dots, p_M^0)$ is the minimum value of (4.6), can be interpreted by a $\chi^2_{N-M}$ random variable. Thus, the statistical $\chi^2$ test can be performed in THORONDOR to check if the actual value of $\Xi(p_1^0, \dots, p_M^0)$ is only due to the residual noise or otherwise it contains unexplained physical information [18].

### 4.6.3 *Finding uncertainties in fitted parameters*

In THORONDOR, the parameter uncertainties retrieved by the fitting procedure can be estimated in different ways. In general, this is done by inverting the Hessian matrix of (4.6) determining the related covariance matrix, whose diagonal elements are the squared parameters errors [49]. However, sometimes the uncertainties cannot be estimated, which generally indicates that Hessian matrix cannot be properly inverted because the fit is not actually sensitive to one of the variables that must be optimized. Moreover, as already introduced in **section 4.6**, the standard errors computation assume that the residuals follow a normal distribution with mean equal to zero, and that a map of probability distributions for pairs of parameters would be elliptical (the size of the ellipse gives the uncertainty while the eccentricity the correlation) [44, 50]. The validity of the uncertainty estimation can be discussed since it ignores outliers, highly asymmetric uncertainties, or complex correlations between the estimated parameters. Nevertheless, the results that yield from this estimation are usually pretty good when it is possible to determine them, which is usually the case if one starts the algorithm with an initial guess close enough to a local minimum.

A more detailed investigation of the probability distribution of the parameters can be performed a posteriori via the *emcee* Markov Chain Monte Carlo package [51] (version 3 or superior) by exploring the parameter space. This additional step is recommended, especially if the estimation of the covariance matrix fails, roadblocks can be present with models composed of numerous parameters and bounds or constraints. Hence, one can estimate the uncertainties and find the correlations between pairs of parameters. A corner plot can be drawn using the corner package [52].

As described before, in THORONDOR, confidence intervals are determined in both methods providing a clear idea of the uncertainties associated to each parameter. Overall, the fitting module of THORONDOR allows one to quickly fit specific features or entire spectra using different approaches and many degrees of freedom, without neglecting the statistical analysis of the fit quality.

## 4.7 REFERENCES

[1] D.H. Simonne, A. Martini, M. Signorile, A. Piovano, L. Braglia, P. Torelli, E. Borfecchia, G. Ricchiardi, THORONDOR: a software for fast treatment and analysis of low-energy XAS data, J. Synchrot. Radiat., 27 (2020).

[2] L. Mino, G. Agostini, E. Borfecchia, D. Gianolio, A. Piovano, E. Gallo, C. Lamberti, Low-dimensional systems investigated by x-ray absorption spectroscopy: a selection of 2D, 1D and 0D cases, J. Phys. D-Appl. Phys., 46 (2013) 72.

[3] A.A. Guda, S.A. Guda, K.A. Lomachenko, M.A. Soldatov, I.A. Pankin, A.V. Soldatov, L. Braglia, A.L. Bugaev, A. Martini, M. Signorile, E. Groppo, A. Piovano, E. Borfecchia, C. Lamberti, Quantitative structural determination of active sites from in situ and operando XANES spectra: From standard ab initio simulations to chemometric and machine learning approaches, Catal. Today, 336 (2019) 3-21.

[4] B. Lassalle-Kaiser, S. Gul, J. Kern, V.K. Yachandra, J. Yano, In situ/Operando studies of electrocatalysts using hard X-ray spectroscopy, J. Electron Spectrosc. Relat. Phenom., 221 (2017) 18-27.

[5] Y. Tamenori, Electron yield soft X-ray photoabsorption spectroscopy under normal ambient-pressure conditions, J. Synchrot. Radiat., 20 (2013) 419-425.

[6] J. Stöhr, NEXAFS Spectroscopy, Springer-Verlag Berlin Heidelberg, Verlag Berlin Heidelberg, 1992.

[7] C. Castan-Guerrero, D. Krizmancic, V. Bonanni, R. Edla, A. Deluisa, F. Salvador, G. Rossi, G. Panaccione, P. Torelli, A reaction cell for ambient pressure soft x-ray absorption spectroscopy, Rev. Sci. Instrum., 89 (2018) 8.
[8] C. Escudero, P. Jiang, E. Pach, F. Borondics, M.W. West, A. Tuxen, M. Chintapalli, S. Carenco, J.H. Guo, M. Salmeron, A reaction cell with sample laser heating for in situ soft X-ray absorption spectroscopy studies under environmental conditions, J. Synchrot. Radiat., 20 (2013) 504-508.
[9] M. Blum, L. Weinhardt, O. Fuchs, M. Bar, Y. Zhang, M. Weigand, S. Krause, S. Pookpanratana, T. Hofmann, W. Yang, J.D. Denlinger, E. Umbach, C. Heske, Solid and liquid spectroscopic analysis (SALSA)-a soft x-ray spectroscopy endstation with a novel flow-through liquid cell, Rev. Sci. Instrum., 80 (2009) 6.
[10] J. Forsberg, L.C. Duda, A. Olsson, T. Schmitt, J. Andersson, J. Nordgren, J. Hedberg, C. Leygraf, T. Aastrup, D. Wallinder, J.H. Guo, System for in situ studies of atmospheric corrosion of metal films using soft x-ray spectroscopy and quartz crystal microbalance, Rev. Sci. Instrum., 78 (2007) 7.
[11] O. Fuchs, F. Maier, L. Weinhardt, M. Weigand, M. Blum, M. Zharnikovc, J. Denlinger, M. Grunze, C. Heske, E. Umbach, A liquid flow cell to study the electronic structure of liquids with soft X-rays, Nucl. Instrum. Methods Phys. Res. Sect. A-Accel. Spectrom. Dect. Assoc. Equip., 585 (2008) 172-177.
[12] J.H. Guo, Y. Luo, Molecular structure in water and solutions studied by photon-in/photon-out soft X-ray spectroscopy, J. Electron Spectrosc. Relat. Phenom., 177 (2010) 181-191.
[13] M. Havecker, A. Knop-Gericke, T. Schedel-Niedrig, High-pressure soft X-ray absorption spectroscopy: application of a new in situ spectroscopic method in catalysis research, Appl. Surf. Sci., 142 (1999) 438-442.
[14] A. Knop-Gericke, M. Havecker, T. Neisius, T. Schedel-Niedrig, New experimental technique: X-ray absorption spectroscopy detector for in situ studies in the soft X-ray range (250eV <= hv <= 1000eV) under reaction conditions, Nucl. Instrum. Methods Phys. Res. Sect. A-Accel. Spectrom. Dect. Assoc. Equip., 406 (1998) 311-322.
[15] T. Tokushima, Y. Horikawa, Y. Harada, O. Takahashi, A. Hiraya, S. Shin, Selective observation of the two oxygen atoms at different sites in the carboxyl group (-COOH) of liquid acetic acid, Phys. Chem. Chem. Phys., 11 (2009) 1679-1682.
[16] F. Zheng, S. Alayoglu, J.H. Guo, V. Pushkarev, Y.M. Li, P.A. Glans, J.L. Chen, G. Somorjai, In-situ X-ray Absorption Study of Evolution of Oxidation States and Structure of Cobalt in Co and CoPt Bimetallic Nanoparticles (4 nm) under Reducing (H-2) and Oxidizing (O-2) Environments, Nano Lett., 11 (2011) 847-853.
[17] S.K. Beaumont, Soft XAS as an in situ technique for the study of heterogeneous catalysts, Phys. Chem. Chem. Phys., (2020).
[18] A. Filipponi, A. DiCicco, X-ray-absorption spectroscopy and n-body distribution functions in condensed matter .2. Data analysis and applications, Phys. Rev. B, 52 (1995) 15135-15149.
[19] K. Hatada, F. Iesari, L. Properzi, M. Minicucci, A. Di Cicco, Iop, New Graphical User Interface for EXAFS analysis with the GNXAS suite of programs, in: 16th International Conference on X-Ray Absorption Fine Structure, Iop Publishing Ltd, Bristol, 2016.

[20] B. Ravel, M. Newville, ATHENA, ARTEMIS, HEPHAESTUS: data analysis for X-ray absorption spectroscopy using IFEFFIT, J. Synchrot. Radiat., 12 (2005) 537-541.

[21] K.V. Klementev, Extraction of the fine structure from x-ray absorption spectra, J. Phys. D-Appl. Phys., 34 (2001) 209-217.

[22] A. Kuzmin, EDA - EXAFS DATA-ANALYSIS SOFTWARE PACKAGE, Physica B, 208 (1995) 175-176.

[23] S.M. Webb, SIXpack: a graphical user interface for XAS analysis using IFEFFIT, Phys. Scr., T115 (2005) 1011-1014.

[24] E. Gann, C.R. McNeill, A. Tadich, B.C.C. Cowie, L. Thomsen, Quick AS NEXAFS Tool (QANT): a program for NEXAFS loading and analysis developed at the Australian Synchrotron, J. Synchrot. Radiat., 23 (2016) 374-380.

[25] M.U. Delgado-Jaime, C.P. Mewis, P. Kennepohl, Blueprint XAS: a Matlab-based toolbox for the fitting and analysis of XAS spectra, J. Synchrot. Radiat., 17 (2010) 132-137.

[26] B. Watts, Calculation of the Kramers-Kronig transform of X-ray spectra by a piecewise Laurent polynomial method, Opt. Express, 22 (2014) 23628-23639.

[27] A. Martini, S.A. Guda, A.A. Guda, G. Smolentsev, A. Algasov, O. Usoltsev, M.A. Soldatov, A. Bugaev, Y. Rusalev, C. Lamberti, A.V. Soldatov, PyFitit: The software for quantitative analysis of XANES spectra using machine-learning algorithms, Comput. Phys. Commun., 250 (2020) 15.

[28] M. Konnecke, F.A. Akeroyd, H.J. Bernstein, A.S. Brewster, S.I. Campbell, B. Clausen, S. Cottrell, J.U. Hoffmann, P.R. Jemian, D. Mannicke, R. Osborn, P.F. Peterson, T. Richter, J. Suzuki, B. Watts, E. Wintersberger, J. Wuttke, The NeXus data format, J. Appl. Crystallogr., 48 (2015) 301-305.

[29] W. McKinney, Data Structures for Statistical Computing in Python, in: Proceedings of the 9th Python in Science Conference, Stèfan van der Walt and Jarrod Millman 2010, pp. 51 - 56.

[30] T.E. Oliphant, A guide to NumPy, Trelgol Publishing USA, 2006.

[31] F.a.G. Perez, B. E., IPython: A System for Interactive Scientific Computing, Computing in Science Engineering, 9 (2007) 21-27.

[32] B. Watts, L. Thomsen, P.C. Dastoor, Methods in carbon K-edge NEXAFS: Experiment and analysis, J. Electron Spectrosc. Relat. Phenom., 151 (2006) 105-120.

[33] S. Calvin, XAFS for Everyone, 2013.

[34] B.L. Henke, E.M. Gullikson, J.C. Davis, X-RAY INTERACTIONS - PHOTOABSORPTION, SCATTERING, TRANSMISSION AND REFLECTION AT E=50-30,000 EV, Z=1-92 (VOL 54, PG 181, 1993), Atom. Data Nucl. Data Tables, 55 (1993) 349-349.

[35] M.F. Qayyum, R. Sarangi, K. Fujisawa, T.D.P. Stack, K.D. Karlin, K.O. Hodgson, B. Hedman, E.I. Solomon, L-Edge X-ray Absorption Spectroscopy and DFT Calculations on Cu2O2 Species: Direct Electrophilic Aromatic Attack by Side-on Peroxo Bridged Dicopper(II) Complexes, J. Am. Chem. Soc., 135 (2013) 17417-17431.

[36] P.a.o. Virtanen, SciPy 1.0: fundamental algorithms for scientific computing in Python, Nat. Methods, (2020) 15.

[37] S.J. Baek, A. Park, Y.J. Ahn, J. Choo, Baseline correction using asymmetrically reweighted penalized least squares smoothing, Analyst, 140 (2015) 250-257.
[38] P.H.C. Eilers, A perfect smoother, Anal. Chem., 75 (2003) 3631-3636.
[39] F. de Groot, Multiplet effects in X-ray spectroscopy, Coord. Chem. Rev., 249 (2005) 31-63.
[40] G.S. Henderson, F.M.F. de Groot, B.J.A. Moulton, X-ray Absorption Near-Edge Structure (XANES) Spectroscopy, in: G.S. Henderson, D.R. Neuville, R.T. Downs (Eds.) Spectroscopic Methods in Mineralology and Materials Sciences, Mineralogical Soc Amer & Geochemical Soc, Chantilly, 2014, pp. 75-+.
[41] B.T. Poe, C. Romano, G. Henderson, Raman and XANES spectroscopy of permanently densified vitreous silica, J. Non-Cryst. Solids, 341 (2004) 162-169.
[42] D.A. Outka, J. Stohr, CURVE FITTING ANALYSIS OF NEAR-EDGE CORE EXCITATION-SPECTRA OF FREE, ADSORBED, AND POLYMERIC MOLECULES, J. Chem. Phys., 88 (1988) 3539-3554.
[43] M. Wilke, F. Farges, P.E. Petit, G.E. Brown, F. Martin, Oxidation state and coordination of Fe in minerals: An FeK-XANES spectroscopic study, Am. Miner., 86 (2001) 714-730.
[44] M. Newville, Stensitzki, Till, Allen, Daniel B., & Ingargiola, Antonino., LMFIT: Non-Linear Least-Square Minimization and Curve-Fitting for Python (Version 0.8.0). Zenodo, (2014).
[45] J.J. Moré, The Levenberg-Marquardt algorithm: Implementation and theory, in: G.A. Watson (Ed.) Numerical Analysis, Springer Berlin Heidelberg, Berlin, Heidelberg, 1978, pp. 105-116.
[46] J.A. Nelder, R. Mead, A Simplex Method for Function Minimization, The Computer Journal, 7 (1965) 308-313.
[47] A.J. Dent, P.C. Stephenson, G.N. Greaves, The Extraction of signal to noise values in X-Ray Absorption-Spectroscopy, Rev. Sci. Instrum., 63 (1992) 856-858.
[48] I.S.a.C. Committee, Error Reporting Recommendations: A Report of the Standards and Criteria Committee, in, 2000.
[49] G. Bunker, Introduction to XAFS: A Practical Guide to X-ray Absorption Fine Structure Spectroscopy, Cambridge University Press, Cambridge, 2010.
[50] P.R.a.R. Bevington, D. Keith, Data reduction and error analysis for the physical sciences, 3rd ed. ed., McGraw-Hill, New York, NY, 2003.
[51] D. Foreman-Mackey, D.W. Hogg, D. Lang, J. Goodman, emcee: The MCMC Hammer, Publ. Astron. Soc. Pac., 125 (2013) 306-312.
[52] D. Foreman-Mackey, corner.py: Scatterplot matrices in Python, The Journal of Open Source Software, 1 (2016).

# 5 INVESTIGATING BY XAS THE ACTIVE SITES FOR THE DIRECT CONVERSION OF METHANE TO METHANOL OVER CU-EXCHANGED ZEOLITES

Methanol is one of the most important *building block* in the chemical industry. It is widely employed as a fuel, it can be converted into many added-value products like dimethyl-ether, and it represents a chemical feedstock to produce ethylene, acetic acid, formaldehyde and olefins. Furthermore, it is used as a solvent for the extraction of bioactive compounds or for water treatment to reduce environmentally damaging effluents [1-5]. Commercially, it has been obtained, for a long time, using Cu/Zn oxide/alumina catalysts leading its synthesis from syngas: a mixture of carbon monoxide and hydrogen [6]. This process requires both elevated temperatures and pressures and the syngas is required to be synthetized beforehand from different sources (e.g. natural gas, coal, biomass and hydrocarbons). More recently there has been a great deal of interest in developing some more direct and energy-efficient methods to produce methanol either from hydrogenation of carbon dioxide or directly from methane [6]. Methane, in particular, is emitted from a great variety of natural and anthropogenic sources as a result of the anaerobic decomposition of organic matter, land-use alteration and fossil-fuel related emissions [7].

However, the conversion of methane to methanol presents a considerable challenge. Methane is, in fact, a highly stable molecule difficult to activate, due to its low electron and proton affinity, low polarity, high ionization energy and strong C-H bond (439 $kJ\cdot mol^{-1}$) [8]. The latter can be kinetically and thermodynamically activated by oxidation. However, the C-H bond in methanol appears to be ca. 47 $kJ\cdot mol^{-1}$, implying that its over-oxidation in carbon monoxide and dioxide is favoured under the reaction conditions for the methane activation. Finally, also from a kinetic point of view, the methane oxidation in methanol and dimethyl-ether (which is another relevant product of the partial oxidation of methane) is slower than the reactions that may subsequently lead to the over-oxidation of the methanol, see **Table 5.1**.

| Possible Cu redox routes to products | | |
|---|---|---|
| $[Cu(II)\text{-}O\text{-}Cu(II)]^{2+}+CH_4\rightarrow[Cu(I)\text{-}(OCH_3)\text{-}Cu(I)]^{+}+H^{+}$ | methanol | Selective Oxidation |
| $2[Cu(I)\text{-}(OCH_3)\text{-}Cu(I)]^{+}+2H^{+}\rightarrow CH_3\text{-}O\text{-}CH_3+4[Cu(I)]^{+}+H_2O$ | dimethyl-ether | |
| $[Cu(I)\text{-}(OCH_3)\text{-}Cu(I)]^{+}+2[Cu(II)\text{-}O\text{-}Cu(II)]^{2+}\rightarrow[HCOO]^{-}+6[Cu(I)]^{+}+H_2O$ | formate | Over Oxidation |
| $[Cu(I)\text{-}(OCH_3)\text{-}Cu(I)]^{+}+2[Cu(II)\text{-}O\text{-}Cu(II)]^{2+}\rightarrow CO+6[Cu(I)]^{+}+2H_2O$ | carbon monoxide | |
| $[Cu(I)\text{-}(OCH_3)\text{-}Cu(I)]^{+}+2[Cu(II)\text{-}O\text{-}Cu(II)]^{2+}\rightarrow CO_2+3[Cu(I)]^{+}$ | carbon dioxide | |

**Table 5.1:** Notional description on how methane may be converted to both selective and unselective oxidation products. Adapted from [6].

One promising pathway for the direct conversion of methane to methanol (DMTM) can be realised *via* the partial oxidation of methane over metal-containing zeolite catalysts, which appear to mimic the methane oxidation process realised by certain enzymes founded upon Cu and Fe centers (i.e. the methane monoxygenases) [9, 10]. Zeolites are microporous crystalline aluminosilicates of natural or synthetic origin with highly ordered structures. Structurally, zeolites are constituted by $TO_4$ tetrahedral units ($T = Si^{4+}$, $Al^{3+}$) which are linked to each other by shared oxygen atoms to give a three-dimensional network which can assume various topologies. This framework structure is relatively open and characterized by the presence of channels and cavities. In the literature, the Si/Al ratio ranges from a minimum of 1 (where the Si and Al atoms are in strict alternation) till to infinity. Most of the systems with channels contain rings with even number of T sites, for example: 6, 8, 10, 12 and 14 rings. Due to the four oxygen bonds, the $Al^{3+}$ site induces a net negative charge to the framework, which can be compensated by an extra framework cation. The latter can be simply a proton ($H^+$) or a metal site such as Cu that is hosted inside the zeolite rings and coordinated with the lattice oxygen adjacent to the Al sites. These extra-framework cations are considered the main responsible of the cleavage of the C-H bond in $CH_4$ and of the stabilization of the methyl group that will be hydrolysed later into methanol. The description of the synthesis procedure regarding these materials, named generally as Cu-exchanged zeolites, is out the scope of this thesis. However, the interested reader can find more information about this topic in references [11, 12].

The ability to convert the methane to methanol in a selective manner has its origins in the capacity to stabilise the intermediate species, such as the methoxy groups (which are at the basis of the formation of the methanol molecules) and protecting them from subsequent oxidation processes. For Cu-zeolites, the Cu sites must be activated by an oxidant in order to create one or more active sites. These sites serve to activate the C-H bond and to stabilise the methoxy formed species from further oxidation processes. This evidence determined the design of well-defined procedures which can be followed to convert the methane in methanol over Cu exchanged zeolites, following a step-wise approach. Among them, the most frequently employed approach foresees a three-step process characterized by an *activation* in oxygen, the methane reaction and finally the methanol extraction [8, 13]. Under typical operation conditions, the Cu- exchanged zeolite is activated for several hours at 450°C or 500 °C in an oxygen atmosphere and subsequently cooled and treated with an inert gas, such as He, in order to remove the $O_2$ used in the activation of Cu-zeolite. Then methane is sent over the Cu-exchanged zeolite for some time at about 135°C or 200°C, and the produced methanol or methoxy group is desorbed or extracted from the Cu-zeolite using a solvent such as water to obtain methanol [14]. A graphical representation of this procedure is reported in **Figure 5.1**.

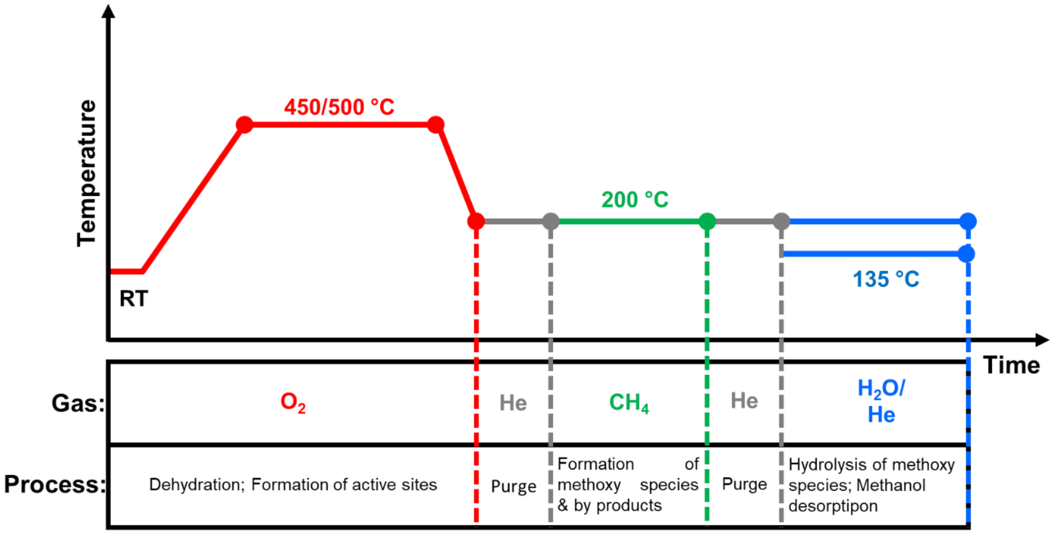

**Figure 5.1:** Schematic representation of the stepwise process described in the text and employed in the investigations described in the next sections. In the bottom is reported the description of the possible oxidant gases and types of processes occurring within the step-wise approaches to methane oxidation over copper containing zeolites. The double blue linear curve at 200 and 135 °C indicates the possible extractions temperatures.

A large variety of Cu-zeolite catalysts have been evaluated during the last decade for such step-wise DMTM process. In particular, it is worth to underlie that the Cu exchanged zeolites possessing the chabazite (CHA) and the mordenite (MOR) frameworks have been distinguished, among the various zeolite topologies, for their high-activity for the methane to methanol conversion [6, 8, 15, 16]. The CHA topology is built up by an arrangement of double 6-membered rings (6r), connected via 4-membered ring units, giving rise to the so-called CHA cages, which are accessible through 8-membered rings (8r), see **Figure 5.2**(a). On the other hand, the MOR structure possesses 12 membered ring pores (12r) interconnected by 8r channels, as showed in **Figure 5.2**(b).
More information about the geometrical properties can be found on the IZA database: http://www.iza-structure.org/databases/.

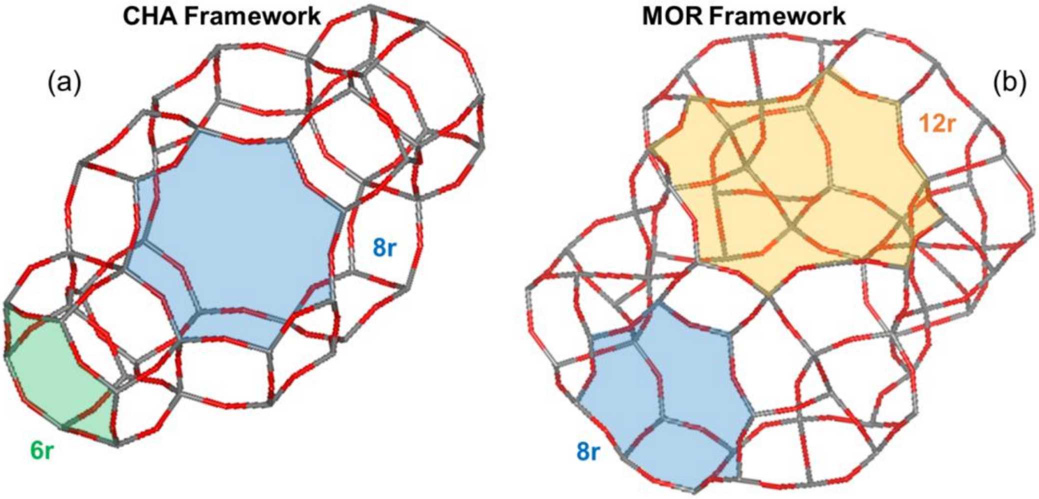

**Figure 5.2:** Pictorial representation of the main rings characterising the CHA (a) and MOR (b) zeolites frameworks and suitable to host the active site for the direct conversion of methane to methanol. Colour code: O: red, Si: grey.

Although the structure of copper-oxo active species inside zeolite pores involved in the methanol production has been proposed since the beginning of the investigation [14], it remains controversial. In particular, the main open questions about this topic regard the nuclearity (i.e. the number of Cu atoms) and the geometry of these active sites. The knowledge of these properties is fundamental and can shed light on the mechanism for DMTM conversion over Cu-zeolites. Moreover, they can provide clear information concerning how to optimise these materials in terms of their structure and composition.

This chapter is organized in the following way. First at all in **section 5.1**, it is showed how XAS in connection with the MCR-ALS approach can help to elucidate the impact of the catalyst composition on the temperature-dependent Cu-speciation and reducibility in Cu-CHA zeolites during the activation process. In **section 5.2** the individual process steps for the direct conversion of methane to methanol, showed in **Figure 5.1**, are investigated in detail over a batch of Cu-CHA materials and a relationship between their methane productivity and the Cu-speciation is established. **Section 5.3** proceeds on the analysis reported in the precedent section and shows an attempt to identify, for a selected Cu-CHA sample, the spectral profile associated to the active sites involved in the DMTM process. Herein, the MCR-ALS method was employed on a large dataset composed by HERFD-XANES collected during the oxygen and He activation of the catalysts. The use the MCR-ALS algorithm is discussed also in **section 5.4**, where it is showed how this approach has been employed to accurately quantify the fraction of active Cu sites in Cu-MOR, allowing to obtain, in this case, an unambiguous determination of the active site nuclearity as dicopper site (with unknown structure). In **section 5.5**, a theoretical screening of the EXAFS profiles, proper of a series of Cu(II)-oxo-species, suggested from the literature to be the most probable active sites for the DMTM conversion, is provided. These results, set the bases for an easier and more robust interpretation of the XAS data collected on Cu-zeolite systems, moreover it is demonstrated how, differently for the XANES analysis, the application of the WTA on these simulated signals is able to enhance the EXAFS sensitivity towards the nuclearity of Cu-oxo species in Cu-zeolites. Focusing on this topic, in **section 5.6** and in **section 5.7** it is showed, for a selected set of Cu-MOR samples how, combining *ex situ* XAS measurements under model red-ox conditions with *in situ* data collected after the key steps of the DMTM process, the EXAFS-WT enables the unambiguous detection of Cu–Cu scattering contributions from multimeric Cu-species. The latter is also demonstrated quantitatively through the employment of the EXAFS fit in the WT space, which reveals a Cu local coordination environment consistent with mono-(μ-oxo) di-copper cores.

## 5.1 UNDERSTANDING THE CU SPECIATION AND REDUCIBILITY OF CU-CHA CATALYSTS EMPLOYING AN *IN SITU* XAS STUDY

From the recent literature, it clearly emerges that Cu location in the framework strongly depends on the sample composition in terms of Si/Al ratio and Cu loading [20–24]. In particular, two major Cu–sites in dehydrated Cu–CHA have been proposed. These include reduction-resistant $Z_2Cu(II)$ species (where $Z_2$ represents the bonds to the zeolite framework oxygens $O_{fw}$ next to two neighbouring Al sites in framework T-sites) hosted in the 6r and redox-active ZCu(II)OH complexes (where Z indicates bonds to $O_{fw}$ next to an isolated Al atom in a framework T-site) preferentially stabilized in the 8r. The ZCu(II)OH species are known to undergo towards the so-called *self-reduction* process [25, 26] to ZCu(I) complexes during thermal treatment in vacuum or in inert gas flow from ~ 200 °C upwards [18, 23, 24, 27]. In particular, how it will be showed in the next section (**section 5.2**), the presence of these last sites appears to be strongly correlated with the formation of the active species for the DMTM conversion. It follows that it is necessary to explore the composition-dependence associated to the Cu-speciation for this catalyst trying to differentiate between the different reducibility phenomena involving the Cu-sites and gain deeper insights into the self-reduction process.

In order to track the dynamic rearrangements of Cu ions as a function of determined environmental parameters (i.e. temperature, gas feed composition Si/Al and Cu/Al ration), different set of *in situ* XANES measurements have been collected during the He-activation, from 25 °C till to 400 °C (flow rate 100 ml/min; heating rate 5 °C/min; XANES scan duration ~ 6 min), for six Cu-CHA samples with Si/Al ratios of ~ 5, 15, 19, 29 and Cu/Al ratios from ~ 0.1 to ~ 0.6. The technical details concerning the XAS data acquisition process are reported in **section 5.8.1** of the appendix. The activation in He (heating ramp 5 °C/min) was required in order to have a higher level of discrimination between reducible and not reducible sites. The detailed list of analysed samples is reported in **Table 5.2**. From now, for all the cases of study reported in all the sections of this chapter, the following notation will be used to denote the composition of an arbitrary Cu-exchanged zeolite: *zeolite framework type* (Cu/Al; Si/Al).

| Sample name (Cu/Al; Si/Al) | % wt Cu | Cu/Al | %wt Al | %wt Si | Si/Al |
|---|---|---|---|---|---|
| (0.1; 5) | 1.51 | 0.11 | 6.03 | 31.0 | 4.94 |
| (0.3; 5) | 4.20 | 0.33 | 5.42 | 27.6 | 4.89 |
| (0.1; 14) | 0.76 | 0.13 | 2.47 | 36.1 | 14.06 |
| (0.5; 15) | 2.64 | 0.47 | 2.38 | 37.5 | 15.12 |
| (0.6; 19) | 2.59 | 0.56 | 1.98 | 38.5 | 18.68 |
| (0.6; 29) | 1.71 | 0.56 | 1.30 | 39.5 | 29.17 |

**Table 5.2:** Detailed description of the composition of the samples treated in this study.

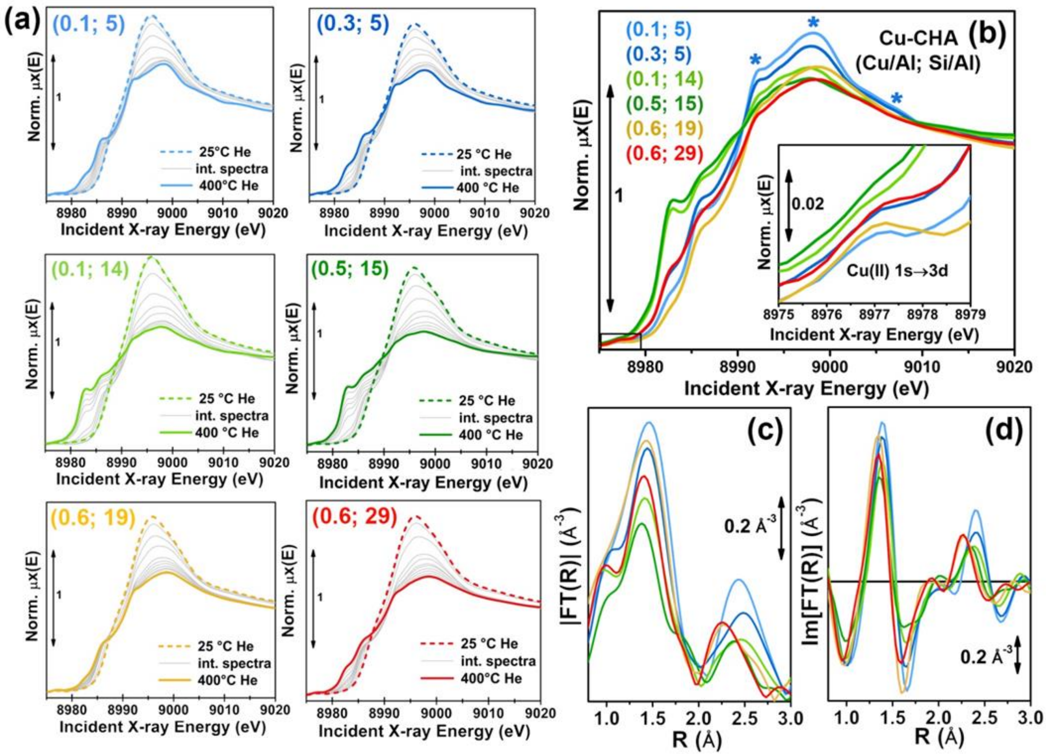

**Figure 5.3**: (a) In situ XANES of Cu-CHA catalysts referring to different composition samples (different samples are denoted with (Cu/Al; Si/Al) labels) during dehydration in He flow from 25 °C to 400 °C, heating rate 5 °C/min. (b) Comparison between XANES spectra of He-activated Cu-CHA samples with different composition, collected at 400 °C. The inset reports a magnification of the weak pre-edge peak mostly deriving from the dipole-forbidden 1s→ 3d transition in Cu(II) sites. (c, d) Magnitude (c) and imaginary parts (d) of the $k^2$-weighted, phase uncorrected, Fourier transformed EXAFS spectra (plotted in modulus) ($k$-range 2.4-12.4 Å$^{-1}$) of He-activated Cu-CHA samples with different composition, collected at 400 °C. Colour code in all the panels: dashed thick lines: hydrated sample at 25 °C; solid thick lines: dehydrated sample at 400 °C; grey thin lines: intermediate spectra.

**Figure 5.3**(a) shows the evolution of the collected *in situ* XANES employed in the investigated Cu-CHA catalysts during the entire activation process. The XANES features follow a similar trends in the whole series of samples, in agreement with previous studies [17, 18]. The spectroscopic features emerging during the activation process can be qualitatively interpreted on the basis of the abundant literature on Cu K-edge XANES in metal-exchanged zeolites [1, 2, 19-23]. In particular, a progressive decrease of the intense white-line (W.L.) peak at ~ 8996 eV, characteristic of mobile five/six-coordinated Cu aquo-complexes [9, 10, 24, 25] is observed as the activation proceeds, paralleled by the development of the rising-edge peaks in the 8985−8987 eV range, reflecting an increase in the population of three/four/five-coordinated (intermediates of dehydration) Cu(II) sites [9, 10, 24-29]. From ~ 230 °C upwards, the reduction of Cu(II) in Cu(I) occurs in all the samples. This phenomenon can be tracked by the development of determined XANES features in the 8981−8985 eV range, typical of Cu(I) sites, localised in non-linear, low-coordination-number environments [19, 30, 31].

Higher-quality *in situ* XAS spectra on the whole sample series upon stabilization at 400 °C have been collected too. The acquisition time was adjusted to achieve a satisfactory S/N ratio in the EXAFS region, enabling to quantitative fitting of the resulting spectra. **Figure 5.3**(b-d) compares the final states reached in He flow at 400 °C for all samples, in both XANES (**Figure 5.3**(b)) and EXAFS regions (**Figure 5.3**(c,d)). A progressive modulation of the XAS features as a function of the composition can be appreciated. The rising-edge and post-edge peaks in the XANES occur at very similar positions in the whole sample series, although their relative intensity is different depending on the composition. The reducibility (relative abundance of Cu(I) sites obtained from Cu(II) complexes) of the samples seems to be mostly determined, in a non-monotonous way, by the Si/Al ratio. Lower reducibility is observed for both Si/Al = 5 and Si/Al =19, 29 samples, although the dominant dehydrated Cu(II) species appear to be different in the two cases. In particular, the XANES for He-activated Cu-CHA at Si/Al = 5 shows a more intense and structured white line region, with well-resolved peaks at ~ 8998 and ~ 8992 eV, and a broad post-edge peak in the 9005−9010 eV range (blue asterisks in **Figure 5.3**(b)), in agreement with the XAS spectra reported by Paolucci *et al.* [5] for a Cu-CHA catalyst with similar composition (Cu/Al = 0.08; Si/Al = 5). Conversely, the samples with Si/Al = 19, 29 show broader and less pronounced W.L. peaks, as well as a smoother post-edge region. The catalysts with intermediate Al content, Si/Al = 14, 15, are characterized by very pronounced Cu(I) XANES features, pointing out the presence of a majority of Cu(I) sites at 400 °C in He, independently from the Cu-loading.

The reducibility trends qualitatively identified throughout the series of samples are also supported by the modulations in the intensity of the weak pre-edge peak at ca. 8977 eV, mostly deriving from the 1s→3d transition, which is an unambiguous fingerprint of the presence of $d^9$ Cu(II) ions in the catalysts [20, 28, 32] (see **Figure 5.3**(b), inset). Such peak is clearly visible for all the investigated samples except for the Si/Al ~ 14, 15 ones, where it appears almost completely smeared at both high (Cu/Al = 0.5) and low (Cu/Al = 0.1) Cu-loading.

For all the He-activated samples, two well defined maxima are distinguishable in the phase-uncorrected FT (Fourier Transform) -EXAFS spectra (**Figure 5.3**(c,d)), occurring in the 1.4–1.5 Å and 2.2–2.4 Å ranges. On the basis of DFT-assisted EXAFS analysis, previously performed on a Cu-CHA sample with Cu/Al ~ 0.44, Si/Al ~ 13 [17], it is possible to safely assign the first maximum to single scattering (SS) paths involving extra-framework ($O_{efw}$) and framework ($O_{fw}$) oxygen atoms in framework-coordinated Cu-species. Remarkably, the composition-induced modulation in the first-shell intensity correlates with the level of Cu(I) species as evaluated from XANES. Indeed, samples with Si/Al = 5 and Si/Al = 19, 29 show higher first-shell intensities, suggesting a major population of Cu(II) sites characterized by three/four-fold coordination to O ligands. Conversely, a lower first-shell intensity is observed at Si/Al 14, 15, corresponding to a higher relative fraction of two-fold O coordinated Cu(I) sites [17].

Considering several recent XAS studies on Cu-CHA [17, 33-36] it is possible to associate the principal contribution in the second maximum of the FT-EXAFS spectra to SS paths, involving the second-shell, to the Al/Si T-atoms of the zeolite framework. A clear composition-driven trend, in both intensity and position, becomes evident looking at the imaginary part of the FT-EXAFS second shell of the spectra in **Figure 5.3**(d). As the Si/Al ratio increases from 5 to 29, the peak progressively shifts towards lower R-values, evidencing an average shortening in Cu–$T_{fw}$ bond distances. In particular, the intensity of the second-shell peak is mostly determined by the Si/Al ratio and a minimum is found in correspondence of the Si/Al = 14, 15 samples, according to the following trend: Si/Al = 5 > 19, 29 > 14, 15.

Interestingly, the highest amount of Cu(I) features at Si/Al ~ 15 is accompanied by damped and broadened second shell peaks, possibly connected with a higher heterogeneity in Cu(I) siting. The higher second-shell intensity observed for Si/Al = 5 is in good agreement with the presence of a major contribution from $Z_2$Cu(II) sites. For these Cu-sites, DFT-optimized geometries previously reported in the literature [17, 36, 37] evidence two almost degenerated Cu−Al and Cu−Si SS paths at ~ 2.8 Å contributing to the second maximum in the FT-EXAFS (please note that Si and Al atomic neighbours are not distinguishable by EXAFS due to the very similar scattering amplitude, as discussed in **section 3.1** of **Chapter 3**). Conversely, for the case of ZCu(II)OH sites, only one Al neighbour at ~ 2.7 Å is predicted, which would result in a lower second-shell peak in the FT-EXAFS spectra.

The qualitative observations presented so far is rationalized in the following section, by combining the MCR-ALS decomposition of the temperature-dependent XANES dataset shown in **Figure 5.3**(a) with multi-component fitting of the EXAFS spectra reported in **Figure 5.3**(c,d).

### 5.1.1 *Multivariate analysis of temperature-dependent in situ XANES*

As highlighted in the previous section, the qualitative analysis of the *in situ* XAS dataset during He-activation reported in **Figure 5.3** strongly supports the presence of a common set of Cu-species, occurring with different relative abundance as a function of the temperature and composition (Cu/Al; Si/Al). Herein the MCR-ALS approach initialised through the SIMPLISMA algorithm, described in detail in **section 2.1.3.2.1** of **Chapter 2**, has been employed to analyse the multi-composition temperature-dependent dataset reported in **Figure 5.3**, in order to deduce the XANES spectra of *pure* Cu-species directly from the available experimental data.

The first step in the analysis consisted the determination of the number of pure species: $N_{pure}$ affecting the datasets reported in **Figure 5.3**(a). To this aim, the PCA of the *in situ* XANES series (He-activation from 25 to 400 °C) for each catalyst composition was performed.

The PCA has been employed assuming that any systematic thermal dependence of the XANES signal is negligible with respect to the Cu-speciation-related contributions to the experimental variance. From the inspection of the quantitative statistical indicators such as the Malinowski F-test (with $\alpha$=5%) and IND-factor, it has been possible to identify an average number of pure common species $\langle N_{pure} \rangle = 5 \pm 1$, see **Table 5.3**.

| **Sample (Cu-CHA, Cu/Al_Si/Al)** | **$N_{PC}$(F-test) Malinowski F-test ($\alpha$=5%)** | **$N_{PC}$(IND) IND-factor** |
|---|---|---|
| 0.1; 5 | 6 | 6 |
| 0.5; 5 | 4 | 4 |
| 0.1; 14 | 4 | 6 |
| 0.5; 15 | 5 | 7 |
| 0.6; 19 | 5 | 6 |
| 0.6; 29 | 5 | 5 |
| $\langle N_{PC}. \rangle \pm \sigma$ | 5 ± 1 | 6 ± 1 |

**Table 5.3:** Number of PCs ($N_{PC}$) identified using the Malinowski's F-Test and IND Factor. How it is possible to see the average number of PCs stands around five main components.

Having established the existence of five main species in the datasets and supposing their presence in all the analysed samples, it is possible to create an enlarged dataset composed by the all the spectra (76 in total) appearing in **Figure 5.3**. This choice results extremely important because it allows to reduce the rotational ambiguity phenomena, affecting the reconstructed solutions. The five theoretical XANES pure components are shown in **Figure 5.4**(a) while the bar plots in **Figure 5.4**(b) report their correspondent temperature-dependent concentration profiles for each compositional point. By matching the characteristic XANES features of each pure spectrum and the evolution trends for their weights with the rich experimental background currently available on Cu-CHA, it is possible to safely assign each pure component to the Cu-species depicted in **Figure 5.4**(c). For sake of comprehension, from now, the term *species* or simply *pure component* (PC) (of the chemical mixture) will be used to indicate the signal associated to the chemical sites extracted through the MCR-ALS algorithm. Although the acronym PC reminds the one used in **chapter 1** to indicate the principal components extracted through the PCA procedure, it is worth to underlie that the two thing are quite different. In particular, the principal components are mathematical solution, without chemical physical meaning, of the spectral decomposition problem, while the pure spectra extracted by means of the MCR-ALS algorithm can be seen as a combination of the principal components.

A first clue to identify the Cu oxidation state in each of the retrieved pure components is provided by the 1s → 3d pre-edge peak in the theoretical pure spectra (see **Figure 5.4**(a), inset). The peak is clearly present in all the retrieved curves except in the XANES spectrum for the second specie (red line in **Figure 5.4**(a)). Hence, this latter component can be unambiguously assigned to a $d^{10}$ Cu(I) species, whereas the other four components correspond to Cu(II) moieties.

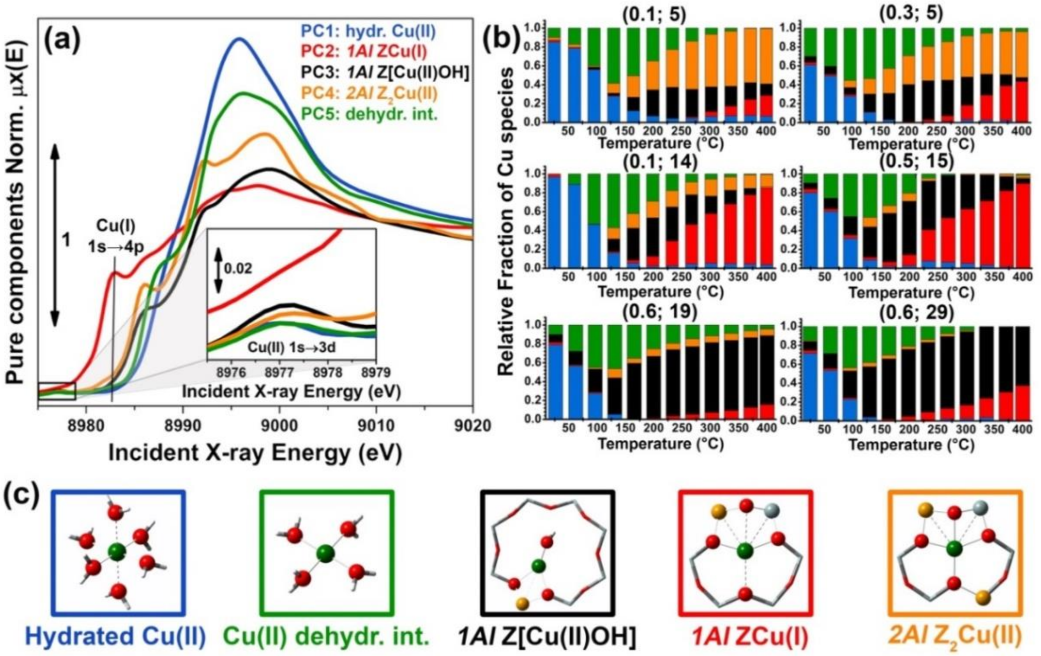

**Figure 5.4:** Results of MCR-ALS analysis of global temperature-dependent XANES dataset collected on six Cu-CHA samples with different composition during He-activation from 25 to 400 °C (**Figure 5.3** (a)), assuming $N_{pure} = 5$. (a) XANES spectra of pure components derived from MCR-ALS. The inset reports a magnification of the Cu(II) 1s → 3d transition region in the theoretical spectra. (b) Temperature-dependent abundance of pure species (concentrations) in each of the catalysts (bars have the same colours as the corresponding spectra in panel (a). (c) Proposed assignment of the five pure components to specific Cu-species/sites formed in the Cu-CHA catalyst as a function of composition and activation temperature, using the same colour code as in parts (a,b). Blue (PC 1): mobile Cu(II)-aquo-complexes $[Cu(II)(H_2O)_n]^{2+}/[Cu(II)(H_2O)_{n-1}(OH)]^+$ with n = 6; green (5 PC): Cu(II) dehydration intermediate, possibly represented by mobile $[Cu(II)(H_2O)_n]^{2+}/[Cu(II)(H_2O)_{n-1}(OH)]^+$ complexes with n = 4; black (PC 3): ZCu(II)OH sites in their oxidized form; red (PC 2): ZCu(I) sites in their reduced form, resulting from self-reduction of ZCu(II)OH species;

orange (PC 4): $Z_2Cu(II)$ sites. Atom colour code: Cu: green H: white; O: red; Si: grey; Al: orange.

Considering the characteristic shape of the XANES spectrum, the first specie (PC 1) is easily assigned to mobile Cu(II)-aquo-complexes, namely $[Cu(II)(H_2O)_n]^{2+}$ or $[Cu(II)(H_2O)_{n-1}(OH^-)]^+$ with n = 6. For all the probed compositions, these fully hydrated Cu(II) ions represent the dominant component at the beginning of the activation process, and their concentration drops rapidly to values <10% of the total Cu as the temperature reaches 150 °C. The decrease in the relative fraction of fully hydrated Cu(II) is paralleled by the transient growth in the contribution of a different component, whose concentration peaks in the 100–130 °C range for all of the samples. The correspondent spectrum (PC 5) is characterized by a lower intensity and a broader shape in the XANES W.L. region. A shoulder becomes evident in the edge-rising region at ~ 8987 eV. This component was associated to a four coordinated, pseudo square-planar Cu(II) *dehydration intermediate*, based on the similarity of the corresponding MCR-ALS XANES to the spectra of reference corresponding to four-coordinated Cu(II) species, i.e. $[Cu(II)(H_2O)_4]^{2+}$ or $[Cu(II)(NH_3)_4]^{2+}$. Mobile Cu(II) complexes such as $[Cu(II)(H_2O)_3(OH)]^+$, or alternatively, four-coordinated Cu(II) moieties with mixed $O_{fw}/O_{efw}$ ligation could be envisaged. Remarkably, the contribution from this species is appreciable until 250−280 °C (albeit with longer tails in the Si/Al = 19, 29 samples), which matches well the temperature threshold at which no more adsorbed molecular water was observed by FTIR (Fourier Transform Infrared Spectroscopy) on a Cu-CHA catalyst with Si/Al ~ 13; Cu/Al ~ 0.44 [17].

The decay in the population of the dehydration intermediate, described above, paves the way to the actual birth of fully dehydrated framework-interacting Cu-species. It is here that the impact of the catalyst composition on temperature-dependent Cu-speciation comes strikingly into play. Two Cu(II) species start to form almost simultaneously after ~ 130 °C, namely the third and fourth component, that have been assigned to ZCu(II)OH and $Z_2Cu(II)$ sites, respectively. Such assignment is supported by several evidences. Firstly, the fourth specie (PC 4) dominates the high-temperature Cu-speciation at Si/Al = 5, reaching at 400 °C a relative fractions from ~ 40 to ~ 60% of the total Cu depending on the loading. Conversely, it always represents a minor component (< 20% total Cu) at both intermediate (Si/Al = 14, 15) and low (Si/Al= 19, 29) Al content. Moreover, after 250 °C, its contribution is substantially stable (it doesn't go towards its self-reduction in Cu(I)), while the third specie population (PC 3) is progressively eroded in favour of the second (PC 2): the only Cu(I) component extracted by MCR-ALS. Spectroscopically, the pure spectra correspondent the PC 3 and PC 4 reflect, properly, the differences observed in the experimental data as a function of the composition. In particular, the PC 4 XANES curve, associated to the $Z_2Cu(II)$ sites, optimally reproduces both the higher, highly structured, white line peak and the post-edge peak observed in the experimental XANES of He-activated samples at Si/Al = 5.

Finally, the contribution of the second pure component is straightforwardly attributed to the ZCu(I) sites, resulting from the reduction of the ZCu(II)OH species. The correspondent spectrum shows all the characteristic fingerprints of two-coordinated (two fold) non-linear Cu(I) sites [17, 20, 31, 38] with a prominent rising-edge peaks developing from ~ 8982 eV and a lower W.L. intensity with respect to the other Cu-species identified so far.

To further support these assignments the Cu K-edge XANES spectra for all the five model structures, reported in **Figure 5.4**(c), and proposed to interpret the MCR-ALS retrieved spectra; have been simulated using TD-DFT calculation realised through the Amsterdam Density Functional (ADF) code [39], see **Figure 5.5**.

Focusing on the three framework-interacting Cu-species, which dominate the Cu-speciation in the He-activated catalysts, it is possible to observe how the simulated XANES curves properly reproduce the distinctive relative energy shifts (and partially, intensity ratios) of the rising-edge peaks for each Cu-site. The ZCu(I) model, in agreement with the PC 2 spectrum, results in prominent peaks significantly shifted at lower energies and more intense with respect to the ZCu(II)OH and $Z_2$Cu(II) geometries. In line with the assignment to the fourth species, the $Z_2$Cu(II) site gives rise to a sharp peak at ~ 8986 eV, to two well defined maxima in the white-line region at ~ 8992 eV and ~ 8998 eV and a broad post-edge peak around 9007 eV. The alternative Cu(II) environment, ZCu(II)OH, is associated to a broader rising-edge peak and less defined features in the white line region, globally shifted to higher energy, in qualitative agreement with the third component curve.

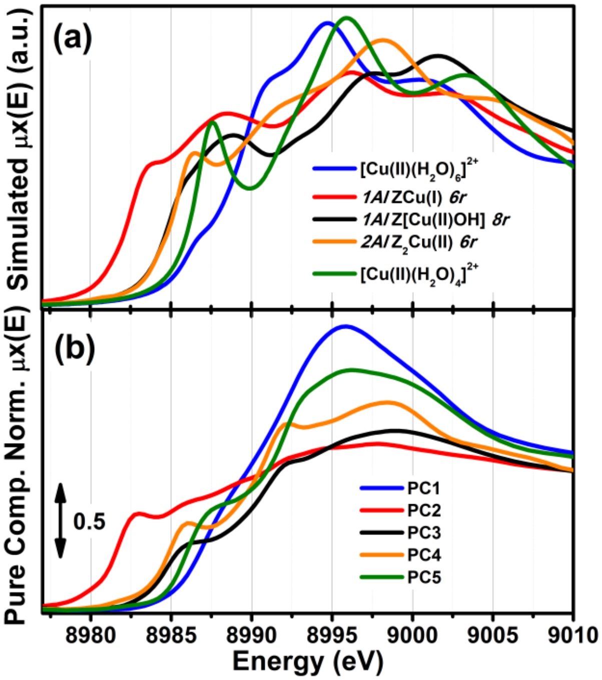

**Figure 5.5:** (a) Simulated Cu K-edge XANES spectra for the five DFT-optimized model structures reported in **Figure 5.4** and proposed to interpret the MCR-ALS pure spectra. (b) Pure set of spectra obtained from the MCR-ALS analysis for comparison.

Theoretical spectra for fully- and under-coordinated Cu(II) aquo-complexes are clearly distinguished from the ones of framework-interacting Cu-species due to the presence of high-intensity transitions in the 8990-8998 eV range, as observed in the MCR-ALS spectra for PC 1 and PC 5. Interestingly, the simulations evidence how, while decreasing the number of $H_2O$ ligands in the first Cu(II) coordination sphere from six to four, a well-defined rising-edge peak develops at ~ 8987 eV. The same behaviour is recognized while comparing the first and fifth MCR-ALS derived-curves, together with a slight shift at higher energies of the W.L. peak for the fifth component, which is also reproduced in the simulated spectra for $[Cu(II)(H_2O)_4]^{2+}$ and $[Cu(II)(H_2O)_6]^{2+}$. Although the similarity with four-coordinated reference compounds suggests predominant ligation to four $H_2O$ ligands, simulations (see the supporting information of [40]) indicate that the spectrum proper of the fifth component could actually evidence a dynamic mix of four-, five-, and, possibly, even lower-coordinated Cu(II) aquo complexes, which are however not readily resolvable within time- and energy-resolution of the available dataset. To resolve the additional complexity associated with the transition between mobile and framework-interacting Cu-species, it is necessary to envisage additional studies employing molecular dynamics-assisted XANES simulations as showed by D'Angelo et al. in [41-43].

### 5.1.2 *Interpretation of the MCR-ALS results: novel elements of complexity affecting reducibility in Cu-CHA*

From the MCR-ALS analysis discussed above, several insights into the impact of the catalyst composition on Cu-speciation during He-activation can be derived. At RT, the Cu-speciation is largely dominated by mobile, fully-coordinated Cu aquo-complexes (always > 60% total Cu). Nonetheless, small populations of partially dehydrated Cu(II) species together with traces (< 5% total Cu) of framework-interacting Cu(II) and Cu(I) sites are already found at the beginning of the activation process. The birth of fully dehydrated Cu-sites occurs in all samples through the transient development of a common Cu(II) *dehydration intermediate*, as described before. As shown in **Figure 5.4**(b), Cu-speciation for all the He-activated catalysts at 400 °C can be described as a combination of redox-active 1Al sites (in their oxidized ZCu(II)OH or reduced ZCu(I) form) and redox-inert 2Al, $Z_2Cu(II)$ sites (i.e. which do not show self-reduction effects as a function of the temperature), in agreement with the picture proposed in the recent report by Paolucci et al. [36].

Nonetheless, the results obtained through the MCR-ALS analysis reveals novel elements of complexity. To this aim, **Figure 5.6** details the MCR-ALS results for the most representative compositional points, comparing the experimental and reconstructed XANES at key temperatures during the He-activation (left panels) and reporting concentration profiles (right panels) for the five pure Cu-species identified by the statistical analysis and assigned as described in **section 5.1.1**. The residuals and the related R-factor values, calculated on the selected set of time-dependent spectra, demonstrates that the MCR-ALS procedure ensures an good reproduction of the experimental XANES dataset for all the investigated samples. The description of these two estimators is described in detail in **section 2.1.2** of **Chapter 2**.

The highest deviations (peaks in R-factor *vs* temperature profiles, which however is always well below 2%) are generally observed at the maximum population of the Cu(II) dehydration intermediate or nearby, when different dehydrated Cu(II) sites starts to develop. As already discussed at the end of **section 5.1.1**, the transition from mobile aquo-complexes to framework-interacting species could occur *via* additional intermediate states (possibly composition-specific), which however are not resolvable within the experimental time-resolution and cannot be reliably singled out by the MCR-ALS algorithm.

Paolucci *et al.* have been able to estimate theoretically a Cu-site compositional phase diagram for activated Cu-CHA, predicting the relative fraction of 1Al and 2Al sites as a function of Si/Al and Cu/Al ratios.[36]. Such a diagram, reported in **Figure 5.7**, represents a milestone in Cu-CHA research. However, it involves some assumptions. In particular, it is derived assuming that the $Z_2Cu(II)$ sites in the 6r represent the first framework sites to be populated by the cations during dehydration.

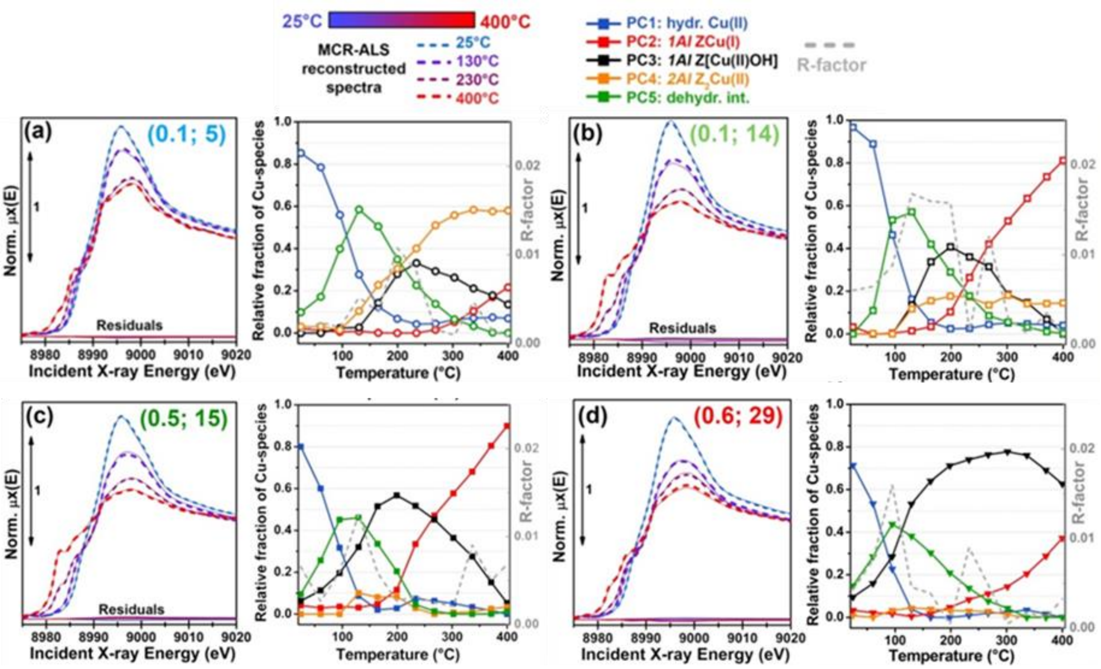

**Figure 5.6:** Detailed MCR-ALS results for the most representative compositional points: (a) Cu/Al = 0.1, Si/Al = 5; (b) Cu/Al = 0.1, Si/Al = 14; (c) Cu/Al = 0.5, Si/Al = 15; (d) Cu/Al = 0.6, Si/Al = 29. Left panels: comparison between experimental *in situ* XANES during He-activation (thin solid lines) and reconstructed spectra from MCR-ALS at the four key temperatures of 25 °C, 125 °C, 230 °C, 400 °C with the corresponding residuals. Right panels: concentration profiles for the five pure Cu-species/sites identified in the model as a function of the activation temperature (coloured symbols) and correspondent R-factor values (grey dashed lines).

Under this hypothesis, only after all the available 2Al sites at a given Si/Al ratio are saturated, Cu is allowed to populate other kind of sites, primarily forming ZCu(II)OH complexes in the 8r. According to this model, catalysts with Cu-loadings below the saturation threshold would contain, after dehydration, only $Z_2Cu(II)$ sites: for Si/Al = 5, 15 and 29, saturation is predicted at Cu/Al ≈ 0.24, 0.09, and 0.05 respectively.

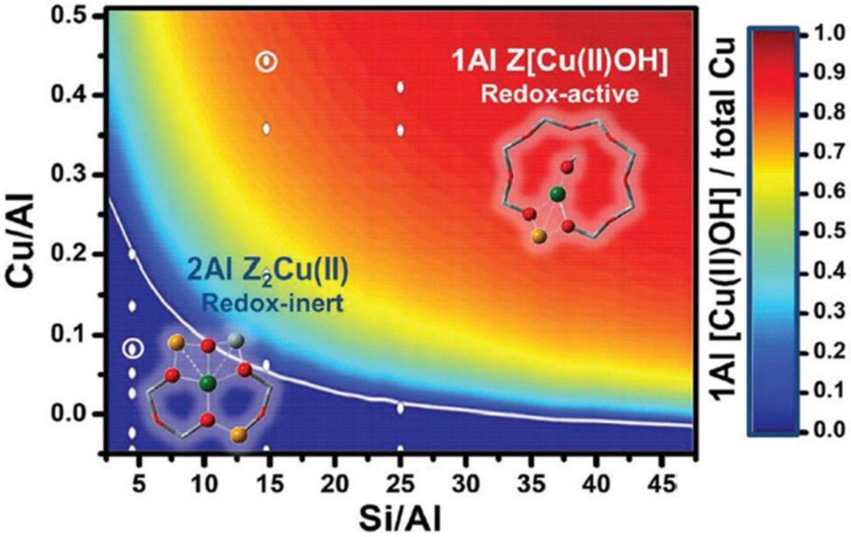

**Figure 5.7:** Predicted Cu site compositional phase diagram versus Si/Al and Cu/Al ratios. Colour scale indicates predicted fraction of ZCuOH. White line demarcates the theoretical transition from $Z_2Cu(II)$ -only region to mixed $Z_2Cu(II)$ = ZCu(II)OH region. White circles indicated compositions of synthesized Cu-CHA samples analysed by Paolucci et al. [36]. This graph is based on two assumptions: i) the framework Al atoms are randomly sited during zeolite crystallization following the Löwenstein's rule (i.e. 2 neighbouring Al sites must be separated by at least one $SiO_2$ unit), and second, that 2Al sites in the 6r are populated by Cu(II) cations till to the saturation before the 1Al sites are populated by ZCu(II)OH. Adapted from [36, 44].

However, the results reported in **Figure 5.6** reveal a more complex picture in relation with the population of $Z_2Cu(II)$ sites, particularly evident at intermediate Si/Al values. It is possible to note, in fact, that for all the investigated samples, $Z_2Cu(II)$ and ZCu(II)OH sites (orange and black lines in **Figure 5.6**, respectively) start to form almost simultaneously during dehydration, which deviates from an ideal 2Al saturation scenario. Comparing the MCR-ALS results for the Si/Al = 5 catalysts with lower (Cu/Al = 0.1) and higher (Cu/Al = 0.3) loading, a saturation tendency is confirmed: due to the finite availability of 6rs hosting 2Al sites, at higher Cu-loading a lower relative fraction of $Z_2Cu(II)$ species is observed, counterbalanced by a larger population of reducible 1Al sites. Nevertheless, for the catalyst with Cu/Al = 0.1, Si/Al = 14 (**Figure 5.6**(b)), the final state at 400 °C is characterized by a substantial fraction of reduced ZCu(I) sites (~ 80%), whereas the $Z_2Cu(II)$ contribution reaches a maximum abundance of only ~ 18%. Assuming the saturation of the 2Al sites, this sample should be dominated by redox-inert 2Al sites due to its low Cu-loading (> 90% total Cu according to the compositional phase diagram in reported in **Figure 5.7** and the saturation threshold evaluated by Bates *et al.* [45]). Experimentally, this is however clearly not the case: MCR-ALS evidences only a relatively small increase in the abundance of 2Al sites with respect to the high-loading catalyst with comparable Si/Al ratio (Cu/Al = 0.5; Si/Al = 15, **Figure 5.6**(c)). This effect could be connected with high barriers for Cu migration towards 2Al sites, possibly trapping the cations into local energy minima at 1Al sites.

Another intriguing result, emerging from MCR-ALS analysis, is that the reducibility level for the 1Al sites is clearly dependent on the Al distribution, with highest reducibility for Si/Al ~ 15 (< 10% Cu is observed as ZCu(II)OH at 400 °C) and lower reducibility at Si/Al = 19 and 29, with ~ 70% and ~ 60% of the 1Al sites still surviving in the oxidized form, respectively (see **Figure 5.6**(b) and **Figure 5.6**(d)). These results unambiguously demonstrate that the reduction proceeds though a cooperative multi-step process involving proximal acid sites whose availability is ultimately determined by the Al density and distribution in the zeolite. This is in line with previously suggested mechanisms in the literature [3-5]. Plausibly, the process initiates with the thermally-driven reduction of ZCu(II)OH to ZCu(I), accompanied by the release of an hydroxyl radical, OH▪. The availability/spatial proximity of a reactive channel for the OH▪ radical might then determine the overall efficiency of the reduction process, and the final balance between 1Al sites in the oxidized/reduced form observed in the He-activated catalysts. Consequently, Al-rich frameworks facilitate the reduction process. With respect to the Cu-loading impact on the reducibility, when comparing concentration profiles for ZCu(I) on low- (Cu/Al ~ 0.1) and high- (Cu/Al ~ 0.5) loading Cu-CHA at almost equivalent Si/Al of ~ 15, a very similar temperature onsets and rates for the self-reduction (see **Figure 5.6**(b,c)) can be identified. A slightly lower Cu(I) fraction is observed at 400 °C in the low-loading sample, but it excellently correlates with the small increase in the concentration of $Z_2Cu(II)$ sites. Hence, at optimal Si/Al values, Cu-loading seems to poorly affect the reduction efficiency, which can be conjecturally connected with a role of proximal Brønsted sites along alterative pathways efficiently affording by ZCu(I) species. Within the time-resolution (~ 6 min) of the XANES experiments, intermediate Cu(II) species eventually formed along the transformation from ZCu(II)OH to ZCu(I) are not detected.

Finally, it is possible to note that for most of the samples, the MCR-ALS analysis evidences a non-monotonous trend in the concentration profiles of the hydrated Cu(II)-species (the first species of in **Figure 5.4**), showing a small peak in the high-temperature range (230-350 °C) which account for the 5% of the total Cu increments in the relative fractions of fully hydrated Cu(II). Due to the reduced entity of the variations and the absolute weakness of the contribution from this structural component in the high-temperature range, it is difficult to conclusively establish the physico-chemical meaningfulness of the effect. However, it is interesting to note that the temperature position of the peak correlates with the initial rise in the ZCu(I) component, supporting that the initial steps in the pathway(s) of reduction involve the formation of small amounts of $H_2O$. These traces of water could transiently re-solvate and mobilize a small fraction of Cu sites: for samples (Cu/Al = 0.5; Si/Al = 15) and (Cu/Al = 0.6; Si/Al = 29), the increase in relative fractions of hydrated Cu(II) apparently occurs to the expenses of $Z_2Cu(II)$ sites (see **Figure 5.6**(c,d)).

### 5.1.3 *Structural analysis of the Cu-sites by multi-component EXAFS fits*

Aiming to obtain a further validation of the composition-speciation relationships discussed above and a deeper structural characterization of the local coordination environment of the Cu ions hosted in the zeolite ring, a quantitative analysis of the *in situ* EXAFS spectra collected at 400 °C after dehydration in He (experimental data reported in **Figure 5.3**(c,d)) was performed. Herein, as already mentioned in the precedent sections, singling out the contributions from the different Cu-sites is not straightforward due to the existence of different Cu locations. Unconstrained multi-component fits can help to shed light on the Cu speciation, however it would results in an excess of strongly correlated free parameters, definitely yielding to not reliable results. In order to obtain a robust set of constrains to be further used in the multi-component fit procedure, it is necessary to carried out a preliminary fitting step by selecting the compositional points characterized by the purest Cu-speciation at 400 °C, showing the dominant contributions from each of the framework-interacting Cu-species evidenced by MCR-ALS, i.e. 1Al sites in their oxidized ZCu(II)OH or reduced ZCu(I) form and the $Z_2$Cu(II) sites.

Importantly, at this stage, it is also necessary to examine some alternative environments for the ZCu(I) and $Z_2$Cu(II) complexes, based on the DFT models obtained in previous works [17]. It is worth noting, in fact, that the ZCu(I) species, initially formed from the reduction of ZCu(II)OH moieties in the 8r, could either remain in 8r plane, or migrate to the energetically-favoured site in the 6r, as showed in [17]. The two locations are associated to different Cu local environments (especially in the second coordination sphere), which might result in rather similar XANES signatures but different EXAFS features in the 2−3 Å range. On the other hand, with respect to the $Z_2$Cu(II) in the 6r sites, within the limits imposed by the Löwenstein's rule [46], two possible configurations exist, depending on the siting for the two charge-balancing Al atoms within the 6r. In particular, –Al–Si–Al– and –Al–Si–Si–Al– linkages result in different Cu(II) local environments: in the latter case, Cu is shifted towards the centre of the 6r, adopting a less distorted four-fold coordination of the $O_{fw}$.

### 5.1.4 *Results of single-component fit on the purest He-activated states*

The preliminary single component EXAFS fits were performed selecting the spectra corresponding to the compositional points of the MCR-ALS concentrations plot characterized by the *purest* Cu-speciation at 400 °C. In particular, looking at **Figure 5.4**, it is possible to identify the samples where each of the dehydrated Cu-species listed above is present in more abundance. These are: i) sample (Cu/Al=0.5; Si/Al=15) where the ZCu(II)OH constituent is present with a fraction of ca. 75%, ii) sample (Cu/Al=0.6; 19) characterized by an amount of ZCu(I) species of ca. 90% and finally iii) sample (Cu/Al=0.1; Si/Al=5) showing ca. a 60% of $Z_2$Cu(II). As starting points for the EXAFS fits, the corresponding DFT-optimized geometry/geometries described in the previous **section 5.1.3**, have been adopted. The parametrizations adopted for each fit is described in detail in **section 5.1.4.1**. The results of mono-component fits on the samples showing the purest final state at 400 °C are reported in **Table 5.4-5.6**. These fits inherently represent an approximate description of the samples, and the refined parameters will suffer of a certain level of *contamination* from the other minor Cu-species. However, due to the presence of a largely dominant Cu-species, the refined structural parameters represent a good starting point for the subsequent multi-component fitting step. This is also supported by the good quality reached in the mono-component fits (at least in correspondence of the preferred structural environments) in terms of R-factor and physical reliability of the optimized parameters values. While for sample (Cu/Al=0.6; Si/Al=19) the refined parameters provided by the EXAFS fit are in good agreement with the related DFT model (ZCu(II)OH), see **Table 5.4**, for sample

(Cu/Al=0.5; Si/Al=15) the situation is less neat, see **Table 5.5**. Unfortunately, the local environment for ZCu(I) in 6r and 8r is difficulty distinguishable by EXAFS, albeit structurally different. Indeed, in the 6r configuration, an intrinsic antiphase is expected between the $T_{fw}$ shell ($N_{T(fw)} = 2$, $\langle R_{T(fw)} \rangle = 2.81$ Å from DFT) and the $O'_{fw}$ shells ($N_{O'(fw)} = 2$, $\langle R_{O'(fw)} \rangle = 2.51$ Å from DFT), making the resulting EXAFS signal rather similar to the one deriving from ZCu(I) sites in the 8r, where the $T_{fw}$ shell possess a lower coordination number $N_{T(fw)} = 1$. Considering the higher R-factor = 0.071 observed for ZCu(I) sites in the 8r and, in general, on the higher quality observed using the 6r model, this latter geometry was considered as the most representative for the ZCu(I) sites. Finally, as shown in **Table 5.6**, for sample (Cu/Al=0.1; Si/Al=5), a test fit performed using the $Z_2$Cu(II) Al−Si−Al configuration yielded significantly worse agreement with experimental spectrum (R-factor = 0.02826) with respect to what obtained for the Al−Si−Si−Al configuration (R-factor = 0.0065) and very high deviations from the DFT geometry (e.g. $\Delta R_{O'(fw)} \sim 0.2$ Å). The $Z_2$Cu(II) site hosted in 6r with Al−Si−Si−Al linkages is hence assumed as the most likely configuration describing the PC 4 species.

| **Composition: Cu/Al = 0.6; Si/Al = 19** | **Cu-species: Z[Cu(II)OH]** |
|---|---|
| DFT-model of dominant Cu-species | 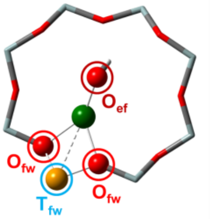 |
| R-factor | 0.0058 |
| $N_{par}$ ($N_{ind}$) | 8 (13) |
| $S_0^2$ | 1.0 ± 0.1 |
| ΔE (eV) | − 3 ± 2 |
| $R_{O(ef)}$ (Å) | 1.81 ± 0.01 (1.76) |
| $\langle R_{O(fw)} \rangle$ (Å) | 1.90 ± 0.04 (1.99) |
| $R_{T(fw)}$ (Å) | 2.72 ± 0.02 (2.73) |
| $\alpha_{fw}$ | − 0.04 ± 0.01 |
| $\sigma^2_{O(ef)}$ (Å$^2$) | 0.007 ± 0.003 |
| $\sigma^2_{O(fw)}$ (Å$^2$) | 0.004 ± 0.003 |
| $\sigma^2_{T(fw)}$ (Å$^2$) | 0.010 ± 0.003 |
| $ss_{fw}$ (Å$^2$) | 0.02 ± 0.1 |

**Table 5.4:** Results from mono-component EXAFS fits of He-activated Cu-CHA with composition (Cu/Al = 0.6; Si/Al = 19) using the ZCu(II)OH model. Average bond distances from Cu in the DFT-optimized geometry are reported in parentheses.

| **Composition:** | **Cu-species: 1Al ZCu(I)** | |
|---|---|---|
| **Cu/Al = 0.5; Si/Al = 15** | **Preferred environment ZCu(I) 6r** | **Alternative environment ZCu(I) 8r** |
| DFT-model of dominant Cu species | 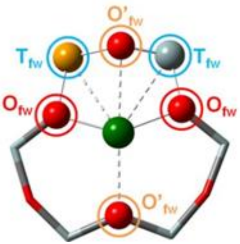 | 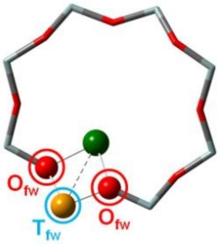 |
| Fit R-factor | 0.019 | 0.071 |
| $N_{par}$ ($N_{ind}$) | 10 (13) | 8 (13) |
| $S_0^2$ | 1.0 ± 0.1 | 1.0 ± 0.1 |
| $\Delta E$ (eV) | − 7.7 ± 0.4 | − 7 ± 1 |
| $<R_{O(fw)}>$ (Å) | 1.86 ± 0.02 (1.91) | 1.91 ± 0.01 (1.96) |
| $<R_{O'(fw)}>$ (Å) | 2.59 ± 0.05 (2.51) | - |
| $<R_{T(fw)}>$ (Å) | 2.70 ± 0.06 (2.81) | 2.73 ± 0.04 (2.71) |
| $\alpha_{fw}$ | − 0.05 ± 0.03 | − 0.02 ± 0.04 |
| $\sigma^2_{O(fw)}$ (Å$^2$) | 0.008 ± 0.001 | 0.009 ± 0.001 |
| $\sigma^2_{O'(fw)}$ (Å$^2$) | 0.008 ± 0.001 | - |
| $\sigma^2_{T(fw)}$ (Å$^2$) | 0.011 ± 0.004 | 0.014 ± 0.005 |
| $ss_{fw}$ (Å$^2$) | 0.017 ± 0.008 | 0.011 ± 0.008 |

**Table 5.5:** Results from mono-component EXAFS fits for He-activated Cu-CHA with composition (Cu/Al = 0.5; Si/Al = 15) using the ZCu(I) models in both d6r (preferred environment) and 8r (alternative environment). Average bond distances from Cu in the DFT-optimized geometry are reported in parentheses.

| **Composition:** | **Cu-species: $Z_2Cu(II)$** | |
|---|---|---|
| **Cu/Al = 0.1; Si/Al = 5** | **Preferred environment $Z_2Cu(II)$ "Al-Si-Si-Al"** | **Alternative environment $Z_2Cu(II)$ "Al-Si-Al"** |
| DFT-model of dominant Cu species | 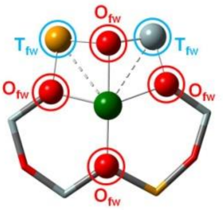 | 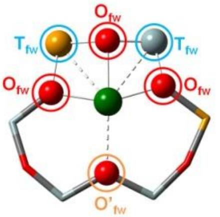 |
| Fit R-factor | 0.0065 | 0.017 |
| $N_{par}$ ($N_{ind}$) | 8 (13) | 10 (13) |
| $S_0^2$ | 0.9 ± 0.1 | 0.9 ± 0.1 |
| $\Delta E$ (eV) | − 5 ± 2 | − 1 ± 2 |
| $<R_{O(fw)}>$ (Å) | 1.96 ± 0.01 (2.03) | 1.98 ± 0.01 (1.97) |
| $R_{O'}$ (Å) | - | 2.62 ± 0.08 (2.39) |
| $R_{T(fw)}$ (Å) | 2.79 ± 0.01 (2.80) | 2.74 ± 0.04 (2.71) |
| $\alpha_{fw}$ | − 0.02 ± 0.01 | − 0.01 ± 0.01 |
| $\sigma^2_{O(fw)}$ (Å$^2$) | 0.007 ± 0.002 | 0.003 ± 0.001 |
| $\sigma^2_{O'(fw)}$ (Å$^2$) | - | 0.001± 0.001 |
| $\sigma^2_{T(fw)}$ (Å$^2$) | 0.011 ± 0.002 | 0.007 ± 0.005 |
| $ss_{fw}$ (Å$^2$) | 0.017 ± 0.004 | 0.003 ± 0.004 |

**Table 5.6.:** Results from mono-component EXAFS fits for He-activated Cu-CHA with composition (Cu/Al = 0.1; Si/Al = 5) using the $Z_2Cu(II)$ in 6r with either Al−Si−Al (alternative environment) or Al−Si−Si−Al linkages (preferred environment). Average bond distances from Cu in the DFT-optimized geometry are reported in parentheses.

### 5.1.4.1 *Fit details and shell model adopted for the EXAFS analysis*

Both mono-component and multi-component fits of the *in situ* EXAFS spectra collected at 400 °C on the He-activated Cu-CHA catalysts were performed in R-space in the $\Delta R$ = 1.0 − 3.2 Å range, on the FT of the $k^2$-weigthed $\chi(k)$ EXAFS spectra transformed in the 2.4 – 11.0 Å$^{-1}$ range, resulting in 13 independent points ($2\Delta k\Delta R/\pi + 1$ > 13). Phases and amplitudes have been calculated by FEFF6l code [47] and the minimization was realised using the Artemis (IFEFFIT) code [48]

The model included all the single-scattering (SS) paths contributing in the analysed R-space range. In order to limit the number of optimized variables, all the SS paths included in the fitting model have been associated to the same passive amplitude reduction factor ($S_0^2$) and to the same energy shift parameter ($\Delta E$). The Coordination numbers were fixed according to the relevant DFT-models discussed above, see **section 5.1.4**.

In the employed fitting model, the following coordination shells around the Cu absorber were identified:

- First-shell extra-framework oxygen atom ($O_{ef}$), only present in the ZCu(II)OH geometry with coordination number $N_{O(ef)}$ = 1; parametrized with specific radial shift $\Delta R_{O(efw)}$ and $\sigma^2_{O(efw)}$ parameters to properly account for the different chemical nature of extra-framework O-ligands with respect to the zeolite $O_{fw}$ atoms.

- First-shell framework oxygen atoms ($O_{fw}$), present in all the examined geometries with coordination numbers $N_{O(fw)}$ in the 2−4 range; parameterized with an independent radial shift ($\Delta R_{O(fw)}$) applied to the individual DFT-optimized bond distances and Debye-Waller (DW) factor ($\sigma^2_{O(fw)}$).
- Second-shell framework oxygen atoms ($O'_{fw}$), present in the geometries for ZCu(I) in 6r (coordination number $N_{O'(fw)} = 2$), and $Z_2Cu(II)$ in 6r with Al−Si−Al linkages (coordination number $N_{O'(fw)} = 1$; parametrized with an independent $\Delta R_{O'(fw)}$ and the same DW used for the SS contribution involving the first shell framework oxygens: $\sigma^2_{O'(fw)} = \sigma^2_{O(fw)}$.
- Second-shell framework Si/Al atoms ($T_{fw}$), present in all the geometries, with coordination number $N_{T(fw)} = 1$ in ZCu(II)OH in 8r and ZCu(I) in 8r and of $N_{T(fw)} = 2$ in all the other geometries; parameterized with an independent radial shift ($\Delta R_{T(fw)}$) and DW factor ($\sigma^2_{T(fw)}$).
- SS paths involving farer Si and O neighbours of the 6r and 8r (fw), with distances from the Cu absorber in the 2.8–3.5 Å range and coordination number of $N_{fw} = 6$ and $N_{fw} = 4$ for 6r and 8r geometries, respectively; modelled considering a common contraction/expansion factor $\alpha_{fw}$ and DW factor $\sigma^2_{fw}$ increasing as the square root of the distance $R_{eff,i}$ of the i^th^ scattering atom from the absorber ($\Delta R_{fw,i} = \alpha_{fw} R_{eff,i}$, $\sigma^2_{fw,i} = ss_{fw} (R_{eff,i}/R_0)^{1/2}$, where $R_0$ denotes the shortest $R_{eff}$ for the group of paths).

The number of fit parameters varied from 8 to 10, depending on the specific DFT-optimized geometries employed as starting guess, being always below the number of employed independent points (13). The fit quality was evaluated considering the R-factor values.

### 5.1.5 *Result of the multi-component fits on the purest He-activated states*

Mono-component EXAFS fits provides the experimentally-optimized geometries for the three framework-interacting Cu-species expected to dominate Cu-speciation in He-activated Cu-CHA (see **Figure 5.8**(a)), setting the scene for a multi-component fitting protocol extended to the whole series of catalysts. To this aim, three sets of EXAFS paths including all the SS paths contributing in the 1.0 – 3.2 Å range for the Cu-sites shown in **Figure 5.8**(a) have been considered. For each geometry, the bond distances to the best-fit values obtained in the correspondent mono-component fit were fixed, moreover a global $S_0^2$ has been set to the ideal value of 1. Hence, for each catalyst composition, the fitted parameters consisted in: i) the DW factors for the relevant shell of atomic neighbours, and most importantly, ii) the relative fractions $x_i$ for each component, i = ZCu(II)OH, ZCu(I), $Z_2Cu(II)$. The results of the multi-component EXAFS fits are summarized in **Figure 5.8**(b) and in **Table 5.7**. For all catalysts, a very good level of reproduction of the experimental EXAFS spectra was achieved by combining the three structural components singled out by MCR-ALS.

The highest levels of structural disorder are still seen for Si/Al = 14, 15 samples. This is not surprising, due to the fickle nature of the Cu(I) component which dominates in these highly-reducible catalysts. For all the other samples, R-factor values well below 2% are obtained, in line with the lower mobility of Cu(II) ions.

| **Composition (Cu/Al; Si/Al)** | **(0.1; 5)** | **(0.3; 5)** | **(0.1; 14)** | **(0.5; 15)** | **(0.6; 19)** | **(0.6; 29)** |
|---|---|---|---|---|---|---|
| Fit R-factor | 0.007 | 0.007 | 0.044 | 0.017 | 0.006 | 0.014 |
| $N_{par}$ ($N_{ind}$) | 8 (12) | 8 (12) | 8 (12) | 8 (12) | 8 (12) | 8 (12) |
| $\Delta E$ (eV) | −5.8 ± 0.6 | −6.0 ± 0.5 | −7 ± 1 | −7.0 ± 0.8 | −3.2 ± 0.4 | −3.8 ± 0.4 |
| $x_{ZCu(II)OH}$ | 0.0 ± 0.2 | 0.0 ± 0.1 | 0.0 ± 0.3 | 0.1 ± 0.2 | 1.0 ± 0.2 | 0.4 ± 0.1 |
| $x_{ZCu(I)}$ | 0.2 ± 0.1 | 0.4 ± 0.1 | 0.7 ± 0.1 | 0.8 ± 0.2 | 0.0 ± 0.1 | 0.6 ± 0.2 |
| $x_{Z2Cu(II)}$ | 0.8 ± 0.2 | 0.6 ± 0.1 | 0.3 ± 0.1 | 0.1 ± 0.1 | 0.0 ± 0.1 | 0.0 ± 0.1 |
| $\sigma^2_{O(ef)}$ (Å$^2$) | 0.007±0.002 | 0.008±0.002 | 0.008±0.002 | 0.007±0.002 | 0.007±0.001 | 0.007±0.001 |
| $\sigma^2_{O(fw)}$ (Å$^2$) | 0.007±0.001 | 0.007±0.001 | 0.008±0.001 | 0.009±0.001 | 0.004±0.001 | 0.007±0.001 |
| $\sigma^2_{T(fw)}$ (Å$^2$) | 0.011±0.002 | 0.014±0.003 | 0.010±0.002 | 0.012±0.002 | 0.014±0.003 | 0.009±0.001 |

**Table 5.7:** Results from multi-component EXAFS fits of He-activated state at 400 °C for the whole multi-composition sample series. Fits performed in the $k$-range (2.4−11.0) Å$^{-1}$ and $R$-range (1.0−3.2) Å. For all the fits, geometries of ZCu(II)OH, ZCu(I), and $Z_2$Cu(II) Cu-species (i.e. radial shift parameters $\Delta R_i$) have been fixed based on the results on mono-component fits on *purest* He-activated states ZCu(II)OH model for sample (0.6; 19), ZCu(I) in 6r for sample (0.5; 15), $Z_2$Cu(II) in 6r with Al-Si-Si-Al linkage for sample (0.1; 5). Finally, the $S_0^2$ have been set to unity

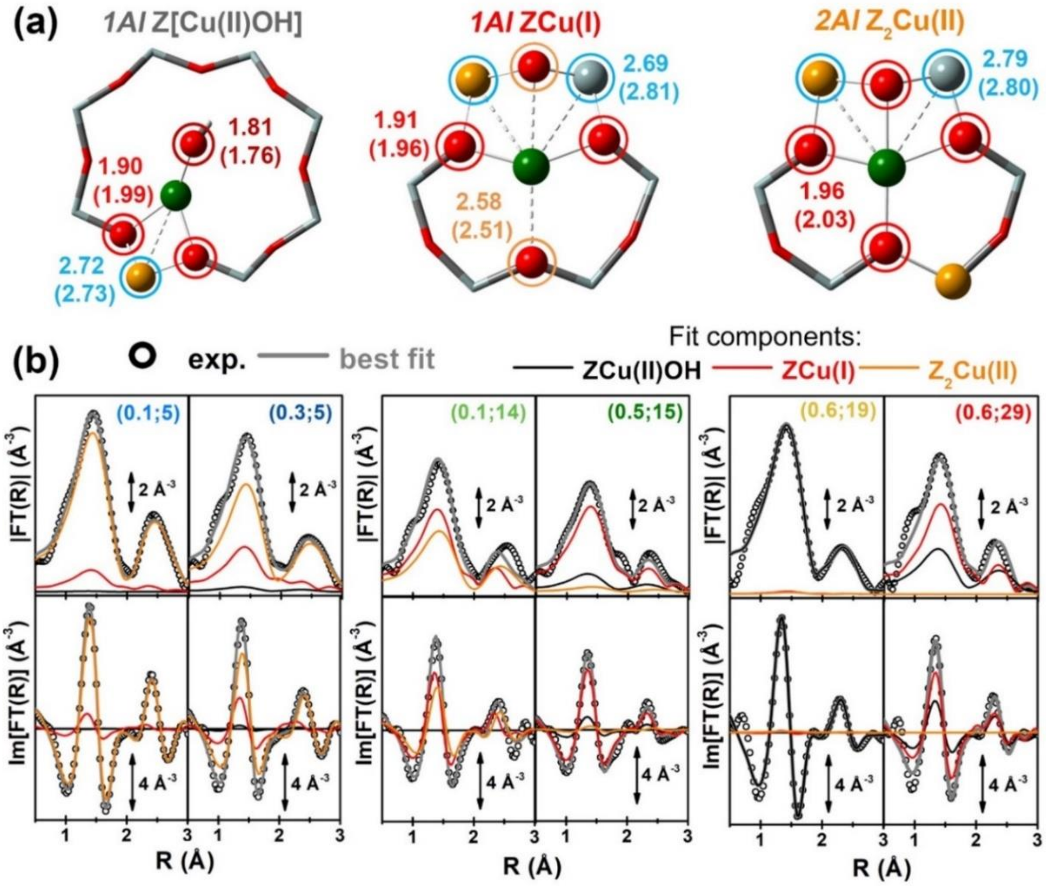

**Figure 5.8:** (a) DFT-optimized structural models for framework-interacting Cu-species dominating Cu-speciation in He-activated Cu-CHA at 400 °C, namely ZCu(II)(OH), ZCu(I), and $Z_2$Cu(II) sites. The atoms located the first and second coordination shell of Cu are shown in ball-and-stick mode (atom colour code: Cu, green; H, white; O, red; Si, grey; Al, yellow) and highlighted with coloured circles indicating the different coordination shells included in the EXAFS fitting model (Cu−$O_{ef}$: wine; Cu−$O_{fw}$: red; Cu−$O'_{fw}$: orange; Cu−$T_{fw}$: blue). For each shell, the average bond distances from Cu refined by mono-component EXAFS fits are reported in Å, whereas the correspondent starting values from DFT are reported in parentheses. (b) Comparison between experimental (black circles) and best fit (light grey thick lines) FT-EXAFS spectra (top panel: magnitude, bottom panels: imaginary part) obtained from multi-component fits on the whole Cu-CHA sample series; for each sample, the weighted contributions from the three dehydrated Cu-species included in the fitting model are also reported as thin solid lines (ZCu(II)OH: grey, ZCu(I): red; $Z_2$Cu(II): orange).

Noteworthy, for all the investigated samples, the second-shell peak in the FT-EXAFS spectra is properly reproduced solely considering Cu−$T_{fw}$ contributions, in excellent agreement with the different environments predicted for 1Al and 2Al sites shown in **Figure 5.8**(a). In general, the multi-component fits reported in **Figure 5.8**(b) discourage a significant contribution of Cu−Cu paths in the second-shell region, i.e. in the 2.0−2.8 Å range of the phase-uncorrected FT-EXAFS. However, it is not possible to exclude that such Cu−Cu scattering contributions could emerge at higher distances, where unfortunately the technique is not accurate enough. Further experiments, as the ones that will be discussed in the **sections 5.2** and **5.3**, focusing on high-temperature activation in $O_2$ and employing enhanced data collection statistics to improve the S/N ratio in the high k-range, are able to provide a more conclusive results on the presence of diluted multimeric Cu-oxo moieties.

In the view of a cross-validation of the employed methods, **Figure 5.9** compares, as a function of the catalyst composition, the relative fractions of ZCu(II)OH, ZCu(I), and $Z_2$Cu(II) species in He-activated Cu-CHA at 400 °C evaluated from MCR-ALS XANES analysis and multi-component EXAFS fits. Within the EXAFS fitting errors, the two methods yield a substantially comparable Cu-speciation in the final He-activated state, corroborating the speciation-composition trends discussed in the precedent sections.

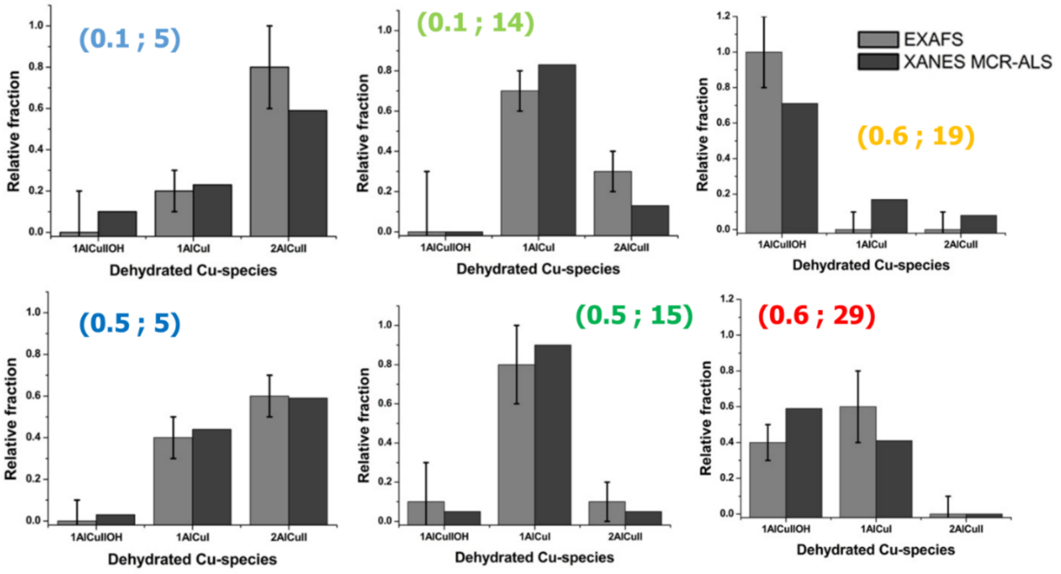

**Figure 5.9:** Result of the fraction retrieved form the EXAFS LCF fit plotted together with the fraction of species retrieved by the MCR-ALS analysis.

## 5.2 CORRELATING CU-SPECIATION FROM XAS ANALYSIS WITH DMTM PRODUCTIVITY FOR CU-CHA

XAS spectroscopy is a technique able to provide important information on the average coordination and on the oxidation state of the Cu species resulting from different activation procedures. This fact determines that it can be employed properly to understand the inner relation between the Cu-speciation and the sample performance. To this aim, a representative Cu-CHA sample, possessing a Cu/Al=0.5 and Si/Al=12 ratio, has been subjected to four different treatments. These are: (i) standard $O_2$-activation at 500 °C, (ii) activation in He at 500 °C, (iii-iv) activation in He at 500 °C followed by the reaction with $O_2$, either at 500 °C or at 200 °C, see **section 5.8.1** of the appendix for technical detail about the data acquisition. It is worth noting that the sample (0.5; 12) resulted in an optimal performance for the DMTM process (normalized productivity of ca. 0.17 mol$CH_3OH$/mol Cu) using optimized process conditions as described in details in [15], this fact lead to the possibility to consider it as a good reference. For testing purposes, the sample, after the different activation processes, was subsequently put in contact with 1000 mbar of $CH_4$ at 200 °C for 60 min and finally the steam-assisted extraction of the products was performed at 135 °C.

The characteristic XANES features detected after the different activation protocols, showed in **Figure 5.10** can be interpreted on the basis of previous studies on the Cu K-edge XANES in Cu-zeolites [17, 20, 29, 49, 50]. The XANES spectrum associated to the high-temperature $O_2$-activation results appears to be in a virtually pure Cu(II) state.

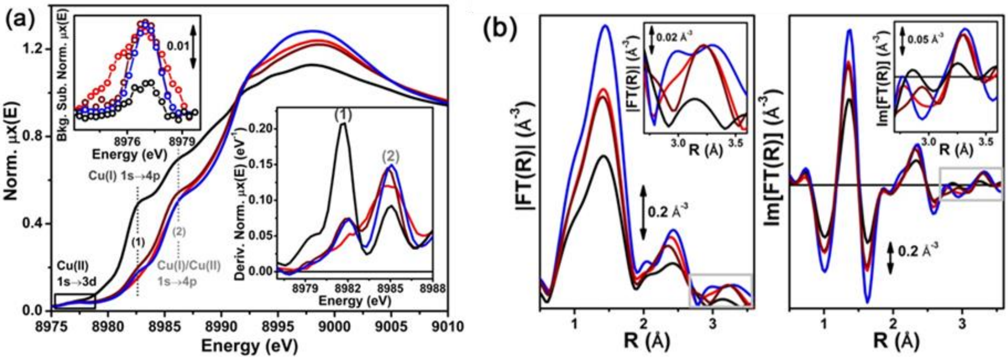

**Figure 5.10:** XAS characterization of the (0.5;12) Cu-CHA sample after different pre-treatment and impact of the pre-treatment on productivity. (a) Main panel: Cu K-edge XANES of the (0.5;12) Cu-CHA sample after standard $O_2$-activation at 500 °C (red curves), activation in He at 500 °C (black curves), activation in He at 500 °C followed by oxidative treatment in pure $O_2$ at 500 °C (violet curves) and at 200 °C (blue curves), after cooling the He-activated sample from 500 to 200 °C in He; left inset: background-subtracted pre-edge 1s → 3d peak fingerprinting the presence of $d^9$ Cu(II) ions in the system; please note that XANES of the $O_2$-activated sample has been measured using a slightly different energy sampling step, which results in an apparent broadening of the background-subtracted pre-edge peak with respect to the other investigated cases. Right inset: first derivative of the XANES spectra reported in the main panel in the rising-edge region. Labels (1) and (2) in main panel and right inset refer to the rising-edge 1s → 4p peaks characteristic of Cu(I) and Cu(I)/Cu(II) ions, respectively. (b) Magnitude (left) and imaginary part (right) of the FT-EXAFS spectra for the (0.5; 12) Cu-CHA sample realised in the $k$ range within (2.4–10.8) $Å^{-3}$ using the same colour code as in part (a). The insets report a magnification of the high-$R$ region of FT-EXAFS spectra, highlighted by light grey boxes in the main panels.

A pronounced rising-edge shoulder is, in fact, observed in the 8985–8990 eV range, assigned to 1s → 4p transitions in three-/four-fold coordinated Cu(II) sites. The weak pre-edge peak, arising from the 1s → 3d transition in $d^9$ orbitals of the Cu(II) ions, is also well evident (see **Figure 5.10**(a) , left inset). Within the spectral resolution of this data, no evidence of Cu(I) species is found after the $O_2$-activation step. Indeed, the presence of Cu(I) would be fingerprinted by well-defined rising-edge peak at energies below 8984 eV, yielding a maximum around 8982 eV in the first derivative of the XANES spectrum. This is visible also at very low relative abundance of Cu(I) species, see the right inset in **Figure 5.10**(a). It follows that the presence of oxygen during thermal treatment from RT to 500 °C completely inhibits the formation of Cu(I) sited during the activation that, in **section 5.1**, has been named as self-reduction effect [1, 3, 27].

The $k^2$-weighted, phase uncorrected, Fourier transform (modulus and imaginary part) of the EXAFS spectra collected at 500 °C after $O_2$-activation (**Figure 5.10**(b), red curves) shows three well defined maxima, peaking at ca. 1.4, 2.4, and 3.2 Å in the phase-uncorrected spectrum. In the first- and second-shell region the spectrum is very similar to what was observed in a previous study performed by Borfecchia et al. [17] on a set of $O_2$-activated CHA zeolites. In particular, the EXAFS fitting, whose description is reported in **section 5.2.1**, reveals that the first maximum derives from the Cu-O single scattering (SS) paths involving two framework ($O_{fw}$) and one extra-framework ($O_{efw}$) oxygen in the first coordination shell of Cu at 1.97 ± 0.04 and 1.86 ± 0.05 Å, respectively. As described in in **section 5.1**, the second maximum in the FT-EXAFS is associated to the EXAFS features of SS paths involving the second-shell of Al/Si atoms occupying the T-sites of the zeolite lattice. The EXAFS fit refines, in fact, the location of the Cu-Al contribution at 2.72 ± 0.02 Å. Finally, it is plausible to connect the third maximum in the FT-EXAFS spectra with neighboring Cu sites in diluted $Cu_xO_y$ moieties with metal-metal separations around 3.5 Å, also considering the lack of other important scattering contributions in this $R$-space range. This supposition is confirmed by the Cu-Cu distance refined by the EXAFS fit at 3.41 ± 0.06 Å.

When the sample is activated in He at 500 °C, a picture similar to the ones described in **section 5.1** is proposed again. The XANES (**Figure 5.10**(a), black lines) prominently exhibit the characteristic Cu(I) 1s → 4p peak at 8982.5 eV while the pre-edge peak mostly arising from the Cu(II) 1s → 3d transition is significantly abated, although not completely. The overall XANES spectral shape is, in this case, representative of a largely dominant Cu(I) state. In the corresponding FT-EXAFS spectrum (**Figure 5.10**(b)) it is possible to observe a distinctly lower intensity in the whole range confirming the presence of states consisting in *bare* ZCu(I) ions sited in both 6r and 8r of the CHA framework [17, 40]. Such heterogeneity, together with the higher mobility of Cu(I) ions with respect to Cu(II) causes a broadened and dampened second-shell signal in the FT-EXAFS spectrum. After He-activation, the third maximum at ca. 3.2 Å, well evident after $O_2$-activation and tentatively associated with high-R Cu-Cu scattering contributions as discussed above, is barely detectable.

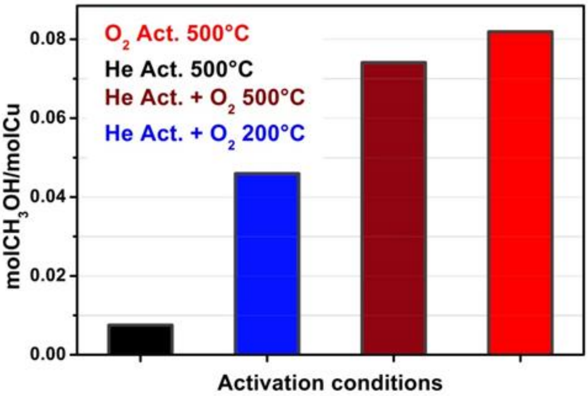

**Figure 5.11:** Normalized methanol productivity (molCH$_3$OH/mol Cu) over the (0.15; 12) sample in correspondence of each pre-treatment described above,

followed by $CH_4$ activation at 200 °C for 60 min using 1000 mbar $CH_4$ feed, and $H_2O$ assisted extraction at 135 °C.

After the two different pretreatments, the productivities of $CH_3OH$, normalized for the total amount of Cu for each sample (measured by D. Pappas (Oslo University)), are equal to 0.008 mol$CH_3OH$/mol Cu (4.65 μmol/g) and 0.082 mol$CH_3OH$/mo lCu (50.8 μmol/g) for He and $O_2$ activation, respectively, see **Figure 5.11**. This graph clearly indicates a positive correlation between $CH_3OH$ yield and the existence of Cu(II) species in the activated materials. Clearly, a drastic reduction of the productivity is seen when the pretreatment is carried out in the absence of $O_2$. Focusing more in detail on **Figure 5.10**(a) it is possible to note that, though significantly dampened, the Cu(II) 1s → 3d peak is still detectable after the He-activation, indicating that a small fraction of Cu(II) remains in the sample even after thermal-treatment in He at 500 °C. It follows that the residual $CH_3OH$ yield observed after He-activation is most likely to be connected with the minor contribution from such residual Cu(II) species. Among these, it is possible to safely include the redox-inert bare $Z_2$Cu(II) in the 6r, that compose a minor structural component in high Cu-loading . Other possible configurations could include diluted $Cu_xO_y$ moieties and minor CuO aggregates, escaping from the self-reduction as suggested by EPR studies [51]. However, based on the results reported in the following (see **section 5.2.2**), a contribution from bare $Z_2$Cu(II) sites in 6r is discouraged. Hence, diluted $Cu_xO_y$ moieties in CHA not undergoing self-reduction during pre-treatment could be responsible for C−H bond cleavage at these conditions.

To decouple the high-temperature treatment in inert, leading to dehydration, and self-reduction of Cu from the reaction with $O_2$ resulting in the oxidation of Cu(I) species, the He-activated sample was subjected to a flow of $O_2$ for 30 min at two different temperatures (i.e. 500 and 200 °C, violet and blue curves/bars in **Figure 5.10**(a-c)). The subsequent oxidation at 500 °C yields very similar XAS spectra with respect to the sample activated directly in $O_2$. Similarly, the productivity after the two different activations is almost equivalent, only a ca. 10 % of difference was observed, see **Figure 5.11**. Nonetheless, as it can be clearly noted by looking at the first derivative of the XANES spectrum, a small Cu(I) amount (ca. 10% total Cu) is still present after the subsequent oxidation, which is in line with the slightly lower productivity. Persistent Cu(I) sites may have positioned into less accessible locations during the He-activation, which seemingly does not occur during direct $O_2$-activation. Upon subsequent oxidation at 500 °C, FT-EXAFS clearly evidences an increased coordination number in the first shell of Cu with respect to the He-activated state: the intensity of the first maximum becomes only slightly lower with respect to the one observed after $O_2$-activation, in line with the presence of a minor fraction of two-fold coordinated Cu(I) sites. The second-shell peak in the FT-EXAFS of the material exposed to $O_2$ at 500 °C is more intense and well defined compared to what has been observed after He-activation. The third maximum at ca. 3.2 Å also markedly develops, reaching a very similar intensity as after $O_2$-activation.

Carrying out the reaction with $O_2$ at 200 °C, it results in the same relative Cu(II)/Cu(I) abundance as observed at 500 °C (this evidence emerges looking at the intensities of the 1s → 3d peak transition for both the activations typologies). Herein a largely dominant Cu(II) state is formed, with a residual fraction of ca.

10% Cu(I), indicating that the same fraction of Cu(I) species, formed during inert treatment react with oxygen even at lower temperature. Although XAS evidences that the relative fraction of Cu(II) species formed upon re-oxidation at 500 °C and 200 °C is virtually equivalent, performance evaluation indicates a yield equal to 0.046 mol$CH_3OH$/mol Cu, 45% less compared to the highest-one. Hence, low temperature oxidation alters the balance between active and inactive Cu(II) species, making it less efficient with respect to the re-oxidation process at the higher temperature.

Further insights can be obtained by comparing to each other the XAS spectra of the material contacted with $O_2$ at 500 °C and 200 °C, which reveal significant differences in the average coordination environment of the Cu(II) component. In particular, re-oxidation at 200 °C yield a higher intensity of the XANES W.L. peak around 8998 eV and of the first-shell peak in the FT-EXAFS. Both these observations point towards a higher relative fraction of four-fold coordinated Cu(II) sites formed when Cu(I) is reacted with $O_2$ at 200 °C, possibly connected with a preference towards a side-on $O_2$ binding mode in Cu(II) complexes. Matching these evidences, it is possible to suppose that the Cu(II) complexes, stemming either from $O_2$-activation or oxidation of a pre-reduced sample, have temperature-dependent coordination preferences: three-coordinated species are favored at 500 °C but undergo a partial conversion to four-coordinated species at 200 °C. If the reaction between Cu(I) and $O_2$ is directly conducted at 200 °C, the preference towards four-coordinated Cu(II) complexes appears more pronounced. The significantly lower productivity observed in the latter conditions suggests that the tridentate coordination mode of the Cu(II) centers, with first-shell ligation to two $O_{fw}$ and one $O_{efw}$ atom, should be the most favorable one for the active Cu sites responsible of methane to methanol conversion of the sample.

Such a coordination mode is the one characteristic of ZCu(II)OH species, which are currently considered as the prototypes for redox-active framework-interacting Cu-sites in Cu-CHA. It is worth noting that their presence after the $O_2$-activation at 400 °C has been ascertained by *in situ* FTIR [18, 36, 44] detecting their $\nu$(OH) fingerprint band at 3656 $cm^{-1}$ and their high stability in the proximity of 1Al sites in the 8r has been confirmed by DFT [5, 33, 36]. Nevertheless, from the results discussed above, it is difficult to conclude that the ZCu(II)OH could be the Cu(II) species responsible for the $CH_4$ conversion, as it has been suggested theoretically [52]. Indeed, it is reasonable to expect a significant population of such species after both He and $O_2$ activation at 250 °C, i.e. when dehydration is completed and before the self-reduction process initiates [17, 40]. However, these kinds of pre-treatment does not yield significant methanol productivity, as proved by the testing results reported in the S.I. of ref. [15].

The reaction involving the (0.15; 12) reduced sample at 500 ºC with $O_2$, most likely yield Cu-$O_2$* moieties which give much higher productivity, fully comparable with $O_2$-activation.

### 5.2.1 *EXAFS analysis on CHA (0.5; 12) after $O_2$ Activation at 500 °C*

The EXAFS fitting for the CHA (0.5; 12) sample after $O_2$ activation at 500 °C was performed in the R-space, in the $\Delta R$ = 1.0 – 4.0 Å range, on the FT of the $k^2$-weigthed $\chi(k)$ EXAFS spectrum transformed in the 2.4 – 10.8 $Å^{-1}$ range, resulting in 17 independent points ($2\Delta k\Delta R/\pi +1> 17$). As starting guess for the EXAFS fit the DFT-optimized geometry of the ZCu(II)OH site reported in **section 5.1.1** was used. Here, the local environment of Cu includes one extra-framework oxygen atom ($O_{efw}$, $R_{O(efw)}$ = 1.76 Å from DFT) and two framework oxygen atoms ($O_{fw}$, $<R_{O(fw)}>$ = 1.99 Å from DFT) in the first-shell; one Al atom ($T_{fw}$, $R_{T(fw)}$ = 2.73 Å from DFT) in the second shell and eight framework Si/O neighbours (fw) in the 2.8–3.5 Å range. Similarly to the fitting procedure reported in for the 400 °C - He activated sample (see **section 5.1.4**), the SS paths involving these far atomic neighbours were modelled considering a common contraction/expansion factor $\alpha_{fw}$ and a DW factor $\sigma^2_{fw}$ increasing as the square root of the distance $R_{eff,i}$ of the i$^{th}$ scattering atom from the absorber ($\Delta R_{fw,i} = \alpha_{fw}$, $R_{eff,i}$, $\sigma^2_{fw,i} = ss_{fw} (R_{eff,i}/R_0)^{1/2}$, where $R_0$ indicates the shortest first-shell path present in the fitting model). Excluding the contribution of H atoms, in principle, the analysed structural model can be representative also for other tridentate Cu(II)-moieties formed in the presence of $O_2$.

The best-fit values for the 10 parameters optimized in this fit are reported in **Table 5.8** (second column), while the best-fit and experimental spectra are compared in **Figure 5.12**(b,c).

| **EXAFS Parameters** | **Z[Cu(II)O$_{efw}$]** | **Z[Cu(II)O$_{efw}$] + Cu−Cu @ 3.5 Å** |
|---|---|---|
| R-factor | 0.011 | 0.009 |
| $N_{par}$ ($N_{ind}$) | 10 (16) | 11 (16) |
| $S_0^2$ | 0.9 ± 0.1 | 0.9 |
| $\Delta E$ (eV) | − 3 ± 1 | − 2 ± 1 |
| $R_{O(ef)}$ (Å) | 1.86 ± 0.05 | 1.86 ± 0.05 |
| $\sigma^2_{O(ef)}$ (Å$^2$) | 0.005 ± 0.003 | 0.005 ± 0.003 |
| $<R_{O(fw)}>$ (Å) | 1.97 ± 0.04 | 1.97 ± 0.04 |
| $\sigma^2_{O(fw)}$ (Å$^2$) | 0.004 ± 0.003 | 0.004 ± 0.003 |
| $R_{T(fw)}$ (Å) | 2.75 ± 0.02 | 2.72 ± 0.02 |
| $\sigma^2_{T(fw)}$ (Å$^2$) | 0.009 ± 0.003 | 0.009 ± 0.003 |
| $\alpha_{fw}$ | − 0.03 ± 0.01 | − 0.03 ± 0.01 |
| $ss_{fw}$ (Å$^2$) | 0.017 ± 0.005 | 0.016 ± 0.005 |
| $x_{Cu(ef)}$ | − | 0.3 ± 0.3 |
| $N_{Cu(ef)}$ | − | 1 |
| $R_{Cu(efw)}$ (Å) | − | 3.41 ± 0.06 |
| $\sigma^2_{Cu(ef)}$ (Å$^2$) | − | 0.01 |

**Table 5.8:** Results from EXAFS fit for the (0.5; 12) sample after $O_2$ activation at 500 °C using as starting guess for the fit: (i) only the ZCu(II)$O_{efw}$ model, second column; (ii) the ZCu(II)$O_{efw}$ model plus a Cu-Cu SS path. Fixed parameters in fit (ii) are underlined.

Overall, a good fit is obtained (R-factor = 0.01). All the guessed parameters are refined to physically-meaningful values falling within the expectation ranges for high-temperature data collection. EXAFS analysis confirms that the average local environment for the Cu(II) sites in the $O_2$-activated material at 500 °C is well described by a tridentate sites with asymmetric first-shell ligation to one $O_{efw}$ atom, at a shorter distance from the Cu centre, and to two $O_{fw}$ from the zeolite lattice, with longer Cu−$O_{fw}$ bond lengths. A significantly elongated Cu−$O_{ef}$ distance of (1.86 ± 0.05) Å was found with respect to the Cu-$O_{OH}$ bond length of 1.76 Å predicted by DFT for the ZCu(II)OH model. Although such deviation is still acceptable within the respective errors of DFT and EXAFS fit, it could also supports the possible conversion of a fraction of ZCu(II)OH into other tridentate Cu(II) species, formed at high temperature in the presence of $O_2$ and characterized by longer Cu−$O_{efw}$ bond distances.

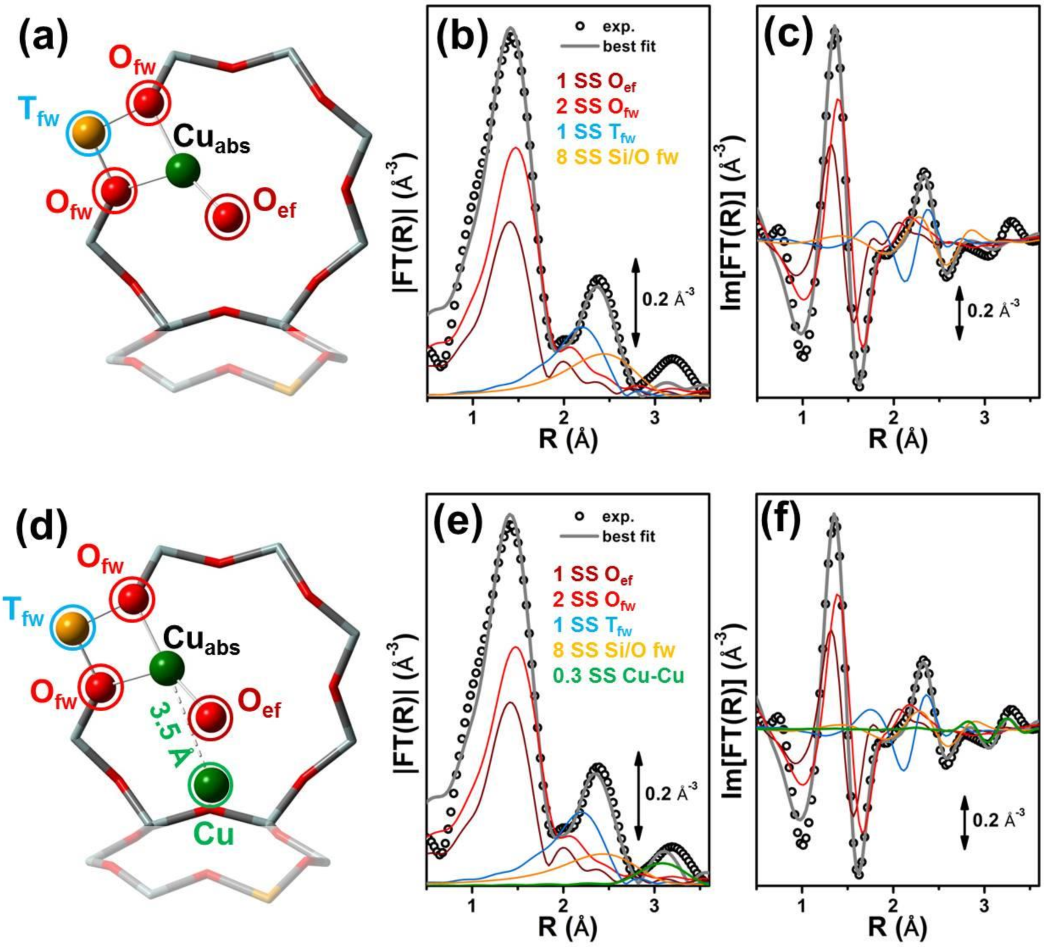

**Figure 5.12:** (a) Geometry for $ZCu(II)O_{efw}$ sites: Cu (absorber), green; O, red, Al, orange; Si, grey; the atoms belonging to the first and second coordination shells of Cu are shown in ball-and-stick mode and highlighted by coloured circles according to the following color code: violet, $O_{efw}$; red $O_{fw}$; light blue, $T_{fw}$. (b, c) Magnitude (b) and imaginary part (c) of the experimental phase-uncorrected FT-EXAFS spectra for the (0.5;12) sample after $O_2$ activation at 500 °C (black circles) compared with correspondent best fit curves (grey thick lines) obtained using the $ZCu(II)O_{efw}$ geometry reported in part (a). The principal contributions to the EXAFS signal are also reported as coloured thin lines, using the same colour code as in part (a). (d) As part (a) but including in the model geometry an additional $Cu_{efw}$ atom (green circle) at 3.5 Å from the Cu absorber. (e, f) As parts (b, c) but using the geometry shown in part (d); the Cu−Cu SS path at 3.5 Å has been modelled with a guessed coordination number ($N_{Cu}$) and a fixed DW factor ($\sigma^2_{Cu}$ = 0.01 Å$^2$). The $Cu_{efw}$ contribution is reported in green and allows reproducing the third maximum peaking at ca. 3.2 Å in the experimental FT-EXAFS spectrum.

As it can be observed in **Figure 5.12**(b,c), the second-shell peak at ca. 2.4 Å mostly derives from the SS path involving the $Al_{fw}$ atom refined at (2.75 ± 0.02) Å from the Cu center. Conversely, by exclusively considering the scattering contributions from the $ZCu(II)O_{efw}$ geometry, the third maximum at ca. 3.2 Å in the experimental FT-EXAFS spectrum is basically not reproduced. Indeed, the contributions from the farer Si/O atoms of the 8r give rise to a broad feature peaking around 2.5 Å and are not adequate to fit the well-defined peak observed in the FT-EXAFS spectrum of the $O_2$-activated sample at ca. 3.2 Å. In the absence of high-amplitude multiple scattering paths, the shape and the R-space location of this feature suggest a long-range contribution from a high-Z atomic neighbour, plausibly an additional $Cu_{efw}$ center in multinuclear Cu(II) moieties. To qualitatively explore such possibility, a Cu−$Cu_{ef}$ SS path was added to the previously described $ZCu(II)O_{efw}$ fitting model, simulated for $R_{Cu(ef)}$= 3.5 Å, with a fixed coordination number $N_{Cu(ef)}$ = 1 and fixed DW factor $\sigma^2_{Cu(ef)}$ = 0.01 Å$^2$ (adequate to account for the high thermal disorder due to 500 °C data collection and to the high static disorder expected in a long-range metal-metal shell). Conversely, the corresponding relative weight $x_{Cu(efw)}$ and radial shift $\Delta R_{Cu(ef)}$ were guessed. The results of this fit are also reported in **Table 5.8** (third column), and the best fit and experimental spectra are compared in **Figure 5.12**(e,f). The fit R-factor lowers to 0.009 and the optimized values of the common parameters are mostly unchanged with respect to the initial fit using only the $ZCu(II)O_{efw}$ model. However, the addition of the Cu−$Cu_{efw}$ contribution significantly improves the reproduction of the experimental spectrum in the high-R range: the third peak the FT-EXAFS is well modelled in correspondence of $R_{Cu(ef)}$= (3.41 ± 0.06) Å and $x_{Cu(ef)}$ = 0.3 ± 0.3 (i.e. ca. 30% of Cu-sites in the material have another Cu neighbour at ~ 3.4 Å).

### 5.2.2 *XAS analysis of composition-dependent reducibility in Cu-CHA and correlation with DMTM productivity*

In the precedent section (**5.2**) the impact of the different process parameters on the methanol yield and Cu-speciation for the Cu-CHA (0.5; 12) reference material has been described. In the following, the same investigation is proposed for a batch of four Cu-CHA samples with different compositional characteristics (Cu:Al ratio (~ 0.5) and Si:Al ratios varying within 5−29). The samples were studied by XAS after He activation at 500 °C followed by the subsequent reaction with $O_2$ at the same temperature.

The $CH_3OH$ productivity trend (whose measurement approach can be found in [15]), normalized with respect to the Cu loading (i.e. mol$CH_3OH$/mo lCu) exhibits a maximum, equal to 0.172 mol$CH_3OH$/mol Cu, for the sample with Si:Al = 12 among the four tested materials while, in the case of the sample with the highest aluminum content (i.e: Si/Al=5), the productivity is equal to 0.112 mol$CH_3OH$/mol Cu. For samples with Si:Al ratios of 12 and 15 a very similar normalized productivity, in line with the similar compositional characteristics is found. Conversely, increasing Si:Al to 29 results in a decrease of the productivity; it lowers to 0.131 mol$CH_3OH$/mol Cu, see **Figure 5.13**.

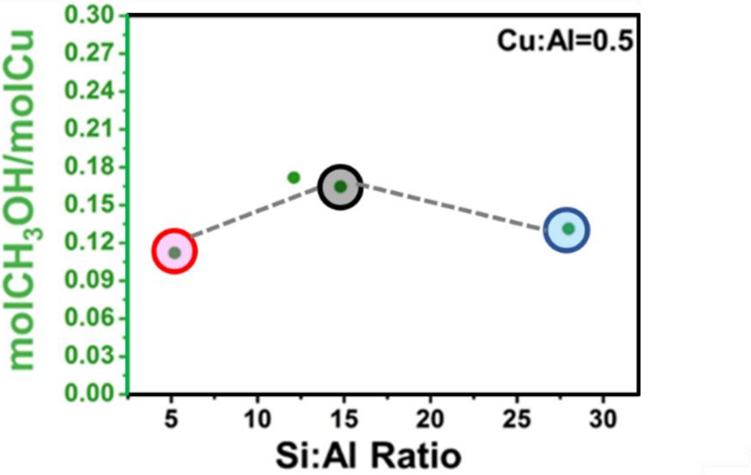

**Figure 5.13:** Normalized methanol productivity (mol$CH_3OH$/mol Cu) (green points) as a function of Si:Al (5, 12, 15 and 29) ratio for four CHA samples with Cu:Al=0.5.

The XAS measurements were hence employed in order to interpret the normalized methanol yield derived from the samples with different Si:Al and also to gain in-depth knowledge on the Cu speciation in the pre-treated materials. Having established in **section 5.2** that the $O_2$-activation and high-temperature reaction with $O_2$ of the He-activated state result in equivalent performance, it is possible to safely infer that the two pre-treatments result in equivalent populations of active Cu-sites. **Figure 5.14**(a-c) shows the XANES and FT-EXAFS spectra of He-activated Cu-CHA samples with fixed Cu:Al ratio of 0.5 and Si:Al ratios f 5, 15, 29. The corresponding spectra collected on the same materials after subsequent oxidation at 500 °C are reported in **Figure 5.14**(d-f).

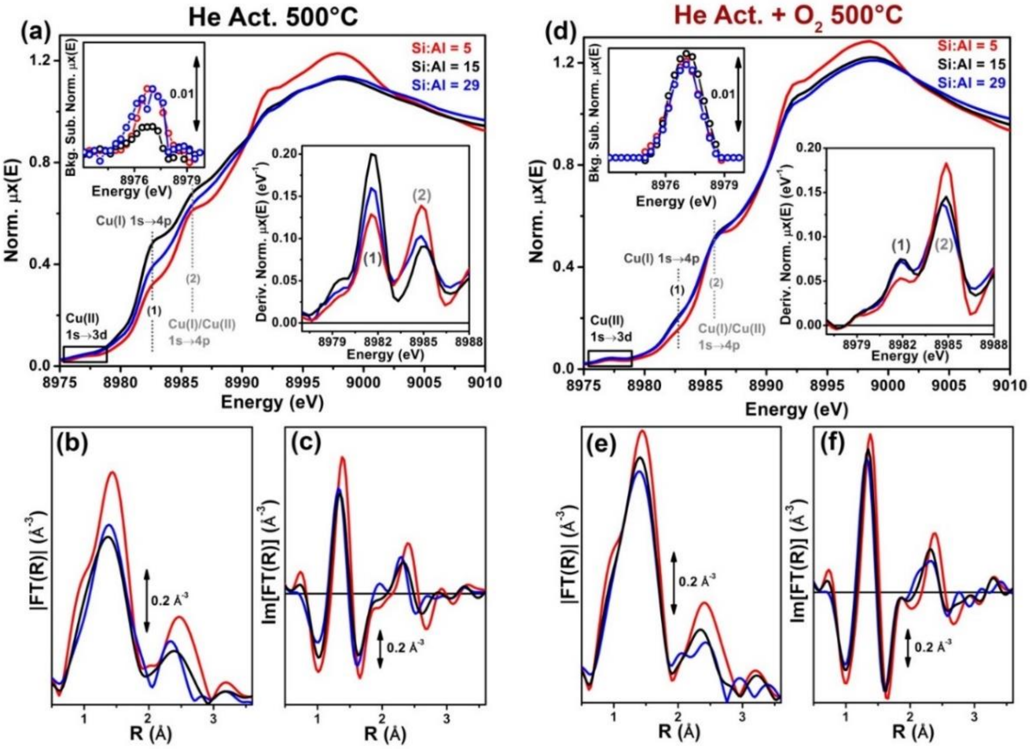

**Figure 5.14:** (a) Main panel: XANES spectra collected on samples (0.5; 5) (red curves), (0.5; 15) (black curves) and (0.5; 29) (blue curves) after He-activation at 500 °C; left inset: background-subtracted pre-edge 1s → 3d peak; right inset: first derivative of the XANES spectra reported in the main panel in the rising-edge region. (b, c) Magnitude (b) and imaginary part (c) of the FT-EXAFS spectra for the He-activated samples reported in part (a). Herein the (2.4–10.8) Å$^{-3}$ range of transformation has been employed. (d-f) XAS spectra for the same materials of part (a-c) but collected after re-oxidation in $O_2$ at 500 °C of the He-activated samples.

The XANES spectra of all the He-activated samples show the presence of a certain fraction of Cu(I) ions and the abundance of reduced Cu(I) sites influenced, increases in the following order: Si:Al = 15 > 29 > 5, as can be qualitatively derived by monitoring both the intensity of the characteristic Cu(I) 1s→4p peak at 8982.5 eV and the background-subtracted Cu(II) 1s→3d pre-edge peak. These results are in line with the results of **section 5.1,** where it has been demonstrated that the self-reducibility is dependent on the compositional characteristics of the sample. The pure XANES curves, retrieved by the MCR-ALS algorithm, have been employed here as references to accurately assess, by simple LCF analysis, the Cu-speciation in the spectra reported in **Figure 5.14**(a). The best-fit curves obtained through the LCF procedure are reported in **Figure 5.15**, while the fractions associated to each component involved in the fitting procedure are showed as histograms in **Figure 5.16**.

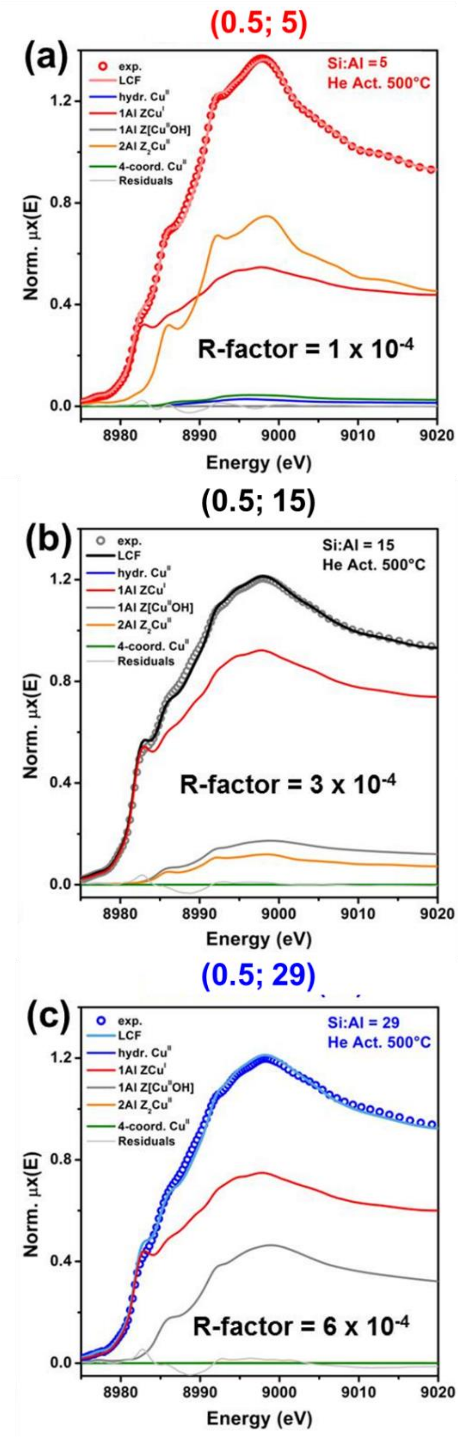

**Figure 5.15:** Comparison between experimental in situ XANES of He-activated Cu-CHA samples with equivalent Cu:Al = 0.5 and different Si:Al, namely (a) (0.5; 5) , (b) (0.5; 15), (c) (0.5; 29), with the correspondent best-fit curves. LCF analysis has been performed employing, as references, the XANES spectra of the five the *pure* Cu-species derived from MCR-ALS analysis showed in **section 5.1.1.**For each fitted spectrum, the LCF components scaled by their respective optimized weights, the LCF residuals and the fit R-factor are also reported.

Focusing on **Figure 5.16**, at Si:Al = 5, the He-activated state is found to contain ca. 50% of redox-inert $Z_2$Cu(II) sites in 6r, whereas the remaining Cu is present as ZCu(I). The substantial contribution from $Z_2$Cu(II) sites in 6r is also evident in the corresponding FT-EXAFS spectrum (**Figure 5.14**(b,c)). There, it is possible to observe an enhanced intensity for both of the first and second maximum with respect to the other He-activated materials, in line with the increased coordination numbers for the first Cu−$O_{fw}$ ($N_{O(fw)}$ = 4) and the second Cu−$T_{fw}$ ($N_{T(fw)}$ = 2) coordination shells in $Z_2$Cu(II) sites. The sample with Si:Al = 15 shows an optimal reducibility: the LCF analysis reveals ca. 80% of ZCu(I) species plus some minor contributions around 10% from both residual ZCu(II)OH species and $Z_2$Cu(II) sites in 6r. Concomitantly, the FT-EXAFS spectrum is equivalent to that already described in the previous section for the He-activated (0.15; 12). Such conditions result into lower first-shell intensity, due to the presence of a majority of twofold-coordinated sites, and a dampened/broadened second-shell peak, in relation with higher mobility of Cu(I) cations and heterogeneity in ZCu(I) siting [40, 53]. Finally, the sample with Si:Al = 29 shows an intermediate reducibility, with an estimated percentage of ca. 60% of ZCu(I) and ca. 40% of ZCu(II)OH surviving in their oxidized state; at such low Al-loading while the $Z_2$Cu(II) sites are actually undetectable. In the FT-EXAFS, a slightly higher first-shell intensity and an enhanced definition in the second-shell peak with respect to the Si:Al = 15 case are in good agreements with the higher relative fraction of threefold-coordinated ZCu(II)OH complexes to the expenses of self-reduced ZCu(I) species, see **Figure 5.14**(b, c).

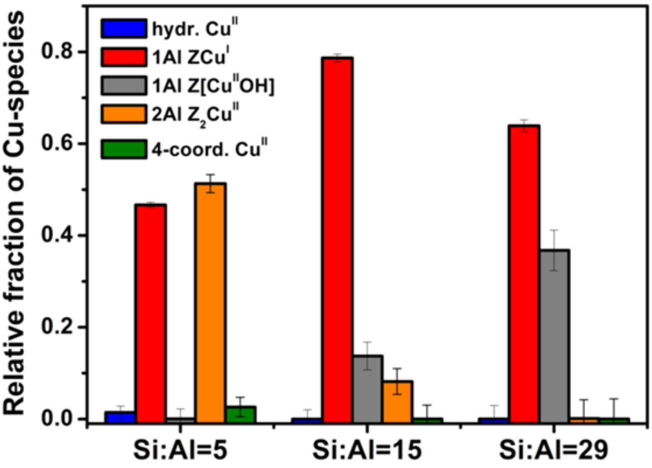

**Figure 5.16:** Bar plot describing Cu-speciation in Cu-CHA samples with Cu:Al = 0.5 and Si:Al = 5, 15 and 29 after He-activation at 500 °C, as derived from LCF using the theoretical XANES spectra retrieved in **section 5.1.1** as references.

**Figure 5.14**(d-f) shows how the re-oxidation in $O_2$ at 500 °C effectively restores a largely dominant Cu(II) state irrespectively of the composition, as evidenced by the rise in the Cu(II) 1s→3d pre-edge peak, reaching the same background-subtracted intensity in the three samples, and by the simultaneous decrease in the Cu(I) 1s→4p rising-edge peak, apparently more complete at Si:Al = 5. Noteworthy, the re-oxidized (0.5; 29) and (0.5; 15) samples show a very similar XANES. However, significant differences are found for the FT-EXAFS. In particular, at Si:Al

= 29, a lower first-shell peak is observed, together with an evident deterioration of the EXAFS signal in correspondence of the second and third maxima, possibly deriving from a higher heterogeneity in the Cu(II) component. Indeed, in terms of Cu(II)-speciation. The absence of a well-defined third maximum in the high-R region of the FT-EXAFS does not point to the formation of multinuclear oxo or peroxo Cu(II) species upon re-oxidation. This observation is in line with the statistical scarcity, at Si:Al = 29, of suitable docking sites with Al-Al separation < 10 Å, as predicted by theoretical studies [54, 55].

Correlating the spectroscopic features discussed above with the performance of the investigated Cu-zeolites with Si:Al = 5, 15, 29, it is possible to find a linear dependence between the normalized productivity and the sample reducibility in the He-activated state, quantified through the relative fraction of ZCu(I) sites from the LCF of the XANES spectra reported in **Figure 5.14**(a). The productivity-reducibility correlation is highlighted in **Figure 5.17**, demonstrating that the normalized $CH_3OH$ yield is directly proportional to the relative abundance of Cu(I) sites available for high-temperature reaction with $O_2$ to a set of $Cu(II)_xO_y$ species among which the active sites should be searched.

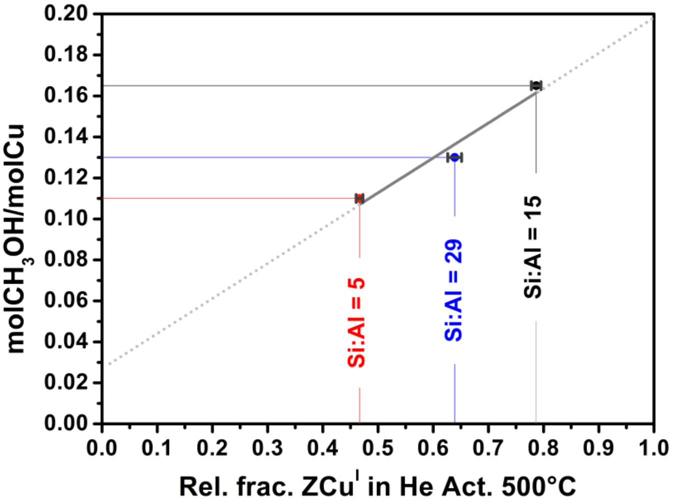

**Figure 5.17:** Correlation between the normalized productivity of Cu-CHA samples with Si:Al = 5, 15, 29 and their reducibility in the He-activated state, quantified through the relative fraction on ZCu(I) from LCF of the XANES spectra reported in **Figure 5.14**(a). The best fit line through the experimental points is reported in grey.

An attempt based on the usage of HERFD XANES to discern the spectral signature associated to the $Cu(II)_xO_y$ species formed during the activation in $O_2$ is reported in the following section (**5.3**).

Two major causes are identified for a low reducibility – and thus productivity – in Cu-CHA, as detailed here below. (i) At low Si:Al values (e.g. Si:Al = 5) large populations of $Z_2Cu(II)$ are formed along the dehydration process: the productivity results clearly show that these redox-inert Cu(II) species are not active towards the direct methane conversion, and basically *block* the corresponding relative fraction of Cu centers. Therefore, it is possible to link the lower normalized productivity observed in low-loading CHA samples (Cu:Al ≈ 0.15) at Si:Al = 12, see **Figure 5.10** and **Figure 5.11** with a higher relative abundance of $Z_2Cu(II)$ species. (ii) At very high Si:Al (e.g. Si/Al = 29) values, although Cu-speciation is largely dominated by *potentially* redox-active species, self-reduction is hindered, confirming the existence of a critical threshold in the material acid site density to efficiently progress with self-reduction [40]. As already suggested in **section 5.2** and supported by the lower productivity at Si:Al = 29, most likely ZCu(II)OH is the precursor to the active Cu(II) moieties but it is inactive for the conversion.

It still remains an open question about the nuclearity of $Cu(II)_xO_y$ species derived from the re-oxidation of ZCu(I), and how their nuclearity correlates with productivity in Cu-CHA. Unfortunately, the EXAFS signature of such species is only found in the high-R range, where the technique sensitivity inherently decreases (especially for high-temperature measurements on complex, multi-component systems). Moreover, Cu-Cu contributions prevail over the more abundant Cu-O ones only in high k-range, where the increased noise could significantly affect the FT-EXAFS signal.

## 5.3 COMPARING HE- AND $O_2$-ACTIVATION IN CU-CHA THROUGH A MCR ANALYSIS OF HERFD-XANES DATA

As discussed in **sections 5.1** and **5.2.2**, the availability of redox-active Cu-species, efficiently undergoing self-reduction during thermal treatment, represents a crucial requirement for the DMTM conversion over Cu-CHA. Although ZCu(II)OH species are inactive by themselves, most likely they represent the precursors to different Cu(II) active sites, whose formation requires high-temperature reaction with $O_2$. To obtain deeper insights in this point, a detailed XAS analysis, focused on a selected Cu-CHA sample (0.5; 12) (resulting in an optimal performance for the MTM process, see **section 5.2**), was employed. In particular, the MCR-ALS analysis on a combined HERFD-XANES dataset including both $O_2$- and He-activation for the selected material was performed in order to attempt to single out the contribution from the $O_2$-derived Cu-species.

### 5.3.1 *HERFD-XANES during $O_2$- and He-activation: qualitative analysis*

**Figure 5.18** shows the two *in situ* HERFD-XANES datasets collected for the investigated Cu-CHA sample during the activation in $O_2$ (**Figure 5.18**(a)) and in He (**Figure 5.18**(b)) (temperature ramp 5 °C/min). More details about the data acquisition procedure can be found in **section 5.8.3** of the appendix. From a qualitative analysis, it is clear that the evolution of XANES features, during both activations, is consistent with thermally driven dehydration of the Cu centres: the intensity of W.L. peak gradually decreases as the temperature increases, reflecting the progressive lowering in the average first-shell coordination number of Cu. In line with what has been stated in **section 5.1** , the spectral evolution is rather insensitive to the gaseous environment up to ~ 250 °C. In both $O_2$ and He flow, the lowering in the W.L. intensity is accompanied by the development of a rising-edge shoulder around 8986 eV, which is imputable to the $1s \rightarrow 4p$ transition in a four-fold or three-fold coordinated Cu(II) sites.

The use of HERFD-XANES instead of the conventional XANES spectra allows an optimal detection of the $1s \rightarrow 3d$ weak pre-edge peak at 8977.5 eV (see **Figure 5.18**, insets) . The pre-edge peak is observed to slightly shift to higher energies and gain in its intensity as dehydration proceeds. Overall, the distinctive traits of the final spectrum at 500 °C in $O_2$ are in agreement with previous studies [44, 56] indicating a largely dominant Cu(II) oxidation state. However, it is possible to observe that in the high-temperature range in $O_2$, certain modifications occur in the intensity and position of the Cu(II) $1s \rightarrow 4p$ rising-edge peak at 8986 eV, which could be connected with the presence of different dehydrated Cu(II) species.

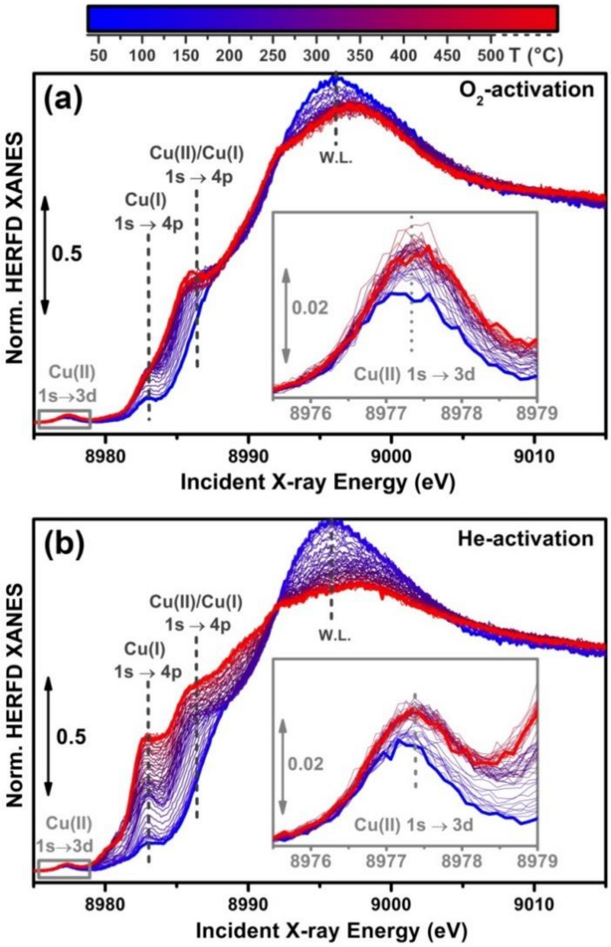

**Figure 5.18:** In situ temperature-dependent HERFD-XANES data collected at the ID26 beamline of the ESRF during (a) $O_2$-activation and (b) He-activation for Cu-CHA (Si/Al = 12, Cu/Al = 0.5). The top bar reports the colour code adopted to indicate the collection temperature for each scan, with the starting spectrum (37 °C) and ending spectrum (after ca. 10 min at 500 °C) reported as blue and red thick lines, respectively. The insets report a magnification of the 1s→3d Cu(II) pre-edge peak, highlighted by a grey box in the main panels; the energy positions for Cu(I) and Cu(II) 1s→4prising-edge peaks and of the white-line peak (W.L.) are also indicated.

Regarding the activation in He, from ~ 250 °C upwards, the same trend already discussed in **sections 5.1.1** and **5.2** is repeated. The development of prominent rising-edge peaks from 8983 eV, is characteristic of ZCu(I) sites formed after self-reduction of redox-active Cu-species hosted at 1Al sites. The presence of a minor, but still significant, fraction of Cu(II) species in the He-activated sample is evidenced by the persistence of the pre-edge $1s \rightarrow 3d$ peak after ca. 15 min at 500 °C (see inset of **Figure 5.18**(b), red thick curve). As anticipated, it can be better identified thanks to the improved energy resolution and lower signal-to-background ratio offered by HERFD-XANES. Similarly, it is possible to note the presence of a weak but well-defined peak in the characteristic Cu(I) $1s \rightarrow 4p$ energy region already at 37 °C, in both $O_2$ and He atmosphere. In $O_2$, this feature remains visible until 250 °C, while at higher temperature it is no more distinguishable from the tail of the rising-edge peak at 8986 eV. Conversely, in He, from 250 °C upwards, the 8983 eV peak it is observed to progressively develop in intensity, concomitantly with the formation of a large Cu(I) population *via* self-reduction.

In the following section, these qualitative insights will be translated into a quantitative evaluation of the Cu speciation during the $O_2$ and He-activation processes recurring again to the MCR-ALS algorithm.

### 5.3.2 *MCR-ALS results: evidences for $O_2$-derived Cu(II) species*

**Figure 5.19** reports the set of spectral and concentration profiles provided by the MCR-ALS analysis initialised using the SIMPLISMA algorithm.

The same statistical procedure described in **section 5.1.1** was executed on both the datasets resulting in a number of components equal to six and five for the $O_2$ and He activated samples, respectively. In order to reduce the level of ambiguity affection the retrieved XANES profiles provided by the ALS algorithm an enlarged dataset composed by 106 spectra, joining together the $O_2$ and He activated XANES dataset (containing, respectively, 53 HERFD-XANES spectra), was generated.

The pure HERFD-XANES spectra in **Figure 5.19**(a) show a substantial correspondence with the ones reported in **Figure 5.4**, derived by applying MCR-ALS analysis to the conventional transmission-mode XANES data on a compositionally larger dataset. Overall, beside some specific limitations in the reconstruction which will be discussed below, the resulting MCR-ALS spectra could be safely attributed to physically-chemically meaningful contributions, involving the same set of Cu-species identified in the previous study summarized in **section 5.1.2** (namely PC 1, PC 2, PC 3, PC 5, PC 6, assigned as indicated in **Figure 5.4** to hydrated Cu(II), ZCu(I), $Z_2$Cu(II), ZCu(II)OH and under-coordinated Cu(II) dehydration intermediate, respectively) plus an additional $O_2$-derived Cu(II) species, PC 4 (yellow curve and bars).

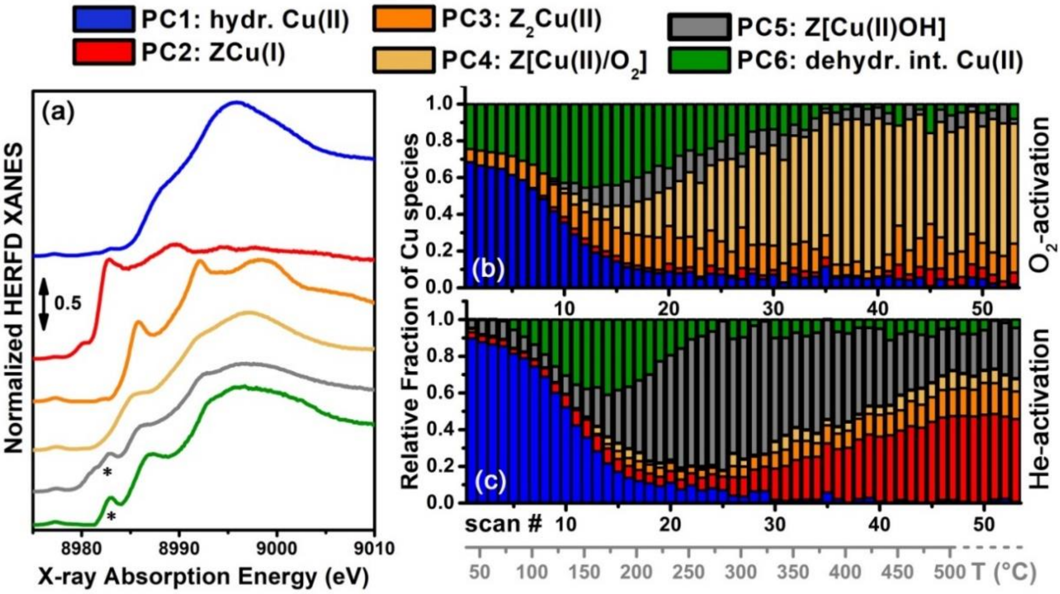

**Figure 5.19:** (a) Pure spectra isolated through combined MCR-ALS analysis of the in situ HERFD-XANES data collected during $O_2$-activation and He-activation of a Cu-CHA samples with Cu/Al = 0.5; Si/Al = 12 (experimental data reported in **Figure 5.18**). The spectra have been vertically translated for the sake of clarity. The * symbol indicates the presence of reconstruction artefacts in the form of spurious rising-edge peaks for the spectra of PC 5 and PC 6. (b, c) Concentration profiles for the pure HERFD-XANES spectra reported in part (a) during (b) $O_2$-activation and (c) He-activation, plotted as a function of the scan number (2 min/scan, black axis and labels) and of the correspondent data collection temperature (grey axis and labels, from 37 °C to 500 °C, plus ~ 15 min dwelling time in isothermal conditions at 500 °C). For both parts (a) and (b), the same colour code is adopted to indicate the identified Cu-species, according to the legend reported in the top panel of the figure; the colour code is the same as in **Figure 5.4** for the five PCs present in both studies, namely PC 1, PC 2, PC 3, PC 5, PC 6. PC 4 (yellow curves and bars) is assigned to a novel $O_2$-derived Cu(II) species.

In the present case, the reconstruction suffered of some limitations connected with the use of a one-composition dataset, which appeared to be enhanced due to higher energy resolution employed. In particular, some spurious peaks are observed in the energy range 8980 – 8984 eV (typical of Cu(I) $1s \rightarrow 4p$ transitions), in the MCR-ALS spectra for the last two components, PC 5 and PC 6 (denoted with * symbols in **Figure 5.19**(a)). As described in **section 5.3.1**, a weak contribution in this range is observed experimentally already in the low-temperature range during both $O_2$ and He activation and could derive from traces of Cu(I) species other than ZCu(I), which could easily escape detection in conventional XANES due to their low concentration. Dealing with a very minor contribution, whose concentration profile is completely embedded in the concentration window of much more abundant Cu species, it was impossible to retrieve its spectral signature from the ALS approach, and its most distinctive trait, *i.e.* the peak around 8982 eV, is fictitiously embedded into the PC 5 and PC 6 *pure* XANES spectra.

Further insights can be derived from the analysis of the concentration profiles in **Figure 5.19**(b,c). Starting from the activation in He (**Figure 5.19**(c)), the trends in the Cu-speciation evolution are qualitatively consistent with the one reported in **Figure 5.4** for the sample with Cu/Al=0.5 and Si/Al=15. The decreasing in the population of fully hydrated Cu(II) correlates with the appearance of the Cu(II) species previously described as a four-coordinated dehydration intermediate. At higher temperature, from ca. 170 °C upwards, ZCu(II)OH, progressively forms. The ZCu(II)OH concentration reaches a maximum of 80% at 200 °C and then progressively diminishes in the favour of ZCu(I). The $Z_2$Cu(II) species appear from ~ 200 °C. Their concentration linearly growths with temperature until 400 °C, remaining then stable at ~ 15% of the total Cu during the final part of the heating ramp. The final state probed during He-activation, after 15 min in He at 500 °C, is characterized by a substantial fraction of reduced ZCu(I) sites, accounting for 51% of total Cu. The new Cu(II) species identified in this dataset, PC 4, shows a very marginal role in the total signal representation. Its formation seems to be linked to the appearance of $Z_2$Cu(II) species, although its concentration during He-activation always remains below 7%.

During $O_2$-activation, the MCR analysis evidences important differences in temperature-dependent Cu speciation with respect to the treatment in He. For the initial state, fully hydrated Cu(II) complexes are still the largely dominant structural component, but an important contribution from under-coordinated Cu(II) aquo-complexes (PC 6) is already observed, representing the 24% of the total Cu at 37 °C. Similarly, a minor population of $Z_2$Cu(II) sites (ca. 7%) is detected at the very beginning of the activation ramp. The concentration of these species undergoes to a linear increase up to ca. 16%, reached at 170 °C. At higher temperature, their abundance remains rather stable, although in the 400−500 °C range larger fluctuations are observed. Noteworthy, the final abundance of redox-inert $Z_2$Cu(II) species is poorly influenced by the activation atmosphere. It appears to be determined by the Si/Al ratio of the zeolite framework, which gives the statistical availability of docking sites in 6r hosting two charge-balancing Al sites.

The most intriguing result is connected with the dynamics of ZCu(II)OH and the new Cu(II) species (PC 4) only detected in significant abundance in $O_2$ atmosphere. In particular, the two Cu(II) components seem to simultaneously develop from ca. 150 °C upwards, correlating with the diminution of the Cu(II) dehydration intermediate. Nonetheless, the ZCu(II)OH species concentration remains rather low, oscillating around 13% until 400 °C, and further decreasing to below 10% at higher temperature. In parallel, the concentration of PC 4 component progressively increases, becoming the dominant Cu component in the high-temperature range (70% total Cu at the end of the protocol). All along the $O_2$-activation, ZCu(I) always occurs only as a very minor species, with concentrations in the 2−5% ranges.

Comparing the behaviour of the PC 4 component during thermal treatment under oxidant and inert conditions, it appears that this species is strongly associated with the availability of $O_2$ in the feed, whereas the Z[Cu(OH)] species is transiently present in large abundance also in He, before it undergoes self-reduction to ZCu(I). The XANES signatures of these two Cu(II) species are overall quite similar, indicating a similar Cu coordination geometry in the two cases. However, they do differ in the intensity and shape of the white line peak, being more intense for PC 4 with a sharper maximum at 8997 eV, as well as in the energy position of the rising-edge peak, shifted at lower energies of 1 eV for the PC 4 with respect to PC

5. With this evidence, the use of HERFD-XANES it is crucial to discriminate the two structural components.

These results highlight how the components space for the $O_2$-activation has a higher dimensionality with respect to what found for He-activation. The additional Cu-oxo component was associated with an $O_2$-derived Cu(II) species which could continuously originate from ZCu(II)OH precursor species, possibly though their transient reduction, on a timescale faster than time resolution employed here (2 min), and the re-oxidation of the newly formed Cu(I) species by $O_2$.

The similarity of the MCR-ALS XANES spectra for the PC 4 with the one assigned to ZCu(II)(OH) suggests a similar three-fold coordinated Cu species, which most likely plays a crucial role in the DMTM conversion. Possible candidates could include monomeric Z[Cu(II)$O_2^-$] superoxo species with end-on coordination mode, as well as three-coordinated di-nuclear peroxo and oxo Cu(II) moieties, already identified in $O_2$-activated Cu-CHA from Raman spectroscopy [15].

## 5.4 Assessing the Nuclearity of the Active sites for the DMTM conversion in Cu-MOR

As already discussed in the introduction of this chapter, similarly to the CHA topology, also Cu-exchanged MOR zeolites have been widely employed in the step-wise DMTM conversion. Also in this case, the main question arising from the spectroscopic data acquired during operando measurements, concerns the structure of the Cu active involved in the methanol formation [6]. The results showed and discusses in this section take their origin from the analysis of the normalized $CH_3OH$ yield trend showed in the following figure (**Figure 5.20**).

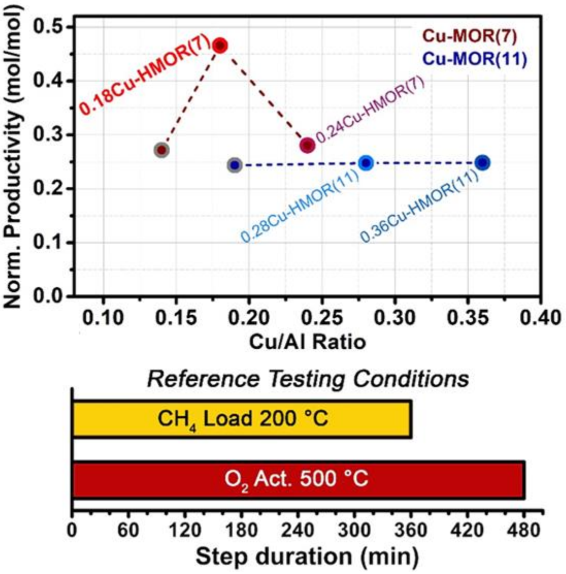

**Figure 5.20:** (Top panel) Normalized productivity (mol $CH_3OH$/mol Cu) as a function of the Cu/Al ratio, comparing the Cu-MOR Si/Al=7 and 11 series. (Bottom panel) Bar plot representing the duration b of the $O_2$ activation and $CH_4$ loading steps employed to obtain the productivity trend showed in the top panel.

**Figure 5.20** shows the normalized productivity (measured by D. Pappas) for a batch of Cu-MOR zeolites having Si/Al ratio of 7 and 11. From the plot, it is possible to see that the Cu-MOR samples with Si/Al=11 exhibit a flat trend of the yield with increasing Cu loading. A similar behaviour is exhibited also by the materials with Si/Al=7, having the lowest and highest Cu-loading in the series. These finding are in agreement with the reports concentring Cu-MOR [6]. However, the material with intermediate Cu loading (Cu/Al=0.18) shows a normalized productivity of 0.47 mol$CH_3OH$/mol Cu close to the maximum value allowed by the stoichiometry assuming a dicopper active site and pointing towards the existence of a uniquely high density of active species [16].

### 5.4.1 *Cu active site spectroscopic fingerprints from operando XAS*

To rationalize the composition-productivity trends highlighted in **Figure 5.20**, an *operando* XAS experiment at the Cu K-edge was performed, the interested reader can find the data acquisition details in **section 5.8.2**. Two representative materials for each Si/Al ratio, namely MOR (0.18; 7) and (0.36; 11) were selected. Using a capillary reactor, the MTM stepwise reaction over each material was performed, while the average electronic and structural properties of the Cu ions were monitored by XAS. The experimental protocol is analogous to the one presented in **Figure 5.1**. It is constituted by the $O_2$ activation at 500 °C in pure $O_2$ (90 min), pure $CH_4$ loading at 200 °C (120 min), and $CH_3OH$ extraction by steam admission at 200 °C (70 min). The heating and cooling ramps were always performed using a rate of +/– 5 °C/min. For the extraction step, a flow of Ne/He was passed through a saturator containing deionized water at 44 °C. The steam was then introduced to the sample and the effluent was analyzed by a quadrupole MS (Pfeiffer Vacuum), to quantity the productivity for investigated samples at the *operando* XAS conditions. It is clear from the precedent sections that the methane-converting Cu sites are formed during the high-temperature activation step in an oxidizing atmosphere. Hence, the comparison of the XANES and the FT-EXAFS spectra of the $O_2$-activated materials constitutes the basis of the analysis, see **Figure 5.21**(a,b and c).

The XANES features can be interpreted based on previous studies on Cu-CHA [1, 2, 5, 17, 56, 57]. For all the samples, $O_2$-activation results in a virtually pure Cu(II) state; no Cu(I) contribution is observed within the detection limit. The XANES spectra of the four Cu-MOR zeolites show remarkable similarities, thus revealing comparable coordination environments for the Cu ions in the frameworks. Nonetheless, a trend is observed in the intensity of the so-called W.L. peak at ca. 9.0 keV in the XANES (faded grey arrow in the inset of **Figure 5.21**(a)). Low Si/Al and low Cu/Al both appear to promote a higher W.L. intensity, with the outperforming MOR (0.18; 7) showing the highest W.L. peak.

As already showed for the Cu-CHA cases, also here a higher W.L. intensity in Cu K-edge XANES is commonly associated with a higher coordination number in the first shell of the cation and/or a more symmetrical coordination environment. The FT-EXAFS spectra in **Figure 5.21**(b,c) confirm this observation. The intensity of the first-shell peak, stemming from scattering contributions by $O_{fw}$ and $O_{efw}$ oxygen atoms, follows the same trend. The FT-EXAFS for the four catalysts also shows a well-defined peak in the second shell region, extending from 2 to 3 Å in the phase-uncorrected spectra. On the basis of previous studies [1], it is possible to expect both Al and Si atoms belonging to the framework ($T_{fw}$) and Cu–Cu scattering from $Cu_xO_y$ multimeric moieties to contribute in this R-space range. Notably, the peak undergoes intensity modifications as a function of the composition (insets of **Figure 5.21**(b) faded grey arrow). MOR (0.18; 7) displays the highest intensity, followed by MOR (0.24; 7) and then by the two Si/Al=11 catalysts. The latter show an equivalent development of the EXAFS features in this R-space range.

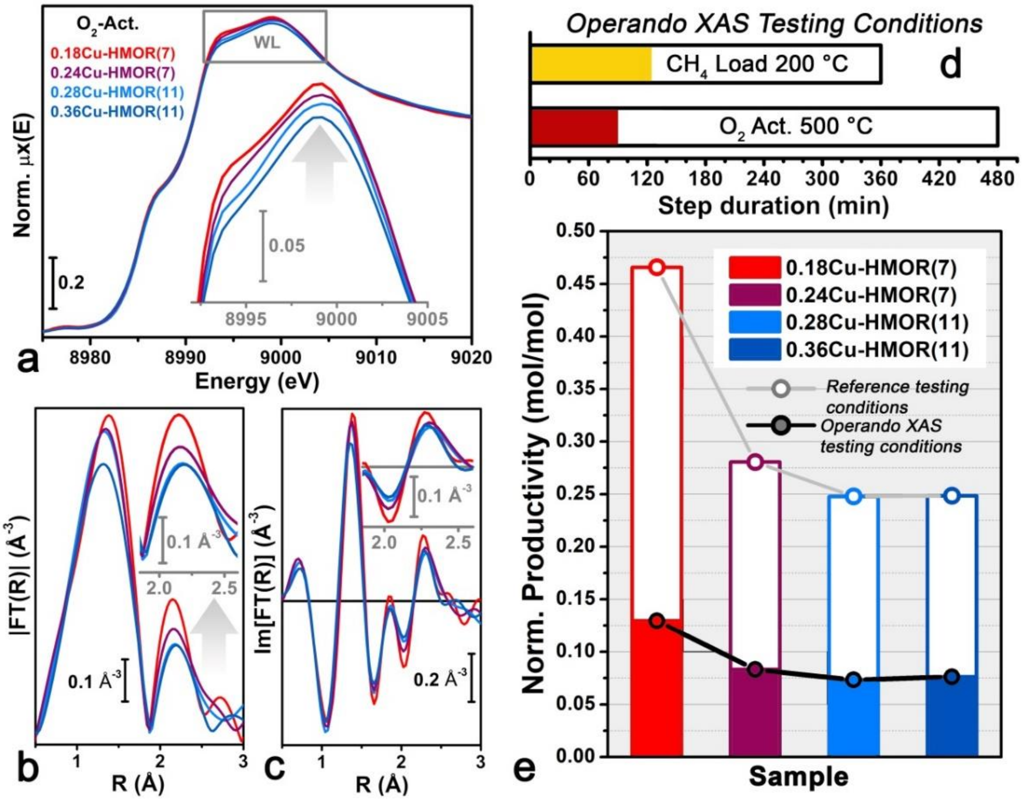

**Figure 5.21:** (a) Normalized Cu K-edge XANES spectra of selected Cu-MOR catalysts after $O_2$-activation at 500 °C. For all the catalysts, a virtually pure Cu(II) state is detected. This is evident from the rising-edge shoulder at 8986 eV, in the typical range of 1s→4p transitions in three-/four-coordinated Cu(II) sites and the weak pre-edge peak at 8977 eV, mostly arising from the dipole-forbidden 1s→3d transition in $d^9$ Cu(II) ions. The inset reports a magnification of the so-called W.L. peak, highlighted by the grey box in the main panel. (b, c) Magnitude (b) and imaginary part (c) of the corresponding phase-uncorrected FT-EXAFS spectra. FT have been calculated transforming the $k^2\chi(k)$ curves in the (2.4-8.7) $Å^{-1}$ range. The insets in both part (b) and (c) report a magnification of the second-shell peak, directly correlating with the normalized productivity of the catalysts shown in part (e). (d) Bar plots representing the duration of the $O_2$-activation and $CH_4$ loading steps and, (e) corresponding normalized productivity at the *operando* XAS conditions (full coloured bars and circles) in comparison with the reference testing conditions (empty bars and circles). In all the panels, the same colour code is used to indicate the different investigated materials.

After 90 min in $O_2$ at 500 °C, the catalysts were cooled to 200 °C and reacted with methane for 120 min. The MS analysis of the reactor effluent during the final steam-assisted $CH_3OH$ extraction step allowed for on-line quantification of the methanol yield obtained from each sample. **Figure 5.21**(e) compares the normalized productivity evaluated at the *operando* XAS conditions **Figure 5.21**(d) as well as at the reference testing conditions measure by D. Pappas (**Figure 5.21**(e)). On the one hand, the results demonstrate that these materials were active under the XAS conditions pointing out the impact of the reaction times (taking into account that the temperature as well as gas composition were identical) on the methanol yield. At the *operando* XAS conditions, the normalized productivity decrease on average by ca.70 % with respect to the reference conditions. However, exactly the same trend is maintained in the performance of the investigated materials.

Intriguingly, the normalized productivity directly correlates with the intensity of the second-shell peak in the FT-EXAFS spectra discussed before. A higher second-shell peak results into a higher fraction of active Cu in the materials. Cu–$T_{fw}$ scattering contributions are expected to be equally present into both monomeric and multimeric framework-interacting Cu(II) moieties (fw-Cu(II)). Hence, such a correlation provides direct structural evidence for a multicopper active sites in Cu-MOR, resulting in a stronger Cu–Cu contribution in the second-shell region of the EXAFS. Nonetheless, the relatively low abundance of active species formed at the XAS conditions, together with the limited contrast between the spectral signatures of active and inactive Cu(II), hampered the quantification of the fraction of active Cu from the *operando* XAS data in **Figure 5.21**.

### 5.4.2 *Enhancing the spectroscopic contrast by MCR analysis of HERFD-XANES*

In order to retrieve a quantitative understanding of the structure-activity relationships for Cu-MOR, time-dependent High Energy Resolution Fluorescence Detected (HERFD)-XANES were employed during high-temperature treatment in $O_2$ and inert gas (He) flow for Cu-MOR (0.18; 7) and (0.36; 11). As showed in **sections 5.1** and **5.2**, inert treatment at high temperature has been proven an excellent probe of the different barrier towards self-reduction, assisting in the discrimination among different Cu(II) species hosted in the zeolite framework. In parallel, the higher energy-resolution, ensured by using an X-ray spectrometer, [58, 59] was crucial to successfully resolve the XANES of active and inactive Cu. As for **section 5.3** the data acquisition detail are reported in **section 5.8.3** of the chapter appendix.

**Figure 5.22**(a) displays the evolution of the HERFD-XANES for the two Cu-MOR samples as a function of the temperature, from 60 to 500 °C. In line with the CHA case described in the precedent sections, the XANES evolution up to ~ 250 °C is poorly affected by the gaseous environment. All the observed spectral modifications in this temperature window are consistent with thermally-driven dehydration of the Cu centers. However, at higher temperatures, the pre-treatment environment drastically impacts the XANES features, resulting into distinct $O_2$- and He-activated finale states.

The HERFD-XANES spectra at 500 °C in $O_2$ match the respective conventional XANES in **Figure 5.21**, indicating largely dominant framework interacting Cu(II) species. However, considerably more defined peaks are observed in line with the adopted detection scheme. A substantial population of self-reduced Cu(I) species is instead detected at 500 °C in He. The intense peak developing at 8983 eV points to quasi-linear Cu(I) configurations in line with what has been proposed by Solomon et al. in [9, 10]. The outperforming MOR (0.18; 7) appears to be more resistant to self-reduction compared to (0.36; 11). Indeed, it shows an almost halved intensity of the Cu(I) peak at 8983 eV, a significantly higher Cu(II) 1s→3d pre-edge peak and a W.L. peak more similar to what is otherwise observed after $O_2$-activation.

Similarly to what has been showed in **section 5.3**, the He and $O_2$ activated XANES dataset were joined together in order to create an enlarged set of spectra composed, in total, by 180 XANES profiles. The PCA analysis executed on the entire dataset suggested the existence of five common species. On the basis on this statistical evidence, the MCR-ALS algorithm was applied on these data employing as initialization step the SIMPLISMA algorithm. The MCR results are summarized in **Figure 5.22**(c,d), reporting the theoretical HERFD-XANES spectra and their concentration profiles for the tested catalyst/activation protocols combinations.

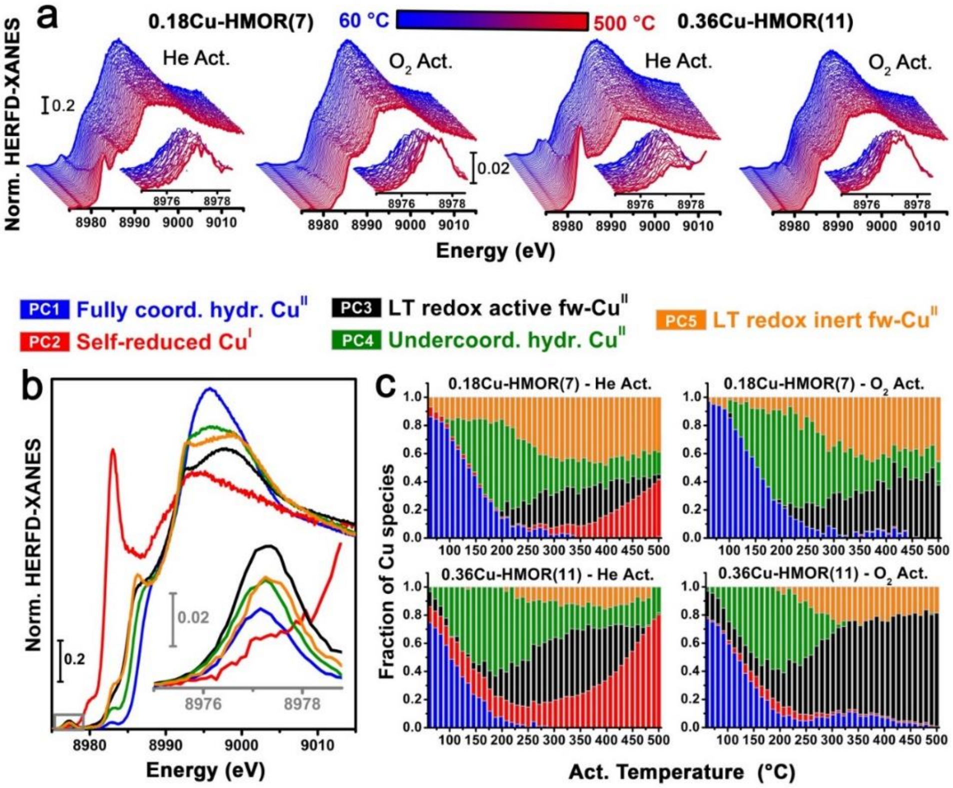

**Figure 5.22:** (a) Time-dependent HERFD-XANES collected on MOR (0.18; 7), left panels, and MOR (0.36; 11), right panels, during thermal treatment in $O_2$ (*$O_2$ Act.*) and inert gas flow (*He Act*). Spectra have been collected with a time-resolution of 2 min, while increasing the sample temperature from 60 °C (blue curves) to 500 °C (red curves). The insets report, for each sample/activation protocol, a magnification of the weak pre-edge peak mostly deriving from the dipole forbidden 1s→3d transition in $d^9$ Cu(II) centers. The global dataset consists into 180 time/temperature-dependent spectra (45 scans per sample/activation protocol). (b) Theoretical HERFD-XANES spectra of pure Cu-species from MCR-ALS analysis of the dataset in part (a). (c) Corresponding bar plots reporting the temperature-dependent concentration profiles of each pure Cu-species. In a similar way as recently found for Cu-CHA in **section 5.1.1**, fully coordinated, pseudo-octahedral Cu(II) aquo-complexes (PC 1)

undergoes partial dehydration to a four-coordinated Cu(II) species (PC 4). These intermediate Cu(II) species reach maximum concentration around 200 °C, and then progressively converts into framework-interacting Cu(II) species (fw-Cu(II)). Among these, a low-temperature (LT) redox-active component (PC 3) is found, efficiently undergoing self-reduction to fw-Cu(I) (PC 2) in inert atmosphere from 250 °C upwards. A LT redox-inert component is also identified (PC 5): it remains stable in inert atmosphere up to 400 °C and is more abundantly formed in the highly active MOR (0.18;7) catalyst.

The characteristic XANES features of theoretical spectra, together with their temperature-dependent dynamics, provide the basis for a robust assignment to well defined Cu-species, as detailed in the caption of **Figure 5.22**. The MCR analysis reveals two framework interacting (fw) Cu(II) species, characterized by different barrier towards self-reduction, and distinct XANES features. A first Cu(II) species is found to efficiently undergo self-reduction already from 250 °C in He low-temperature (LT) redox-active fw-Cu(II), PC 3 in **Figure 5.22**(b,c). In contrast, the specie referred to as low temperature (LT) redox-inert fw-Cu(II) (PC 5 in **Figure 5.22**(b,c)), remains stable until 400 °C in inert atmosphere. This behaviour is consistent with the higher stability predicted for multimeric Cu-oxo cores [60], with respect to monomeric Cu(II) species. The latter could include $[Cu(II)(OH)]^+$, $[Cu(II)O]^+$, and, in the presence of $O_2$, $[Cu(II)O_2]^+$formed at a single-Al docking site during dehydration. LT redox-inert fw-Cu(II) is significantly more abundant in the highly productive (0.18; 7). Its XANES is characterized by more intense and sharper peaks with respect to the LT redox-active component, especially in the W.L. region. LT redox-inert fw-Cu(II) is observed in both inert and oxidant environments, which supports anaerobic pathways (e.g. through condensation of neighbouring $[Cu(II)(OH)]^+$ complexes) as a viable alternative to direct routes involving molecular oxygen activation at Cu sites. Nonetheless, after 400 °C, an oxidant environment appears necessary to its stabilization, in agreement with $O_2$ temperature-programmed desorption results reported by Solomon and co-workers for Cu-ZSM-5 [61].

### 5.4.3 *Quantitative evidences for a di-copper active site*

The same Cu-MOR materials were further investigated by *operando* XAS by collecting higher-quality HERFD-XANES after the samples were kept at 500 °C in $O_2$ for 30 min. Using the *pure* spectra in **Figure 5.22** as references, the linear combination fit (LCF) analysis was employed to accurately determine the Cu-speciation in the four $O_2$-activated Cu-zeolites (see **Figure 5.23**(b)). In these conditions, the outperforming Cu-MOR (0.18; 7) contains the highest fraction of LT redox-inert fw-Cu(II) (47% of total Cu) and 42% of LT redox-active fw-Cu(II). Instead, in the other three materials, the LT redox-active species is promoted: it accounts for 52-78% of total Cu, at the expense of the presumed active site (18-24%). Contributions from the Cu(II) species denoted as four-coordinated dehydration intermediate (PC 4) in the 10-20% total Cu range are still detected in all the samples except for the (0.36; 11) sample.

Having discovered how the duration of each process step impacts the performance of the tested materials, as reported in **Figure 5.21**(e), the batch of four Cu-MOR zeolites were re-evaluated under an *ad hoc* set of conditions (HERFD-XANES testing conditions depicted in **Figure 5.23**(a)). Here, the $O_2$-activation step was set to 30 min, as probed by HERFD-XANES, whereas a 360-min-long $CH_4$ loading step was employed to efficiently saturate all the available active sites. This ensured that the measured yield of C-containing products ($CH_3OH$ along with CO and $CO_2$ from minor over-oxidation during steam-assisted extraction at 200 °C) per Cu was a trustworthy measure of the fraction of active Cu formed during the $O_2$-activation step at the HERFD-XANES conditions, able to activate $CH_4$ in the subsequent step. **Figure 5.23**(d) correlates the determined moles of activated $CH_4$ per mol Cu with the fraction of LT redox-inert fw-Cu(II) (PC 5) from LCF analysis. The experimental points for this Cu-MOR sample series after $O_2$-activation (full coloured circles in **Figure 5.23**(d)) excellently approximate the ideal trend line for stoichiometric DMTM conversion over a di-copper active site (dashed dark red line in **Figure 5.23**(d)), unambiguously demonstrating that two Cu ions are cooperatively involved in the activation of a $CH_4$ molecule over these materials.

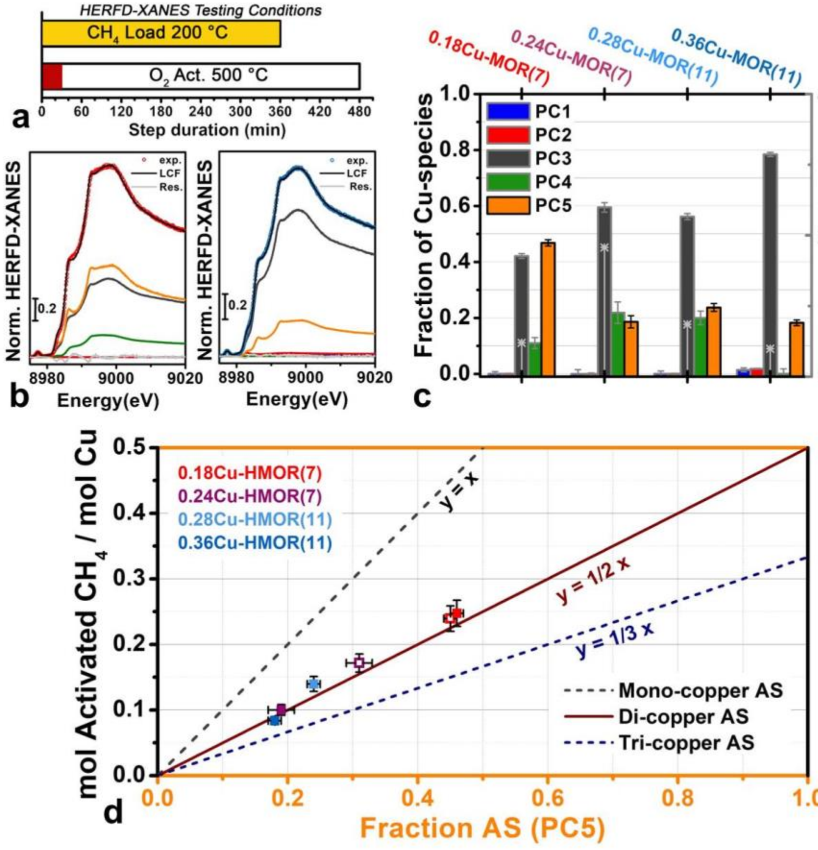

**Figure 5.23:** (a) Bar plot representing the duration of the $O_2$ activation and $CH_4$ loading steps at the HERFD-XANES testing conditions, adopted into parallel laboratory tests to effectively correlate spectroscopy results and performance. (b), Comparison between experimental HERFD-XANES of representative $O_2$-activated Cu-MOR samples, namely MOR (0.18; 7) and MOR (0.36; 11), with the correspondent best-fit curves from LCF analysis, using the *pure* spectra from MCR analysis (**Figure 5.22**(b)) as references. For each fitted spectrum, the LCF components scaled by their respective optimized weights and the LCF residuals are also reported. (c), Cu-speciation in (0.18; 7) and (0.36; 11) as determined from LCF analysis of HERFD-XANES spectra. The PCs corresponding to pure Cu-species are indicated using the same colour code as used in **Figure 5.22**(b,c). The LCF R-factor is also reported (grey stars, right ordinate axis). (c), Quantitative correlation between the normalized productivity evaluated at the HERFD-XANES testing conditions and the fraction

of LT redox-inert fw-Cu(II) (PC5 – the presumed DMTM active site) from LCF analysis ($O_2$-activation: full coloured circles; He-activation + $O_2$: empty coloured circles). All the experimentally-determined values match the ideal trend line for stoichiometric conversion over a di-copper active site, [mol activated $CH_4$/mol Cu] = 0.5 [Fraction Cu in active site], reported as a full dark red line.

For the Si/Al = 7 Cu-MOR samples a different pre-treatment was also investigated. It consisted in the exposition of the He-activated materials to $O_2$ at 500 °C, similarly to what has been described in **section 5.2** for the Cu-CHA. The corresponding experimental points, obtained correlating results of HERFD-XANES LCF analysis and productivity per Cu evaluated after the same pre-treatment, are reported as empty squares in **Figure 5.23**(d). The points keep following the di-copper active site trend line, evidencing how the same active site nuclearity is conserved also when the latter is obtained by interacting self-reduced Cu(I) with molecular $O_2$.
Interpolating the normalized yield obtained at the reference testing conditions (480 min-long $O_2$-activation) for the (0.18; 7) on the spectroscopically-validated di-copper trend line, it is possible to estimate more than 90% of total Cu coordinated into $Cu_2O_x$ active species for this outperforming material, resulting in the highest productivity per Cu reported to date for MTM over Cu-exchanged zeolites. Hence, prolonged exposure to $O_2$ at 500 °C promotes important reorganization phenomena in the Cu ions siting, resulting in the dynamic transformation of inactive Cu into active species (or possibly precursor to active species). In the presence of the most favourable compositional landscape, such as in (0.18; 7), these processes finally yield a *quasi-single-site* catalyst, where virtually all Cu is organized into active $Cu_2O_x$ cores.

## 5.5 IDENTIFYING CU-OXO SPECIES IN CU-ZEOLITES BY XAS: A THEORETICAL SURVEY BY DFT-ASSISTED XANES SIMULATION AND EXAFS WAVELET TRANSFORM

In the precedent sections, it has been showed that Cu-CHA and Cu-MOR zeolites possess Cu-oxo active sites able to cleave the C–H bond of methane at temperatures ≤ 200 °C, enabling its partial conversion into methanol. Clearly, to understand their reliability and the potential towards the DMTM conversion, it is crucial to accurately characterize the Cu-speciation during the $O_2$ activation, when Cu active sites are formed.
The previous experimental XAS data for Cu-CHA and Cu-MOR demonstrated that there is no sharp spectroscopic contrast in the $O_2$-activated state for the two topologies, neither in the XANES nor in the EXAFS region, once samples with equivalent Si/Al and Cu/Al ratios are considered. Moreover, the behavior of these two Cu-zeolites along the stepwise DMTM process, as probed by operando XAS, is rather similar [17, 62]. Nonetheless, the structural models adopted for the quantitative analysis of the related EXAFS spectra significantly differs for the two topologies. While the first peak of the magnitude of the EXAFS Fourier Transform (FT) is fully recognized to be associated to Cu–O single scattering path (SS), the interpretation of the well-defined second-shell peak, most often observed in $O_2$-activated samples, appears to be more uncertain, see **sections 5.1.4** and **5.2.1**. In particular, this feature in Cu-CHA has been associated to the single scattering

(SS) paths involving the second-shell Al/Si atoms in monomeric Cu-complexes. Conversely, for Cu-MOR, the second-shell region is often modelled solely by the Cu−Cu SS paths characteristic of multimeric Cu species [1, 63].

This issue lead my friend and colleague Ilia A. Pankin (The Smart Materials Center-Southern Federal University) to build a set of theoretical models of Cu(II)-oxo complexes hosted in the CHA and MOR zeolites. These structures constituted the basis for further simulations involving the related Cu K-edge XANES spectra, whose characteristic features should represent a useful tool to aid the analysis of the experiments. Concerning the structural screening regarding all the possible siting of the Cu(II) ions, only the larger rings offered by the CHA (8r) and MOR (8r and 12r) topologies were considered. The main reason behind this choice must be found in the fact that these sites are intuitively more accessible to $O_2$. A quantitative demonstration of this last assertion can be also found in the detailed computational study realized by Vilella et al. [55].

Focusing on the location of Cu(II) sites, and excluding the $Z_2$Cu(II) sites, because considered inactive for the MTM reaction, see **section 5.2**, the complete batch of analyzed Cu(II) structures consisted of ten sites and it is reported in **Figure 5.24**.

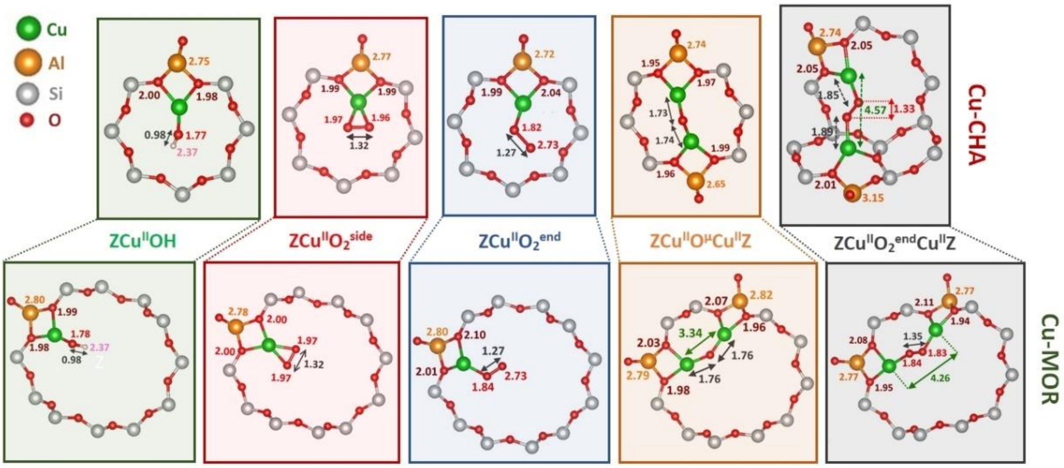

**Figure 5.24.** DFT-optimized geometries of different monomeric and dimeric Cu-oxo species incorporated into 8r of CHA and 12r of MOR frameworks (the rest of the zeolite framework is omitted for clarity). DFT-optimized interatomic distances are indicated in Å.

The technical details about the DFT optimizations can be found in the supporting information of [64].

How it is possible to see, concerning the monomeric species, in addition to the Z[Cu(II)OH] site, two super-oxo Cu(II) moieties with four-fold coordinated side-on (ZCu(II)$O_2^{side}$) and three-fold coordinated end-on (ZCu(II)$O_2^{end}$) binding mode were considered. With respect to the dimeric Cu(II) species, three-fold coordinated mono-(μ-oxo) cores ZCu(II)O$^{\mu}$Cu(II)Z and ZCu(II)$O_2^{end}$Cu(II)Z peroxides, with end-on $O_2$ binding mode were investigated. Finally, for the CHA topology, on the basis of previous theoretical investigation realized by Falsig et al. [54], the ZCu(II)$O_2^{end}$Cu(II)Z geometry locating the two Al atoms in adjacent 6r and 8r of the framework were considered too.

The overall selection of structures was motivated by previous works [1, 2, 15, 16, 55], which point towards to two possible routes to form Cu-oxo framework-coordinated species: (i) from a self-reduced ZCu(I) by interaction with an oxygen molecule which can result to the formation of monomeric superoxo or dimeric peroxo species or (ii) due to internal pathways e.g. *via* condensation of proximal ZCu(II)OH yielding to mono μ-oxo dicopper(II) cores. In both mechanisms, redox-active ZCu(II)OH species represent a viable starting point, which also implies quite abundant population of this species in the activated samples.

### 5.5.1 *XANES simulations results*

**Figure 5.25**(a) reports the Cu K-edge XANES spectra simulated using the FDM (full potential finite difference method) approach, provided by FDMNES, for the DFT-optimized monomeric and dimeric Cu-species in the CHA framework reported in **Figure 5.24**. The XANES spectrum simulated for the sole four-fold coordinated geometry, namely ZCu(II)O$_2^{side}$, demonstrates a sharper difference with respect to the rest of the theoretical curves for the models considered, exhibiting quite similar shape of the profiles. The XANES spectrum of ZCu(II)O$_2^{side}$ is characterized by a well-defined W.L. peak (denoted as **C** in **Figure 5.25**(a)) and two less intense rising-edge shoulders (denoted as **A** and **B** in **Figure 5.25**(a)). Conversely, the theoretical spectrum stemming from ZCu(II)O$_2^{end}$ shows less intense W.L. peak and more pronounced rising-edge peaks. The latter is also shifted towards higher energy. Another appreciable difference between the theoretical XANES for ZCu(II)O$_2^{side}$ and ZCu(II)O$_2^{end}$ is the energy positions of the white line peak, that is shifted towards higher energy in correspondence of end-on O$_2$ binding mode.
Overall, the shape of the theoretical XANES spectrum for ZCu(II)O$_2^{end}$ is almost overlapped in the W.L. region with the spectra calculated for the other dimeric and monomeric Cu species, where the Cu(II) centers are three-fold coordinated to two O$_{fw}$ and one O$_{efw}$ atom.

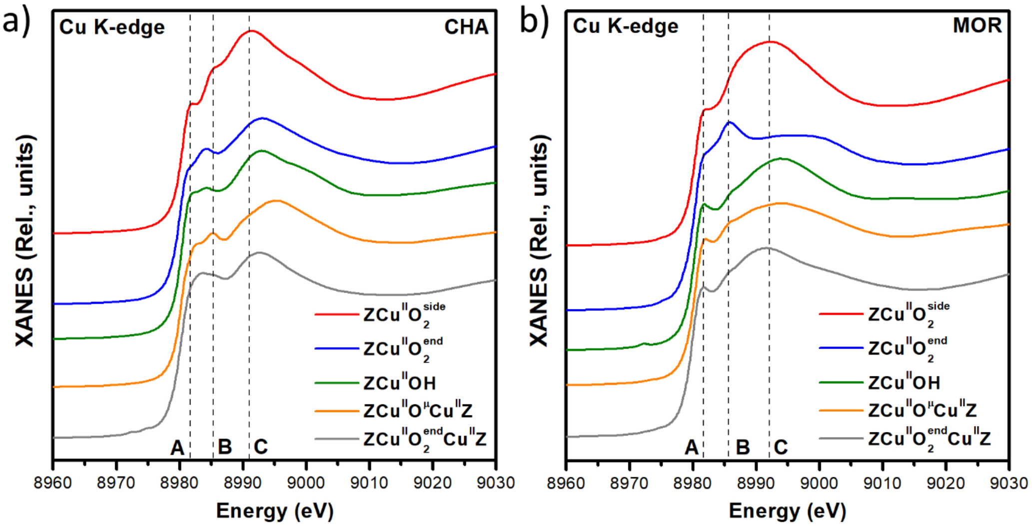

**Figure 5.25.** Cu K-edge XANES simulations for DFT-optimized Cu-oxo species in CHA (a) and MOR (b). Vertical dashed lines correspond to the energy position of the features **A**, **B** and **C** defined, for indication, based on ZCu(II)O$_2^{side}$ model for CHA in part (a) and for ZCu(II)O$_2^{end}$Cu(II)Z for MOR in part (b).

Subtle differences can be noted in the relative intensities of the **A** and **B** contributions in the rising-edge shoulder. In particular, for ZCu(II)O$_2^{end}$ and

$ZCu(II)O^{\mu}Cu(II)Z$, feature **B** is more pronounced with respect to the rest of three-fold coordinated geometries. Moreover, the theoretical spectrum obtained for $ZCu(II)O^{\mu}Cu(II)Z$ shows a slight shift to higher energy of the rising-edge feature **A** and significant shift of the white line peak **C**, while retaining the same energy localization in the absorption edge region. There is also a clear trend in the energy distance between the absorption edge and the white line peak **C** obtained for different Cu(II) species, increasing as the $Cu–O_{efw}$ distance decreases, thus being minimum for $ZCu(II)O_2^{side}$ ($<Cu–O_{efw}>=1.97$ Å) and maximum for $ZCu(II)O^{\mu}Cu(II)Z$ ($<Cu–O_{efw}> = 1.74$ Å).

Similar trends can be emphasized also from qualitative analysis of the theoretical spectra for the DFT-optimized monomeric and dimeric Cu-species hosted in 12r of MOR, reported in **Figure 5.25**(b). Again, the spectrum simulated for the four-fold coordinated $ZCu(II)O_2^{side}$ exhibits larger differences with respect to all the other models, reflecting into higher intensity of white peak **C** and lower intensity of rising-edge features **A** and **B**. It should be noted that in case of $ZCu(II)O_2^{side}$ in MOR, the feature **B** is not visible, being instead present in the spectrum of the same species in CHA. At the same time the feature **B** for $ZCu(II)O_2^{end}$ is significantly more intense with respect to what it is observed for the other Cu-species in the MOR framework, being even more intensive than the W.L. peak itself. For the others three-fold coordinated species incorporated into MOR framework, feature **B** appears to be less intensive and more convoluted with respect to the spectra simulated for the same moieties in CHA.

Overall, the observed differences in the shape of the XANES spectra computed for the geometry of the same Cu-species hosted in different framework - resulting into very similar DFT-optimized distances - highlight an appreciable effect of the distant framework environment on the simulated XANES.

In summary, the XANES simulations do not allow to highlight *nuclearity-sensitive* fingerprints in the spectra simulated for the selected monomeric and dimeric species incorporated into CHA and MOR topologies to conclusively discriminate between them. However, it is evident that in both cases, the larger differences are obtained for the $ZCu(II)O_2^{side}$ species, representative of four-fold coordinated Cu(II) sites. Conversely, for the other three-fold coordinated monomeric and dimeric moieties, no pronounced differences are observed. In all the cases, the computed curves show more intense rising-edge features and a less developed W.L. peak with respect to $ZCu(II)O_2^{side}$ with very similar XANES shape between the different three-fold coordinated models.

### 5.5.2 *Wavelet Transform Analysis on simulated EXAFS spectra*

Herein, similarly to what has been shown in **section 5.5.1** the EXAFS signal simulation stemming from two Cu(II) species, namely $ZCu(II)OH$ and $ZCu(II)O^{\mu}Cu(II)Z$ are provided. This species are representative of the Cu(II) monomers and dimers in the CHA and MOR framework, characterized by a similar, three-fold coordinated Cu local environment. As discussed in the previous section, they are difficulty discriminated solely based on their Cu K-edge XANES spectra. The procedure employed to simulate reasonably the EXAFS spectra can be described as follow. For each Cu site in the CHA and MOR framework, the phases and amplitudes of each path were calculated using the FEFF 6.0l code. Herein, the simulations were based on the assumption, supported by experimental results [40, 44, 49, 62, 65], that in the $R$-space range of interest (up to 4 Å), the SS paths represent the dominant contribution to the EXAFS signal. The structural parameters (i.e. coordination number $N_i$ and bond distances $R_i$) for all the included coordination shells were set to the DFT values. The Debye Waller (DW) parameters have been chosen for each shell according to the types of atoms and their distances from the absorber. This was done similarly to the single and multi-component fit showed in **section 5.1.4**. For the extra-framework oxygen ($O_{efw}$), a DW parameter was fixed to 0.005 Å$^2$ with the exception of the second extra-framework oxygen ($O_{efw2}$) in the ZCu(II)$O_2^{end}$ and ZCu(II)$O_2^{end}$Cu(II)Z geometries where, in order to account for the higher disorder effect, the DW was set to 0.006 Å$^2$. The same value (0.005 Å$^2$) has been used to describe the contributions involving the second sub-shell of framework oxygens ($O_{fw}$). The DW factor related to the Al coordination shell was fixed to 0.008 Å$^2$, while always at 0.008 Å$^2$ DW value was also fixed for the second Cu site in di-copper species. For the farer O and Si framework atoms, which provide a minor but not negligible contribution to the EXAFS signals, a lower-level parametrization strategy was employed. A DW factor defined in the following way: $\sigma^2 = \sigma_{fw}^2 \cdot \sqrt{R_i/R_Z}$, where $\sigma_{fw}^2$ has been fixed to a global value of 0.01 Å$^2$, $R_i$ is the optimized distance from the Cu absorber for i$^{th}$ atom, while the term $R_Z$ represents the distance of the nearest framework atom from the Cu absorber. This choice seems appropriate; in fact, it provides a slow increasing of the DW factor as the distance increases (*i.e.* isotropic increasing), accounting for the structural variation or thermal motion typically more pronounced at higher distances [66]. Finally, the amplitude factor $S_0$ was set to 1 (ideal value) and the absorption edge energy shift to 0 eV. In case of di-copper sites, the local environments associated to the two Cu-absorbers are not fully equivalent, some small but not negligible differences appear, see **Figure 5.24**. For this reason, initially, each Cu atom was considered separately (i.e. one Cu atom has been set as the absorber while the second-one as the scattering atom) applying the parametrization described above for each Cu site. Afterwards, the two simulated $k^2\chi(k)$ EXAFS signals were merged in order to obtain a single common spectrum. Once that the set of theoretical EXAFS spectra were calculated, they have been processed through the WT integral representation employing the Cauchy mother function [67]:,

$$\psi(k) = \left(\frac{i}{k+i}\right)^{\eta+1} \tag{5.1}$$

Where $i$ denotes the complex unit. The choice of this function must be attributed to its ability to simplify the WT integral showed in **chapter 3**, moreover the usage of a complex-valued function seems to be suitable for analyzing frequency-modulated signals indeed, through equation (5.1), the signal resolution is controlled by just one parameter (i.e. $\eta$) instead of additional terms, as in the case of the Morlet mother function. However, it is worth noting that, despite the reduction of the computational time required for the calculation of the WT integral, the results obtained through the Cauchy and Morlet wavelet are approximatively the same, as demonstrated in [68].

For all the selected theoretical signals, the Cauchy parameter $\eta$ was set to 200, which allows the best compromise, in term of resolution, among the $k$ and $R$ spaces. Finally, it is worth noting that for all the structures analyzed, the Fourier transforms of the EXAFS signals are phase-uncorrected and they have been obtained transforming the simulated $k^2\chi(k)$ EXAFS signals in the 2.4-11.0 Å$^{-1}$ range.

The atomic contributions of the simulated conventional EXAFS-FT signal for the two species hosted in CHA and MOR are described at first. The results, reported in **Figure 5.26**, underpin the complexity related to the interpretation of the second-shell signal, due to the simultaneous presence of single scattering (SS) paths involving the Al and Cu atomic neighbors, as well as the distant framework Si/O atoms. Moreover, the analysis of the magnitude and the imaginary part of each contribution provides deeper insights into the EXAFS-FT peaks assignment. The same simulated EXAFS spectra were further subjected to WTA, as illustrated in **Figure 5.27**, aiming to assess the potential of this alternative EXAFS analysis approach in discriminating among monomeric and dimeric Cu(II) moieties.

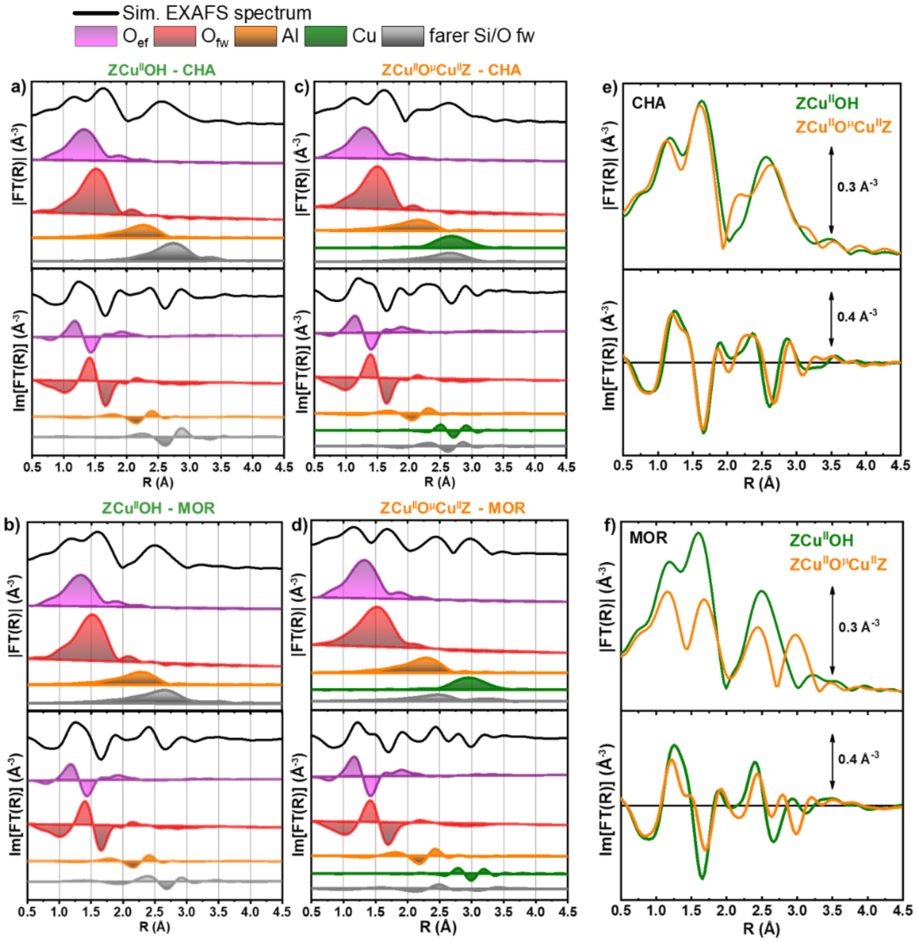

**Figure 5.26:** EXAFS-FT contributions of the simulated signals (magnitude: top panels, imaginary part: bottom panels) for ZCu(II)OH monomers (CHA: (a); MOR: (b)) and ZCu(II)O$^{\mu}$Cu(II)Z dimers (CHA: (c); MOR: (d)), vertically translated for the sake of clarity. (e, f) Direct comparison between the magnitude (top panel) and the imaginary part (bottom panel) of the simulated EXAFS-FT for monomeric ZCu(II)OH and dimeric ZCu(II)O$^{\mu}$Cu(II)Z species (e) in CHA and (f) in MOR. The selected range in k-space for all the EXAFS-FT spectra goes from 2.4 to 11.0 Å$^{-1}$. All the reported EXAFS-FT spectra are phase uncorrected.

Starting from the monomeric Z[Cu(II)OH] structures, a common trend is evident for both the framework topologies, consistently with the high similarity between ZCu(II)OH geometries in both CHA 8r and MOR 12r (see **Figure 5.24**). The ZCu(II)OH site results into a structured first-shell peak in the EXAFS-FT, where two sub-peaks are evident. The first sub-peak, less intense, is due to the $O_{efw}$ atom from the hydroxyl ligand, while the second one is related to the two nearest $O_{fw}$ atoms from the zeolite lattice, see **Figure 5.26**(a,b). Scattering contributions stemming from Al and framework Si/O atoms are mostly in phase, thus promoting the growth of a well-defined second-shell peak at ca. 2.5 Å in the phase-uncorrected EXAFS-FT spectrum.

Considering the WTA results for ZCu(II)OH, two main lobes are visible (**Figure 5.27**(a,b)). The first one, localized in the $\Delta R$ = (1.0–1.8) Å and $\Delta k$ = (0–12) Å$^{-1}$ range, is associated to the $O_{fw}$ contributions, with a sub-lobe, due to the $O_{efw}$ atomic neighbor localized at lower $R$ values. These features tend to be stretched in $k$ −space towards higher $k$-values (around 12 Å$^{-1}$). Nevertheless, only the atoms much heavier than oxygen should typically populate this region. The reason for this particular behavior represents a limitation of the analysis and it is due to the so-called *broadening effect,* whose description is provided in **Chapter 3**. The second main lobe collects the contributions coming from the Al atom and the farer Si/O atoms from the zeolite lattice. It elongates till ca. 10 Å$^{-1}$ because of the separate contributions coming from the Si and Al atoms from one side and the framework oxygens from the other, having a backscattering amplitude factor less intense at high $k$-values. It is worth noting that for all the analyzed cases, the spectral features related to the Si and Al atoms cannot be discriminated through WTA, because of their virtually equivalent backscattering amplitude factor.

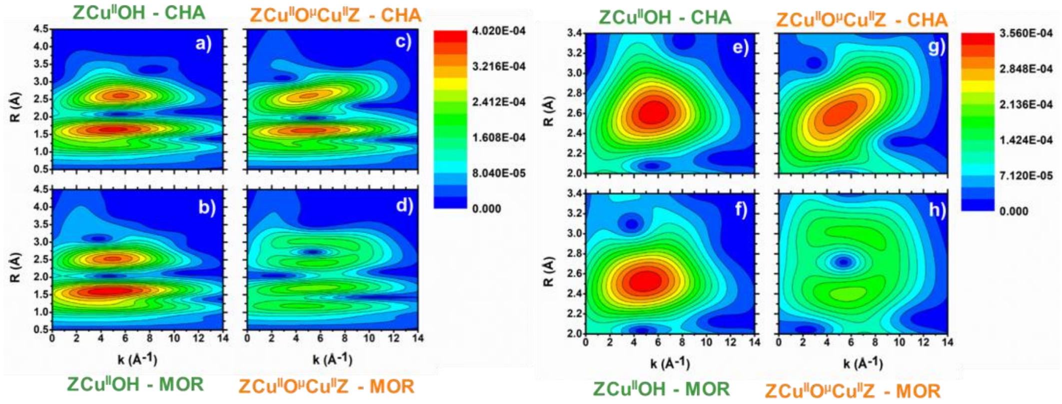

**Figure 5.27:** (a-d) Full-range EXAFS WT 2D plots for monomeric ZCu(II)OH and dimeric ZCu(II)O$^{\mu}$Cu(II)Z species in CHA 8r, parts (a) and (c), and MOR 12r, parts (b) and (d). (e-h) Respective magnifications of the second WT lobe located between 2.0 and 3.5 Å, corresponding to the second-shell region in conventional EXAFS-FT.

Analyzing the dimeric ZCu(II)O$^{\mu}$Cu(II)Z configurations, more differences appear between the two framework topologies. In CHA framework, the mono-(μ-oxo) dicopper(II) complex is located in the 8r, while in MOR it lies on the 12r plane. This implies that in CHA, from the second coordination shell upward, the distances between the Cu absorbers and its atomic neighbors (Al, farer framework Si/O and

Cu) are lower than in MOR. Consequently, a higher overlap of the atomic contributions in the 2.0–3.5 Å range is observed for ZCu(II)O$^{\mu}$Cu(II)Z in CHA with respect to the same species in MOR, see **Figure 5.26**(c,d).

The simulated EXAFS-FT spectra for ZCu(II)O$^{\mu}$Cu(II)Z and ZCu(II)OH in the CHA 8r are almost overlapped (**Figure 5.26**(e)): by standard EXAFS analysis it would be very challenging to discriminate among these mono- and di-copper(II) species. Conversely, for ZCu(II)O$^{\mu}$Cu(II)Z in the MOR 12r, the second-shell peak in the standard EXAFS-FT shows two sub-peaks, whose conformation is more complex if compared to what observed for ZCu(II)OH in the same framework (**Figure 5.26**(f)). The first sub-Al shell peak is principally due to the SS contributions from the Al and framework Si/O atoms, while the second one is mostly related to the presence of the framework Si/O atoms and the second Cu site.

A more evident representation comes, in this case, from the WT analysis of the EXAFS signal (**Figure 5.27**). At low $\mathrm{R}$ values the WT plots show the characteristic structured lobe due to the first-shell $O_{fw}$ and $O_{efw}$ contributions, broadened in $\mathrm{k}$-space as discussed before for monomeric ZCu(II)OH species. However, the second main lobe, extending in the region between $\Delta\mathrm{R}$ = (2.0–3.5 Å) and $\Delta\mathrm{k}$ = (0.5–12.0 Å$^{-1}$) presents an interesting conformation. As visible in the magnification reported in **Figure 5.27** (g,h), it is clearly composed by the combination of two sub-lobes. The first one, in the $\Delta\mathrm{k}$ = (0.5–5.0 Å$^{-1}$), stems from the contributions of Al and farer framework Si/O and atoms, whose backscattering amplitude factor peaks in the $\mathrm{k}$-space around 3-4 Å$^{-1}$, see the backscattering amplitudes plot of **Chapter 3**. The second sub-lobe extends in the $\Delta\mathrm{k}$ = (6.0–12.0 Å$^{-1}$) range. The maximum of the Cu backscattering amplitude falls exactly within this $\mathrm{k}$-space region, allowing an unambiguous assignment of this sub-lobe to Cu–Cu contributions.

Standard EXAFS-FT analysis highlights how for ZCu(II)O$^{\mu}$Cu(II)Z in the CHA 8r the Si/O framework contributions overlap with the Cu–Cu one in the same $\mathrm{R}$ space range (**Figure 5.26**(d)). The Si SS paths are characterized by a backscattering amplitude factor that is lower in magnitude at high $\mathrm{k}$-values than for Cu, but still not negligible. This is the main reason why the Cu sub-lobe is not completely separated from the sub-lobe collectively stemming from O, Al, and Si scatterers, making its complete resolution impossible to realize for this structural configuration of the dimeric core. Nevertheless, considering the poor contrast between the standard EXAFS-FT spectra simulated for ZCu(II)O$^{\mu}$Cu(II)Z and ZCu(II)OH in CHA (**Figure 5.26**(e)), it clearly emerges how WTA can, in such case, provide enhanced sensitivity to the nuclearity of the investigated Cu-species.

For ZCu(II)O$^{\mu}$Cu(II)Z in the MOR 12r, the larger ring size reflects into a better peak resolution in the EXAFS-FT plot, see **Figure 5.26**(d). Here, the Cu–Cu path is associated to a well-resolved third-shell maximum and its contribution becomes clearly evident in the WT representation, where a lobe extends in the region included between $\Delta\mathrm{R}$ = (2.7–3.4 Å) and $\Delta\mathrm{k}$ =(6.0–12.0 Å$^{-1}$), characteristic of Cu (**Figure 5.27**(d,h)).

### 5.5.3 *Critical comparison between theoretical and experimental XAS results*

In the previous sections, the characteristic XANES and EXAFS features for well-defined Cu(II)-oxo species in the CHA and MOR frameworks have been analyzed by computational modelling and DFT-assisted simulations. In the following, a critical comparison of these theoretical findings with some representative experimental result is provided. With this respect, **Figure 5.28** reports a selection of experimental XAS spectra for the $O_2$-activated Cu-CHA and Cu-MOR zeolites, with similar compositional characteristics (CHA (0.5; 12) and MOR (0.36, 11)) and measured after identical activation protocols, similar to the ones showed in the precedent section and showed in **Figure 5.1** and described in **section 5.2**.

In line with simulations reported in **section 5.5.1** , Cu-MOR and Cu-CHA show very similar Cu K-edge XANES spectra. The experimental XANES, characteristic of Cu(II) centers, show a rising-edge peak at ca. 8987 eV and an intense W.L. peak at ca. 8997 eV, with a shoulder on the low-energy side at ca. 8993 eV. Simulations reasonably reproduced the major experimental XANES features and their energy location. However, the relative intensity of rising-edge peaks with respect to the W.L. peak is over estimated, especially for three-fold coordinated Cu(II) moieties. Herein one should recall that the full potential FDM approach tends to overestimate the intensity and sharpness of rising-edge feature for Cu(II)O. Assuming a similar behavior for XANES simulation of Cu-oxo species in zeolites, it is possible explain the difference with the experimental XANES reported in **Figure 5.28**(a), as well as in other XAS studies [15, 16], where a broader, lower-intensity rising edge peak is detected. Also, different Cu(II) species have been shown to be simultaneously present in Cu-CHA [15, 40] and Cu-MOR [1, 16, 69] after activation – plausibly involving a mixture of three- and four-fold coordinated Cu centers. In addition, especially at high temperature, a significant mobility level have been proposed even for framework-coordinated ions [53]. All these factors are expected to contribute to a dampening/broadening effect in the experimental XANES features.

The experimental FT-EXAFS spectra in **Figure 5.28**(b,c) also corroborate the indications by DFT-modelling about the similarity of local environment of Cu-centers in the two investigated zeolites. In both cases, three maxima are observed, at equivalent $R$-values for the two frameworks. The rather broad first-shell peak contains contributions from O atoms in the first coordination shell of Cu centers. In line with previous EXAFS fit for Cu-CHA showed in **section 5.2.1** , two Cu-$O_{efw}$ and Cu-$O_{fw}$ sub-shells at slightly different distances (refined e.g. at 1.86 ± 0.05 Å and 1.97 ± 0.04 Å, respectively) are required to reach a satisfactory fit of the EXAFS spectra. This asymmetric coordination mode is typically observed in DFT geometries of three-coordinated Cu-species. Nonetheless, it is clear that $O_{efw}$ and $O_{fw}$ contributions in the experimental spectra are more overlapped in $R$-space with respect to what has been observed in the simulated EXAFS spectra in **section 5.5.2**, reflecting larger differences between Cu-$O_{efw}$ and Cu-$O_{fw}$ distances in the DFT models of the three-fold coordinated Cu(II)-sites.

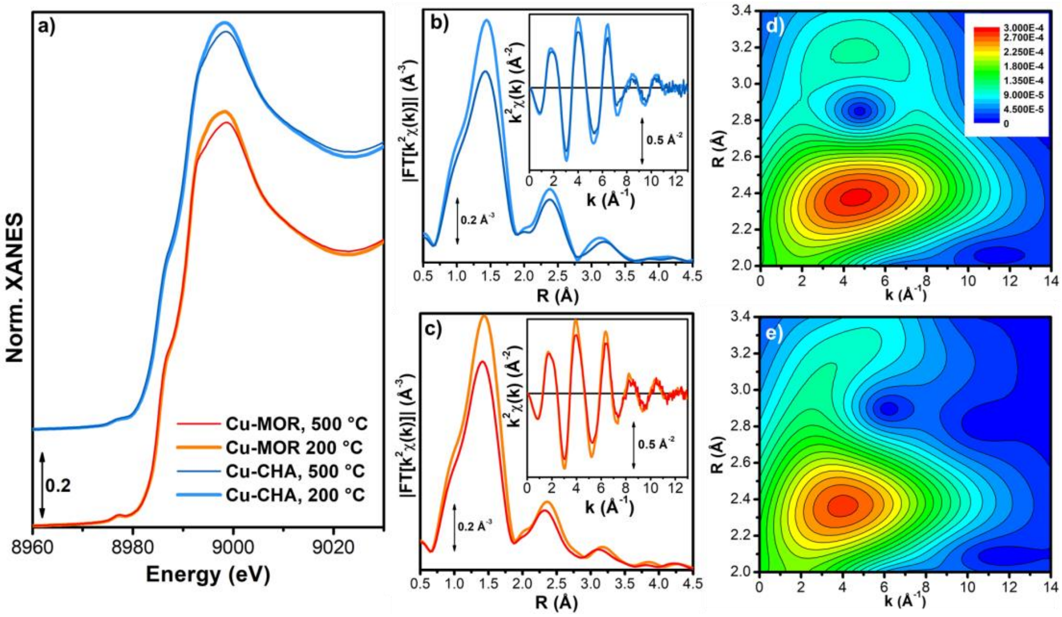

**Figure 5.28:** Selection of experimental *in situ* XAS results collected at 500 °C and 200 °C on $O_2$-activated Cu-CHA (0.15; 12) and Cu-MOR (0.36; 11) zeolites. (a) Cu K-edge XANES spectra, vertically translated for the sake of clarity. (b. c) Magnitude of FT-EXAFS spectra for (b) Cu-CHA and (c) Cu-MOR, obtained transforming the $k^2\chi(k)$ curves shown in the respective insets, in the $k$-range 2.4-11.0 Å$^{-1}$. (d, e) Experimental EXAFS WT 2D plots for the 200 °C EXAFS spectra reported in part (b, c), chosen for its better S/N ratio in the EXAFS and magnified in the region of the second WT lobe between 2.0 and 3.5 Å. The same ranges in $k$ and $R$ spaces and Cauchy resolution parameter employed in the theoretical WT plots have been adopted also in this case.

It is interesting to observe how, for both Cu-CHA and Cu-MOR, cooling to 200 °C in $O_2$ results into an appreciable increase in the intensity of the white line peak in the experimental XANES spectra together with an intensity enhancement of the EXAFS first-shell peak, beside what is expected is only due to lower thermal contribution to Debye-Waller factors. In line with the XANES simulations, such behavior could be connected with an increased relative fraction of four-fold coordinated Cu(II) moieties, such as $ZCu(II)O_2^{side}$, at lower temperature.

The WTA to the experimental EXAFS spectra is reported in **Figure 5.28**(b,c). **Figure 5.28**(d,e) reports the resulting of the EXAFS WT 2D plots, magnified in the 2.0-3.4 Å range. Indeed, the interpretation of the experimental signal is more demanding in this region, due to overlapping contributions from different types of atomic neighbors. For both Cu-zeolites, it is possible to observe some lobes extending in the $\Delta k$ = (6.0–10.0 Å$^{-1}$) interval, characteristic of the Cu-Cu scattering contributions. Thus, WTA supports the presence of an appreciable fraction of multimeric Cu-species in both cases, which would have been difficult to unambiguously assess only from conventional FT-EXAFS spectra in **Figure 5.28**(b,c). Interestingly, the WT plots for Cu-CHA and MOR also show a slightly different morphology. For Cu-CHA, the high-$k$ lobe appears at higher $R$-values than in Cu-MOR, in the $\Delta R$ = (2.7–3.0 Å) range - across the second and third maxima are observed in the FT-EXAFS spectrum. Conversely, for the Cu-MOR, a more pronounced high-k lobe is observed in the $\Delta R$ = (2.2–2.6 Å) range, corresponding to the second maximum in the FT-EXAFS spectrum.

## 5.6 EXAFS WTA OF CU-MOR UNDER MODEL RED-OX CONDITIONS: THE IMPACT OF TREATMENT AND COMPOSITION

In this section, as a further proof of the potential of EXAFS WTA in the advanced characterization of Cu-zeolites, a study regarding how the reaction conditions can influence the Cu speciation and nuclearity for a batch of different Cu-zeolites, possessing the MOR framework, is provided. In particular, the results obtained from an *ex-situ* experiment involving four kind of Cu-MOR samples are described. These are the Cu-MOR: (0.24; 7) , (0.18; 7) , (0.36; 11) and (0.1; 11).

Each sample underwent to two distinct treatments: (i) *vacuum activation* – heating in vacuum from room temperature (RT) till to 400 °C keeping the sample at 400 °C for 1 hour and cooling down to RT always in vacuum. (ii) Vacuum activation + $O_2$ 200 °C – starting from the vacuum-activated sample, pre-heating in vacuum up to 80 °C to 200 °C, keeping the sample at 200 °C for 1 hour in $O_2$, cooling down to RT (always in $O_2$), finally outgassing $O_2$ from the cell at RT. In both cases, the Cu-MOR samples were measured at RT. The data acquisition procedure followed the methodology described in **section 5.8.1**.

**Figure 5.29**(a,b) reports an overview of the *ex situ* XAS data, collected at RT for the investigated Cu-MOR zeolites, after thermal treatment in vacuum and in $O_2$, according to the protocol described above. Considering the XANES spectra obtained for the vacuum-activated samples, it is clear that, for all the Cu-MOR compositions, that the Cu ions in the systems exist in a virtually pure Cu(I) oxidation state. Cu(I) species are formed *via* self-reduction. Within the resolution of these measurements, no trace of the pre-edge peak, arising from 1s →3d transition in $d^9$ Cu(II) ions, is in fact detected. All these XANES spectra are dominated by a prominent rising-edge peak at 8982.5 eV, assigned to the 1s→4p transition in Cu(I) ions. Overall, all the acquired XANES spectra for the Cu(I) state closely resemble the one of the linear $[Cu(I)(NH_3)_2]^+$ model compound [33, 56, 70]. In line with the previous studies on Cu K-edge XANES [10] the characteristic XANES features observed here point to quasi-linear Cu(I) sites.

In the phase-uncorrected FT-EXAFS, it is possible to note a first maximum at 1.5 Å, with a broad shoulder at 2.1 Å. At longer R-values, only a broad feature peaking at 2.9 Å is observed. The first shell intensity is comparable with the one observed for the $[Cu(I)(NH_3)_2]^+$ model compound, suggesting, on average, the presence of two framework O atoms ($O_{fw}$) in the first coordination shell of Cu(I) species. For the MOR (0.36; 11), the EXAFS signal at higher R-values has been previously found consistent with partially overlapped scattering contributions involving framework Al/Si as well as Cu atomic neighbours [10, 70]. Nonetheless, the fit results were blurred by rather high correlations among the parameters employed to model the Al and Cu scattering paths, translating into a general accuracy loss in the structural refinement.

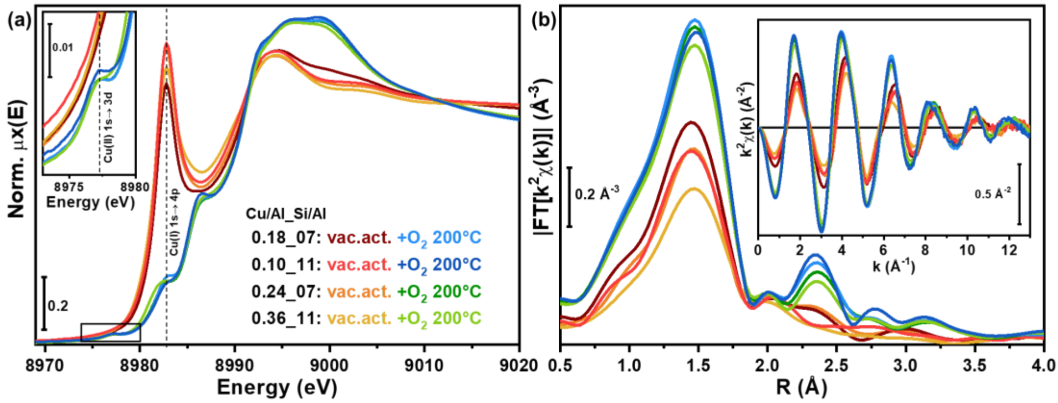

**Figure 5.29:** (a) *Ex situ* Cu K-edge XANES spectra for Cu-MOR zeolites with different compositions, obtained after vacuum-activation at 400 °C (warm colours) and exposure to $O_2$ until 200 °C (cold colours). The inset reports a magnification of the pre-edge peak arising from 1s →3d transition in $d^9$ Cu(II) ions. (b) Correspondent phase-uncorrected moduli of the Fourier transform obtained transforming the $k^2\,\chi(k)$ EXAFS signals (showed in the inset), in the 2.4-13.0 $Å^{-1}$ range. Compositional characteristics of each sample are indicated by Cu/Al_Si/Al labels.

Focusing on the *in situ* XAS of Cu-MOR after exposure to $O_2$, the related XANES features can be qualitatively interpreted based on the results showed in the precedent sections .For all the samples, the thermal treatment in $O_2$ up to 200 °C results into oxidation to Cu(II) of most of the Cu-species, characterized to occur as Cu(I) after vacuum activation. Nonetheless, a minor Cu(I) contribution is still detectable, as indicated by the residual peak at 8982.5 eV. Compared to the spectra collected after vacuum activation, it is possible to observe that the XANES of the four Cu-MOR zeolites after exposure to $O_2$ show remarkable similarities. This evidence points to comparable coordination environments for the Cu(II) ions in the zeolite cages across the investigated compositional series.

More pronounced variations are instead visible analysing the FT-EXAFS spectra reported in **Figure 5.29**(b). Here, the first-shell peaks, arising from scattering contributions by framework ($O_{fw}$) and extra-framework ($O_{efw}$) oxygen atoms, exhibit almost equivalent intensity. For all the four compositions, a well-defined feature is visible in the second-shell region, peaking at ca. 2.4 Å and extending with rather broad tails until 3.5 Å in the phase-uncorrected EXAFS spectra. Such feature exhibits composition-dependent intensity variations, being more intense for the samples MOR (0.10; 11) and (0.18; 7). Based on previous findings [1, 71] it is possible to expect that both scattering paths involving Al/Si atoms from the zeolite framework (for both mono- and multimeric Cu-species) and Cu–Cu scattering contributions are due to the contribution coming from $Cu_xO_y$ multimeric moieties influencing this R-space range.

Due to its sensitivity to the chemical nature of the scatterers surrounding the absorbing atom, the WT analysis can be exploited to validate the existence of Cu-Cu EXAFS paths, thus providing a more robust assignment to the high-R EXAFS features discussed before, based on classical FT analysis. To this aim, the WT analysis was applied on the Cu-MOR EXAFS spectra reported in **Figure 5.29**(b): an overview of the obtained results is presented in **Figure 5.30**.

Differently from **section 5.5.2**, for all the wavelet representations, a Morlet mother wavelet with the following set of parameters controlling the WT resolution was chosen: $\sigma = 1$ and $\eta = 7$. The reason of this choice must be identified in the fact that, as suggested theoretically by the models showed in **Figure 5.24**, the typical distances for Cu pairs forming during the investigated treatments fall in the 3-4 Å range, with average values of ~3.5 Å. On this basis, for all the representations, the condition of *optimal resolution* at a given distance of interest was satisfied, see **chapter 3** for a more detailed explanation.

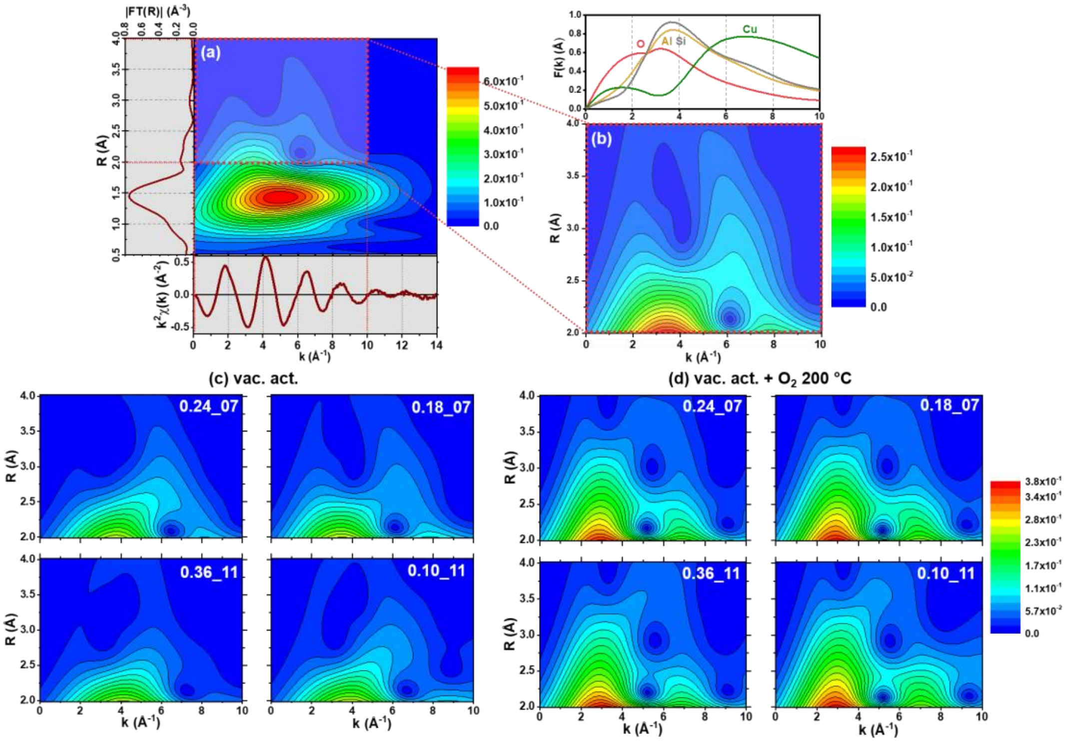

**Figure 5.30.** (a) Full-range WT representation of the EXAFS signal for a representative Cu-MOR sample, namely (0.18; 7) measured at RT after vacuum activation at 400 °C. (b) Magnification of the high-R WT region highlighted by the red dashed box in (a), in the ranges $\Delta k$ (0-10) Å$^{-1}$ and $\Delta R$ (2-4) Å. On the top is reported a plot of the relevant backscattering amplitude functions $F(k)$ as the one showed in **chapter 3**, calculated from FEFF6.0l considering the SS paths involving O, Si, Al and Cu scatterers. (c, d) High-$R$ WT region for the *ex situ* EXAFS of Cu-MOR samples (c) after vacuum activation and (d) after subsequent thermal treatment in $O_2$ up to 200 °C. Compositional characteristics of each sample are indicated by Cu/Al, Si/Al labels.

All the WT representations show a main lobe at low $R$ values ($\Delta k$ (0-12.5) Å$^{-1}$ × $\Delta R$ (0.5-2.0) Å): **Figure 5.30**(a) reports a representative example for vacuum-activated MOR (0.18; 7). As described before, this feature is associated with the single scattering contributions (SS) arising from $O_{fw}$ and $O_{efw}$ atoms. The evident elongation of the first lobe toward large $k$-values should not be connected with the presence of heavier scatterers. Rather, it is explained in **section 5.5.2** introducing the concept of spectral broadening.

**Figure 5.30**(b) shows, for the same exemplificative case, a magnification of the WT-EXAFS in the high-$R$ region (2.0-3.5 Å $\Delta R$ range). Here, two distinct sub-lobes can be visualized: the first one extends at lower $\mathrm{k}$ –values, $\Delta\mathrm{k}$ (3-5) Å$^{-1}$, while the second occurs in the range $\Delta\mathrm{k}$ (5-9) Å$^{-1}$. Comparing the $\mathrm{k}$-space ranges where these sub-lobes extends with the relevant backscattering amplitude factor curves $\mathrm{F(k)}$, also reported in **Figure 5.30**(b), it is possible to safely assert that the first sub-lobe is dominated by the contributions of lighter elements (O, Si, Al). Conversely, the second sub-lobe peaks at ca. 7 Å$^{-1}$, precisely matching the $\mathrm{k}$-value where the Cu backscattering function has its maximum. Thus, it can be unambiguously assigned to Cu-Cu scattering contributions.

**Figure 5.30**(c) compares the high-R WT maps obtained for the vacuum-activated Cu-MOR samples. Here, the two sub-lobes discussed above are always distinguishable, albeit certain differences as a function of the sample composition can be appreciated. These results provide direct structural evidence for the presence of coupled Cu(I)···Cu(I) sites [70] giving rise to the high-$\mathrm{k}$ sub-lobe in the WT maps. However, such feature appears to be more emphasized at lower Si/Al and Cu/Al ratios.

Considering the *ex situ* EXAFS data obtained upon thermal treatment in $O_2$, the same considerations about the WT main lobe at low $\mathrm{R}$-values made for the vacuum-activated materials, remain valid. This feature is always associated to the contributions involving $O_{fw}$ and $O_{efw}$ atoms, which may be located at different distances from the Cu centre, but possess the same elemental identity.

Focusing on the high-R WT features summarized in **Figure 5.30**(d), it is possible to observe clearly, for all the investigated compositions, the presence of two sub-lobes. Again, their localization in $\mathrm{k}$-space is consistent with major contributions from framework elements (O, Si, Al) and Cu, for the first and second sub-lobe, respectively. Thus, WT analysis visually demonstrates the presence of framework-coordinated multimeric $Cu_xO_y$ cores, plausibly formed upon interaction with $O_2$ with the coupled Cu(I)···Cu(I) ions detected after vacuum activation.

Comparing these WT representations with the ones obtained after vacuum activation, it becomes evident that the high-$\mathrm{R}$ the WT features are morphologically different. In particular, the high-$\mathrm{k}$ sub-lobe, fingerprinting Cu-Cu scattering, is shifted towards lower values of $\mathrm{R}$. At the same time, all the low-$\mathrm{k}$ sub-lobes become more intense and expand to higher distances. This behaviour can be rationalized assuming that, upon interaction with $O_2$, Cu···Cu pairs undergo substantial structural rearrangement, involving contraction of the interatomic distances between the Cu(II) centres in multimeric cores and approaching to the framework of Cu(II) ions.

The WT results reported here for Cu-MOR provide direct structural support to these theoretical insights, which would have been difficult to access solely by conventional FT-EXAFS analysis.

In order to better compare the different compositions and treatments explored in this work in term of presence/relative abundance of Cu-Cu contributions, the power density $\mathrm{k}$-dependent function $\Phi^{R}(\mathrm{k})$, described in **chapter 3** has been calculated in the $\mathrm{R}$ range within 2 and 4 Å and it is reported in **Figure 5.31**.

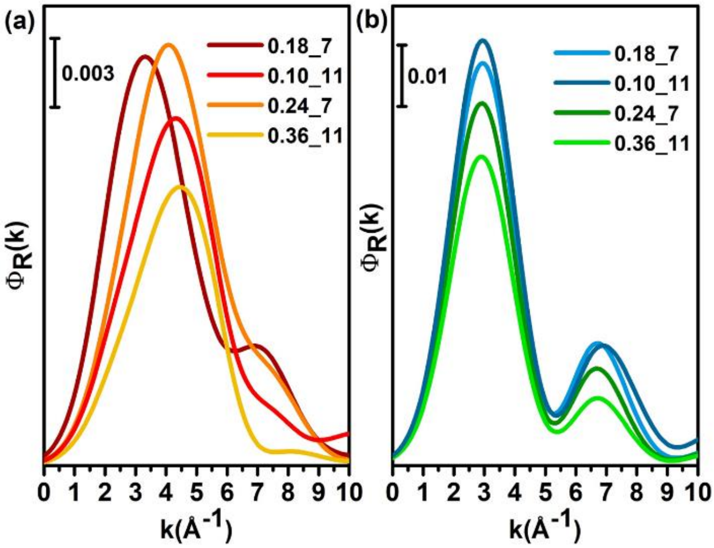

**Figure 5.31:** Wavelet power density functions $\Phi^R(k)$ calculated for all the investigated samples from *ex situ* EXAFS data collected (a) after vacuum activation and (b) after subsequent thermal treatment in $O_2$ up to 200 °C. The range of calculation is within 2 and 4 Å.

All the $\Phi^R(k)$ functions in **Figure 5.31** show a main peak localized at lower $k$-values followed by a weaker peak localized at around 7 Å$^{-1}$. The peak FWHM essentially depends on the broadening of the FT-EXAFS features in the relevant $R$-space range, which is higher after the vacuum activation with respect to the following treatment in $O_2$. Based on the previous considerations about $k$-dependency of $F(k)$ functions, the main peak can be associated with SS and MS contributions involving lighter elements (i.e. Si, Al, and $O_{fw}$ atoms belonging to the zeolite lattice, as well as $O_2$-derived $O_{efw}$ after $O_2$ thermal treatment). More interesting is the localization of the second peak. This last feature corresponds with the maximum of the backscattering amplitude function associated to Cu-Cu SS paths and can be considered as a direct fingerprint for the presence of this kind of contributions, reflecting the high-$k$ sub-lobe in the WT maps discussed before. While the 2D representations in **Figure 5.30**(c,d) carry out simultaneous information in both $R$- and $k$-space, the $\Phi^R(k)$ integral functions offer a more practical way to compare different samples/conditions over the relevant $R$-space range. Indeed, analysing **Figure 5.31**(a,b), it is possible to note a characteristic trend for the intensity associated with the Cu-Cu feature. At fixed Si/Al ratio in the zeolite framework, the peak intensity is higher for that samples having a lower content of Cu (i.e. Cu/Al = 0.18 and 0.10, at Si/Al = 7 and 11, respectively). The same trend can be observed after both vacuum activation and subsequent thermal treatment in $O_2$. This observation points to a *saturation* mechanism driving the formation of Cu-Cu pairs in MOR, whose abundance appears, counterintuitively, seems to be inversely correlated with the amount of Cu in the sample. Notably, a similar behaviour is well documented for 2Al sites in the same six-member ring of the CHA topology, ions, as properly described in **section 5.1.2**. Framework composition and synthesis parameters are known to shape the Al distribution in the zeolite lattice [72], giving rise to a limited number of 2Al docking sites, with Al···Al separation potentially suitable to support multi-copper moieties once Cu is exchanged into the zeolite. The compositional trend emerging from this analysis suggests that, along the dehydration process, Cu should preferentially occupy such 2Al sites, resulting into Cu-Cu pair detectable by EXAFS WT. Once the available 2Al exchange sites are saturated, Cu ions will start to populated isolated 1Al sites, forming monomeric Cu-species, which are silent in the high-$k$ region of the WT plane. In this scenario, for the same parent zeolite, higher Cu-loading translates in a higher relative abundance of mono-copper species over total Cu in the system. Remembering that XAS is an absorber-averaged technique, this causes an abatement of the spectral features associated to multimeric configurations (sub-lobes and peaks around 7 $Å^{-1}$ in **Figure 5.30**(c,d) and **Figure 5.31**(a,b), respectively) in the EXAFS-WT response, representing an average over all the Cu-species present weighted by their relative abundance.

## 5.7 FOLLOWING BY EXAFS-WTA THE DMTM CONVERSION OVER MOR (0.18; 7)

This section shows the results obtained monitoring through the XAS technique the key steps of the DMTM process over the MOR (0.18; 7). In particular, similarly to **section 5.1,** XAS was used here to monitor the dynamic evolution of the Cu local environment along the MTM reaction protocol. The MOR (0.18; 7) was selected because of its outstanding activity towards the target reaction, resulting in a methanol productivity per Cu of 0.47 mol activated $CH_4$/mol Cu, at optimal process conditions [16, 62]. Moreover, as already discussed in **section 5.4**, by combining MCR analysis of HERFD XANES data with DMTM testing at consistent conditions has been shown how for this specific Cu-MOR sample, the $CH_4$ is activated over a dicopper(II) site, involving the large majority of the Cu ions in the system.

### 5.7.1 *Key DMTM reaction steps monitored by EXAFS WT*

**Figure 5.32**(a,b) shows the *in situ* XANES and EXAFS spectra acquired for each step involved in the DMTM conversion (the inset of **Figure 5.32**(a) shows the scheme of the followed protocol, which appears to be analogous to the one depicted in **Figure 5.1**).

The $O_2$-activation at 500 °C results into a largely dominant Cu(II) oxidation state. The observed XAS features are consistent with tridentate O-ligated Cu(II) units, located at defined ion-exchange sites in the zeolite framework. Certain modifications are observed in the XANES spectra at the end of the $O_2$-activaton step at 200 °C, principally regarding the W.L. region. In particular, a higher W.L. intensity is observed, pointing to a higher first-shell coordination number. A similar trend is observable analysing the related FT-EXAFS where the diminution of the temperature correlates with an increasing of the intensity of the first and second shell. This behaviour is primarily due to the diminution of the Debye-Waller (DW) factors as a function of the temperature. However, the thermal effect is accompanied by a structural rearranging in the first coordination sphere of Cu, upon cooling from 500 to 200 °C in $O_2$, as also observed in Cu-CHA, see **section 5.2**.

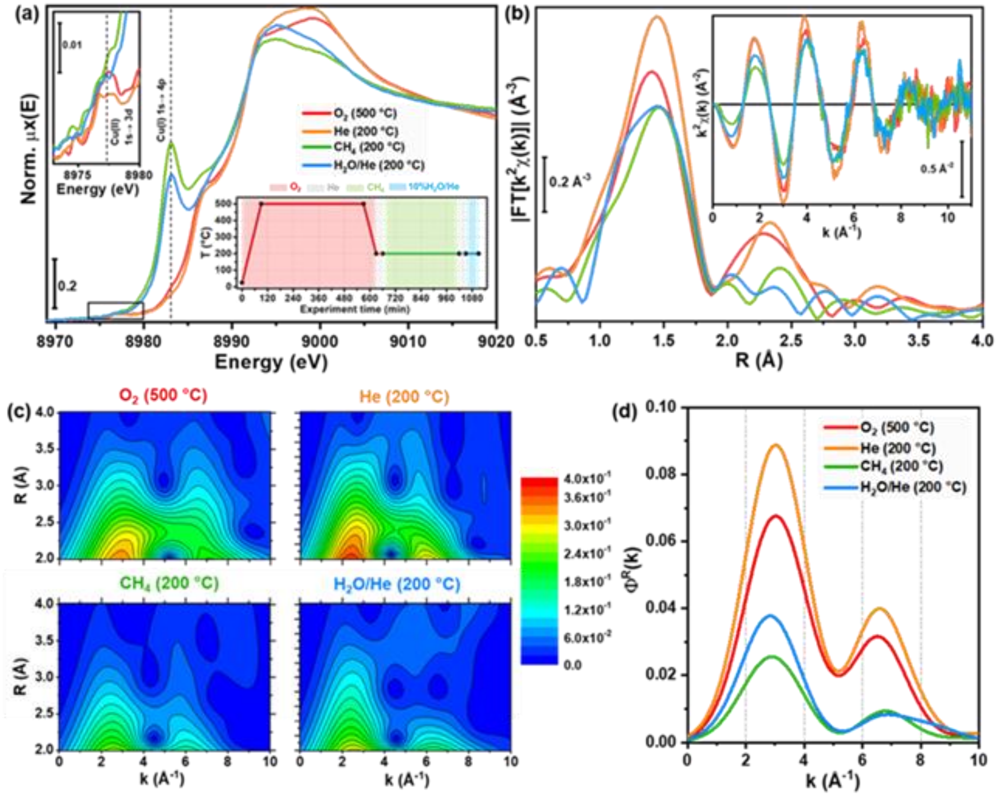

**Figure 5.32**. (a) XANES spectra of MOR (0.18; 7) after the key steps of the DMTM process. The upper inset reports a magnification of the pre-edge region. (b) $k^2\chi(k)$ signals and related magnitudes of the EXAFS-FT modulus. (c) High-$R$ WT region for the EXAFS spectra reported in (b). (d) Power density functions calculated for the WT plots reported in (c) in the integration range within 2 and 4 Å.

A comparison of the WT-EXAFS plots for the states at 500 and 200 °C, **Figure 5.32**(c) - top panels, does not evidence important differences in the high-$R$ range, except for a general increase of signal intensity at 200 °C, attributable to the natural reduction of DW factors at the lower data collection temperature. Importantly, it is possible to recognize a very similar morphology of WT as the one discussed in **section 5.6** for $O_2$-treated MOR (0.18; 7) measured *ex situ*, with sub-lobes stemming from both Cu-O/Si/Al and Cu-Cu scattering contributions. In agreement with the results showed in **section 5.6** framework-coordinated $Cu_xO_y$ species are thus confirmed to form during high-temperature $O_2$-activation. Such multimeric species persist with a virtually equivalent second-shell coordination environment during the subsequent cooling step in $O_2$, preceding to $CH_4$ loading.

The pronounced modifications occurring in the XAS spectra during the $CH_4$-loading and steam-assisted $CH_3OH$ extraction step reflect the Cu(II) to Cu(I) reduction process and the subsequent hydration phenomena. From the spectra reported in **Figure 5.32**(a,b), it is clear that Cu(I) species are formed during $CH_4$-loading at 200 °C and persist after the $CH_3OH$ extraction step. This is evidenced in the XANES by the 1s→4p rising edge peak at 8982.5 eV, characteristic of Cu(I) sites in a linear of quasi-linear coordination geometry, as already observed in the *ex situ* XAS of (0.18; 7) after vacuum activation (**section 5.6**). In parallel, the first-shell intensity in the EXAFS diminishes, consistently with the formation of a fraction of two-fold coordinated Cu(I) species. At higher $\mathrm{R}$-values, standard FT-EXAFS highlight a substantial decrease of the well-defined feature observed in the $O_2$-activated material, evolving towards an almost unstructured signal after steam-assisted $CH_3OH$ extraction.

Wavelet analysis performed on these two steps, **Figure 5.32**(c) – bottom panels, evidences a simultaneous attenuation of both sub-lobes associated to framework and Cu contributions. This result is further supported from the WT power density functions $\Phi^{\mathrm{R}}(\mathrm{k})$ for the four steps of the DMTM process and reported in **Figure 5.32**(d). Here, it is possible to see that the contribution associated to the Cu-Cu paths, peaking at 7 Å$^{-1}$, undergoes to a substantial attenuation after the $CH_4$ loading step, albeit remaining detectable. A closer look at the corresponding WT map in **Figure 5.32**(c) evidences a weak, residual sub-lobe in the $\mathrm{k}$-range diagnostic for Cu-Cu contributions, shifting to higher $\mathrm{R}$-values (3.0-3.5 Å) with respect to the $O_2$-activated state. After $CH_3OH$ extraction, the Cu-Cu peak in $\Phi^{R}(\mathrm{k})$ remains very weak and further it broads so that it is difficult to resolve it as a distinct feature. Here, the features associated with low-Z scatterers in both $\Phi^{R}(\mathrm{k})$ and WT map appear slightly intensified with respect to the $CH_4$-loading step. Conventional FT-EXAFS shows an intensity enhancement of the low-$\mathrm{R}$ side of the first-shell peak, consistent with an increased coordination number in a fraction of Cu-sites, most likely undergoing to partial hydration upon exposure to steam. This translates in an average enhancement of MS contribution involving first-shell O ligands, hence accounting for the intensity increase of the WT features in the low-$\mathrm{k}$ range.

The structural insights emerging from WT analysis prove how the $CH_4$ activation on Cu-active sites is accompanied by severe rearrangements in the local coordination environment of Cu ions, involving the breakage of $Cu_xO_y$ multicopper moieties, and the average elongation of interatomic distances between Cu and framework atoms. These resemble, in an inverse order, the structural transformations detected in *ex situ* experiments upon thermal treatment in $O_2$ of self-reduced Cu-MOR, presented in **section 5.6**.

### 5.7.2 *EXAFS fitting using the WT representation*

An important pre-requisite to advance in the understanding of the DMTM process is the experimental determination of the local structure of the active Cu species. Due to its sensitivity to the chemical nature of the scatterers and to the possibility to conjugate the information coming from the $\mathrm{k}$-space with the $\mathrm{R}$-space, here it is proposed a fit of the EXAFS spectrum using the WT representation. A technical description of the strategy employed to implement this novel fitting technique is provided in **chapter 3**.

To assess the feasibility and potential of the WT EXAFS fitting, the EXAFS spectrum of the $O_2$-activated MOR (0.18; 7) after cooling to 200 °C in $O_2$ and He flush (orange curves in **Figure 5.32**(b)) was employed. This choice it is principally due to the fact that that this state immediately precedes the $CH_4$ loading step, while ensuring a better S/N ratio with respect to the EXAFS data collected at 500 °C. Moreover, as showed in **section 5.4.3** at the process conditions adopted in the *in situ* XAS experiments, this state should contain almost exclusively active dicopper $Cu_2O_x$ moieties.

A simple SS shell model for the fitting procedure was considered. In particular, a first-shell composed by both $O_{fw}$ and $O_{efw}$ atoms was used, while the signal at high-$R$ was modelled including three separate coordination shells, involving framework Al and Si scatterers, as well as Cu atoms form multicopper species. The distances used to initialize the minimization procedure were defined according to the DFT models provided showed in **section 5.5**. In the fitting procedure, for each shell, the average distances $<R_i>$ and the coordination numbers $N_i$ were refined, resulting into a number of guessed parameters $N°_{par} = 9$. On the basis of previous results obtained from standard EXAFS fits of $O_2$-activated Cu-zeolites, as the one showed in **section 5.2.1**, all the SS paths were fixed on a common amplitude reduction factor ($S_0^2$) as well as the DW factors associated to each shell; a global energy shift parameter ($\Delta E$) was instead optimized in the fit. The fitting procedure was performed in the two dimensional range within $\Delta k$=(2.4-10.5) $Å^{-1}$ and $\Delta R$=(1.0-3.5), resulting into a number of independent point $N°_{ind} = 13$. **Figure 5.33** compares experimental and best-fit full-range WT plots while the results of the WT fitting procedure are reported in **Table 5.9**.

The best-fit WT plot in **Figure 5.33**(a) properly reproduces all the main features associated to the experimental WT features, as quantified by the R-factor associated to the reconstruction, equal to 0.01. At the same time, from the graphical analysis of the individual WT contributions in **Figure 5.33**(b), it is possible to observe how their location in the ($k$, $R$) space falls in line with the qualitative analysis and the assignments provided before.

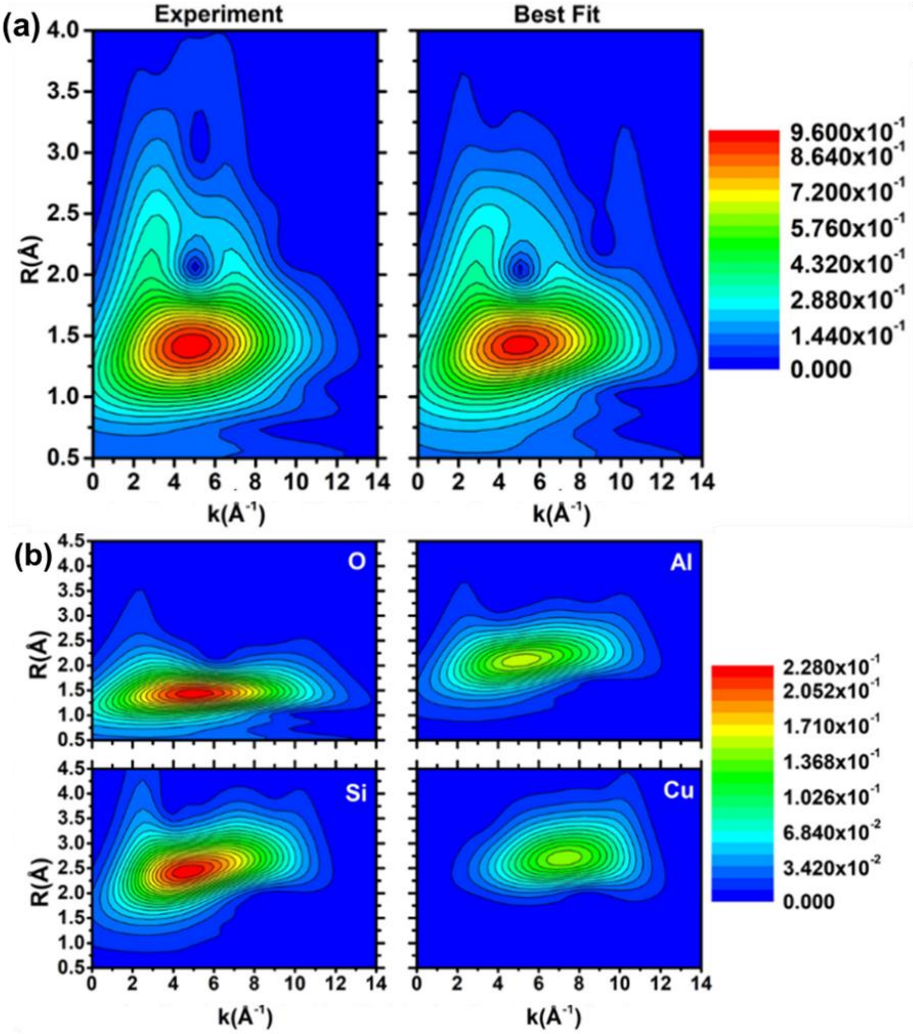

**Figure 5.33.** (a) Comparison between the best fit and the experimental WT representation of the EXAFS signal acquired on $O_2$-activated MOR (0.18; 7). (b) WT representation associated to the individual scattering contributions (Cu-O, Cu-Al, Cu-Si and Cu-Cu) extracted from the fit. The intensity for the Cu-O contribution (top left plot) refers to the colour scale displayed in part (a), whereas all the other (high-R) contributions have been plotted according to the colour scale reported in part (b), to facilitate comparison among the relevant WT features.

| EXAFS Parameters | Best Fit values |
|---|---|
| $\Delta R$ (Å) | 2.5 |
| $\Delta k$ (Å$^{-1}$) | 8.1 |
| $N°_{par}/N°_{ind}$ | 9/13 |
| $R_{factor}$ | 0.01 |
| $S_0^2$ | <u>0.9</u> |
| $\Delta E$ (eV) | -1.93 ± 0.07 |
| $<R_O>$ (Å) | 1.939 ± 0.001 |
| $<R_{Al}>$ (Å) | 2.724 ± 0.002 |
| $<R_{Cu}>$ (Å) | 3.112 ± 0.003 |
| $<R_{Si}>$ (Å) | 3.138 ± 0.003 |
| $\sigma_O^2$ (Å$^2$) | <u>0.004</u> |
| $\sigma_{Al}^2$ (Å$^2$) | <u>0.006</u> |
| $\sigma_{Cu}^2$ (Å$^2$) | <u>0.007</u> |
| $\sigma_{Si}^2$ (Å$^2$) | <u>0.008</u> |
| $N_O$ | 3.03 ± 0.01 |
| $N_{Al}$ | 0.90 ± 0.02 |
| $N_{Cu}$ | 0.99 ± 0.03 |
| $N_{Si}$ | 2.22 ± 0.04 |

**Table 5.9:** Results of the WT EXAFS fit for $O_2$-activated MOR (0.18; 7) after cooling to 200 °C in $O_2$ and He flush (orange curves in **Figure 5.32**(b)). The parameters fixed in the fit are underlined.

The Fitting results support the dominant presence of di-copper species ($N_{Cu}$ ~1) surrounded by a first shell of O atoms with coordination number $N_O$ ~ 3. The number of Al and Si atoms, identified by the fit, is refined to ca. 1 and 2 respectively. These values are in accordance with the coordination numbers associated to Al and Si shells previously found in $O_2$ activated Cu-zeolites [1]. At the same time, the optimized interatomic distances are consistent with the DFT values showed in **Figure 5.24** by precedent theoretical works [55, 64]. Based on these available models for Cu local environment, it is possible to envisage the presence of two $O_{fw}$ and one $O_{efw}$ atoms, bridging the two Cu centres. A possible configuration compatible with the obtained results could involve Cu-mono-(μ-oxo) dimers. The presence of Cu-peroxo dicopper species with an end-on $O_2$-binding mode is instead discouraged, based on the Cu-Cu distance found by the fit. Indeed, the optimized value of $<R_{Cu}>$ ~ 3.1 Å is significantly shorter than the DFT value of ca. 4.3 Å predicted for the latter species in Cu-MOR [64].

It is worth to note that several constraints have been adopted in this initial, exploratory EXAFT-WT fit. In the model was considered a single O shell entailing both $O_{fw}$ and $O_{efw}$, to fix the DW factors and neglect the farer O atoms of the zeolite lattice. These choices had the purpose to building of a flexible structural model, capable of describing different types of Cu-species, allowing to obtain a first screening on the most likely configuration [68].

## 5.8 APPENDIX: EXPERIMENTAL METHODS

### 5.8.1 *In situ Cu K-edge XAS*

Experimental data were collected in transmission mode at the BM23 of the European Synchrotron Radiation Facility (ESRF), using double-crystal Si(111) monochromator for the incident energy scan and ionization chambers for the detection of incident and transmitted photons. The chambers were filled with a He/Ar mixture up to 2.2 bar with the partial pressure of argon of 0.1 and 0.3 bar for $I_0$ and $I_1$ chambers, respectively. For an accurate edge energy calibration, a copper foil was measured simultaneously with all the acquired spectra using a third ionization chamber $I_2$. The Cu-CHA and MOR catalysts were measured in the form of a self-supporting wafers (optimized samples weights in the 90−140 mg range for 1.3 cm$^2$ area pellets, resulting in edge jumps $\Delta\mu x$ in the 0.3−1.1 range for a total absorption after the edge of $\mu x = 2.5$) fixed inside the Microtomo reactor cell developed at the ESRF [73]. Two different XAS acquisition modes were employed. The evolution of the XANES features during the He, $O_2$–activation or other kind of gas flux was monitored with faster acquisitions of ~ 6 min, from 8900 to 9182 eV (up to ~ 7 Å$^{-1}$), allowing to appreciate the variation of the XAS signal as a function of the temperature (pre-edge region energy step = 5 eV, edge region energy step = 0.3 eV. On the other hand, the EXAFS part was collected with variable sampling step in energy, resulting in $\Delta k = 0.08$ Å$^{-1}$; integration time was 1 s/point in all regions). Two consecutive higher-quality XAS scans of ~ 30 min each were collected from 8800 to 9955 eV (up to ~ 16 Å$^{-1}$) with enhanced $k$-space sampling ($\Delta k = 0.035$ Å$^{-1}$) and acquisition time in the EXAFS region, quadratically increasing with $k$ from 1 to 4 s/point to account for the lower signal-to-noise ratio as $k$ increases. The final spectra employed for EXAFS fitting were obtained as the average of the two $\mu(E)$ curves corresponding to the consecutive scans, after checking reproducibility among the two acquisitions. All the collected XAS spectra were aligned in energy using the corresponding Cu metal foil spectra detected by the $I_2$ ionization chamber and normalized to unity edge jump

### 5.8.2 *Operando XAS*

*Operando* XAS experiments were performed at the BM31 beamline (Swiss Norwegian Beamline, SNBL-II) of the ESRF. Cu K-edge XAS spectra were collected in transmission mode, using a water-cooled flat Si(111) double crystal monochromator. To measure the incident ($I_0$) and transmitted ($I_1$) X-ray intensity, 30 cm-length ionization chambers filled with a mixture of He and Ar were used. Continuous scans were performed in the 8800–10000 eV range, with an energy

step of 0.7 eV in the pre-edge range, of 0.5 eV in the edge region, and a fixed $k$ step of 0.05 $Å^{-1}$ in the EXAFS region. Collection of one XAS spectrum required 10 min. The $O_2$-activated state for each catalyst were characterized collecting two consecutive XAS scans and averaging the corresponding $\mu(E)$ curves after checking for signal reproducibility. For the measurements, the Cu-MOR powder was ground and sieved with 425 to 250 µm sieves; ca. 3 mg of catalyst were then packed in a capillary reactor (1 mm diameter) connected to an appropriate gas-flow setup for the stepwise MTM reaction. Temperature at the measurement position was controlled by a heat gun. A total flow rate of 2 ml/min was employed for all the reaction steps, including. XAS spectra were normalized to unity edge jump.
The gas composition of the outlet gas from the reactor has been continuously monitored by means of a mass spectrometer.

### 5.8.3 *In situ and Operando HERFD XANES*

The measurements were performed at the ID26 beamline of the ESRF. The spectra were acquired in fluorescence mode, detecting only photons whose energy corresponded to the maximum intensity of the Cu $K_{\beta}$ 1,3 emission line (~8906 eV). This energy selection was performed using five Si(553) analyser crystals ($\theta$ = 79.92°), set up in vertical Rowland geometry, resulting in spectra resolution of 1.06 eV (elastic peak). The crystals were spherically bent following the Johann scheme to focus the fluorescence radiation onto an avalanche photodiode (APD) detector. For the incident beam a flat double-crystal Si (311) monochromator was employed. The time acquisition for each spectrum was set to 2 min. The measurements were conducted using a well-established gas flow setup, based on the Microtomo reactor [73] cell (developed by the ESRF Sample Environment team), that allowed to precisely control the gas composition and the temperature inside. The Cu-CHA and MOR samples were prepared in the form of self-supporting wafers (ca. 100 mg of sample) and fixed inside the reactor cell.

## 5.9 REFERENCES

[1] E.M.C. Alayon, M. Nachtegaal, A. Bodi, M. Ranocchiari, J.A. van Bokhoven, Bis(mu-oxo) versus mono(mu-oxo)dicopper cores in a zeolite for converting methane to methanol: an in situ XAS and DFT investigation, Phys Chem Chem Phys, 17 (2015) 7681-7693.
[2] E.M.C. Alayon, M. Nachtegaal, A. Bodi, J.A. van Bokhoven, Reaction conditions of methane-to-methanol conversion affect the structure of active copper sites, ACS Catal., 4 (2014) 16-22.
[3] S.C. Larsen, A. Aylor, A.T. Bell, J.A. Reimer, Electron Paramagnetic Resonance Studies of Copper Ion-Exchanged ZSM-5, J. Phys. Chem., 98 (1994) 11533-11540.
[4] G.T. Palomino, P. Fisicaro, S. Bordiga, A. Zecchina, E. Giamello, C. Lamberti, Oxidation states of copper ions in ZSM-5 zeolites. A multitechnique investigation, J. Phys. Chem. B, 104 (2000) 4064-4073.
[5] C. Paolucci, A.A. Verma, S.A. Bates, V.F. Kispersky, J.T. Miller, R. Gounder, W.N. Delgass, F.H. Ribeiro, W.F. Schneider, Isolation of the Copper Redox Steps in

the Standard Selective Catalytic Reduction on Cu-SSZ-13, Angew. Chem.-Int. Edit., 53 (2014) 11828-11833.
[6] M.A. Newton, A.J. Knorpp, V.L. Sushkevich, D. Palagin, J.A. van Bokhoven, Active sites and mechanisms in the direct conversion of methane to methanol using Cu in zeolitic hosts: a critical examination, Chem. Soc. Rev., 49 (2020) 1449-1486.
[7] G.A. Olah, Beyond oil and gas: The methanol economy, Angew. Chem.-Int. Edit., 44 (2005) 2636-2639.
[8] M. Ravi, M. Ranocchiari, J.A. van Bokhoven, The Direct Catalytic Oxidation of Methane to Methanol-A Critical Assessment, Angew. Chem.-Int. Edit., 56 (2017) 16464-16483.
[9] E.I. Solomon, J.W. Ginsbach, D.E. Heppner, M.T. Kieber-Emmons, C.H. Kjaergaard, P.J. Smeets, L. Tian, J.S. Woertink, Copper dioxygen (bio) inorganic chemistry, Faraday Discuss., 148 (2011) 11-39.
[10] E.I. Solomon, D.E. Heppner, E.M. Johnston, J.W. Ginsbach, J. Cirera, M. Qayyum, M.T. Kieber-Emmons, C.H. Kjaergaard, R.G. Hadt, L. Tian, Copper Active Sites in Biology, Chem. Rev., 114 (2014) 3659-3853.
[11] R.M. Barrer, P.J. Denny, 201. Hydrothermal chemistry of the silicates. Part IX. Nitrogenous aluminosilicates, Journal of the Chemical Society (Resumed), (1961) 971-982.
[12] X.J. Meng, F.S. Xiao, Green Routes for Synthesis of Zeolites, Chem. Rev., 114 (2014) 1521-1543.
[13] P. Tomkins, M. Ranocchiari, J.A. van Bokhoven, Direct Conversion of Methane to Methanol under Mild Conditions over Cu-Zeolites and beyond, Accounts Chem. Res., 50 (2017) 418-425.
[14] M.B. Park, E.D. Park, W.S. Ahn, Recent Progress in Direct Conversion of Methane to Methanol Over Copper-Exchanged Zeolites, Front. Chem., 7 (2019) 7.
[15] D.K. Pappas, E. Borfecchia, M. Dyballa, I.A. Pankin, K.A. Lomachenko, A. Martini, M. Signorile, S. Teketel, B. Arstad, G. Berlier, C. Lamberti, S. Bordiga, U. Olsbye, K.P. Lillerud, S. Svelle, P. Beato, Methane to Methanol: Structure Activity Relationships for Cu-CHA, J. Am. Chem. Soc., 139 (2017) 14961-14975.
[16] D.K. Pappas, A. Martini, M. Dyballa, K. Kvande, S. Teketel, K.A. Lomachenko, R. Baran, P. Glatzel, B. Arstad, G. Berlier, C. Lamberti, S. Bordiga, U. Olsbye, S. Svelle, P. Beato, E. Borfecchia, The Nuclearity of the Active Site for Methane to Methanol Conversion in Cu-Mordenite: A Quantitative Assessment, J. Am. Chem. Soc., 140 (2018) 15270-15278.
[17] E. Borfecchia, K.A. Lomachenko, F. Giordanino, H. Falsig, P. Beato, A.V. Soldatov, S. Bordiga, C. Lamberti, Revisiting the nature of Cu sites in the activated Cu-SSZ-13 catalyst for SCR reaction, Chem. Sci., 6 (2015) 548-563.
[18] F. Giordanino, P.N.R. Vennestrom, L.F. Lundegaard, F.N. Stappen, S.L. Mossin, P. Beato, S. Bordiga, C. Lamberti, Characterization of Cu-exchanged SSZ-13: a compared FTIR, UV-Vis and EPR study with Cu-ZSM-5 and Cu-b with similar Si/Al and Cu/Al ratios, Dalton Trans., 42 (2013) 12741-12761.
[19] C. Lamberti, S. Bordiga, F. Bonino, C. Prestipino, G. Berlier, L. Capello, F. D'Acapito, F. Xamena, A. Zecchina, Determination of the oxidation and coordination state of copper on different Cu-based catalysts by XANES spectroscopy in situ or in operando conditions, Phys Chem Chem Phys, 5 (2003) 4502-4509.

[20] C. Lamberti, S. Bordiga, M. Salvalaggio, G. Spoto, A. Zecchina, F. Geobaldo, G. Vlaic, M. Bellatreccia, XAFS, IR, and UV-vis study of the Cu-I environment in Cu-I-ZSM-5, J. Phys. Chem. B, 101 (1997) 344-360.
[21] C. Lamberti, S. Bordiga, A. Zecchina, M. Salvalaggio, F. Geobaldo, C.O. Arean, XANES, EXAFS and FTIR characterization of copper-exchanged mordenite, J. Chem. Soc.-Faraday Trans., 94 (1998) 1519-1525.
[22] C. Lamberti, G. Spoto, D. Scarano, C. Pazé, M. Salvalaggio, S. Bordiga, A. Zecchina, G.T. Palomino, F. Dacapito, Cu-I-Y and Cu-II-Y zeolites: A XANES, EXAFS and visible-NIR study, Chem. Phys. Lett., 269 (1997) 500-508.
[23] C. Lamberti, A. Zecchina, E. Groppo, S. Bordiga, Probing the surfaces of heterogeneous catalysts by in situ IR spectroscopy, Chem. Soc. Rev., 39 (2010) 4951-5001.
[24] M. Benfatto, P. D'Angelo, S. Della Longa, N.V. Pavel, Evidence of distorted fivefold coordination of the $Cu^{2+}$ aqua ion from an x-ray-absorption spectroscopy quantitative analysis, Phys. Rev. B, 65 (2002) 174205.
[25] P. Frank, M. Benfatto, B. Hedman, K.O. Hodgson, Solution $[Cu(amm)]^{2+}$ is a strongly solvated square pyramid: A full account of the copper K-edge XAS spectrum within single-electron theory, Inorg. Chem., 47 (2008) 4126-4139.
[26] K. Kervinen, P.C.A. Bruijnincx, A.M. Beale, J.G. Mesu, G. van Koten, R. Gebbink, B.M. Weckhuysen, Zeolite framework stabilized copper complex inspired by the 2-His-1-carboxylate facial triad motif yielding oxidation catalysts, J. Am. Chem. Soc., 128 (2006) 3208-3217.
[27] G.T. Palomino, E. Giamello, P. Fisicaro, S. Bordiga, C. Lamberti, A. Zecchina, Polycarbonylic and polynitrosylic species in CuI-exchanged ZSM-5, b, Mordenite and Y zeolites: comparison with homogeneous complexes, Stud. Surf. Sci. Catal., 130 (2000) 2915-2920.
[28] M. Sano, S. Komorita, H. Yamatera, XANES spectra of copper(II) complexes - correlation of the intensity of the 1s-3d transition and the shape of the complex, Inorg. Chem., 31 (1992) 459-463.
[29] F. Xamena, P. Fisicaro, G. Berlier, A. Zecchina, G.T. Palomino, C. Prestipino, S. Bordiga, E. Giamello, C. Lamberti, Thermal reduction of $Cu^{2+}$-mordenite and Re-oxidation upon interaction with $H_2O$, $O_2$, and NO, J. Phys. Chem. B, 107 (2003) 7036-7044.
[30] C. Prestipino, L. Capello, F. D'Acapito, C. Lamberti, Local structure of $[Cu(I)(CO)_2]^+$ adducts hosted inside ZSM-5 zeolite probed by EXAFS, XANES and IR spectroscopies, Phys Chem Chem Phys, 7 (2005) 1743-1746.
[31] J.M. Tranquada, S.M. Heald, A.R. Moodenbaugh, X-ray-absorption near-edge-structure study of $La_{2-x}(Ba,Sr)_xCuO_{4-y}$ superconductors, Phys. Rev. B, 36 (1987) 5263-5274.
[32] L.S. Kau, K.O. Hodgson, E.I. Solomon, X-ray absorption edge and EXAFS study of the copper sites in zinc oxide methanol synthesis catalysts, J. Am. Chem. Soc., 111 (1989) 7103-7109.
[33] T.V.W. Janssens, H. Falsig, L.F. Lundegaard, P.N.R. Vennestrøm, S.B. Rasmussen, P.G. Moses, F. Giordanino, E. Borfecchia, K.A. Lomachenko, C. Lamberti, S. Bordiga, A. Godiksen, S. Mossin, P. Beato, A Consistent Reaction Scheme for the Selective Catalytic Reduction of Nitrogen Oxides with Ammonia, ACS Catal., 5 (2015) 2832-2845.

[34] K.A. Lomachenko, E. Borfecchia, S. Bordiga, A.V. Soldatov, P. Beato, C. Lamberti, Active sites in Cu-SSZ-13 deNOx catalyst under reaction conditions: a XAS/XES perspective, J. Phys.: Conf. Ser., 712 (2016) 012041.
[35] J.S. McEwen, T. Anggara, W.F. Schneider, V.F. Kispersky, J.T. Miller, W.N. Delgass, F.H. Ribeiro, Integrated operando X-ray absorption and DFT characterization of Cu-SSZ-13 exchange sites during the selective catalytic reduction of $NO_x$ with $NH_3$, Catal Today, 184 (2012) 129-144.
[36] C. Paolucci, A.A. Parekh, I. Khurana, J.R. Di Iorio, H. Li, J.D. Albarracin Caballero, A.J. Shih, T. Anggara, W.N. Delgass, J.T. Miller, F.H. Ribeiro, R. Gounder, W.F. Schneider, Catalysis in a Cage: Condition-Dependent Speciation and Dynamics of Exchanged Cu Cations in SSZ-13 Zeolites, J. Am. Chem. Soc., 138 (2016) 6028-6048.
[37] C. Andersen, M. Bremholm, P. Vennestrøm, A. Blichfeld, L. Lundegaard, I. B., Locating Cu in Zeolite SSZ-13 by Synchrotron PXRD Using Maximum Entropy Method, IUCrJ, 1 (2014) doi:10.1107/S2052252514020181.
[38] L.S. Kau, D.J. Spirasolomon, J.E. Pennerhahn, K.O. Hodgson, E.I. Solomon, X-ray absorption-edge determination of the oxidation-state and coordination-number of copper - application to the type-3 site in rhus-vernicifera laccase and its reaction with oxygen, J. Am. Chem. Soc., 109 (1987) 6433-6442.
[39] ADF2012, SCM, Theoretical Chemistry, Vrije Universiteit, Amsterdam, The Netherlands, http://www.scm.com, in.
[40] A. Martini, E. Borfecchia, K.A. Lomachenko, I.A. Pankin, C. Negri, G. Berlier, P. Beato, H. Falsig, S. Bordiga, C. Lamberti, Composition-driven Cu-speciation and reducibility in Cu-CHA zeolite catalysts: a multivariate XAS/FTIR approach to complexity, Chem. Sci., 8 (2017) 6836-6851.
[41] P.D. Angelo, E. Bottari, M.R. Festa, H.F. Nolting, N.V. Pavel, Structural investigation of copper(II) chloride solutions using x-ray absorption spectroscopy, J. Chem. Phys., 107 (1997) 2807-2812.
[42] P. D'Angelo, S. Della Longa, A. Arcovito, G. Mancini, A. Zitolo, G. Chillemi, G. Giachin, G. Legname, F. Benetti, Effects of the Pathological Q212P Mutation on Human Prion Protein Non-Octarepeat Copper-Binding Site, Biochemistry, 51 (2012) 6068-6079.
[43] P. D'Angelo, F. Pacello, G. Mancini, O. Proux, J.L. Hazemann, A. Desideri, A. Battistoni, X-ray absorption investigation of a unique protein domain able to bind both copper(I) and copper(II) at adjacent sites of the N-terminus of Haemophilus ducreyi Cu,Zn superoxide dismutase, Biochemistry, 44 (2005) 13144-13150.
[44] E. Borfecchia, P. Beato, S. Svelle, U. Olsbye, C. Lamberti, S. Bordiga, Cu-CHA - a model system for applied selective redox catalysis, Chem. Soc. Rev., 47 (2018) 8097-8133.
[45] S.A. Bates, A.A. Verma, C. Paolucci, A.A. Parekh, T. Anggara, A. Yezerets, W.F. Schneider, J.T. Miller, W.N. Delgass, F.H. Ribeiro, Identification of the active Cu site in standard selective catalytic reduction with ammonia on Cu-SSZ-13, J Catal, 312 (2014) 87-97.
[46] J.S. Woertink, P.J. Smeets, M.H. Groothaert, M.A. Vance, B.F. Sels, R.A. Schoonheydt, E.I. Solomon, A $[Cu_2O]^{2+}$ core in Cu-ZSM-5, the active site in the oxidation of methane to methanol, P. Natl. Acad. Sci. USA., 106 (2009) 18908-18913.

[47] S.I. Zabinsky, J.J. Rehr, A. Ankudinov, R.C. Albers, M.J. Eller, Multiple-scattering calculations of x-ray-absorption spectra, Phys. Rev. B, 52 (1995) 2995-3009.

[48] B. Ravel, M. Newville, ATHENA, ARTEMIS, HEPHAESTUS: data analysis for X-ray absorption spectroscopy using IFEFFIT, J. Synchrot. Radiat., 12 (2005) 537-541.

[49] K.A. Lomachenko, E. Borfecchia, C. Negri, G. Berlier, C. Lamberti, P. Beato, H. Falsig, S. Bordiga, The Cu-CHA deNO(x) Catalyst in Action: Temperature-Dependent NH3-Assisted Selective Catalytic Reduction Monitored by Operando XAS and XES, J. Am. Chem. Soc., 138 (2016) 12025-12028.

[50] C. Prestipino, G. Berlier, F. Xamena, G. Spoto, S. Bordiga, A. Zecchina, G.T. Palomino, T. Yamamoto, C. Lamberti, An in situ temperature dependent IR, EPR and high resolution XANES study on the NO/$Cu^+$-ZSM-5 interaction, Chem. Phys. Lett., 363 (2002) 389-396.

[51] A. Godiksen, F.N. Stappen, P.N.R. Vennestrom, F. Giordanino, S.B. Rasmussen, L.F. Lundegaard, S. Mossin, Coordination Environment of Copper Sites in Cu-CHA Zeolite Investigated by Electron Paramagnetic Resonance, J. Phys. Chem. C, 118 (2014) 23126-23138.

[52] A.R. Kulkarni, Z.J. Zhao, S. Siahrostami, J.K. Norskov, F. Studt, Monocopper Active Site for Partial Methane Oxidation in Cu-Exchanged 8MR Zeolites, ACS Catal., 6 (2016) 6531-6536.

[53] F. Göltl, P. Sautet, I. Hermans, The impact of finite temperature on the coordination of Cu cations in the zeolite SSZ-13, Catal Today, 267 (2016) 41-46.

[54] H. Falsig, P.N.R. Vennestrøm, P.G. Moses, T.V.W. Janssens, Activation of Oxygen and NO in NH3-SCR over Cu-CHA Catalysts Evaluated by Density Functional Theory, Top. Catal., 59 (2016) 861-865.

[55] L. Vilella, F. Studt, The Stability of Copper Oxo Species in Zeolite Frameworks, Eur. J. Inorg. Chem., (2016) 1514-1520.

[56] F. Giordanino, E. Borfecchia, K.A. Lomachenko, A. Lazzarini, G. Agostini, E. Gallo, A.V. Soldatov, P. Beato, S. Bordiga, C. Lamberti, Interaction of $NH_3$ with Cu-SSZ-13 Catalyst: A Complementary FTIR, XANES, and XES Study, J. Phys. Chem. Lett., 5 (2014) 1552-1559.

[57] M.H. Groothaert, P.J. Smeets, B.F. Sels, P.A. Jacobs, R.A. Schoonheydt, Selective oxidation of methane by the bis(mu-oxo)dicopper core stabilized on ZSM-5 and mordenite zeolites, J. Am. Chem. Soc., 127 (2005) 1394-1395.

[58] P. Glatzel, U. Bergmann, High resolution 1s core hole X-ray spectroscopy in 3d transition metal complexes - electronic and structural information, Coord. Chem. Rev., 249 (2005) 65-95.

[59] J. Singh, C. Lamberti, J.A. van Bokhoven, Advanced X-ray absorption and emission spectroscopy: in situ catalytic studies, Chem. Soc. Rev., 39 (2010) 4754-4766.

[60] E.A. Pidko, E.J.M. Hensen, R.A. van Santen, Self-organization of extraframework cations in zeolites, Proc. R. Soc. A-Math. Phys. Eng. Sci., 468 (2012) 2070-2086.

[61] P.J. Smeets, R.G. Hadt, J.S. Woertink, P. Vanelderen, R.A. Schoonheydt, B.F. Sels, E.I. Solomon, Oxygen Precursor to the Reactive Intermediate in Methanol Synthesis by Cu-ZSM-5, J. Am. Chem. Soc., 132 (2010) 14736-14738.

[62] K.A. Lomachenko, A. Martini, D.K. Pappas, C. Negri, M. Dyballa, G. Berlier, S. Bordiga, C. Lamberti, U. Olsbye, S. Svelle, P. Beato, E. Borfecchia, The impact of reaction conditions and material composition on the stepwise methane to methanol conversion over Cu-MOR: An operando XAS study, Catal Today, 336 (2019) 99-108.
[63] S. Grundner, M.A.C. Markovits, G. Li, M. Tromp, E.A. Pidko, E.J.M. Hensen, A. Jentys, M. Sanchez-Sanchez, J.A. Lercher, Single-site trinuclear copper oxygen clusters in mordenite for selective conversion of methane to methanol, Nat. Commun., 6 (2015).
[64] I.A. Pankin, A. Martini, K.A. Lomachenko, A.V. Soldatov, S. Bordiga, E. Borfecchia, Identifying Cu-oxo species in Cu-zeolites by XAS: A theoretical survey by DFT-assisted XANES simulation and EXAFS wavelet transform, Catal Today, 345 (2020) 125-135.
[65] A. Martini, E. Alladio, E. Borfecchia, Determining Cu-Speciation in the Cu-CHA Zeolite Catalyst: The Potential of Multivariate Curve Resolution Analysis of In Situ XAS Data, Top. Catal., 61 (2018) 1396-1407.
[66] E. Sevillano, H. Meuth, J.J. Rehr, Extended x-ray absorption fine structure Debye-Waller factors. I. Monatomic crystals, Phys. Rev. B, 20 (1979) 4908-4911.
[67] M. Munoz, P. Argoul, F. Farges, Continuous Cauchy wavelet transform analyses of EXAFS spectra: A qualitative approach, Am. Mineral., 88 (2003) 694-700.
[68] A. Martini, M. Signorile, C. Negri, K. Kvande, K.A. Lomachenko, S. Svelle, P. Beato, G. Berlier, E. Borfecchia, S. Bordiga, EXAFS wavelet transform analysis of Cu-MOR zeolites for the direct methane to methanol conversion, Phys Chem Chem Phys, 22 (2020) 18950-18963.
[69] V.L. Sushkevich, D. Palagin, J.A. van Bokhoven, The Effect of the Active-Site Structure on the Activity of Copper Mordenite in the Aerobic and Anaerobic Conversion of Methane into Methanol, Angew. Chem.-Int. Edit., 57 (2018) 8906-8910.
[70] C. Buono, A. Martini, I.A. Pankin, D.K. Pappas, C. Negri, K. Kvande, K.A. Lomachenko, E. Borfecchia, Local structure of Cu(I) ions in the MOR zeolite: A DFT-assisted XAS study, Radiat. Phys. Chem., (2018) 108111.
[71] P. Vanelderen, J. Vancauwenbergh, B.F. Sels, R.A. Schoonheydt, Coordination chemistry and reactivity of copper in zeolites, Coord. Chem. Rev., 257 (2013) 483-494.
[72] J. Dedecek, Z. Sobalik, B. Wichterlova, Siting and Distribution of Framework Aluminium Atoms in Silicon-Rich Zeolites and Impact on Catalysis, Catal. Rev., 54 (2012) 135-223.
[73] G. Agostini, D. Meira, M. Monte, H. Vitoux, A. Iglesias-Juez, M. Fernandez-Garcia, O. Mathon, F. Meunier, G. Berruyer, F. Perrin, S. Pasternak, T. Mairs, S. Pascarelli, B. Gorges, XAS/DRIFTS/MS spectroscopy for time-resolved operando investigations at high temperature, J. Synchrot. Radiat., 25 (2018) 1745-1752.

# 6 STRUCTURE AND REACTIVITY OF $[Cu_2(NH_3)_4O_2]^{2+}$ COMPLEXES IN CU-CHA CATALYST FOR $NH_3$-MEDIATED SELECTIVE CATALYTIC REDUCTION: A XAS STUDY

The selective catalytic reduction of $NO_x$ to $N_2$ by ammonia (SCR-$NH_3$) has played an important role in the abatement of the $NO_x$ emissions in the exhaust of diesel engines and power plants since 1970s. Catalysts based on Cu-ion exchanged chabazite (Cu-CHA) are very effective for this reaction and are commonly applied today in the automotive sector. These catalysts feature a high activity around 200 °C, a good selectivity for $N_2$ formation, and excellent thermal stability in the harsh conditions of exhaust after-treatment systems [1, 2].
The standard $NH_3$-SCR reaction is a redox reaction following the equation:

$$4NO + 4NH_3 + O_2 \rightarrow 4N_2 + 6H_2O$$

Concerning Cu-zeolites, a few standard SCR mechanism proposals have appeared in recent literature, derived from combined experimental and theoretical works. All of them agree on the fact that the $NH_3$-SCR activity of Cu-CHA catalysts is due to the capability of the Cu ions to reversibly change the oxidation state between Cu(I) and Cu(II) [3-6]. The reaction cycle can be performed stepwise, by alternating a reduction in a mixture of NO and $NH_3$, and an oxidation in a mixture of NO and $O_2$ [5, 7]. For the reduction half-cycle, there is converging evidence that the reduction of Cu(II) by NO and $NH_3$ at around 200 °C results in the formation of linear $[Cu(I)(NH_3)_2]^+$ complexes. These complexes are weakly bound to the zeolite, and therefore mobile [5, 7-9].
In the oxidation half cycle, the Cu(I) species reacts with $O_2$ to form a Cu(II) species. Therefore, the reaction of $O_2$ with the linear $[Cu(I)(NH_3)_2]^+$ complexes is an essential step in the $NH_3$-SCR reaction cycle at low temperature. In a milestone work, Paolucci et al. [9], demonstrated that due to the effective diffusion of $[Cu(I)(NH_3)_2]^+$ complexes inside the zeolite cage (ca. 9 Å, although still constrained by the electrostatic tethering to charge balancing Al sites), it is possible that in presence of $O_2$ two $[Cu(I)(NH_3)_2]^+$ could determine the formation of a $NH_3$ -solvated dicopper Cu(II)-oxo complex. In particular, the structures that are formed after the reaction of an $O_2$ molecule and two $[Cu(I)(NH_3)_2]^+$ complexes are Cu molecules containing two Cu-centers bridged by oxygen. The general formula of these complexes is $[Cu_2(NH_3)_4O_2]^{2+}$ [9]. Efforts to determine the structure of this complex have mainly been based on DFT calculations. **Figure 6.1**(a,b,c) shows three possible structures assumed to be plausible candidates to represent the $[Cu_2(NH_3)_4O_2]^{2+}$ complexes, which differ in the way the oxygen molecule is bound to the Cu, and whether dissociation of the O-O bond takes place or not [4, 9-11]. The calculated stabilities of these structures with DFT have been shown to strongly depend on the method and functionals chosen in the calculation and an experimental verification is needed [10].

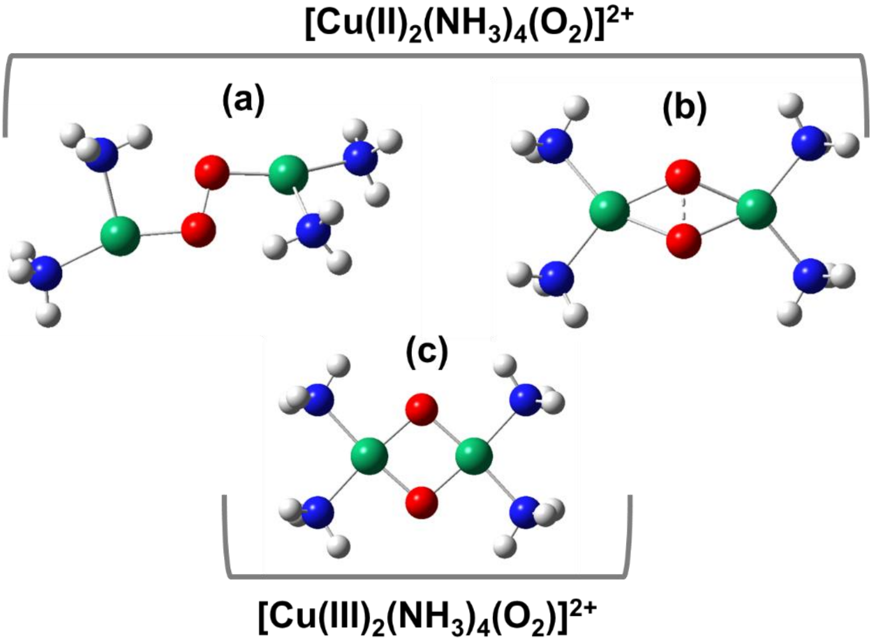

**Figure 6.1:** Pictorial representation of the $[Cu_2(NH_3)_4O_2]^{2+}$ complexes proposed in [9] : a) trans μ-1,2-peroxo diamino dicopper (II) (peroxo end-on); b) μ-$\eta^2$,$\eta^2$-peroxo diamino dicopper (II) (peroxo side-on) and c) bis-μ-oxo diamino dicopper (III).

In the following, the XAS investigation and analysis of the structure and reactivity of the $[Cu_2(NH_3)_4O_2]^{2+}$ complexes, formed upon reaction of $O_2$ with the mobile $[Cu(I)(NH_3)_2]^+$ complexes in a Cu-CHA catalyst for $NH_3$-SCR, is showed (**section 6.1**). Therefore, the the reactivity of the $[Cu_2(NH_3)_4O_2]^{2+}$ complexes towards NO and $NH_3$ is analyzed and discussed (**section 6.2**).

The catalyst used in this study was a Cu-CHA zeolite possessing the following composition: (0.5; 15) (see **chapter 5** for the nomenclature criteria here adopted). The selection of this composition was led by the knowledge of its higher yield of $N_2$ during the $NH_3$ mediated SCR reaction [8]. The steps depicted in **Figure 6.2** were used to form the $[Cu_2(NH_3)_4O_2]^{2+}$ complexes, and to study the reactivity towards NO and $NH_3$ experimentally. They can be divided in four parts:

- pretreatment in $O_2$ at 400 °C;
- reduction in a mixture of 1000 ppm NO and 1000 ppm $NH_3$ at 200 °C to form $[Cu(I) (NH_3)_2]^+$ [4, 7-9]; oxidation of the $[Cu(I)(NH_3)_2]^+$ complexes by $O_2$ at 200 °C to form the $[Cu_2(NH_3)_4O_2]^{2+}$ complexes [9];
- reaction of the $[Cu_2(NH_3)_4O_2]^{2+}$ complexes with NO or $NH_3$ at 200 °C

The steps in this protocol were followed by XAS coupled to an online mass spectrometer for effluent gas analysis (BM23 beamline of the European Synchrotron Radiation Facility) [12]. The description regarding the XAS data acquisition protocol can be found in **section 5.8.1**of the appendix part in **chapter 5**.

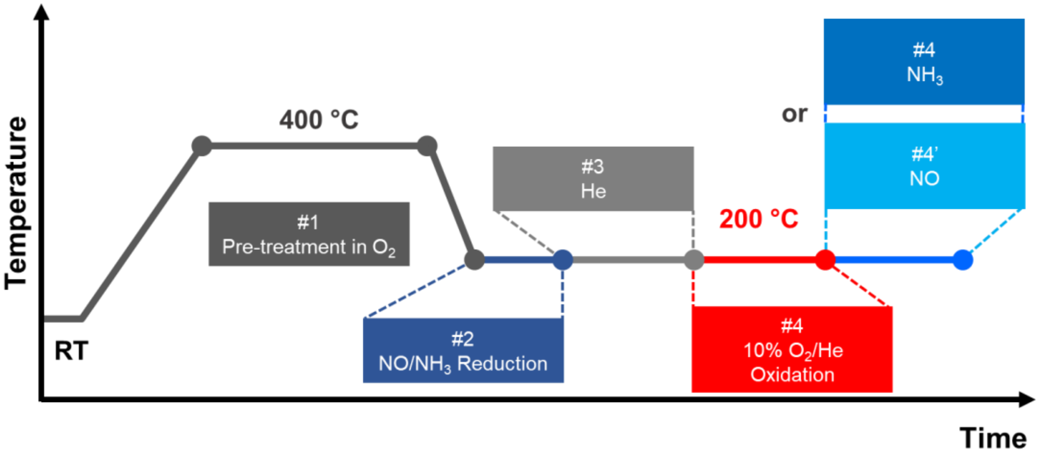

**Figure 6.2:** Experimental protocol followed by XAS: #1) pre-treatment at 400 °C in pure $O_2$; #2) reduction in 1000 ppm NO/1000 ppm $NH_3$/He; #3) oxidation in 10%$O_2$/He; #4) reaction with 1000 ppm $NH_3$/He or 1000 ppm NO/He (#4'). Total gas flow: 100 ml/min.

## 6.1 OXIDATION AND COORDINATION STATE OF CU IONS

The starting point of the experiment is represented by the formation of the linear $[Cu(I)(NH_3)_2]^+$ complexes. These complexes are formed by exposure of the Cu-CHA catalyst to a NO/$NH_3$ mixture at 200 °C. The presence of this state is indicated by a characteristic rising-edge peak at ~8982.5 eV in the Cu K-edge XANES spectrum, corresponding to the $1s \rightarrow 4p$ transition of linearly coordinated Cu(I) centers (**Figure 6.3**(a), blue curve). Upon reaction of this linear $[Cu(I)(NH_3)_2]^+$ complex with a mixture of 10% $O_2$ in He, this distinct peak at 8982.5 eV disappears almost completely, the XANES resembles that observed after pre-treatment in $O_2$ (**Figure 6.3**(a), red and grey dashed lines) and the dipole-forbidden $1s \rightarrow 3d$ transition of Cu(II) becomes visible at 8977.3 eV (**Figure 6.3**(b)). These changes clearly indicate that the linear $[Cu(I) (NH_3)_2]^+$ complex is oxidized by $O_2$. After 30 minutes in $O_2$/He, a small feature at 8982.5 eV is still recognized, but the spectra do not change any more. This indicates, that not all $[Cu(I)(NH_3)_2]^+$ complexes are oxidized: in agreement with the earlier observations [9] about 10-20% of the $[Cu(I)(NH_3)_2]^+$ complexes do not react, based on qualitative XANES analysis.

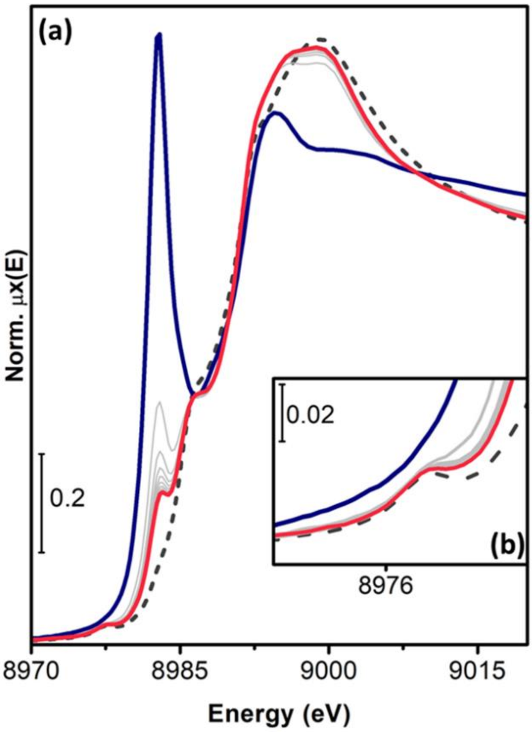

**Figure 6.3:** Evolution of the Cu K-edge XANES (a) of Cu-CHA during exposure to 10% $O_2$/He at 200 °C after reduction in NO/$NH_3$/He at 200 °C. The Inset in panel (b) reports a magnification of the pre-edge peak arising from the Cu(II) $1s \rightarrow 3d$ transition. Dark blue thick line: after NO/$NH_3$/He exposure; red thick line: final spectrum after exposure to 10% $O_2$; grey thin lines: intermediates; dark grey dashed line: Cu-CHA pre-treated in $O_2$.

### 6.1.1 *Structure of the $[Cu_2(NH_3)_4O_2]^{2+}$ complexes*

To determine the precise structure of the Cu(II) complex formed by the oxidation of the linear $[Cu(I)(NH_3)_2]^+$ species with $O_2$, it appears necessary to analyse the FT (Fourier Transform) -EXAFS spectra. **Figure 6.4**(a) shows these data without phase correction. The first-shell peak is almost doubled in intensity after the $O_2$ interaction (from blue to red), indicating that the coordination number of Cu in the Cu(II) complexes is higher than in the linear $[Cu(I)(NH_3)_2]^+$ complex. In the next shell, the unstructured feature observed for the mobile $[Cu(I)(NH_3)_2]^+$ complex evolves towards a broad scattering feature peaking at ca. 2.4 Å. Even though this feature is close to the second-shell EXAFS signature of framework-coordinated Cu(II) ions after pre-treatment in $O_2$ (dashed grey line), it can be clearly distinguished, indicating that, at least a substantial part of the Cu(II) complex is still mobile in the cage. Finally, a third peak around 3.2 Å develops, which could correspond to contributions from a Cu-Cu scattering in the Cu complexes shown in **Figure 6.1**. All these features in the FT-EXAFS are consistent with the formation of $[Cu_2(NH_3)_4O_2]^{2+}$ complexes, though a more detailed analysis is required to identify the precise structure, based on the three possibilities shown in **Figure 6.1**.

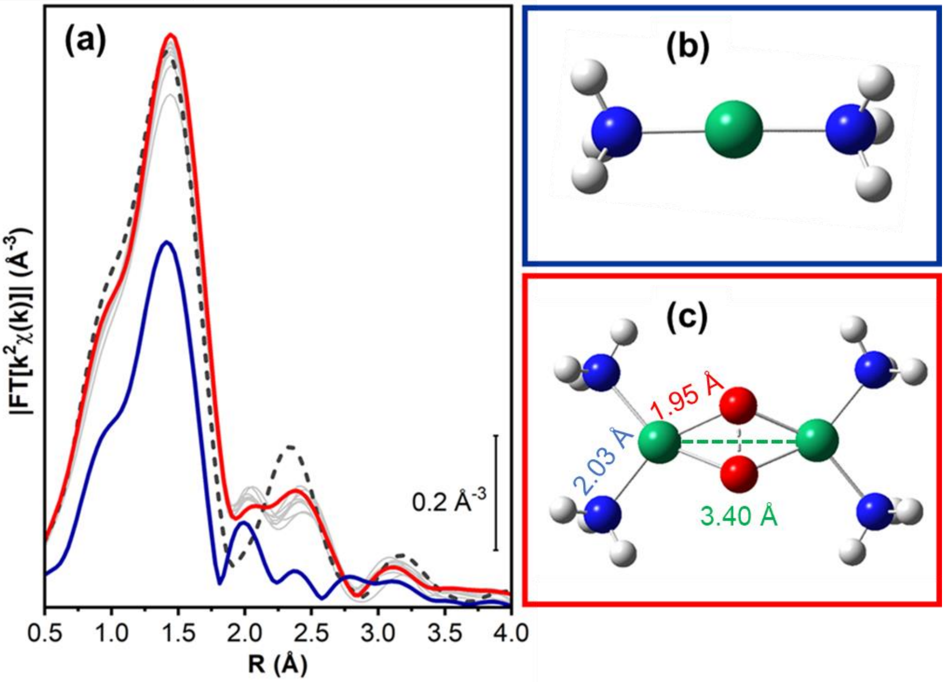

**Figure 6.4:** (a) Phase-uncorrected $k^2$-weighted FT-EXAFS curves during exposure of the Cu-CHA catalyst to NO/$NH_3$/He (dark blue thick line), followed by 10% $O_2$ in He (grey thin lines; red thick dashed: pretreatment in $O_2$. (b) Illustration of $[Cu(I)(NH_3)_2]^+$ and (c) $\mu$-$\eta^2$,$\eta^2$-peroxo diamino dicopper (II) (side-on) complexes. Atom colour code: Cu, green; H, white; O, red; N, blue. Part (c) also report selected DFT bond distances in Å.

To determine the precise structure of the $[Cu_2(NH_3)_4O_2]^{2+}$ complexes, first the structures for the three complexes shown in **Figure 6.1** have been optimized by DFT (based on the HSE06-HF hybrid functional [13]), including $NH_3$-solvated side-on and end-on peroxides as well as the bis-(μ-oxo)-dicopper core proposed earlier [9]. Then, these structures were used as input to fit the observed EXAFS features.

### 6.1.2 *EXAFS fitting methods and results*

The EXAFS fits, reported in **Table 6.1**, have been performed taking into account the experimental $k^2$-weighted EXAFS spectrum of the sample re-oxidized at 200 °C in $O_2$, after reduction of the $O_2$-activated sample in the $NH_3$ + NO mixture (red curve in **Figure 6.4**). The DFT-optimized structures shown in **Figure 6.1** for three candidate $[Cu_2(NH_3)_4(O_2)]^{2+}$ species have been used as initial guesses for the fitting procedure. The fit was performed on the experimental FT curve obtained by transforming the $k^2 \chi(k)$ curves in the $\Delta k$ 2.4 – 13.0 Å$^{-1}$ range.

For the peroxo side-on and bis-μ-oxo geometries, a common $\Delta R$ = (1 – 4) Å range of fit was chosen while for the peroxo end-on complex, a larger range $\Delta R$ = (1 – 4.4) Å was selected, in accordance with the higher DFT Cu–Cu distance for this structure. This choice implied that the number of independent points ($N_{ind}$) is equal to 20 for the peroxo side-on and bis-μ-oxo geometries, while for the peroxo end-on complex it is equal to 23.

Phases and backscattering amplitudes have been calculated by means of FEFF6.0l, using the Arthemis software from the Demeter package [14]. The selected fitting models included all the single (SS) and multiple (MS) scattering paths contributing in the defined $\mathrm{R}$-ranges of fitting. An exception is represented by the SS and MS contributions coming from the H scatterers, whose scattering amplitude in the analysed models was found to be negligible in the fitting procedure. In order to limit the number of optimized variables, all the SS and MS paths have been parametrized using the same passive amplitude reduction factor ($S_0^2$) and the same energy shift parameter ($\Delta E$). The coordination numbers were fixed according to the related DFT-models.

In the employed complexes, all the SS paths were identified, and the related distances from the absorber were parametrized using a common guess value of radial shifts $\Delta R_x$ (with x=$O^1$, $O^2$, N and Cu) guessed starting from an initial value of 0 Å (i.e. no structural variation from the initial DFT distances). At the same time, the related Debye-Waller (DW) parameters were guessed on the basis of precedent fitting results, as reported in **chapter 5**.

The identified SS path can be then grouped as follow:

- SS involving first-shell bridging oxygen(s): Cu-$O^1$, with coordination number equal to 2 for the peroxo side-on and bis-μ-oxo geometries and equal to 1 for the peroxo end-on complex.
- SS involving first-shell nitrogen atoms of the two $NH_3$ molecules coordinated to the Cu absorber: Cu-N. In this case the DW factor, associated to the Cu-N paths, has been set to a value of 0.0041 Å$^2$ obtained by fitting with the $[Cu(I)NH_3)_2]^+$ model structure the Cu K-edge EXAFS spectrum acquired at 200 °C under NO + $NH_3$ gas flow (dashed dark blue line in **Figure 6.4**).
- SS involving second-shell bridging oxygen of the peroxo end-on configuration: Cu-$O^2$.
- SS involving the second Cu atom of the di-copper species.

Finally, all the MS paths have been parametrized, using the radial shifts $\Delta R$ proper of the SS paths on the basis of geometrical considerations. The DW parameters associated to each MS path were evaluated as the square root of the sum of squares of the DW terms of each paths involved in the process.

In the analysed models, as it is possible to see from **Table 6.1**, the number of identified fitting parameters is equal to 7 for the peroxo side-on and bis-μ-oxo geometries, while for the peroxo end-on configuration this number is increased up to 8, because of the second bridging oxygen $O^2$, closer to the second Cu atom. However, in both of cases, the number of retrieved fitting parameters remains always significantly lower than the number of employed independent points (i.e. ~ $\frac{2\Delta k\Delta R}{\pi}+1$) of 20 and 23.

The fit quality was evaluated considering the R-factor ($R_{factor}$) values and following this criterion of acceptance described in **chapter 1**.

### 6.1.2.1 *Results from single-component EXAFS fits based on DFT-optimized candidate geometries*

**Table 6.1** reports the fitting results using, as initial models, the DFT-optimized geometries of various $[Cu_2(NH_3)_4(O_2)]^{2+}$ moieties: peroxo side-on, peroxo end-on and bis-μ-oxo geometries. How it is possible to observe, these last two complexes lead to unreliable results in terms of distances from the Cu absorber, showed in red in **Table 6.1**. In particular, the EXAFS fit starting from the bis-μ-oxo resulted in a large elongation of the Cu-Cu (~ +0.28 Å) and Cu-O$^1$ (~ +0.14 Å) distances, if compared to the respective DFT models. In the same way, high variation of the Cu-Cu (~ +0.1 Å) and Cu-O$^2$ (~ +0.23 Å) DFT-optimized distances are found for the peroxo end-on configuration. For the fit starting from the peroxo end-on geometry, also certain DWs assumed unphysical values (highlighted in orange in **Table 6.1**), excessively small for the Cu-O$^1$ path (3× $10^{-4}$ Å$^2$) and too large for the Cu-Cu (0.02 Å$^2$) contribution.

| **EXAFS Fit** | **Peroxo side-on** | **Peroxo end-on** | **Bis-μ-oxo** |
|---|---|---|---|
| **Parameters** | 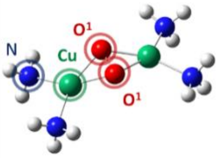 | 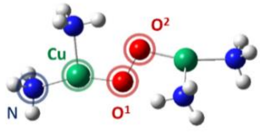 | 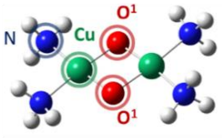 |
| ΔR (Å) | 1-4 | 1-4.4 | 1-4 |
| $N°_{par}/N°_{ind}$ | 7/20 | 7/23 | 7/20 |
| $R_{factor}$ | 0.021 | 0.004 | 0.011 |
| $S_0^2$ | 0.82 ± 0.05 | 1.05±0.06 | 0.80 ± 0.03 |
| ΔE (eV) | 1 ± 1 | 2±1 | 1.7 ± 0.8 |
| $\langle R_{O1} \rangle$ (Å) | 1.911 ± 0.009 (1.95) | 1.903 ± 0.008 (1.86) | 1.912 ± 0.006 (1.77) |
| $R_{O2}$ (Å) | - | 2.86 ± 0.04 (2.63) | - |
| $\langle R_N \rangle$ (Å) | 2.06 ± 0.02 (2.03) | 2.04 ± 0.01 (2.02) | 2.06 ± 0.01 (1.93) |
| $R_{Cu}$ (Å) | 3.40 ± 0.05 (3.44) | 4.4 ± 0.2 (4.3) | 2.93 ± 0.02 (2.65) |
| $\sigma_{O1}$ (Å$^2$) | 0.0020 ± 0.0008 | 0.0003 ± 0.0009 | 0.0022 ± 0.0006 |
| $\sigma_{O2}$ (Å$^2$) | - | 0.008 ± 0.005 | - |
| $\sigma_N$ (Å$^2$) | 0.0041 | 0.0041 | 0.0041 |
| $\sigma_{Cu}$ (Å$^2$) | 0.014 ± 0.007 | 0.02 ± 0.03 | 0.012 ± 0.002 |

**Table 6.1:** Results of the fits executed on the $k^2$-weighted FT-EXAFS spectrum of Cu-CHA re-oxidized at 200 °C in $O_2$, after reduction of the $O_2$-activated sample in the $NH_3$ + NO mixture (red curve in **Figure 6.3**). The models used as initial guesses for the fitting procedure are also shown, including two Cu-peroxo dimers with side-on (peroxo side-on) and end-on (peroxo end-on) configuration and by a Cu-bis-μ-oxo dimer (bis-μ-oxo). The averaged distances of the oxygens and nitrogen shells of atoms surrounding the Cu absorber are reported in brackets, "< >". Distances retrieved from the fitting procedure having a variation larger than 0.1 Å from the ones reported by the DFT optimized structures are reported in red. Unphysical values of DWs refined from the fit are indicated in orange. Colour code in the structures: white: hydrogen; blue: nitrogen; red: oxygen, green: copper.

As it is possible to see from the first column of **Table 6.1**, among all the analysed models, the only reasonable fit, in terms of physical reliability of the optimised structural parameters, is obtained using the peroxo side-on geometry, see **Figure 6.5**. In particular, the Cu-Cu distance is refined by the EXAFS fit to 3.40 ± 0.05 Å, which is comparable within the fit error with the one provided by the DFT optimised model of 3.44 Å. However, in the 2.2 – 2.8 Å range, the experimental curve profile is not perfectly reproduced by the best fit curve (a possible explanation is provided below in **section 6.1.2.2**).

Nonetheless, the $R_{factor}$ associated to the fitting procedure is still representative of a good agreement with the experimental spectrum. It is interesting to note the higher complexity associated to the third-shell feature, sited around 3.1 Å (phase-uncorrected value). Herein, the fit shows that this feature cannot be attributed solely to the presence of the Cu-Cu path, but it is also shaped by relatively intense MS contributions. This result confirms the representation showed by the WT in **chapter 3** and in the following section (**6.1.3**). In fact, the second lobe projection of the wavelet in the $R$-space falls in the region of the FT-third shell. Here the WT shows two contributions: the first one, localised at low $k$-values $\Delta k \sim (2-4)$ Å$^{-1}$, typical of light scatterers (i.e. O and N) and the second one sited around $k$ ~7 Å$^{-1}$, where the Cu backscattering amplitude $F(k)$ has its maximum value.

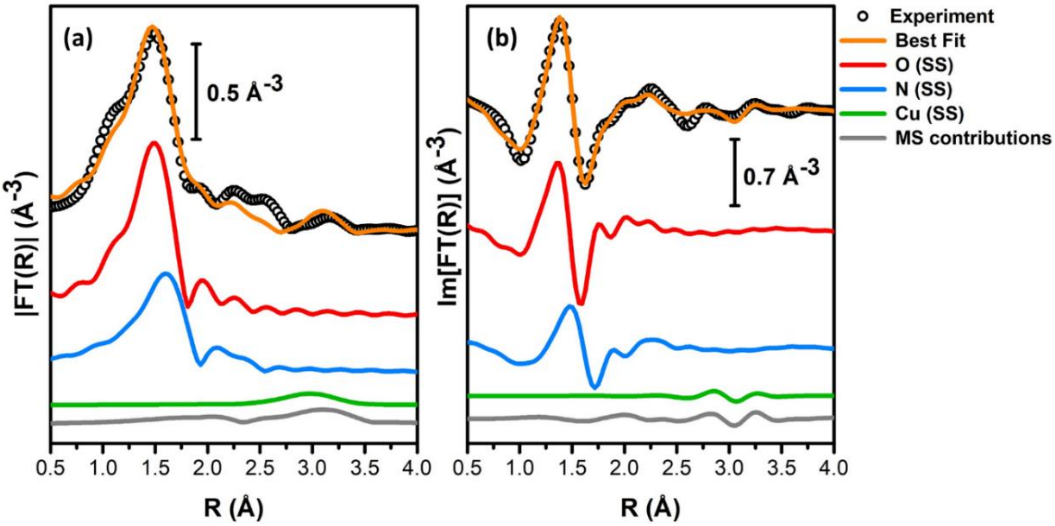

**Figure 6.5:** Phase uncorrected, modulus (a) and imaginary part (b) of the experimental and best fit FT EXAFS spectra. The experimental data are shown as black open circles and the best fits with orange solid lines. The SS and MS contributions are reported as solid lines vertically translated for sake of clarity.

#### 6.1.2.2 *Multi-component fit considering the peroxo side-on dimer and the $[Cu(I)NH_3)_2]^+$ complex*

Analysing the XANES spectrum of Cu-CHA re-oxidized at 200 °C in $O_2$ (red curve in **Figure 6.3**), it is possible to observe the presence of a peak sited at ca. 8982 eV. This feature arises from the $1s \rightarrow 4p$ transition in Cu(I) centres and can be explained supposing that not all the $[Cu(I)NH_3)_2]^+$ complexes formed upon exposure to the NO+$NH_3$ mixture have been oxidized, in presence of $O_2$, to peroxo side-on dimers. In order to quantify the amount of $[Cu(I)NH_3)_2]^+$ complexes still present in the sample after the oxygen treatment, a multi-component EXAFS fit has been performed, considering both the Cu(II) peroxo side-on dimer and the $[Cu(I)NH_3)_2]^+$ complex. In the fit, the amplitude reduction factor $S_0^2$ was set to the value of 0.9 by fitting the EXAFS reference of Cu(II)O, moreover, the Cu(I)-N distances (i.e. $<R_{N(CuI)}>$) were defined to a common value found fitting the spectrum of Cu-CHA reduced in the $NH_3$ + NO mixture at 200 °C using the $[Cu(I)NH_3)_2]^+$ model (how showed for the $\sigma_N$ in the precedent section). In order to estimate the total amount of $[Cu(I)NH_3)_2]^+$, a new parameter $x$, expressing the fraction of Cu(II)-dimers in the zeolites cages, was introduced in the fit. In case of the peroxo side-on dimer, the common $S_0^2$ term was then multiplied for the parameter $x$ expressing the fraction of the dimeric component, while for $[Cu(I)NH_3)_2]^+$, a $(1 - x)$ factor was used. The result of the fit are reported in **Table 6.2** while **Figure 6.6** compares experimental and best-fit curve, as well as scaled contributions by the two structural components.

| Parameters | Peroxo (Side-On) & $[Cu(I)NH_3)_2]^+$ Complexes |
|---|---|
| $\Delta R$ (Å) | 1-4 |
| $N°_{par}/N°_{ind}$ | 7/20 |
| $R_{factor}$ | 0.020 |
| $S_0^2$ | $\underline{0.9}$ |
| $\Delta E$ (eV) | 0 ± 1 |
| $<R_O>$(Å) | 1.916 ± 0.009 (1.95) |
| $<R_N>$(Å) | 2.065 ± 0.009 (2.03) |
| $<R_{N(CuI)}>$(Å) | $\underline{1.913}$ |
| $R_{Cu}$ (Å) | 3.39 ± 0.05 (3.44) |
| $\sigma_O$ (Å$^2$) | 0.0020 ± 0.0009 |
| $\sigma_N$ (Å$^2$) | $\underline{0.0041}$ |
| $\sigma_{Cu}$ (Å$^2$) | 0.013 ± 0.007 |
| $x$ | 0.84 ± 0.08 |

**Table 6.2:** Best fit parameters obtained by two-component EXAFS fitting, including in the fitting model the structures of (1) side-on peroxo Cu(II) dimer and (2) Cu(I) di-ammino complex.

From the fit output, it is possible to observe that the variation of the Cu-Cu distance, together with the new $R_{factor}$ value, remain approximately the same as obtained by the single component fit in **Table 6.1**. The fit refines the fraction of $[Cu(I)NH_3)_2]^+$ to the (16 ± 8) % of total Cu. This value is in good agreement with the intensity of the corresponding Cu(I) features observed in the corresponding XANES spectrum.

Nonetheless, a slight mismatch between the best-fit curve and the experimental one persists in the 2.2–2.8 Å R-space range. It is possible to tentatively connect this local lack in the fit quality to scattering contributions arising from zeolite framework atoms (Si, Al or even O), unaccounted in this model and likely present once the rather bulky peroxo side-on complex is hosted inside the CHA cages.

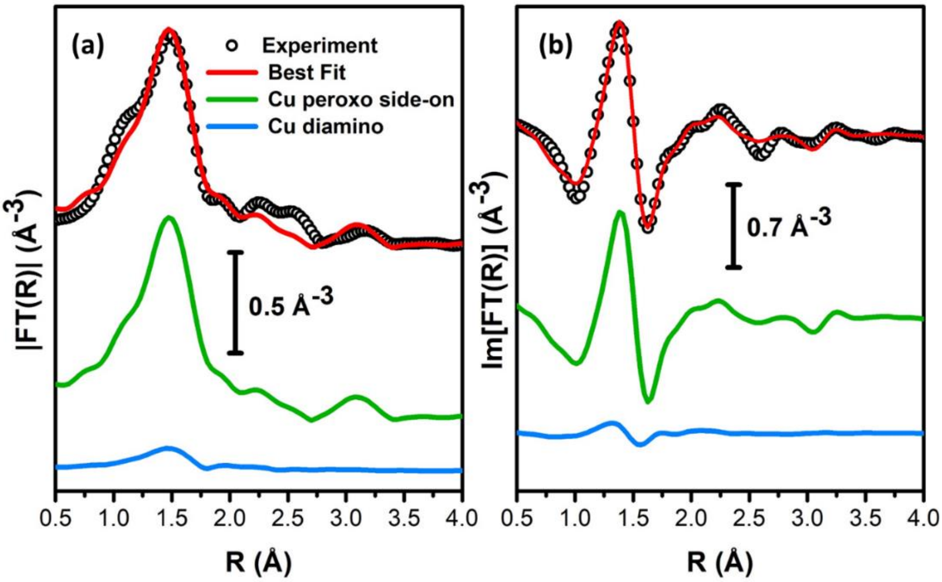

**Figure 6.6:** $k^2$-weighted $\chi(k)$ phase uncorrected, modulus (a) and imaginary part (b) of the experimental and best multicomponent fit FT EXAFS spectra. The experimental data are shown as black open circles and the best fits with red solid lines. The contributions coming from the peroxo side-on Cu dimeric and $[Cu(I)NH_3)_2]^+$ complexes weighted for their respective fractions (see **Table 6.2**) are reported as solid lines, vertically translated for sake of clarity.

### 6.1.3 *Validating the structural dynamics of Cu-species by EXAFS Wavelet Transform analysis*

The DFT-guided EXAFS fitting results allowed to define a consistent experimentally-based model for the $[Cu_2(NH_3)_4(O_2)]^{2+}$ complexes previously proposed [4, 9]. A conclusive assignment of the features observed in conventional FT-EXAFS spectra, however, is hindered by the simultaneous presence of various types of atomic neighbours surrounding the Cu absorber, especially in the high-$R$ region. For the Cu-CHA zeolite showed here, these potentially include single scattering paths from framework Al/Si/O in zeolite-coordinated Cu moieties as well as Cu in multi-copper species, which can be coordinated to the zeolite or mobile. The intense multiple scattering paths involving first-shell O/N neighbours in the proposed $\mu$-$\eta^2$,$\eta^2$-peroxo diamino dicopper (II) moiety mentioned above are also expected to fall in this $R$-space range.

To resolve this this problem, the WTA was applied. A detailed description of this approach can be found in **chapter 3** of this thesis as well as in **chapter 5**.

**Figure 6.7**(b-f) reports the moduli of EXAFS WTs for the key reaction steps explored in this work, carried out isothermally at 200 °C. Herein the a Morlet mother wavelet was employed with the following resolution parameters: $s = 1$ and $\eta = 7$. The latter term was chosen in order to enhnce the Cu-Cu contributions supposing to influence the EXAFS signal at ca. 3.5 Å, see **Table 6.2**. The EXAFS WTs are magnified in the 2–4 Å R-space range, where the signal interpretation with conventional FT-EXAFS approach is mostly complicated by overlapping contributions.

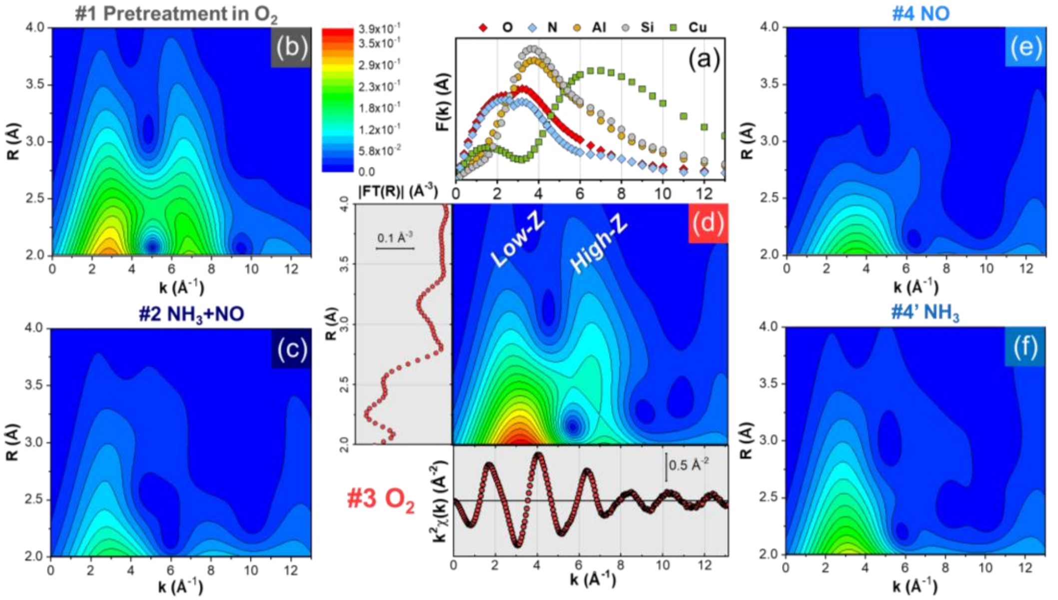

**Figure 6.7:** (a) Backscattering amplitude factors associated to the elements present in the system under study. Moduli of EXAFS WTs magnified in the 2–4 Å R-space range for the following reaction steps: (b) #1 pre-treatment in $O_2$, (c) #2 reduction in NO/$NH_3$/He, (d) #3 oxidation in 10% $O_{2/He}$, (e) #4 exposure to NO/He or (f) #4' to $NH_3$/He. For all the WT representations a common intensity scale is employed. Part (d) also shows the corresponding EXAFS spectra in $k$-space and $R$-space (conventional FT) in the relevant ranges, as well as the $k$-space range characteristic of low-Z (O/N, Si/Al) and high-Z scatterers (Cu). All spectra were measured at 200 °C.

In the relevant $R$-space range, EXAFS WT for the spectrum collected in $O_2$ at 200 °C after pre-treatment in $O_2$ at 400 °C (**Figure 6.7**(b)), clearly splits in two lobes. The first sub-lobe, localised in the $k$ range 1–5 Å$^{-1}$ and $R$ range 2–2.8 Å is associated to the framework atoms: O, Si and Al. The second-one, localised at higher $k$ values (i.e. 6–8 Å$^{-1}$), is principally related to Cu–Cu contributions in oxygen-bridged Cu dimers or, more in general, multi-copper moieties. The presence of Cu-oxo dimeric/polymeric cores in oxygen activated Cu-CHA catalysts represents a novelty with respect to previous literature in the context of the $NH_3$-SCR reaction [2]. The EXAFS backscattering amplitude factors in **Figure 6.7**(a) show that the $F(k)$ functions of lighter elements, such as O/N and Si/Al, have maxima at around 3–4 Å$^{-1}$, while for Cu, the position of the main peak significantly shifts to a $k$-value of around 7 Å$^{-1}$. These differences lead to the observed lobe splitting, enabling an unambiguous, visual discrimination of contributions stemming from Cu or framework atomic contributions. Due to the substantial overlap of the related backscattering amplitude functions, it is not possible to discriminate by means of WT among O/N and Si/Al contributions.

A WT analysis of the EXAFS spectrum for the mobile $[Cu(I)(NH_3)_2]^+$ complexes (**Figure 6.7**(c)), which is obtained after exposure of the catalyst pretreated in $O_2$ to the NO/$NH_3$ gas mixture at 200 °C, shows a complete reduction and mobilization of the Cu ions in the system [2, 5, 7-9]. The second-shell peak in the conventional FT-EXAFS disappears (see, **Figure 6.4**(a)) and all the high-$R$ features are substantially decreased in the corresponding WT map in **Figure 6.7**(c). Even though the sub-lobe at $\mathrm{k} = 7$ Å$^{-1-}$ associated to the Cu–Cu signal is completely lost at this step, a low-intensity feature is still visible in the $\mathrm{k}$-space range 1–5 Å$^{-1}$, which is most likely due to multiple scattering paths involving the first-shell N ligands in the linear $[Cu(I)(NH_3)_2]^+$ moieties.

The crucial step for the activation of oxygen is the isothermal re-oxidation of the $[Cu(I)(NH_3)_2]^+$ complexes, and the corresponding WT analysis is shown in **Figure 6.7**(d). The most important observation here is the appearance of a sub-lobe at around $\mathrm{k} = 7$ Å$^{-1}$ indicating a contribution of Cu–Cu scattering. The presence of this feature unambiguously demonstrates the formation of a Cu complex containing more than one Cu atom. This agrees well with the formation of $[Cu_2(NH_3)_4O_2]^{2+}$ complexes, and is in line with the EXAFS results, see **Table 6.2**. The second sub-lobe occurs in the same $\mathrm{k}$-space range observed in the EXAFS WT after pretreatment in $O_2$ at 400 °C. However, it is possible to note a different morphology of the WT along the $\mathrm{R}$ direction in the two probed states, indicating that there is a difference in Cu-Cu coordination after pre-treatment in $O_2$ or oxidation of $[Cu(I)(NH_3)_2]^+$ at 200 °C. After oxidation of $[Cu(I)(NH_3)_2]^+$ (step #3, **Figure 6.7**(d)), the WT intensity is rather localized in $\mathrm{R}$-space. It peaks at ca. 2.8 Å in the phase-uncorrected $\mathrm{R}$-axis, pointing to a uniform Cu–Cu interatomic distance around 3.5 Å. This indicates, that the reaction of $[Cu(I)(NH_3)_2]^+$ with $O_2$ results in a well-defined structure, compatible with the side-on $\mu$-$\eta^2$,$\eta^2$-peroxo diamino dicopper (II) complex shown in **Figure 6.1**(b) and **Figure 6.4**(c). In contrast, after heating in $O_2$ at 400 °C and subsequent cooling to 200 °C in $O_2$ (step #1, **Figure 6.7**(b)), a broader intensity distribution in $\mathrm{R}$-space is observed in the $\mathrm{k}$-space region characteristic of Cu-Cu scattering, indicating the presence of more heterogeneous multi-copper species in the pretreated Cu-CHA catalyst.

**Figure 6.7** also reports the EXAFS-WTs related to the reactivity of the formed $\mu$-$\eta^2$,$\eta^2$-peroxo diamino dicopper (II) complexes with the key SCR reactants, NO (step #4, **Figure 6.7**(e)) and $NH_3$ (step #4′, **Figure 6.7**(f)). In both cases, the sub-lobe at $\mathrm{k} = 7$ Å$^{-1}$ is clearly lost, providing direct structural evidence for the cleavage of di-copper cores upon separate exposure to NO or $NH_3$ at 200 °C. A moderately intense sub-lobe is instead still visible in the low-$\mathrm{k}$ range, characteristic of low-Z scatterers. As argued before, this feature most likely stems from multiple scattering contributions involving N and O atoms.

Finally, to comparatively assess the presence of Cu–Cu scattering contributions throughout the investigated reaction steps, the power density function $\Phi^R$ of the WT representation was computed. This quantity was obtained integrating the square of the modulus of the WT over the $\mathrm{R}$-range 2–4 Å, that should contain the Cu–Cu signal contribution.

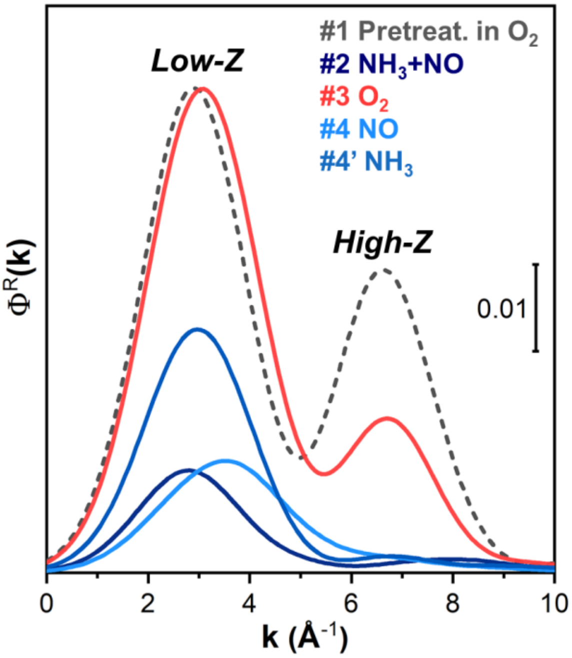

**Figure 6.8:** Density power function $\Phi^R$ calculated for the WT representations showed in **Figure 6.7**(b-f). $k$-space ranges diagnostic for light-Z scatterers (O/N, Si/Al) and high-Z scatterers (Cu), based on backscattering amplitude factors $F(k)$ reported in **Figure 6.7**(a), are indicated.

**Figure 6.8** presents the results of these calculations, summarizing the above observations about EXAFS-WT representations. A common first peak, for all the steps, is localized in the 0.0-5.5 Å$^{-1}$ range: it corresponds to the WT low-k sub-lobe, collectively accounting for the contributions from O, N, Si and Al atoms. The second main peak is present only in catalyst pre-treated in $O_2$ (curve #1) and after $[Cu(I)(NH_3)_2]^+$ reaction with $O_2$ (curve #3). The position of this peak exactly corresponds to the maximum of the Cu backscattering amplitude function shown in (a), clearly indicating the formation of $[Cu_2(NH_3)_4(O_2)]^{2+}$ complexes.

## 6.2 REACTIVITY OF $[Cu_2(NH_3)_4(O_2)]^{2+}$ SPECIES TOWARDS $NH_3$ AND NO

To determine the reactivity of μ-η$^2$,η$^2$-peroxo diamino dicopper (II) complexes towards NO and $NH_3$, which are the main reactants in $NH_3$-SCR, the sample after the re-oxidation process has been exposed to NO and $NH_3$ separately, and in a 1:1 mixture, whose description is reported in the following sections.

### 6.2.1 *Reactivity towards $NH_3$*

As shown by EXAFS-WT analysis above (**Figure 6.7**(f)), the exposure of the μ-η$^2$,η$^2$-peroxo diamino dicopper (II) complexes to $NH_3$ results in the separation of the copper centers. No significant $N_2$ evolution was observed during this transformation through the mass spectrometry measurements. **Figure 6.9** reports the XAS spectra for the μ-η$^2$,η$^2$-peroxo diamino dicopper (II) complexes during exposure to $NH_3$ at 200°C. The characteristic Cu(I) transition at ~8982.5 eV for the linear $[Cu(I)(NH_3)_2]^+$ appears, but does not reach the intensity observed in the fully-reduced catalyst (dashed dark-blue curve in **Figure 6.9**(a)). The intensity of the 1s→3d pre-edge peak (**Figure 6.9**(c)) decreases, corroborating that some reduction of the Cu takes place. In conclusion, exposure of the $\mu$-$\eta^2$,$\eta^2$-peroxo diamino dicopper (II) complexes to $NH_3$ leads to a change in the ligands of the Cu and to a partial reduction to a Cu(I) species.

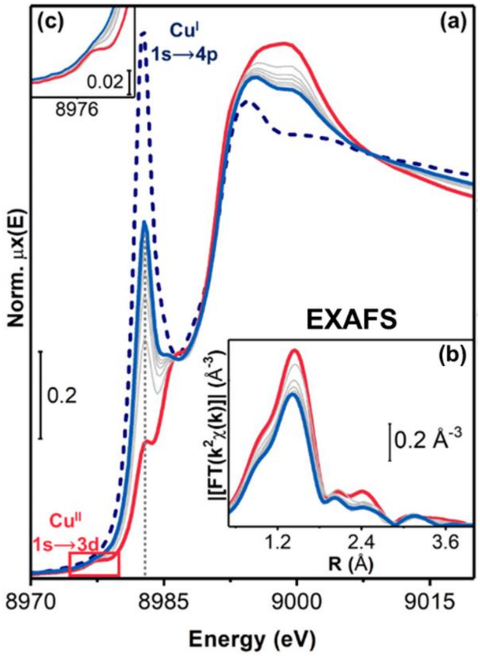

**Figure 6.9:** Exposure to $NH_3$/He at 200 °C of Cu-CHA catalyst after step #3. (a) Cu K-edge XANES spectra; (b) Phase uncorrected $k^2$ -weighted FT-EXAFS curves; (c) Magnification of the Cu(II) $1s \rightarrow 3d$ transition. Red thick line: spectrum collected in step #3 (same as **Figure 6.3** and **Figure 6.4**); blue thick line: after $NH_3$/He exposure; grey thin lines: intermediates; dashed dark blue: step #2 (NO/$NH_3$ at 200 °C after pre-treatment in $O_2$, same as dark blue in Figures 2 and 3.

Globally, the XANES and EXAFS give average information on all copper species formed in this reaction step. A decrease in the average number of ligands surrounding Cu ions is indicated by the reduced intensity of the EXAFS first shell peak (**Figure 6.9**(b)). The intensity, shape and energy position of the XANES features suggest the presence of a mixture of $[Cu(I)(NH_3)_2]^+$ and $[Cu(II)(NH_3)_3(X)]^+$ complexes, with a geometry similar to the $[Cu(II)(NH_3)_3(OH)]^{2+}$ species, as reported earlier [15]. A XANES linear combination fit, reported in **Figure 6.10**(a,b), indicates that the fractions of $[Cu(I)(NH_3)_2]^+$ and $[Cu(II)(NH_3)_3(X)]^+$ at equilibrium are 65% and 35%, respectively. Herein, the XANES spectrum referring to the $[Cu(II)(NH_3)_4]^{2+}$complex was used as reference, which is supposed to possess a coordination and a local environment (in terms of chemical elements) similar to $[Cu(II)(NH_3)_3(X)]^+$. Considering the presence of ca. 16% Cu(I) and 84% Cu(II) before exposure to $NH_3$ (see the result from the estimation provided in **Table 6.2** for the multi-component EXAFS fit), it is possible to assert that approximatively the 58% of the amount of the copper ions in the the $\mu$-$\eta^2$,$\eta^2$-peroxo diamino dicopper (II) complexes are reduced to Cu(I). The lack of fit in correspondence of the XANES white line (W.L.) peaks are explained remembering that the $[Cu(II)(NH_3)_4]^{2+}$ do not match completely with the $[Cu(II)(NH_3)_3(X)]^+$

species formed, however together with the $[Cu(I)(NH_3)_2]^+$ , it is able to explain properly the intense 1s→4p transition of the XANES pre-edge. This evidence implies that the two references describe properly the Cu oxidation state despite a higher uncertainty connected to the speciation.

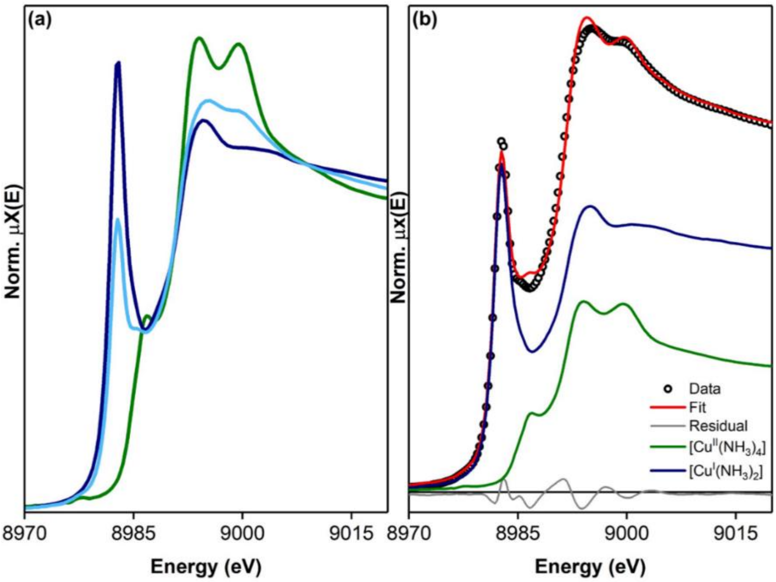

**Figure 6.10:** (a) Cu K-edge XANES spectra of $[Cu(II)(NH_3)_4]$ (green curve), of $[Cu(I)(NH_3)_2]$ (dark blue curve) and after 80 min of 1000 ppm $NH_3$/He exposure at 200 °C (light blue curve); (b) Result for the Linear Combination Fit.

The results described above indicate that $NH_3$ is reacting with the $\mu$-$\eta^2$,$\eta^2$-peroxo diamino dicopper (II) complexes, breaking the copper dimer and reducing a consistent fraction of the Cu(II) ions to Cu(I). The fact that no $N_2$ was observed during this reaction is in agreement with the experimental evidence that direct oxidation of $NH_3$ ammonia only occurs on Cu-CHA at higher temperature [16], see equation (6.1).

$$NH_3+3O_2 \rightarrow 2N_2+6H_2O \qquad (6.1)$$

The XANES spectra showed in **Figure 6.9** (a) are consistent with the presence of Cu(II) ions in a pseudo-square planar geometry, similar to the $[Cu(II)(NH_3)_3(OH)]^+$ species predicted by Paolucci et al [9]. Thus it is possible to hypothesize that the corresponding Cu(II) ions are in the form of a superoxo amino $[Cu(II)(NH_3)_3(OO^\bullet)]^+$ complex possessing a tetragonal geometry. This structure is consistent with the relatively high intensity of the low-k sub-lobe in EXAFS WT data (**Figure 6.7**(f) and curve #4′ in **Figure 6.8**), related to multiple scattering contributions from N/O ligand atoms.

The superoxo $[Cu(II)(NH_3)_3(OO^\bullet)]^+$ complex could be formed by a one-electron transfer from the bridged peroxo group in the $\mu$-$\eta^2$,$\eta^2$-peroxo diamino dicopper (II) complexes to one of the Cu(II) ions, with consequent formation of Cu(I) ions and of the superoxo ligand. The resulting Cu(I) ions are thus stabilized as $[Cu(I)(NH_3)_2]^+$. This could be rationalized with equation (6.2), which should result in the reduction of 50% of the Cu(II) ions in the dimer to Cu(I).

$$[Cu_2(NH_3)_4O_2]^{2+} + NH_3 \rightarrow [Cu^{I}(NH_3)_2]^{+} + [Cu^{II}(NH_3)_3(OO^{\bullet})]^{+} \qquad (6.2)$$

The XANES linear combination fit indicates a higher efficiency of the Cu(II) to Cu(I) reduction with $NH_3$ (ca 58% of Cu(II) reduced) slightly higher from what is predicted from equation (6.2). This could be related to a further reduction of the superoxo $[Cu(II)(NH_3)_3(OO^{\bullet})]^{+}$ complexes by the available $NH_3$ present in the system, with formation of $[Cu(I)(NH_3)_2]^{+}$. Despite the clear indications provided by the linear combination fit, the associated uncertainties are too high to use it as an ultimate proof for the reaction (6.2).

### 6.2.2 *Reactivity towards NO*

The reaction of the $\mu$-$\eta^2$,$\eta^2$-peroxo diamino dicopper (II) complexes with NO results in the separation of the copper centers, as shown by EXAFS-WT analysis (see above, **Figure 6.7**(f)). This is accompanied by some formation of $N_2$, as monitored by online mass spectrometry. This section provides information about the dynamics of the reaction and summarizes the main experimental findings. **Figure 6.11** reports the XAS spectra collected when contacting the $\mu$-$\eta^2$,$\eta^2$-peroxo diamino dicopper (II) complexes formed in step #3 with NO at 200°C.

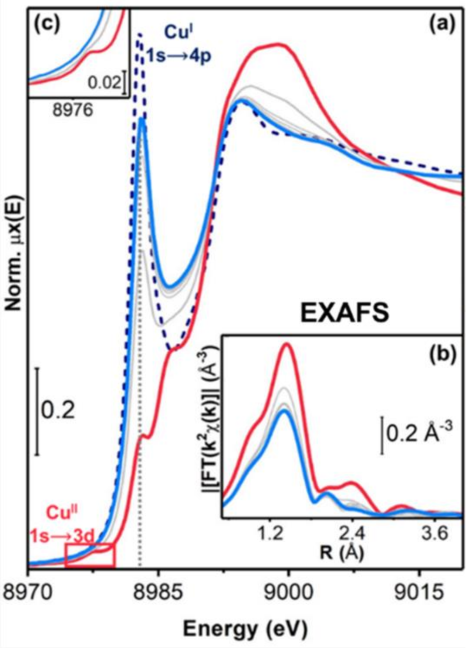

**Figure 6.11:** Exposure to NO/He at 200 °C of Cu-CHA catalyst after step #3. (a) Cu K-edge XANES spectra; (b) Phase uncorrected $k^2$ -weighted FT EXAFS curves; (c) Magnification of Cu(II) $1s \rightarrow 3d$ transition; Red thick line: spectrum collected in step #3 (same as **Figure 6.4**); light blue thick line: after of NO/He exposure; grey thin lines: intermediates; dashed dark blue: step #2 (NO/$NH_3$ at 200 °C after pre-treatment in $O_2$, same as dark blue in **Figure 6.4**).(f) Temporal evolution of the intensity of the Cu(I) $1s \rightarrow 4p$ transition at ~8982.5 eV during exposure to NO or $NH_3$ after step #3. (g) Illustration of Cu species proposed to be formed upon reaction with NO. Atom colour code: Cu, green; H, white; O, red; N, blue; Si, yellow; Al, pink.

The changes in the pre-edge features at the Cu K-edge in XANES reveals a fast and effective Cu(II) to Cu(I) transformation. The characteristic 1s→4p transition at ~8982.5 eV reappears in the spectrum (**Figure 6.11** (a)), and the weak 1s→3d transition at 8977.3 eV, indicative for a Cu(II) species, disappears (**Figure 6.11**(c)). To illustrate the differences in the formation of Cu(I) species in the reactions of the $\mu$-$\eta^2$,$\eta^2$-peroxo diamino dicopper (II) complexes with NO and $NH_3$, the temporal evolution of the 1s→4p transition at ~8982.5 eV in the two cases was compared (see **Figure 6.12**). These data show that the reduction of the $\mu$-$\eta^2$,$\eta^2$-peroxo diamino dicopper (II) complex is faster and more efficient with NO than with $NH_3$, since the Cu(I) peak reaches about 76% of the intensity observed for the fully reduced reference state, i.e. $[Cu(I)(NH_3)_2]^+$ as formed in step #2 (dark blue dashed line in **Figure 6.11**(a)) after only 5 minutes, stabilizing at about 84% after 35 min. In the case of reduction in $NH_3$, the intensity is about 43% after 5 min, and reaches about 62% after 35 min, at the static state. It is possible to note that the intensity of the Cu(I) rising-edge peak can be affected by the geometry of Cu-complexes, as showed in **section 5.1** of the precedent chapter. However, even though these data cannot be used to obtain precise kinetics of the reaction, they clearly show a difference in the reduction behavior in the two cases.

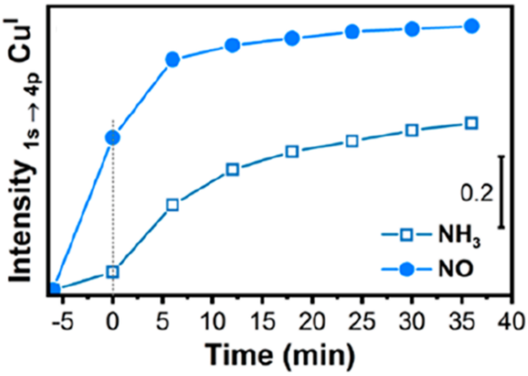

**Figure 6.12:** Temporal evolution of the intensity of the Cu(I) $1s \rightarrow 4p$ transition at ~8982.5 eV during exposure to NO or $NH_3$ after step #3

Looking at **Figure 6.11**, it is possible to observe that the XANES data do not reveal the presence of a Cu(II) species after reaction with NO, suggesting that the observed Cu(II) fraction remains below the XAS detection limit under the experimental conditions, which is estimated at around 10% of the total Cu content. The structure of the Cu(I) ions formed during the reaction of $\mu$-$\eta^2$,$\eta^2$-peroxo diamino dicopper (II) complex with NO is different from those observed after reduction in $NO/NH_3$ at 200 °C or in the reaction with $NH_3$. The shape of the XANES rising-edge and white-line peaks clearly differ from those of the linear $[Cu(I)(NH_3)_2]^+$ complexes, as indicated by the light-blue and dotted dark-blue curves in **Figure 6.11**(a), and those of ligand-free, framework coordinated ZCu(I) showed in **chapter 5**. Overall, the Cu K-edge XANES resembles those observed after the desorption of $NH_3$ in Cu-CHA catalysts of comparable composition as studied here which has been assigned to framework-coordinated linear Cu(I) amino-complexes, $Z[Cu(I)(NH_3)]$. This assignment is supported by the decrease observed in the first-shell peak in EXAFS (**Figure 6.11** (b)), indicating a change from a four-fold to a two-fold coordination of Cu. The broadening of the second and third shell regions can be moreover connected to the relatively high degree of freedom (in terms of bond length and angles) of the proposed Z[Cu(I)($NH_3$)] entities with respect to [Cu(I)$(NH_3)_2$]$^+$ or *bare* ZCu(I) species [7, 8]. Even though the XANES results point to a complete reduction of the Cu(II), a minor fraction of Cu(II) is still present after reaction with NO, which remains below the detection limit of XANES under the experimental conditions. The presence of these Cu(II) moieties in the XAS experiment is indicated by the small amount of $N_2$ that is formed upon adding $NH_3$ to the NO feed after step #4, to restore the fully reduced state consisting of [Cu$(NH_3)_2$]$^+$ complexes. The formation of $N_2$ indicates that some reduction of Cu(II) takes place, thus proving that the reduction with NO alone was not complete. Thus, it is possible to expect that the amount of this residual Cu(II) fraction to depend on the Cu content and Si/Al ratio of the Cu-CHA material.

## 6.3 REFERENCES

[1] A.M. Beale, F. Gao, I. Lezcano-Gonzalez, C.H.F. Peden, J. Szanyi, Recent advances in automotive catalysis for NOx emission control by small-pore microporous materials, Chem. Soc. Rev., 44 (2015) 7371-7405.

[2] E. Borfecchia, P. Beato, S. Svelle, U. Olsbye, C. Lamberti, S. Bordiga, Cu-CHA - a model system for applied selective redox catalysis, Chem. Soc. Rev., 47 (2018) 8097-8133.

[3] F. Gao, J. Kwak, J. Szanyi, C.F. Peden, Current Understanding of Cu-Exchanged Chabazite Molecular Sieves for Use as Commercial Diesel Engine DeNO$_x$ Catalysts, Top. Catal., 56 (2013) 1441-1459.

[4] F. Gao, D. Mei, Y. Wang, J. Szanyi, C.H.F. Peden, Selective Catalytic Reduction over Cu/SSZ-13: Linking Homo- and Heterogeneous Catalysis, J. Am. Chem. Soc., 139 (2017) 4935–4942.

[5] C. Paolucci, A.A. Parekh, I. Khurana, J.R. Di Iorio, H. Li, J.D. Albarracin Caballero, A.J. Shih, T. Anggara, W.N. Delgass, J.T. Miller, F.H. Ribeiro, R. Gounder, W.F. Schneider, Catalysis in a Cage: Condition-Dependent Speciation and Dynamics of Exchanged Cu Cations in SSZ-13 Zeolites, J. Am. Chem. Soc., 138 (2016) 6028-6048.

[6] C. Paolucci, A.A. Verma, S.A. Bates, V.F. Kispersky, J.T. Miller, R. Gounder, W.N. Delgass, F.H. Ribeiro, W.F. Schneider, Isolation of the Copper Redox Steps in the Standard Selective Catalytic Reduction on Cu-SSZ-13, Angew. Chem.-Int. Edit., 53 (2014) 11828-11833.

[7] T.V.W. Janssens, H. Falsig, L.F. Lundegaard, P.N.R. Vennestrøm, S.B. Rasmussen, P.G. Moses, F. Giordanino, E. Borfecchia, K.A. Lomachenko, C. Lamberti, S. Bordiga, A. Godiksen, S. Mossin, P. Beato, A Consistent Reaction Scheme for the Selective Catalytic Reduction of Nitrogen Oxides with Ammonia, ACS Catal., 5 (2015) 2832-2845.

[8] K.A. Lomachenko, E. Borfecchia, S. Bordiga, A.V. Soldatov, P. Beato, C. Lamberti, Active sites in Cu-SSZ-13 deNOx catalyst under reaction conditions: a XAS/XES perspective, J. Phys.: Conf. Ser., 712 (2016) 012041.

[9] C. Paolucci, I. Khurana, A.A. Parekh, S.C. Li, A.J. Shih, H. Li, J.R. Di Iorio, J.D. Albarracin-Caballero, A. Yezerets, J.T. Miller, W.N. Delgass, F.H. Ribeiro, W.F. Schneider, R. Gounder, Dynamic multinuclear sites formed by mobilized copper ions in NOx selective catalytic reduction, Science, 357 (2017) 898.

[10] L. Chen, T.V.W. Janssens, H. Gronbeck, A comparative test of different density functionals for calculations of NH3-SCR over Cu-Chabazite, Phys. Chem. Chem. Phys., 21 (2019) 10923-10930.

[11] C.J. Cramer, A. Kinal, M. Wloch, P. Piecuch, L. Gagliardi, Theoretical characterization of end-on and side-on peroxide coordination in ligated Cu2O2 models, J. Phys. Chem. A, 110 (2006) 11557-11568.

[12] G. Agostini, D. Meira, M. Monte, H. Vitoux, A. Iglesias-Juez, M. Fernandez-Garcia, O. Mathon, F. Meunier, G. Berruyer, F. Perrin, S. Pasternak, T. Mairs, S. Pascarelli, B. Gorges, XAS/DRIFTS/MS spectroscopy for time-resolved operando investigations at high temperature, J. Synchrot. Radiat., 25 (2018) 1745-1752.

[13] C. Negri, T. Selleri, E. Borfecchia, A. Martini, K.A. Lomachenko, T.V.W. Janssens, M. Cutini, S. Bordiga, G. Berlier, Structure and Reactivity of Oxygen-Bridged Diamino Dicopper(II) Complexes in Cu-Ion-Exchanged Chabazite Catalyst for NH3-Mediated Selective Catalytic Reduction, J. Am. Chem. Soc., 142 (2020) 15884-15896.

[14] B. Ravel, M. Newville, ATHENA, ARTEMIS, HEPHAESTUS: data analysis for X-ray absorption spectroscopy using IFEFFIT, J. Synchrot. Radiat., 12 (2005) 537-541.

[15] E. Borfecchia, K.A. Lomachenko, F. Giordanino, H. Falsig, P. Beato, A.V. Soldatov, S. Bordiga, C. Lamberti, Revisiting the nature of Cu sites in the activated Cu-SSZ-13 catalyst for SCR reaction, Chem. Sci., 6 (2015) 548-563.

[16] M. Colombo, G. Koltsakis, I. Nova, E. Tronconi, Modelling the ammonia adsorption-desorption process over an Fe-zeolite catalyst for SCR automotive applications, Catal. Today, 188 (2012) 42-52.

# 7 CONCLUSIONS

In the first part (**chapters 2-4**) of the thesis, a series of techniques, employed to solve the spectral decomposition problem, have been described. All of them are (or will be) implemented inside the PyFItIt and THORONDOR framework. In particular, it has been underlined the superiority of the TM approach over the MCR-ALS algorithm, albeit the latter still represent an extremely useful approach in guiding the interpretation of large XAS datasets characterized by high variance. It has been showed, in fact, that differently from the MCR-ALS algorithm, the TM method, is able to identify, under a proper set of constraints, a set of pure and uncorrelated XAS spectra extremely close to the real solution. The problem connected to the uncertainty associated to the extracted spectral and concentration profiles has been addressed through the introduction of a minimization algorithm executed over the AFS region of the XAS dataset providing the boundaries corresponding to the maxima and minima variation of the spectral and concentration profiles. The pure XANES profiles possessing a chemical/physical meaning can be properly fitted through a series Machine Learning approaches currently implemented in PyFitIt. In particular, in this thesis work, it has been demonstrated how, through the employment of the *indirect methodology* of fit, it is possible to refine a set of user-selected structural parameters influencing more an experimental XANES. In addition, a new method of XANES analysis, based on the combination of a supervised and unsupervised machine learning approach (PCA), was provided. Through this procedure it has been possible to understand which are the combinations of parameters influencing more an experimental XANES spectrum and to derive a linear expression of the structural deformation which can be properly predicted from the indirect (and direct) approach.

The Machine Learning algorithms employed for the XANES fitting routine have been extended to the EXAFS case. Herein, it has been showed that it is possible to retrieve a generalised expression of the EXAFS signal that goes beyond the classical formulation provided by Rehr and Albers in [1], allowing to obtain even a quantitative estimation of the angles characterising the molecular structure under examination. Additional insights on the EXAFS analysis were also derived through the WT analysis that demonstrated to be more suitable to represent the EXAFS spectrum than the classical $k$-space and $R$-space (*via* FT) representations. This new kind of signal visualization appeared to be able, in fact, to single out different contributions from scatter atoms of different Z that, from the classical FT-analysis, could appear of ambiguous identification. For this reason, the fit in the joined $(k,R)$ space, provided by the WT representation, was implemented and tested with success in connection to the identification of the Cu dimeric complexes in Cu-CHA and MOR, supposed to the be the active sites for the conversion of methane to methanol.

Finally, the main interface features of PyFitIt constituted the basis for the design of a second software, named THORONDOR, devoted to the data analysis of the NEXAFS spectra collected under *in situ* conditions. The versatility of this code is principally due to its GUI. The presence of a sophisticated toolbox, developed for the peaks fitting of the NEXAFS pre-edge/edge resonances, and the possibility to treat mathematically the NEXAFS profiles through a series of sliders differentiate it from most of the available XAS codes and it constitutes one of the few codes completely designed to analyse low-energy XAS datasets.

The application of some of the techniques implemented and developed as discussed in the first chapters have been reported in **chapters 5** and **6**. Herein, the results concerning the *in situ* and *operando* spectroscopic characterization of Cu-exchanged zeolites (CHA and MOR frameworks) [2, 3] in different experimental and reaction conditions have been reported.

*In situ* XAS measurements were employed to monitor the He activation process in a multi-composition platform of Cu-CHA zeolites, aiming to clarify the influence of the catalyst composition on the temperature-dependent Cu-speciation and reducibility. After the principal component analysis of the temperature-dependent multi-composition XANES dataset, the MCR-ALS method has been employed to extract chemically-meaningful spectra and concentration profiles of pure components formed during He-activation as a function of the catalyst composition. Based on the spectroscopic fingerprints of each theoretical XANES and the correspondent temperature-dependent concentration profiles, it was possible to reliably assign the theoretical spectra to pure Cu-species/sites. The assignment was subsequently corroborated by simulating the Cu K-edge XANES spectra for the correspondent model geometries. It has been showed that the formation of framework-interacting Cu-species from the mobile Cu(II) aquo-complexes present at RT occurs, irrespectively of catalyst composition, *via* a Cu(II) dehydration intermediate, peaking around 130 °C. Then, ZCu(II)OH and $Z_2$Cu(II) species develop almost simultaneously, with relative abundances strongly influenced by the Si/Al ratio in the parent zeolite. ZCu(II)OH species, dominant for samples with Si/Al in the 15–29 range, peak around 200 °C and then progressively decrease at elevated temperatures, in favour of reduced ZCu(I) species. Conversely, $Z_2$Cu(II) sites, dominant at Si/Al= 5, reach a steady population in the 200–300 °C range and remain stable until 400 °C. In general, the Cu-speciation at 400 °C can be described for all samples as a combination of redox-active Cu-species at 1Al sites, in their oxidised, ZCu(II)OH, and reduced, ZCu(I), form and redox resistant $Z_2$Cu(II) sites. The high reducibility observed in the low-loading sample (Cu/Al =0.1) with Si/Al 14 and the almost simultaneous development of framework-coordinated Cu-species at 1Al and 2Al both contrast with an ideal *2Al site saturation* scenario, often assumed in the current literature. Moreover, the reducibility level of the 1Al sites is shown to depend on the Si/Al (optimal reducibility for Si/Al = 15, lower reducibility at Si/Al = 19 and 29), evidencing that self-reduction proceeds though a cooperative multi-step process possibly involving proximal acid sites, whose availability is ultimately determined by Al density and distribution in the zeolite.

The MCR-ALS XANES results have been also validated with multicomponent fits of the in situ EXAFS spectra collected at 400 °C after He-activation, to independently validate the employed reconstruction method and access detailed structural information on the preferred Cu local coordination environment associated with 1Al and 2Al sites. EXAFS fits substantially confirm the Cu-speciation evaluated from

MCR-ALS analysis of temperature-dependent in situ XANES, but evidence that the self-reduction is accompanied by higher levels of structural disorder in the Cu local environment.

The individual process steps in the direct conversion of methane to methanol over Cu-CHA materials have been investigated in detail and relationships between the productivity and Cu-speciation have been established. It has been demonstrated that high-temperature treatment at 500 °C in oxygen and a prolonged activation in time, positively impact the productivity, as a result of an increased formation of reactive Cu(II) species.

The EXAFS fit executed on the spectrum of a representative Cu-CHA zeolite (05; 15), collected at the end of the activation process in $O_2$, supports tri-coordinated framework-interacting Cu(II) centers, with two $O_{fw}$ and one $O_{efw}$ ligands in the first metal coordination sphere, as the most favourable sites for methane conversion. It has been showed that this coordination motif is the dominant one at 500 °C, whereas at 200 °C four-coordinated Cu(II) species appear to be also present, resulting in a lower productivity. By coupling the XAS spectroscopic insights with the results from activity measurements, it has been possible to exclude the direct involvement of ZCu(II)OH complexes. On this basis, it has been proposed that these species progressively deplete during exposure to high temperature oxidative treatment, and are proposed to be the precursor of the active species. Furthermore, the correlation between elemental composition (Cu:Al and Si:Al ratios) in Cu-CHA and methanol productivity has been explored. The combination of testing and XAS measurements clearly evidence a positive linear correlation between the methanol productivity and the reducibility of the Cu centers. The high redox inertness of the $Z_2$Cu(II) sites in 6r, favoured at low Si:Al and low Cu-loading, results in completely inactive Cu sites for the methane-to-methanol conversion. Instead, intermediate Si:Al ratios (~12−15) and high Cu loading (~0.5) lead to a high population of ZCu(II)OH precursor sites, ultimately resulting in high methanol yields per Cu.

Afterwards, the presence of specific $O_2$-derived Cu(II) species in Cu–CHA, has been deepened by applying the MCR-ALS technique to the analysis of a combined HERFD–XANES dataset including two set of spectra collected during activation in both $O_2$ and He gas flow. With this respect, it has been underlined both the strengths and the weakness of the method, together with possible strategies to improve the quality of the reconstruction. The use of PCA and MCR-ALS, in combination with the superior energy resolution of the HERFD–XANES technique, has allowed to highlight a higher degree of complexity in Cu–speciation during $O_2$-activation with respect to the He-activation, which would have been difficult to appreciate using the conventional approaches in XAS data analysis. The latter revealed the presence of an additional Cu(II) species, different from the previously characterized ZCu(II)OH one. This component, only formed at significant concentrations in the case of $O_2$-activation, it is envisaged to play an important role in the DMTM conversion.

Focusing on Cu-MOR, conventional XAS under operando conditions evidenced specific fingerprints of the active site, revealing that both active and inactive framework interacting Cu(II) species coexist after the $O_2$ activation. Enhancing the spectroscopic contrast by the MCR analysis of HERFD XANES data, it has been possible to capture the XANES signature of each Cu species present in the MOR framework. This approach enabled an accurate quantification of the Cu speciation in the activated materials. The $O_2$ activation and $CH_4$ loading time typical of the DMTM stepwise process were observed to drastically impact the yield. Thus, it has been adopted a consistent protocols for both spectroscopy and testing to quantitatively correlate the Cu speciation to the productivity per Cu. Furthermore, a specific Cu(II)-oxo moiety was linked with the DMTM active sites, characterized by a higher resistance toward the self-reduction process and mostly favoured in MOR (0.18; 7). Herein the abundance of such Cu(II) species have been directly correlated to the yield of $CH_4$ oxidation products per Cu, over several combinations of compositional parameters, demonstrating that the active site for selective methane oxidation over Cu mordenite is a dicopper site.

In order to address the limitations and the potential of the XAS technique applied to the characterization of $O_2$-activated Cu-zeolites, a number of Cu(II)-oxo species hosted in the CHA and MOR frameworks have been then explored by theory. In particular the XAS features, stemming from the DFT-optimized geometries for both monomeric and dimeric Cu(II) moieties in the 8r and 12r of CHA and MOR, respectively, have been simulated and critically compared.

The Cu K-edge XANES simulations indicated that the XANES is mostly sensitive to the first-shell coordination geometry, providing sufficient spectroscopic contrast among four-fold and three-fold coordinated Cu(II) centers. Conversely, it lacks of specific sensitivity to the nuclearity of Cu-species, so that monomers and dimers retaining the same three-fold coordination mode result into very similar XANES spectra. On the other hand, EXAFS is a well-established technique to accurately determine the local structure around dispersed metal centers. However, when the standard EXAFS-FT approach is applied to these specific systems, it also encounters difficulties, mostly due to the co-localization in the second-shell R-space range of scattering contributions from different types of atomic neighbors, including O, Al, Si and Cu atoms. With this respect, the potential of the EXAFS WTA has been explored, computing the theoretical WT 2D-maps for the same monomeric and dimeric species in the CHA and MOR zeolites. For the Z[Cu(II)$O^{\mu}$Cu(II)]Z dimers, specific features unambiguously assigned to Cu–Cu scattering contribution arise in the high-$k$ range of the WT plane, which appear to be absent in the case of ZCu(II)OH monomers. Based on these findings, WTA has been envisaged as a valid complement to conventional EXAFS-FT approach, to unravel the elusive contributions from Cu-oxo dimers, and in general small metal-oxo clusters, stabilized into zeolitic lattices upon high-temperature oxidative treatment.

As a case of study to assess the potential of the WT methodology, the Cu-MOR zeolites has been selected for the DMTM conversion, characterized by XAS both *ex situ*, under model conditions resulting into Cu(I) and Cu(II) states, and *in situ*, along the key DMTM reaction steps over the most productive material, MOR (0.18; 7). Overall, the reported results demonstrate how Cu–Cu scattering contributions can be successfully distinguished from those involving lower-Z atoms (O, Al/Si) through a diagnostic sub-lobe in WT-EXAFS maps, centred at ca.7 Å$^{-1}$ in $k$-space. The WT-EXAFS analysis of Cu-MOR samples with different compositional characteristics provided direct evidences for the presence of Cu(I)···Cu(I) pairs in the vacuum activated, self-reduced state. Thermal treatment in $O_2$ causes the substantial rearrangements in the local coordination environment of the Cu ions. Upon oxidation, the Cu atoms are observed to approach the zeolite framework and to re-organize with shorter Cu–Cu separations, consistently with the formation of multimeric Cu-oxo cores. Aided by WT power density functions, it has been possible to rationalize the intensity trends observed for the Cu–Cu features as a function of the compositional parameters through a possible saturation mechanism of the 2Al sites, driving the docking of Cu ions to zeolite lattice along dehydration. Such dynamical response of Cu coordination motifs to the chemical environment has been then also recognized during the key steps of DMTM. Framework-coordinated multimeric Cu-oxo species have been unambiguously detected in the $O_2$-activated state. Upon $CH_4$ loading and subsequent steam-assisted $CH_3OH$ extraction, EXAFS-WT highlights the breakage of $Cu_xO_y$ multimeric moieties together with the increase of the interatomic distances between Cu ions and zeolite framework.

It has been possible to pass then from a qualitative to quantitative utilisation of WT-EXAFS, proposing an EXAFS fitting procedure based on the wavelet representation. The WT-EXAFS fit of the $O_2$-activated state measured *in situ* for Cu-MOR (0.18;7) revealed a local structure compatible with a $Z[Cu(II)O^{\mu}Cu(II)]Z$ di-copper cores, with a Cu–Cu separation of ca. 3.1 Å. Albeit obtained using a simplified model, the fitting results are encouraging and will pave the way to improved implementations of the method.

In **chapter 6**, the XAS results concerning the activation of oxygen over the mobile linear $[Cu(I)(NH_3)_2]^+$ complexes in a Cu-CHA catalyst for $NH_3$-SCR (Si/Al ratio=15 and 2.6 wt% Cu), have been reported. The reaction of the linear $[Cu(I)(NH_3)_2]^+$ complexes with $O_2$ at 200 °C results in the formation of a side-on $\mu$-$\eta^2$,$\eta^2$ -peroxo diamino dicopper (II) complex ($[Cu_2(NH_3)_4O_2]^{2+}$). Through a multi component EXAFS fit, it has been showed that about 84% of the Cu present is oxidized by $O_2$ while the remaining 16 % stays present as linear $[Cu(NH_3)_2]^+$ species. The structure of the $[Cu_2(NH_3)_4O_2]^{2+}$ complex also indicates that an O-O bond is retained in this reaction. Wavelet transform analysis of the EXAFS data was then employed to verify qualitatively the presence of the Cu-Cu scattering contributions after the reaction with $O_2$, providing unprecedented direct spectroscopic evidence for the formation of Cu-pairs in the $NH_3$-SCR reaction.

The $[Cu_2(NH_3)_4O_2]^{2+}$ complexes showed a different reactivity towards $NH_3$, NO, or a mixture of NO and $NH_3$ at 200 °C. It has been possible to demonstrate that the reaction with a mixture of NO and $NH_3$ leads to a complete reduction of the $[Cu_2(NH_3)_4O_2]^{2+}$ complexes, and the linear $[Cu(NH_3)_2]^+$ complexes are restored, confirming that the $[Cu_2(NH_3)_4O_2]^{2+}$ complex plays a role in the $NH_3$-SCR reaction cycle. In the reaction of the $[Cu_2(NH_3)_4O_2]^{2+}$ complex with $NH_3$, in the absence of NO, ca. 58% of the Cu(II) species is reduced to Cu(I), while no $N_2$ is formed. The $[Cu_2(NH_3)_4O_2]^{2+}$ complexes dissociate and a variety of mononuclear Cu-complexes is formed, consisting of Cu(I) and Cu(II) species with $NH_3$ and oxidic ligands. In the reaction with NO, some $N_2$ is formed and the $[Cu_2(NH_3)_4O_2]^{2+}$ complexes are almost completely reduced. The formation of $N_2$ indicates that the $NH_3$-SCR cycle involves a reaction of the $[Cu_2(NH_3)_4O_2]^{2+}$ complex with NO. The Cu(I) species formed in this reaction could be, probably, a $Z[Cu(I)(NH_3)]$, which is attached to the zeolite framework. A minor part (<10%) of the Cu remains in a Cu(II) state, due to a lack of reactive $NH_3$ in the catalyst. The addition of $NH_3$ at this stage lead to the restoration of the linear $[Cu(I)(NH_3)_2]^+$ complexes, further confirming the role of the reaction of NO with the $[Cu_2(NH_3)_4O_2]^{2+}$ complexes in the $NH_3$-SCR reaction cycle.

## 7.1 REFERENCES

[1] J.J. Rehr, R.C. Albers, Theoretical approaches to x-ray absorption fine structure, Rev. Mod. Phys., 72 (2000) 621-654.
[2] E. Borfecchia, P. Beato, S. Svelle, U. Olsbye, C. Lamberti, S. Bordiga, Cu-CHA - a model system for applied selective redox catalysis, Chem. Soc. Rev., 47 (2018) 8097-8133.
[3] M.A. Newton, A.J. Knorpp, V.L. Sushkevich, D. Palagin, J.A. van Bokhoven, Active sites and mechanisms in the direct conversion of methane to methanol using Cu in zeolitic hosts: a critical examination, Chem. Soc. Rev., 49 (2020) 1449-1486.

# 8 REPORT ON PHD ACTIVITIES

## 8.1 PUBLICATIONS

### 8.1.1 *Papers published in international peer-reviewed journals (ISI Web of Science and/or Scopus).*

The (*) symbol indicates the corresponding author.

[1] L. Braglia, E. Borfecchia, **A. Martini**, A.L. Bugaev, A.V. Soldatov, S. Oien-Odegaard, B.T. Lonstad-Bleken, U. Olsbye, K.P. Lillerud, K.A. Lomachenko, G. Agostini, M. Manzoli, C. Lamberti, *The duality of UiO-67-Pt MOFs: connecting treatment conditions and encapsulated Pt species by operando XAS*, Phys. Chem. Chem. Phys., 19 (2017) 27489-27507.

[2] **A. Martini**, E. Borfecchia, K.A. Lomachenko, I.A. Pankin, C. Negri, G. Berlier, P. Beato, H. Falsig, S. Bordiga, C. Lamberti, *Composition-driven Cu-speciation and reducibility in Cu-CHA zeolite catalysts: a multivariate XAS/FTIR approach to complexity*, Chemical Science, 8 (2017) 6836-6851.

[3] D.K. Pappas, E. Borfecchia, M. Dyballa, I.A. Pankin, K.A. Lomachenko, **A. Martini**, M. Signorile, S. Teketel, B. Arstad, G. Berlier, C. Lamberti, S. Bordiga, U. Olsbye, K.P. Lillerud, S. Svelle, P. Beato, *Methane to Methanol: Structure Activity Relationships for Cu-CHA*, Journal of the American Chemical Society, 139 (2017) 14961-14975.

[4] **A. Martini**, E. Alladio, E. Borfecchia, Determining Cu-Speciation in the Cu-CHA Zeolite Catalyst: *The Potential of Multivariate Curve Resolution Analysis of In Situ XAS Data*, Topics in Catalysis, 61 (2018) 1396-1407.

[5] D.K. Pappas, **A. Martini**, M. Dyballa, K. Kvande, S. Teketel, K.A. Lomachenko, R. Baran, P. Glatzel, B. Arstad, G. Berlier, C. Lamberti, S. Bordiga, U. Olsbye, S. Svelle, P. Beato, E. Borfecchia, *The Nuclearity of the Active Site for Methane to Methanol Conversion in Cu-Mordenite: A Quantitative Assessment*, Journal of the American Chemical Society, 140 (2018) 15270-15278.

[6] M.A. Soldatov, **A. Martini**, A.L. Bugaev, I. Pankin, P.V. Medvedev, A.A. Guda, A.M. Aboraia, Y.S. Podkovyrina, A.P. Budnyk, A.A. Soldatov, C. Lamberti, *The insights from X-ray absorption spectroscopy into the local atomic structure and chemical bonding of Metal-organic frameworks*, Polyhedron, 155 (2018) 232-253.

[7] A.A. Guda, S.A. Guda, K.A. Lomachenko, M.A. Soldatov, I.A. Pankin, A.V. Soldatov, L. Braglia, A.L. Bugaev, **A. Martini**, M. Signorile, E. Groppo, A. Piovano, E. Borfecchia, C. Lamberti, *Quantitative structural determination of active sites from in situ and operando XANES spectra: From standard ab initio simulations to chemometric and machine learning approaches*, Catalysis Today, 336 (2019) 3-21.

[8] K.A. Lomachenko, **A. Martini**, D.K. Pappas, C. Negri, M. Dyballa, G. Berlier, S. Bordiga, C. Lamberti, U. Olsbye, S. Svelle, P. Beato, E. Borfecchia, *The impact of reaction conditions and material composition on the stepwise methane to methanol conversion over Cu-MOR: An operando XAS study*, Catalysis Today, 336 (2019) 99-108.

[9] D.K. Pappas, E. Borfecchia, M. Dyballa, K.A. Lomachenko, **A. Martini**, G. Berlier, B. Arstad, C. Lamberti, S. Bordiga, U. Olsbye, S. Svelle, P. Beato,

*Understanding and Optimizing the Performance of Cu-FER for The Direct CH4 to CH3OH Conversion*, ChemCatChem, 11 (2019) 621-627.
[10] D.K. Pappas, E. Borfecchia, K.A. Lomachenko, A. Lazzarini, E.S. Gutterod, M. Dyballa, **A. Martini**, G. Berlier, S. Bordiga, C. Lamberti, B. Arstad, U. Olsbye, P. Beato, S. Svelle, *Cu-Exchanged Ferrierite Zeolite for the Direct $CH_4$ to $CH_3OH$ Conversion: Insights on Cu Speciation from X-Ray Absorption Spectroscopy*, Topics in Catalysis, 62 (2019) 712-723.
[11] X. Zhang, F. Ponte, E. Borfecchia, **A. Martini**, C. Sanchez-Cano, E. Sicilia, P.J. Sadler, *Glutathione activation of an organometallic half-sandwich anticancer drug candidate by ligand attack*, Chem. Commun., 55 (2019) 14602-14605.
[12] C. Buono, **A. Martini**, I.A. Pankin, D.K. Pappas, C. Negri, K. Kvande, K.A. Lomachenko, E. Borfecchia, *Local structure of Cu(I) ions in the MOR zeolite: A DFT-assisted XAS study*, Radiat. Phys. Chem., 175 (2020) 4.
[13] A.A. Guda, S.A. Guda, **A. Martini**, A.L. Bugaev, M.A. Soldatov, A.V. Soldatov, C. Lamberti, *Machine learning approaches to XANES spectra for quantitative 3D structural determination: The case of CO2 adsorption on CPO-27-Ni MOF*, Radiat. Phys. Chem., 175 (2020) 5.
[14] **A. Martini**, E. Borfecchia, *Spectral Decomposition of X-ray Absorption Spectroscopy Datasets: Methods and Applications*, Crystals, 10 (2020) 664.
[15] **A. Martini**$^*$, S.A. Guda, A.A. Guda, G. Smolentsev, A. Algasov, O. Usoltsev, M.A. Soldatov, A. Bugaev, Y. Rusalev, C. Lamberti, A.V. Soldatov, PyFitit: *The software for quantitative analysis of XANES spectra using machine-learning algorithms*, Computer Physics Communications, 250 (2020) 15.
[16] **A. Martini**$^*$, I.A. Pankin, A. Marsicano, K.A. Lomachenko, E. Borfecchia, *Wavelet analysis of a Cu-oxo zeolite EXAFS simulated spectrum*, Radiat. Phys. Chem., 175 (2020) 4.
[17] **A. Martini**, M. Signorile, C. Negri, K. Kvande, K.A. Lomachenko, S. Svelle, P. Beato, G. Berlier, E. Borfecchia, S. Bordiga, *EXAFS wavelet transform analysis of Cu-MOR zeolites for the direct methane to methanol conversion*, Phys. Chem. Chem. Phys., (2020).
[18] **A. Martini**$^*$, A. A. Guda, S. A. Guda, A. Dulina, F. Tavani, P. D'Angelo, E. Borfecchia, A. V. Soldatov, *Estimating a set of pure XANES spectra from multicomponent chemical mixtures using a transformation matrix-based approach*, XXVII Meeting of the Italian Synchrotron Radiation Society, Springer Proceedings in Physics, (2020), Accepted.
[19] C. Negri, T. Selleri, E. Borfecchia, **A. Martini**, K.A. Lomachenko, T.V.W. Janssens, M. Cutini, S. Bordiga, G. Berlier, *Structure and Reactivity of Oxygen-Bridged Diamino Dicopper(II) Complexes in Cu-Ion-Exchanged Chabazite Catalyst for NH3-Mediated Selective Catalytic Reduction*, Journal of the American Chemical Society, 142 (2020) 15884-15896.
[20] I.A. Pankin, E. Borfecchia, **A. Martini**, K.A. Lomachenko, C. Lamberti, A.V. Soldatov, *DFT-assisted XANES simulations to discriminate different monomeric Cu-II species in CHA catalysts*, Radiat. Phys. Chem., 175 (2020) 4.
[21] I.A. Pankin, **A. Martini**, K.A. Lomachenko, A.V. Soldatov, S. Bordiga, E. Borfecchia, *Identifying Cu-oxo species in Cu-zeolites by XAS: A theoretical survey by DFT-assisted XANES simulation and EXAFS wavelet transform*, Catalysis Today, 345 (2020) 125-135.

[22] E. Priola, G. Volpi, R. Rabezzana, E. Borfecchia, C. Garino, P. Benzi, **A. Martini**, L. Operti, E. Diana, *Bridging Solution and Solid-State Chemistry of Dicyanoaurate: The Case Study of Zn-Au Nucleation Units*, Inorg. Chem., 59 (2020) 203-213.
[23] D.H. Simonne, **A. Martini***, M. Signorile, A. Piovano, L. Braglia, P. Torelli, E. Borfecchia, G. Ricchiardi, *THORONDOR: a software for fast treatment and analysis of low-energy XAS data*, J. Synchrotron Radiat., 27 (2020).
[24] F. Tavani, **A. Martini**, G. Capocasa, S. Di Stefano, O. Lanzalunga, P. D'Angelo, *Direct Mechanistic Evidence for a Nonheme Complex Reaction through a Multivariate XAS Analysis*, Inorg. Chem., 59 (2020) 9979-9989.
[25] I. Pankin, H. I. Houeida, K.A. Lomachenko, S. Rasmussen, **A. Martini**, P. Bazin, V. Valtchev, M. Daturi, C. Lamberti, S. Bordiga, *Cu-and Fe-speciation in composite zeolite catalyst for selective catalytic reduction of* $NO_x$*: insights from operando XAS*, Catal. Sci. Technol., (2020), Accepted, (2020).

### *8.1.2 Papers submitted in international peer-reviewed journals (ISI Web of Science and/or Scopus).*

[1] F. Tavani, G. Capocasa, **A. Martini**, F. Sessa, S. Di Stefano, O. Lanzalunga, P. D'Angelo, *Direct structural and mechanistic insights into fast bimolecular chemical reactions in solution through a coupled XAS/UV-Vis multivariate statistical analysis*, Dalton Trans., (2020), Submitted.
[2] F. Tavani, G. Capocasa, **A. Martini**, F. Sessa, S. Di Stefano, O. Lanzalunga, P. D'Angelo, *Activation of C-H bonds by a nonheme iron(IV)-oxo complex: mechanistic evidence through a coupled EDXAS/UV-Vis multivariate analysis*, Phys. Chem. Chem. Phys., (2020), Submitted.
[3] C. Negri, E. Borfecchia, **A. Martini**, G. Deplano, K.A. Lomachenko, T.V.W. Janssen, G. Berlier, S. Bordiga, *In-situ X-ray absorption study of Cu species in Cu-CHA catalysts for* $NH_3$*-SCR during temperature-programmed reduction of NO/*$NH_3$, Res.Chem. Intermed., (2020), Submitted.

### *8.1.3 Papers in preparation, which will be submitted in international peer-reviewed journals (ISI Web of Science and/or Scopus).*

The (*) symbol indicates the corresponding author.
[1] **A. Martini***, A.A. Guda, A. S. Guda, O. Safonova, A.V. Soldatov, *Machine Learning Powered by Principa Component Descriptors as a Key for Sorted Structural Fit of XANES*.
[2] **A. Martini***, A.A. Guda, S. A. Guda, A. L. Bugaev, E. Borfecchia, A.V. Soldatov, *Revisiting the EXAFS fit through a Machine Learning based Algorithm*.
[3] A.A. Guda, S.A. Guda, **A. Martini**, A.N. Kravtsova, A. Algasov, S.P. Kubrin, A.L. Bugaev, L.V. Guda, D.D. Badyukov, A. V. Soldatov, *Improved Analysis of X-ray Absorption Spectra using Descriptors and Machine Learning Algorithms*.

## 8.2 CONTRIBUTION TO CONGRESSES AND OTHER SCIENTIFIC EVENTS

### *8.2.1 Oral contributions*

- **Martini**: *Application of Multivariate Techniques on in situ XAS data to determine Cu-speciation in zeolite catalysts*. The Smart Materials Research Institute meeting, Southern Federal University- Rostov on Don (Russia), 9/04/2018.
- **Martini**: *Revealing Cu speciation in Cu-CHA zeolites by Multivariate Techniques applied on in situ X-Ray Absorption Spectroscopy*. International Workshop for young researchers, Smart Materials & Mega-Scale Research Facilities, Southern Federal University, Rostov (Russia), 23/04/2018.
- **Martini**: *XAS Multivariate Curve Resolution (MCR) analysis applied to the Cu-CHA zeolite*, NIS Colloquium: *Cu-based zeolites, versatile materials for redox catalysis*, University of Turin (Italy), 20/07/2018.
- **Martini**: *Cu-oxo species: Preliminary results by multivariate and wavelet analysis*. The 7*th* International School for young researchers Smart Nanomaterials workshop, *Design of poly-functional structures: theory and synthesis*, Southern Federal University-Rostov on Don (Russia), 30/10/2018.
- **Martini**: *Multivariate techniques for spectroscopic data analysis*. Week of Science: The Smart Materials and Mega-class research facilities, Southern Federal University-Rostov on Don (Russia), 1/04/2019.
- **Martini**: *Retrieving quantitative structural information from XANES spectra by means of Multivariate and Machine Learning approaches*. Società Italiana Luce di Sincrotrone (SILS), Camerino (Italy), 9/09/2019.
- **Martini**: *PCA for theoretical training sets*. Introductory Machine Learning Seminar, Southern Federal University, Southern Federal University-Rostov on Don (Russia), 29/10/2019.
- **Martini**: *Retrieving quantitative structural information from X-ray absorption data using Machine Learning.* NIS Colloquium: *Machine Learning Meets Chemistry*, University of Turin (Italy), 17/02/2020.
- **Martini:** *Principal Component Analysis vs Linear Combination Fit*, Practical aspects of spectral data analysis powered by machine learning algorithms, Southern Federal University-Rostov on Don (Russia), 29/10/2020.

### *8.2.2 Poster contributions*

- **Martini et al.**: *Multivariate Analysis of in situ XAS to determine Cu-speciation in zeolite catalysts*,17*th* International Conference on X-ray Absorption Fine Structure, Krakow (Poland), 26/07/2018.
- **Martini et al.**: *Cu-oxo species in Zeolites: Preliminary Results by Wavelets Analysis*, 17*th* International Conference on X-ray Absorption Fine Structure, Krakow (Poland), 26/07/2018.
- **Martini et al.**: *Wavelet Analysis of in situ and operando EXAFS data: a qualitative and quantitative approach*. ESRF User-Meeting 2020, Grenoble (France), 3-5/02/2020.

### *8.2.3 School attended during the PhD.*

- MSSC2018 Summer School in *Ab initio Modelling of Solid State Chemistry*, Turin (Italy), 2-7/09/2018.
- Innovative Catalysis and Sustainability (ICS) Winter School, Bardonecchia (Italy), 7-11/01/2019.

## 8.3 TEACHING ACTIVITIES

Laboratory Assistant (25 hours) University of Turin (Dep. of Physics), *Matter Physics Laboratory* 1/10/2018-20/11/2018*,* Supervisor: Prof. E. Vittone.

## 8.4 EXPERIMENTS AT LARGE SCALE SYNCHROTRON FACILITIES

Member of the experimental participating on 15 experiments performed at different international synchrotron sources, mostly at the ESRF (France) and ELETTRA (Trieste) but also at Lund (Sweden):

- ESRF: 9 experiments−Beamlines: BM23, BM31, ID24 and ID26.
- ELETTRA: 5 experiments−Beamline: APE-HE and XAFS.
- MAX IV: 1 experiment−Beamline: Balder.

# ACKNOWLEDGEMENTS

All the results showed in this thesis has been obtained thanks to the help and friendship of several people of different nationalities who, during this three years of PhD, supported me with their advices, encouragements and joy. First of all, I want to express my deepest and sincere gratitude to Prof. Carlo Lamberti, my Mentor and Friend for his guidance and trust. With his constant enthusiasm and encouragements he transmitted the force needed to pursuit my dreams with tenancy and ardour. This thesis work is dedicated to his memory.

I would like to express my gratitude to my Italian supervisor Prof. Silvia Bordiga and co-tutor Dr. Elisa Borfecchia for their supervision, useful comment, patience and help. To Elisa, in particular, a big thanks for all those moment where in front of a cup of coffee she clarified my several doubts concerning Cu-exchanged zeolites and their related XAS spectra. I'm deeply grateful to my Russian supervisor Prof. Alexander V. Soldatov who with his kindness welcomed me inside the Smart Materials Research Institute in Rostov. There I had possibility to enrich my scientific knowledges next to an excellent pool of scientists. In particular I need to say a huge thank to Prof.(s) Alexander A. Guda and Sergey A. Guda who motivated and supported me to face new challenges concerning the XANES theory and were always available to discuss and solve my infinite … but convergent series of theoretical and coding problems. I thanks all the other colleagues of the Institute, in particular Mikhail, Aram, Oleg and Sergey with whom I shared several scientific discussions but also nice trips in the Russian Countryside and funny soccer matches. A special thanks goes to Ilia Pankin who helped me a lot, scientifically and personally demonstrating to be always a good friend especially during the several adventures that we had together in Italy, Russia and even at the ESRF.

I'm indebted with Prof. Gloria Berlier, Prof. Gabriele Ricchiardi, Prof. Elena Groppo, Prof. Paola D'Angelo and Francesco Tavani for the insightful discussions and the fruitful collaborations which allowed to find interesting application of some of the methodologies described in this thesis.

I owe my gratitude to Dr. Lorenzo Mino, who always come to me with a big smile and demonstrated a huge patience sharing with me his office. I'm thankful to all my colleagues and friends of the Departments of Chemistry and Physics with whom I shared several good times and jokes: Cutini, Rosangela, Chiara & Chiara, David, Guille, Ferrero, Panta, Pavlo, Yadi, Laura, Valentina and Sviatoslav plus my theoretical physicist friend Chiara. A big thanks goes also to the (old) guys of Via Quarello: Giorgia, Cesare, Alessandro and Matteo together with Luca Braglia.

Finally I want to thanks my Parents and Elena. They have been an incessant source of love, joy, support and strength during all these years and, for sure, I wouldn't be able to reach these achievements without them.